UNIVERSITÀ DELLA CALABRIA

Dipartimento di Ingegneria Civile

Dottorato di Ricerca in
Scienze e Ingegneria dell’Ambiente delle Costruzioni e dell’Energia

CICLO XXXII

ANALYSIS OF NONLINEAR PHENOMENA IN HETEROGENEOUS MATERIALS BY MEANS OF HOMOGENIZATION AND MULTISCALE TECHNIQUES

Settore Scientifico Disciplinare ICAR/08

Coordinatore:

Ch.mo Prof. *Salvatore Critelli*
Firma ____________________

Dottorando:

D[illegible]ng. *Andrea Pranno*
[redacted]

Supervisore/Tutor:

Ch.mo Prof. *Domenico P*[illegible]
Firma [redacted]

Ch.mo Prof. *F*[illegible]
Firma [redacted]

Abstract

Over the past decade, scientific and industrial communities have shared their expertise to improve mechanical and structural design favoring the exploration and development of new technologies, materials and advanced modeling methods with the aim to design structures with the highest structural performances. The most promising materials used in many advanced engineering applications are fiber- or particle-reinforced composite materials. Specifically, materials with periodically or randomly distributed inclusions embedded in a soft matrix offer excellent mechanical properties with respect to traditional materials (for instance, the capability to undergo large deformations). Recent applications of these innovative materials are advanced reinforced materials in the tire industry, nanostructured materials, high-performance structural components, advanced additive manufactured materials in the form of bio-inspired, functional or metamaterials, artificial muscles, tunable vibration dampers, magnetic actuators, energy-harvesting devices when these materials exhibit magneto- or electro-mechanical properties. Today the scientific community recognizes that, to develop new advanced materials capable of satisfying increasingly restrictive criteria, it is vital fully understanding the relationship between the macroscopic behavior of a material, and its microstructure. Composite materials are characterized by complex microstructures and they are commonly subjected also to complex loadings, therefore their macroscopic response can be evaluated by adopting advanced strategies of micro-macro bridging, such as numerical homogenization and multiscale techniques. The aim of this thesis is to provide theoretical and numerical methods able to model the mechanical response of heterogeneous materials (fiber- or particle-reinforced composite materials) in a large deformation context predicting the failure in terms of loss of stability considering also the interaction between microfractures and contact. In the past literature, several theories have been proposed on this topic, but they are prevalently limited to the analysis of microscopic and macroscopic instabilities for not damaged microstructures, whereas the problem of interaction between different microscopic failure modes in composite materials subjected to large deformations in a multiscale context still has not been investigated in-depth and it represents the main aspect of novelty of the present thesis.

The thesis starts with a literature review on the previously announced topic. Then, the basic hypotheses of the numerical homogenization strategy are given together with a review of the most recurring multiscale strategies in the modeling of the behavior of advanced composite materials following a classification based on the type of coupling between the microscopic and the macroscopic levels. In addition, a theoretical non-linear analysis of the homogenized response of periodic composite solids subjected to macroscopically uniform strains is given by including the effects of instabilities occurring at microscopic levels and the interaction between microfractures and buckling instabilities. Subsequently, the numerical results obtained were reported and discussed.

Firstly, the interaction between microfractures and buckling instabilities in unidirectional fiber-reinforced composite materials was investigated by means of the nonlinear homogenization theory. In such materials, the investigated interaction may lead to a strong decrease in the compressive strength of the composite material because buckling causes a large increase in energy release rate at the tips of preexisting cracks favoring crack propagation or interface debonding. Thus, microcracked composite materials characterized by hyperelastic constituents and subjected to macrostrain-driven loading paths were firstly investigated giving a theoretical formulation of instability and bifurcation phenomena. A quasi-static finite-strain continuum rate approach in a variational setting has been developed including contact and frictionless sliding effects. It worth noting that, the above developments show that non-standard self-contact terms must be included in the analysis for an accurate prediction of microscopic failure; these terms are usually neglected when contact is modelled in the framework of cohesive interface constitutive laws. The influence of the above-mentioned non-standard contributions on the instability and bifurcation critical loads in defected fiber-reinforced composites can be estimated in light of the results which will be presented in this thesis. Thus, the role of non-standard crack self-contact rate contributions to the stability and non-bifurcation conditions was pointed out by means of comparisons with simplified formulations and it was clearly shown that these contributions have a notable role in an accurate prediction of the real failure behavior of the composite solid.

Secondly, two multiscale modeling strategies have been adopted to analyze the microstructural instability in locally periodic fiber-reinforced composite materials subjected to general loading conditions in a large deformation context. The first strategy is a semiconcurrent multiscale method consisting in the derivation of the macroscopic constitutive response of the composite structure together with a microscopic stability analysis through a two-way computational homogenization scheme. The second approach is a novel hybrid hierarchical/concurrent multiscale approach able to combine the advantages inherent in the use of hierarchical and concurrent approaches and based on a two-level domain decomposition; such a method allows to replace the computationally onerous procedure of extracting the homogenized constitutive law for each time step through solving a BVP in each Gauss point by means of a macro-stress/macro-strain database obtained in a pre-processed step. The viability and accuracy of the proposed multiscale approaches in the context of the microscopic stability analysis in defected composite materials have been appropriately evaluated through comparisons with reference direct numerical simulations, by which the ability of the second approach in capturing the exact critical load factor and the boundary layer effects has been highlighted.

Finally, the novel hybrid multiscale strategy has been implemented also to predict the mechanical behavior of nacre-like composite material in a large deformation context with the purpose to design a human body protective bio-inspired material. Therefore, varying the main microstructural geometrical parameters (platelets aspect ratio and stiff-phase volume fraction), a comprehensive parametric analysis was performed analyzing the penetration resistance and flexibility by means of an indentation test and a three-point bending test, respectively. A material performance metric, incorporating the performance requirements of penetration resistance and flexibility in one parameter and called protecto-flexibility, was defined to investigate the role of microstructural parameters in an integrated measure. The results have been revealed that advantageous microstructured configurations can be used for the design and further optimization of the nacre-like composite material.

Sommario

Nell’ultimo decennio, le comunità scientifiche e industriali hanno congiunto le loro competenze con il fine di migliorare la progettazione strutturale e meccanica favorendo così la ricerca e lo sviluppo di nuove tecnologie, nuovi materiali e metodi di modellazione avanzati con l’obiettivo di progettare strutture all’avanguardia dal punto di vista prestazionale. I materiali più utilizzati nelle recenti applicazioni avanzate dell’ingegneria sono i materiali compositi rinforzati con fibre o particelle. Nello specifico, i materiali con inclusioni distribuite in modo periodico o in modo casuale e immerse in una matrice soffice, offrono eccezionali proprietà meccaniche rispetto ai materiali tradizionali, come ad esempio la capacità di poter subire grandi deformazioni.

Le recenti applicazioni ingegneristiche vedono l'applicazione di tali materiali avanzati sotto forma di materiali nanostrutturati, componenti strutturali ad alte prestazioni, materiali funzionali o metamateriali, muscoli artificiali e smorzatori di vibrazioni sintonizzabili.
Oggi la comunità scientifica riconosce che, per sviluppare nuovi materiali avanzati in grado di soddisfare criteri prestazionali sempre più restrittivi, è di vitale importanza comprendere appieno la relazione tra il comportamento macroscopico dei materiali e la loro microstruttura interna. I materiali compositi sono generalmente caratterizzati da microstrutture complesse, pertanto la loro risposta meccanica macroscopica può essere colta adottando strategie avanzate di "bridging micro-macro", come le tecniche di omogeneizzazione numerica e le tecniche multiscala.
La finalità del presente lavoro di tesi è quella di fornire dei modelli numerici atti a riprodurre la risposta meccanica di materiali eterogenei soggetti a deformazioni finite (nello specifico materiali compositi rinforzati con fibre o particelle) prevedendo il carico critico di collasso degli stessi in termini di perdita di stabilità e valutando inoltre l'influenza delle microfratture in presenza di contatto. Nella letteratura del passato sono stati riportati diversi studi sulle tematiche di interesse della presente tesi, tuttavia questi erano prevalentemente mirati all'analisi di instabilità microscopiche e macroscopiche in assenza di danneggiamento, mentre il problema dell'interazione tra le diverse modalità di danneggiamento microscopico in materiali compositi soggetti a deformazioni finite in un contesto di modellazione multiscala non risulta essere ancora studiato in modo approfondito e l'intento di colmare tale carenza rappresenta l'aspetto di novità del presente lavoro di tesi.
La tesi inizia con la ricostruzione dello stato dell'arte dei temi sopra evidenziati. Successivamente, si sono evidenziate le ipotesi alla base

della teoria dell’omogeneizzazione numerica unitamente a una panoramica sulle strategie multiscala più ricorrenti nella modellazione del comportamento dei materiali compositi avanzati seguendo una classificazione basata sulla tipologia di accoppiamento tra le diverse scale di osservazione (microscopica e macroscopica). Inoltre, è stata sviluppata un’analisi teorica non lineare della risposta omogeneizzata dei solidi compositi con microstruttura periodica e soggetti a stati di deformazione macroscopici uniformi includendo gli effetti delle instabilità che si verificano sia a livello macroscopico che a livello microscopico e gli effetti dell’instabilità microscopiche in presenza di contatto. Successivamente, si sono riportati i risultati analitici e numerici ottenuti.
In primo luogo si è studiata l’interazione tra le microfratture e le instabilità per buckling in materiali compositi rinforzati unidirezionalmente con fibre continue. In tali materiali, l’interazione tra le sopracitate forme di danneggiamento può provocare un forte aumento del tasso di rilascio di energia agli apici delle microfratture esistenti favorendo così la propagazione degli stessi o lo scollamento di interfaccia (debonding). Pertanto, si è sviluppata una formulazione teorica sui fenomeni di instabilità a biforcazione nei materiali compositi danneggiati, caratterizzati da componenti microstrutturali di tipo iperelastico e sottoposti a percorsi di carico guidati nelle deformazioni macroscopiche. Un approccio al continuo incrementale quasi-statico in deformazione finite in forma variazionale si è implementato includendo i fenomeni di contatto unilaterale e gli effetti degli scorrimenti in assenza di attrito. Dagli sviluppi teorici si è evinto che, per un’accurata previsione del collasso microscopico, è fondamentale includere i termini non-standard indotti dal contatto unilatero, i quali in genere, risultano essere trascurati adottando leggi di interfacce coesive per la modellazione del contatto tra le facce delle fratture in deformazioni finite.

L'influenza dei suddetti contributi sui carichi critici di instabilità e biforcazione in materiali compositi fibrorinforzati soggetti a danneggiamento può essere stimata alla luce dei risultati che verranno presentati nella presente tesi. Dunque, mediante confronti con formulazioni semplificate, è stato indagato il ruolo dei contributi incrementali non-standard agenti sulle facce delle fratture sottoposte a fenomeni di autocontatto e, da questo, si è chiaramente evinto che tali contributi, per i materiali compositi esaminati, svolgono un ruolo determinante nella previsione del carico critico di instabilità.
In secondo luogo, sono stati implementati due metodi multiscala per analizzare i fenomeni di instabilità microstrutturale in materiali compositi fibrorinforzati localmente periodici soggetti a condizioni di carico generali nell'ipotesi di deformazioni finite. Il primo metodo è un metodo semiconcorrente attraverso il quale la risposta costitutiva macroscopica del materiale composito è derivata, unitamente ad un'analisi di stabilità microscopica, sfruttando una strategia di omogeneizzazione computazionale a due vie in cui il passaggio di informazioni avviene dalla scala microscopica a quella macroscopica e viceversa.
Il secondo metodo è un nuovo approccio multiscala ibrido che combina i vantaggi insiti nell'utilizzo dei modelli gerarchici e concorrenti, basato su uno schema di decomposizione del dominio a due livelli. Tale metodo permette di sostituire l'onerosa procedura computazionale di estrazione della legge costitutiva per ogni passo di carico attraverso la risoluzione di n BVP (con n pari al numero di punti di Gauss) mediante un database macro-tensione/macro-deformazione elaborato in fase di preprocessing. L'applicabilità e l'accuratezza degli approcci multiscala proposti nel contesto dell'analisi di stabilità in materiali compositi danneggiati sono state opportunamente valutate attraverso confronti con simulazioni numeriche dirette di riferimento, grazie alle quali si è evinto

che il secondo metodo risulta essere più accurato nel cogliere agevolmente gli effetti di bordo e nel determinare il fattore di carico critico di instabilità.
Infine, l'innovativa strategia multiscala ibrida si è inoltre implementata, al fine di predire il comportamento meccanico di materiali compositi con una microstruttura ispirata alla madreperla in un contesto di deformazioni finite e di consentire la progettazione di un'efficiente architettura materiale per la protezione del corpo umano. Pertanto, è stata condotta un'ampia analisi parametrica al variare dei principali parametri microstrutturali (frazione di volume e proporzioni delle piastrine di rinforzo) analizzando la resistenza alla penetrazione e la flessibilità, rispettivamente mediante un test alla penetrazione e un test a flessione su tre punti. È stata definita una nuova metrica del materiale che incorpora i requisiti prestazionali di resistenza alla penetrazione e flessibilità, chiamata "protecto-flexibility", al fine di valutare il ruolo dei parametri microstrutturali investigati. Dai risultati ottenuti si è evinto che, tramite una modellazione multiscala ibrida, è possibile fornire configurazioni microstrutturali ottimizzate consentendo quindi di progettare materiali compositi ispirati alla madreperla con elevate prestazioni meccaniche.

Notations

$\boldsymbol{T}$	Cauchy stress tensor
C_e	Crack eccentricity
J'	Determinant of the 2D deformation gradient tensor
$[\![\boldsymbol{u}]\!]_{\Gamma_{c(i)}}$	Displacement jump at the deformed crack contact interface at a contact point pair $\left(\boldsymbol{X}^l,\boldsymbol{X}^u\right)_C$
k	Equivalent 2D bulk modulus
∂V	External RVE boundary in the deformed configuration
$\partial V_{(i)}$	External RVE boundary in the undeformed configuration
$\boldsymbol{T}_R$	First Piola-Kirchhoff stress tensor
$\boldsymbol{C}^R\left(\boldsymbol{X},\boldsymbol{F}\right)$	Fourth-order tensor of nominal moduli
$R\left(\dot{\bar{\boldsymbol{F}}},\dot{\boldsymbol{w}}_1,\dot{\boldsymbol{w}}_2\right)$	Functional associated to the non-bifurcation condition
$H^1\left(V_\#\right)$	Hilbert space of order one of vector valued functions periodic over V
L_c	Initial crack length
H_f	Initial fiber thickness
H_m	Initial matrix thickness
$K\left(\tau\right)$	Kinetic energy of the RVE at time τ
t	Loading parameter
$\boldsymbol{x}\left(\boldsymbol{X},t\right)$	Microscopic deformation field
$\boldsymbol{F}\left(\boldsymbol{X},t\right)$	Microscopic deformation gradient tensor
Λ	Minimum eigenvalue associated to the stability functional

$R_I\left(\dot{\bar{\boldsymbol{F}}},\dot{\boldsymbol{w}}_1,\dot{\boldsymbol{w}}_2\right)$	Modified functional associated to the non-bifurcation condition
$S_I\left(\bar{\boldsymbol{F}},\dot{\boldsymbol{w}}\right)$	Modified stability functional
$\boldsymbol{r}_R{}^u\ \left(\boldsymbol{r}_R{}^l\right)$	Nominal contact reaction on the upper (lower) crack surface
$[\![\boldsymbol{T}_R(\boldsymbol{X})]\!]_{\Gamma_c(i)}$	Nominal stress tensor jump at the undeformed crack contact interface
$\boldsymbol{t}_R$	Nominal traction vector
$\sigma_R{}^u\ \left(\sigma_R{}^l\right)$	Normal component of the nominal contact reaction on the upper (lower) crack surface
$[\![\dot{u}_n(\boldsymbol{X})]\!]_{\Gamma_c}$	Normal displacement rate jump at the deformed crack contact interface at a contact point pair $\left(\boldsymbol{X}^l,\boldsymbol{X}^u\right)_C$
$[\![\dot{w}_n(\boldsymbol{X})]\!]_{\Gamma_c}$	Normal fluctuation rate jump at the deformed crack contact interface at a contact point pair $\left(\boldsymbol{X}^l,\boldsymbol{X}^u\right)_C$
$\boldsymbol{n}_{(i)}$	Outward normal at $\boldsymbol{X}\in\partial V_{(i)}$
$\boldsymbol{n}^u(t)\ \left(\boldsymbol{n}^l(t)\right)$	Outward normal of the deformed upper (lower) contact surface
$\boldsymbol{n}^u_{(i)}\ \left(\boldsymbol{n}^l_{(i)}\right)$	Outward normal of the undeformed upper (lower) crack contact surface
$\left(\boldsymbol{X}^l,\boldsymbol{X}^u\right)_C$	Pair of crack surface points in contact in the deformed configuration
$\left(\boldsymbol{X}^l,\boldsymbol{X}^u\right)_{C(i)}$	Pair of crack surface points in contact in the undeformed configuration
$\boldsymbol{w}(\boldsymbol{X},t)$	Periodic fluctuation field
$\boldsymbol{x}$	Position vector of a material point in the deformed configuration
$\boldsymbol{X}$	Position vector of a material point in the undeformed configuration
$\boldsymbol{X}^u\ \left(\boldsymbol{X}^l\right)$	Position vector of a material point of the upper (lower) crack surface in the undeformed configuration
t_c^{CB}	Primary bifurcation load level of the Completely Bonded rate problem
t_c^{CF}	Primary bifurcation load level of the Completely Free rate problem

t_c^{IM}	Primary bifurcation load level of the crack contact Interface Model
t_c^{NC}	Primary bifurcation load level without crack contact contributions
t_{cE}	Primary eigenstate loading level
t_{cS}	Primary instability load level
t_{cS}^{CF}	Primary instability load level of the Completely Free rate problem
t_{cS}^{F}	Primary instability load level of the Free rate problem
$A^*(\bar{\boldsymbol{F}},\dot{\bar{\boldsymbol{F}}})$	Set of admissible fluctuation rates
$\mu_m\ (\mu_f)$	Shear modulus of the matrix (fiber) at zero strain
$B_{(i)}$	Solid part of the undeformed volume occupied by the RVE
$S(\bar{\boldsymbol{F}},\dot{\boldsymbol{w}})$	Stability functional
W	Strain energy density for plane strain deformations
dS	Surface elements in the deformed configuration
$dS_{(i)}$	Surface elements in the undeformed configuration
$dS_{(i)}^u\ (dS_{(i)}^l)$	Surface elements of the upper (lower) crack contact surface in the deformed configuration
$\boldsymbol{r}$	True contact reaction
σ	True normal contact reaction
$\Gamma_{(i)}^u\ (\Gamma_{(i)}^l)$	Undeformed lower (upper) crack surface
$\Gamma_{c(i)}^l\ (\Gamma_{c(i)}^u)$	Undeformed lower (upper) crack surface undergoing self-contact
L	Unit cell initial length
$U_{(i)}$	Unit cell volume in the undeformed configuration
$\delta\boldsymbol{u}$	Virtual displacement
$\delta L_{rate}(\Gamma_c)$	Virtual work of the contact reaction rate acting on the deformed contact interface
$\delta L_{rate}(\Gamma_{c(i)})$	Virtual work of the contact reaction rate acting on the undeformed contact interface

List of Figures

List of Tables

Contents

Introduction

Scientific and industrial societies have pooled their expertise over the past decades and have worked together to improve materials and structures design. This collaboration has culminated in the exploration and development of new materials, new technologies, and advanced modeling methods with the aim to design structures with the highest structural performances. Certainly, the most significant impact has been the development of new simulation methods. This marked evolution can be explained highlighting that computational potentiality has increased dramatically over the past few years; as a matter of fact both industrial and scientific communities are conscious that designing new complex structures and systems that simultaneously need to meet restrictive security, mechanical and, in some instances, economical constraints can only be accomplished by numerical simulations. Even though significant progress has been made in simulating different phenomena, more developments are still needed. This is particularly true for the computational techniques and algorithms used to investigate the behavior of materials with a heterogeneous microstructure (see for instance Fig. 1) and subjected to complex loading conditions.

This heterogeneity has a substantial impact on the macroscopic behavior of multi-phase materials, in fact, several phenomena arising at the macroscopic level derive from the mechanics and physics of the microstructure. The characteristic size of such materials is typically the scale of the microstructural heterogeneities and defects, in fact, nowadays, the intrinsic role of the observation scales in mechanics of heterogeneous materials is, at this point, well known. Since it has become clear over time that even smaller scales can have a pronounced effect on the macro-level, it is becoming crucial the understanding the mechanical response of the materials at the micro-scale.

In order to model the behavior of materials, two distinct methods can be followed: phenomenological and micromechanical approaches.

In the first one, through the definition of continuous constitutive relations commonly based of phenomenological assumptions, the material characterization is accomplished. The second approach, instead, is based on the strategy to consider information from the microstructure exclusively.

It is clear that the underlying microstructural character cannot be trivially separated from the macroscopic governing equations and, in this way, multi-scale approaches, which incorporate smaller and larger sizes, have arisen recently.

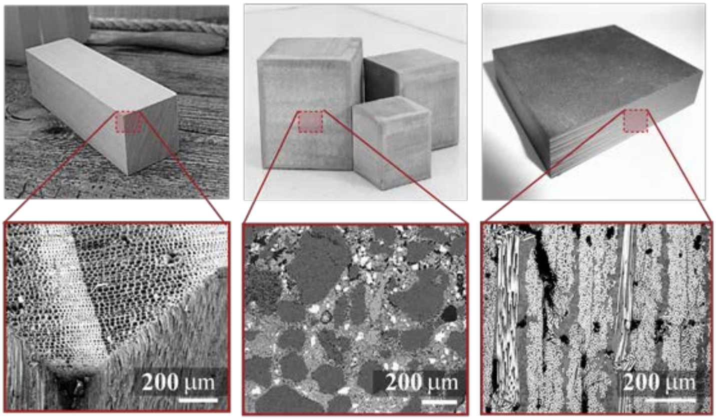

Fig.1 Microstructure examples in wood, concrete and composite laminate.

Although homogenization of heterogeneous materials was one of the first multi-scale mechanical methods, it was initially developed for elastic problems, in which the small scale in the computational process can often be excluded. But, for more complex nonlinear problems, this is obviously not viable.

Since several problems necessitate a multiscale explicit solution, requiring iterative solution processes at each scale with high computational costs, the main focus of this thesis is to develop heuristic advanced computational strategies to study from a numerical point of view the nonlinear phenomena (such as microfractures, contact and instabilities) in heterogeneous materials.

Nonlinearities in heterogeneous materials

The analysis of the interaction between microstructural phenomena and macroscopic behavior not only makes it possible to model accurately the behavior of multi-phase structures, but it also offers a method for designing material microstructures exhibiting a macroscopic behavior with prearranged characteristics. In micro-applications, the microstructure, in relation to the component size, is no longer negligible, resulting in a so-called size effect. Advanced forming operations often require a product to undergo complex loading paths that can produce microstructural evolutions and resulting in various microstructural responses. From an economic point of view, it is hardly feasible to conduct straightforward experimental measurements on a variety of product specimens for different sizes and loading paths, with different phase geometrical properties (volume fraction and aspect ratio). Consequently, modeling approaches that provide a better understanding of micro-macro and structure-property relationships in multi-phase materials are clearly needed. Regardless of the type of material (metal, polymer, natural, composite), for several reasons the homogeneity hypothesis could be a too restrictive assumption; as a matter of fact, diving into the material microstructures of advanced composites, different features can be observed such as: voids, micro-cracks and inclusions, which can interact in a complex manner and have a significant impact on overall material properties and performance.

For instance, in the past few years, materials reinforced with particles, platelets of fibers have been increasingly investigated to meet the increasing demands of a wide range of composite materials used in many fields of engineering [1–7]. Today, these materials find application in the form of advanced composites (for instance advanced metal, ceramic or polymer matrix composites), bio-inspired materials (for instance staggered bone-, tooth- or nacre-like composites) and metamaterials (piezoelectric polymers, shape memory alloys, electro-active or magneto-active polymers). The enhanced mechanical properties and the additional functionalities of such materials are provided by the strong interaction between a weak material, usually known as matrix, and a stiffer material, usually known as reinforcement.

Ideally, the models adopted to simulate the behavior of advanced composite materials should be accurate and relatively simple, so that they can be implemented in standard finite element packages to solve interesting structural issues. For two reasons, the development of accurate modeling strategies represents a significant challenge: firstly, the common constitutive models adopted to model advanced composite materials are nonlinear; secondly, due to the finite geometry changes caused by loadings, there is the additional complication of the evolution of the microstructure.

This context motivates the significance to carry out theoretical studies focused on the finite strain behavior of such materials with special attention to the prediction of the onset of microscopic failure mechanisms by investigating their macroscopic (homogenized) behavior. As a matter of fact, the study of these failure mechanisms, is a challenging task requiring the use of sophisticated techniques able to avoid a direct modeling of all microstructural details, a procedure which is unpractical due to the required large computational effort. Among the variegated failure mechanisms affecting composite materials subjected to large deformations, loss of composite integrity (fracture, delamination and damage, see for instance Fig. 2) and local buckling or loss of microscopic stability are the most common ones.

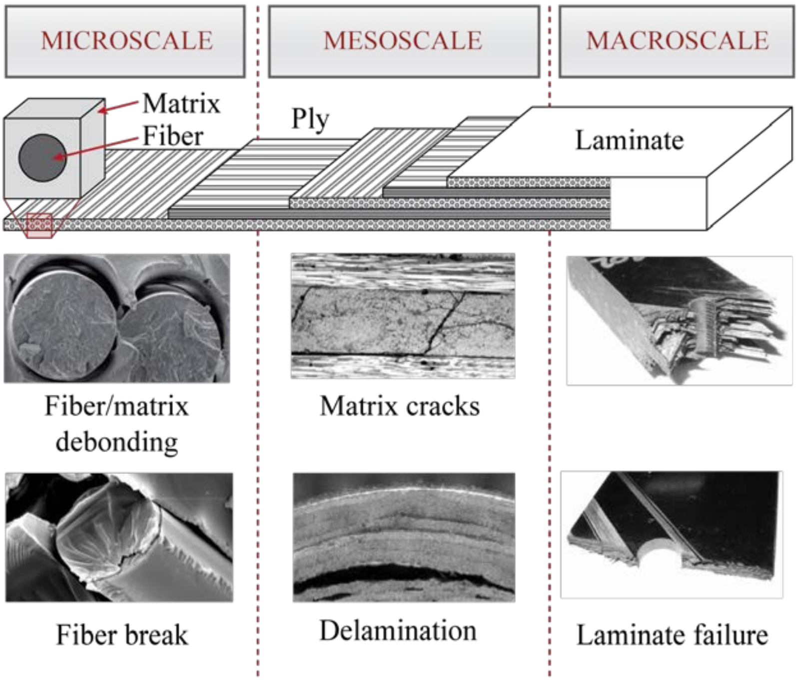

Fig.2 Examples of failure mechanisms affecting composite materials at different scale of observation.

In the former case, different approaches can be adopted in order to account for microstructural evolution associated with crack propagation within each constituent or at their interfaces. These approaches, mainly proposed within the context of small deformations but also generalizable to large deformations with relatively simplicity, frequently adopt first-order homogenization (see, for instance, [8–13]) and/or multi-scale schemes (e.g. [14–19]) often assuming a periodic microstructural scheme and requiring the development of specialized numerical procedures essentially based on the finite element method. Generally speaking the homogenization approaches can be adopted only when the assumptions of periodicity and scale separation are reasonably satisfied,

whereas multiscale schemes (such as the semiconcurrent, concurrent or asymptotic expansion ones), overcome these limitations and are able to accurately represent microstructural evolution due to coalescence of micro-cracks and to material and/or geometrical nonlinearities.
In the latter case, for undefected composite materials several theoretical and numerical studies on the occurrence of instabilities at the scale of the microstructure have been performed in the literature, in order to determine the influence of these phenomena on the nonlinear macroscopic response of the composite solid [20–28]. Generally speaking instability phenomena in composite materials must be investigated at different length scales (see, for instance, [20–24,26]) and both geometrical and constitutive nonlinearities must be incorporated in the analysis (see, for instance, [25,29]).
After the pioneering study of [20] devoted to layered composites, the connections between microscopic and macroscopic instabilities for hyperelastic materials with a periodic microstructure were rigorously investigated in [21], where it was shown that global or long wavelength instabilities lead to the loss of strong ellipticity condition for the unit cell homogenized moduli tensor, a situation corresponding to macroscopic instability. Following the above mentioned works, microscopic and macroscopic instabilities and their interrelationships under plane-strain condition in hyperelastic layered and particle-reinforced periodic composites have been widely investigated (see, for instance, [24,26,27]) by using the Bloch-Floquet technique also in conjunction with the finite element method when analytical solutions are not viable (as in the case of complex 2D particle composites, cellular microstructures, 3D fiber composites). The above investigations have pointed out that while the onset of the macroscopic instabilities, characterized by wavelengths significantly larger than the microstructure characteristic

size, can be predicted by the loss of ellipticity analysis requiring simply the evaluation of the one-cell homogenized tensor of elastic moduli, the prediction of local instability modes with a finite wavelength is a more difficult task due to the theoretically infinite nature of the analysis domain and requires sophisticated techniques such as Bloch wave stability calculations or direct finite element discretization of the unit cell assembly. In this case, the macroscopic constitutive stability measures can be adopted in order to obtain conservative prediction of the microscopic stability region [25].

Since the above studies were prevalently limited to the analysis of microscopic and macroscopic instabilities for undefected microstructures, the problem of interaction between different microscopic failure modes in composite materials subjected to large deformations remains essentially open, although it may have a detrimental effect on the overall failure response of composite materials. This because a detailed continuum analysis of composite solids taking into account the coupling between different failure mechanisms in these materials requires a huge computational effort since a very fine numerical model (usually implemented in a finite element approach) must be adopted in order to accurately describe the different sources of nonlinearity (for instance related to damage, constitutive and geometrical effects). In some recent studies the influence of microscopic fracture processes eventually involving self-contact between crack surfaces on the nonlinear homogenized behavior of composite solids, have been analyzed pointing out some interesting features characterizing the coupled effects of fracture and instability failure mechanisms. Specifically, the relation between intergranular decohesion and macroscopic instabilities has been studied in granular materials with elastic grains by using a two-scale computational homogenization approach in [30], a general analysis of instability and bifurcation phenomena have been carried out by [31] by also formulating upper and lower bounds to primary instability and bifurcation loads, for periodic elastic composites with micro-cracks in unilateral self-contact finitely strained along macroscopic loading paths, whereas special classes of instability and bifurcation behaviors have been determined in [32]. One of the distinctive features occurring in microfractured composite solids with respect to the undefected case is that microscopic primary instabilities may not coincide with primary bifurcations owing to nonlinearities introduced in the analysis by crack surface self-contact incremental loadings ([31,32]). Moreover, the relations between microstructural instability mechanisms and macroscopic instabilities have been studied in [33] for microcracked composites undergoing contact along crack surfaces, by also determining the structure and properties of the resulting macroscopic constitutive response.

For unidirectional fiber-reinforced or layered composites prevalently loaded in compression along the fiber direction, failure initiated by fiber microbuckling can be considered one of the most prevalent failure mode [34–36] and may promote the initiation and propagation of cracks or interface debonding at the microstructural level, a phenomenon similar to delamination buckling or buckling induced debonding in composite laminates or structural elements strengthened using composite layers (see, for instance [37] and [38], respectively).

Recently, new composite materials have been examined in depth promoting new developments by virtue of their enhanced mechanical properties and additional functionalities provided by the strong interaction between a weak material known as matrix and a stiffer material (known as reinforcement). Among these, composite materials inspired by biological structures, such as bone and nacre materials [39], are currently the focus of extensive research devoting significant effort to obtain optimized structural constituents. For instance, a nacre-like composite is usually composed of 95% of high aspect ratio stiff material (in the form of platelets, also referred to as inclusions) and of 5% of soft material in a staggered structure with a brick-and-mortar arrangement, and it exhibits exceptional toughness and strength under tension in the direction parallel to the longitudinal platelet axis but results weak in the transverse direction [40,41]. Several authors reported that the mechanical properties of nacre-like microstructures are mostly characterized by the interaction between the platelets and that the enhanced mechanical performances are provided by several mechanisms acting on distinct length scales [42]. Consequently, understanding the platelet's interaction and the mechanical properties of the bonding interfaces between soft and stiff phases is necessary to elucidate the microstructure-property relations. This understanding will enable design of materials with enhanced mechanical properties – including stiffness, toughness, ductility or impact and penetration resistance – through tailored choices of constituent materials and geometrical arrangements. For instance, the sliding resistance of platelets can be increased actuating an interlocking mechanism by changing the waviness of the platelet surfaces [42]. The capability of producing microstructures with a high geometrical complexity – provided by the recent development in the additive manufacturing (AM) or 3D printing – opened new ways for mechanical characterization of bio-inspired composites at different length scales [43]. For instance, a fracture response was analyzed on a biomaterial composite with a bone-like microstructure [44], the performance of a nacre-like composite panel was investigated in terms of deformation and energy dissipation [45], a design strategy of isotropic two-dimensional structural composites consisting of stiff and soft constituents arranged in

square, triangular, and quasicrystal lattices was defined [46], a structure created by mimicking fish armor was experimentally tested to reveal its ability to provide protection against penetration while preserving flexibility [47], the overall strength of bio-inspired staggered composites was investigated by employing a micromechanical analysis and by experimental tests on 3D printed composite materials [48], the failure mechanisms of bio-inspired composites subjected to nonaligned loadings was investigated using analytical models and experimental tests [49]. Generally speaking, composite materials, owing to their intrinsic heterogeneities, are commonly afflicted by several nonlinear phenomena especially when they are used in high-performance applications involving a microstructural evolution due to loss of composite integrity (coalescence of micro-cracks, delamination, interface debonding, etc. [50,51]) or to geometrical and/or material nonlinearities induced by large deformations (micro-buckling, ovalization, alternate void expansion [52–55]). Recent studies reported the influence of nonlinear phenomena on the macroscopic response in undamaged hyperelastic material models [56–62], and the role of interactions between different microscopic failure modes (fracture and instability) [63–67].
In the next paragraph, the previous attempts to model the effective behavior of heterogeneous materials (for instance, fiber- or particle-reinforced composite) are briefly enumerated to provide an overview of available methods.

Overview on homogenization and multiscale modeling

The biggest task of multiscale modeling consists of deducing the relationships that bridge diverse length scales. Generally, multiscale strategies have the goal to predict macroscopic properties of heterogeneous

materials by taking into account the geometrical and physical details of the microstructure requiring hence an adequate description of the microconstituent phases and of the relative interfaces at the microscale.
A variety of approaches have been suggested in the literature to bridge the scales: homogenization methods represent certainly one of the largest classes of bridging scale methods. The term “homogenization” was coined in 1976 by an American mathematician: Ivo Babuška in its work [68] in which the homogenization has been defined as “an approach which studies the macroscopic behavior of a medium by its microscopic properties”. Early advances in homogenization field were taken a long time ago when the curiosity in the heterogeneous material micromechanics became more prominent.
Preliminary theories date back to the nineteenth century, when the rule of mixtures was first adopted by Voigt (1887) [69] and followed by Sachs (1928) [70] typically for composite systems; later the Reuss estimate (1929) [71] and the Taylor model (1938) [72] were derived typically for polycrystals. Growing interest in composite materials was the main motivation for greater advances in homogenization.
The earliest known contribution probably was the work of Eshelby (1957) [73], in which the elastic solution is given for an ellipsoidal region in an infinite medium having elastic constants different from those of the rest of the material. These first steps led to the foundation of a new field by Hill (1965) [74] called “continuum micromechanics”, that since then, it has been greatly extended and that still have had a marked influence today; as a matter of fact, the use of continuum mechanics at the level of heterogeneities to deduce macroscopic constitutive relations was one of the essential characteristics of the micromechanical methods available at that time.

The second half of the twentieth century (1950-1980), with the pioneering works done by Kröner [75], Hashin and Shtrikman [76], Hill [77], Mori and Tanaka [78], Willis [79] and Babuška [80], was distinguished by significant progress in the homogenization and multiscale modeling applied at heterogeneous elastic solids

In this period, a few authors took first steps towards extending the already developed elastic homogenization theories and variational principles into the nonlinear regime [74,81,82], whereas in the 1980s and 1990s many more papers on these fields appeared, treating subjects as elastoplasticity, viscoelasticity and nonlinear elasticity (for instance the works done by Nemat-Nasser and Obata [83], Ponte Castañeda [84], Suquet [85], Willis [86], Nemat-Nasser and Hori [87], Zaoui and Masson [88] and others).

The developments in numerical homogenization were fundamental to the growth of homogenization engineering applications; in this context, the contribute of Sanchez-Palencia in [89] acted as an inspiration for researchers in computational mechanics.

Artola and Duvaut [90] and Suquet [91] dedicated themselves to the research of homogenization theory within the context of heterogeneous and composite materials mechanics which prompted different engineering applications of numerical simulation performance.

When the common ground has been reached between engineering and mathematical homogenization, the homogenization process, supported by computationally advanced solution methods, has started to dominate in the computational mechanic field; thus, the homogenization approach has become a common tool for characterizing the mechanical properties of heterogeneous materials with (periodic or random) microstructures and it is now recognized as one of the robust theoretical background for the numerical homogenization. At the end of the 20th century, the steady increase in the computational power available has contributed to developing the mathematical discipline called “Multi-scale Mechanics”. Since then, several milestones have been made, and in the (near) future, even more, can be predicted. Multiscale modeling of non-linear behavior of heterogeneous materials is a so large field that it is almost impossible to give a complete outline of all the methods developed in the past; therefore ,a brief overview will be provided here, with particular emphasis on the different classifications that can be identified in the framework of multiscale methods. From a methodological perspective, it is possible to identify different categories of multiscale methods [92–95], closely linked to the location and the geometry of the heterogeneous scale. The first category concerns problems with isolated details such as crack and defects, that need to be treated with high accuracy and resolution. That form of problem is also often referred to as “multiple scales” rather than multiscale because the problem of the fine scale is confined to a small part of the global domain. The second category concerns problems in which the macroscopic response is extracted considering a large part of the domain, revealing self-similarity across the scales.

Another common classification is based on type of coupling between the microscale and macroscale problems and identifies multiscale methods in three different subcategories: hierarchical, semi-concurrent and concurrent methods.

In hierarchical methods, during the micro-to-macro transition step, the information is transferred from lower to higher scales establishing a “one-way” bottom-up coupling between the microscopic and macroscopic problems. Such strategy is efficient computationally and in determining the macroscopic behavior of heterogeneous materials in terms of stiffness and strength, but shows a limited capability in the prediction of nonlinear phenomena. However, they have been applied to investigate a wide range of problems, such as multiphase flow in porous media [96,97], pullout tests and damage in nanocomposites [98], heat affected zone in welded connection [99], fracture in crystalline solids [100].

In semiconcurrent multiscale methods the information is transferred from lower to higher scales and vice versa, establishing a “two-way” coupling performed on the fly during the simulation. Such methods are useful when dealing with microscopic nonlinear phenomena due to evolving defects whose spatial configuration is not known a priori. The classical semiconcurrent model is called FE^2 method [101] that was initially developed for intact materials and then extended to material failure problems [102–106]. The main idea of such approach is to link a microscopic boundary value problem (BPV), defined on an RVE, at each quadrature point (Gauss point) of the macroscopic domain. The macroscopic strain provides the boundary data given in input at the microscopic problem (macro-to-micro transition or localization step). Once the set of all BVPs is solved, the results are passed back in output to the macroscopic problem in terms of overall stress field and tangent operator (micro-to-macro transition or homogenization step). The steps are carried out within an incremental-iterative nested solution scheme defining a weak coupling between the scales, and it is worth noting that the microscopic problems are decoupled to each other leading to a lower computational effort only in presence of an effective core processor parallelization implemented in the solver procedure. Other semiconcurrent approaches have been proposed in the literature to overcome the dependence of the macroscopic problem solution on the RVE size in the case of overall mechanical behaviors exhibiting softening or, generally, in the case of not completely satisfying the scale separation assumption, for instance in the case of localization of deformation. One of them is a coupled-volume method, proposed in [107] and [108], that is developed attaching the BVP at each macroelement of the macroscopic problem, rather than to each Gauss point.

In concurrent multiscale methods the information is transferred from the coarse scale to the fine scale and vice versa in the same macroscopic domain leading to a “two-way” strong coupling. In other words, this approach abandons the concept of scale transition adopting the concept of scale embedding, according to which different scales coexist in the macroscopic model and they are coupled usually at the common interfaces by enforcing the compatibility conditions. Such methods can be regarded as falling within the class of the so-called domain decomposition methods (DDM), since the numerical model describing the composite structure is decomposed into critical domain characterized by a fine discretization and into non critical domains characterized by a coarse discretization, which are simultaneously solved. Such multiscale models are widely adopted to modeling fracture [109,110], for instance in [111] is proposed a concurrent coupling scheme with application to dynamic brittle fracture, in [112] has been proposed to simulate complex crack growth patterns in thin-walled structures. A concurrent multiscale method is proposed also in [113] to study matrix/inter-phase fracture and fiber sliding in brittle ceramics and in [114] to overcome the existing limitations on homogenization in the presence of strain localization in masonry structures, proposing an adaptive zooming-in criterion in a multilevel domain.

While hierarchical and semiconcurrent multiscale approaches fail to fulfill separation of length scales in the case of fracture, on the contrary

concurrent approaches are most suitable to model material failure as the fine scale is directly inserted into the macroscopic model.
In Section 2, more information and computational detailed will be given about the multiscale approaches used in the numerical simulations reported in Sections 4. Particularly, a special attention is given to the coupled-volume multiscale approach and to a novel hybrid hierarchical/concurrent multiscale approach proposed to analyze the nonlinear behavior of composite materials reinforced with continuous or discontinuous fibers.

Scope and outline

Today is widely accepted by the scientific community that it is vital to fully understand the relationship between the material's macroscopic behavior and its microstructure in order to develop new advanced materials capable of satisfying restrictive criteria. The mechanical behavior of the heterogeneous materials subjected to complex loadings strongly dependents on their microstructure and the mechanical characterization is only possible by formulating and developing new micro-macro strategies. Within this framework, computational homogenization and multiscale strategies can be adopted to address this challenge.
The main scope of this thesis is to develop a numerical framework able to model the mechanical response of heterogeneous materials at finite strains (fiber- or particle-reinforced composite materials) and predict the failure in terms of loss of stability evaluating also the interaction with other forms of nonlinearities, such as microfracture and contact, in a multiscale framework. To the best authors' knowledge, this issue has not been investigated previously in the past literature, and thus represents the main aspect of novelty of the present thesis. For this purpose,

the thesis started with an introduction giving a global overview of the state-of-art on the present topic.

In Chapter 1 the basic hypotheses of the numerical homogenization strategy are discussed together with the formulation of the microstructural boundary value problem and the coupling between the micro and macrolevel at finite strains based on the averaging theorems. In addition, some remarks on the admissible kinematical boundary conditions are given.

Chapter 2 is devoted to a review of multiscale approaches for advanced composite materials following a classification based on the type of coupling between the microscopic and the macroscopic levels.

Chapter 3 is concerned with a theoretical non-linear analysis of the homogenized response of damaged composite solids with periodic microstructure subjected to macroscopically uniform strain, by including the effects of instabilities and contact occurring at microscopic level. The theory, formulated for incrementally linear materials, provides an original closed-form representation of homogenized material response which puts in evidence the competing effects of local constitutive response and of microstructural heterogeneity. These analytical developments provide a basis to investigate the effectiveness of the continuum rate formulation of the microscopic equilibrium problem the prediction of microscopic instability phenomena considering also the interaction between buckling instabilities and fracture in unidirectional fiber reinforced composites. In such materials, since buckling causes a large increase in energy release rate at the tips of preexisting cracks favoring crack propagation or interface debonding, the investigated interaction may lead to a strong decrease in the compressive strength of the composite material.

Thus, the theoretical formulation of instability and bifurcation phenomena for microcracked composite materials characterized by hyperelastic constituents and subjected to a macrostrain driven loading path has been firstly considered. A quasi-static finite-strain continuum rate approach in a variational setting was developed by using cohesive models adopting interface traction-separation laws formulated including contact and frictional sliding effects in cases where significant normal compression acts on the interface. When such interface constitutive laws are adopted to model contact between crack faces in a large deformation context, non-standard self-contact terms must be included in the analysis and their influence on the instability and bifurcation critical loads can be estimated in light of the results which will be presented in this thesis. Thus, the role of non-standard crack self-contact rate contributions to the stability and non-bifurcation conditions was pointed out by means of comparisons with simplified formulations which do not adopt a full finite deformation approach to model contact phenomena occurring along crack surfaces. In order to study the compressive failure problem of a periodic elastic fiber reinforced composite material with sufficient generality, an extensive set of numerical applications has been carried out including different geometrical configurations for a composite microstructure driven along macroscopic uniaxial paths (Section 3.4.2) and macroscopic biaxial paths (Section 3.4.3) and containing microcracks within the matrix or at the fiber/matrix interface.

In Chapter 4, two different multiscale modeling approaches have been adopted firstly to analyze the microstructural instability-induced failure in locally periodic fiber-reinforced composite materials subjected to general loading conditions in a large deformation context. The first approach is a semiconcurrent multiscale strategy consisting in the “on-the-fly" derivation of the macroscopic constitutive response of the composite structure together with its microscopic stability properties through a two-way computational homogenization scheme. The second approach is a novel hybrid hierarchical/concurrent multiscale approach relying on a two-level domain decomposition scheme used in conjunction with a nonlinear homogenization scheme performed at the preprocessing stage. The main idea of the proposed hybrid multiscale approach is to combine the advantages of hierarchical and concurrent approaches using a numerical strategy that is able to replace the typical procedure of extracting the homogenized constitutive law for each time step solving a BVP in each Gauss point with a macro-stress/macro-strain database obtained in a pre-processing step. Both multiscale approaches have been appropriately validated through comparisons with reference direct numerical simulations, by which the capability of the hybrid approach in capturing the exact stability critical load factor and the boundary layer effects has been demonstrated. Secondly, the novel hybrid multiscale strategy was proposed also to predict the mechanical behavior of nacre-like composite material in a large deformation context with the purpose of identifying the best compromise between penetration resistance and flexibility to design a body protective bio-inspired material architecture. Therefore, a comprehensive parametric analysis with respect to the main microstructural geometrical parameters (platelets aspect ratio and stiff-phase volume fraction), governing the macroscopic behavior of bio-inspired nacre-like composite was performed. To this end, a material performance metric, called protecto-flexibility, incorporating the performance requirements of penetration resistance and flexibility in one parameter, was analyzed to investigate the role of microstructural parameters in this integrated measure. Thus, advantageous microstructured configurations that can be used for design and further optimization of the nacre-like composite material. Finally, some concluding remarks are given, together with some future perspectives of this work.

1

Finite-strain numerical homogenization

In this chapter the basic hypotheses of finite-strain numerical homogenization strategies are discussed together with the formulation of the microstructural boundary value problem and the coupling between the micro and macrolevel at finite strains based on the averaging theorems. In addition, some remarks on the admissible kinematical boundary conditions are given.

1.1 Basic Hypotheses

Numerical homogenization is a technique based on the derivation of the macroscopic constitutive response of heterogeneous materials from the local microstructure representative of the entire solid continua, by means of the solution of a microstructural boundary value problem (BPV). Generally speaking, the numerical homogenization procedure consists of four steps: (i) definition of a representative volume element (called RVE) or a repeated unit cell (called RUC) for which, the mechanical behavior of each microstructural constituent is assumed to be known; (ii) definition of the microscopic boundary conditions extracted from the macroscopic variables, given as input, and their assignment on the boundaries of the RVE (transition from macro to micro); (iii) extracting the output variables from the solution of the boundary value problem (BVP) associated to the RVE (transition from micro to macro); (iv) obtaining the homogenized response in terms of relation between input and output macroscopic variables. It is worth noting that, since the macroscopic constitutive response is obtained from the solution of the microscopic BVP, no explicit assumptions are required on the constitutive response at the macroscale; and that also the macroscopic constitutive tangent operator could be derived from the microscopic tangent operator in different manners (for instance, static condensation or linear perturbation methods). The homogenized microstructure could be constituted by different phases characterized by arbitrary nonlinear constitutive models, as a matter of fact, if the microstructural constituents are mechanically formulated in a nonlinear framework, the computational homogenization can be formulated at finite strains in a simple way. The procedure of the first-order computational homogenization scheme starts from the assumptions that the solid media can be considered macroscopically homogeneous and microscopically heterogeneous (for instance, microstructures characterized by the presence of inclusions, grains, porous or interfaces) for which a representative volume element is identifiable; and that it is possible to distinguish different length scales in a generic solid media as explained in the following.

1.1.1 Concept of a representative volume element

A representative volume element is a model of the microstructured solid for which is required the response of the related homogenized continuum, hence the choice of the RVE strongly influences the accuracy of the homogenized heterogeneous material response. Different RVE definitions can be found in the literature, for instance:

- The RVE is “the smallest material volume element of the composite for which the usual spatially constant overall modulus macroscopic constitutive representation is a sufficiently accurate model to represent mean constitutive response”, [115].
- The RVE size “should be large enough with respect to the individual grain size in order to define overall quantities such as stresses and strains, but it should be small enough in order not to hide macroscopic heterogeneity”, [116].
- The RVE is a microscopic sample that fulfills all the following requirements: “an increase in its size does not lead to considerable differences in the homogenized properties, the microscopic sample is large enough so that the homogenized properties are independent of the microstructural randomness, and its size is much smaller than the macroscopic dimension”, [117].

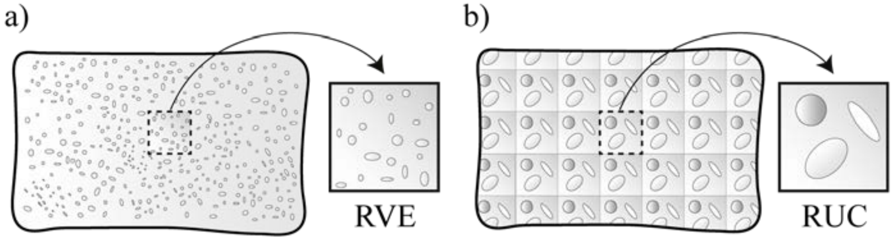

Fig. 1.1 Geometric representation of solid microstructures adopted in micromechanical analyses: statistically representative sample characterized by a RVE (a) and periodic samples characterized by a RUC (b).

- The RVE is "a sample that is structurally entirely typical of the whole mixture on average, and contains a sufficient number of inclusions for the apparent overall moduli to be effectively independent of the surface values of traction and displacement, so long as these values are macroscopically uniform", [118].
- The RVE is a material sample that "includes the most dominant features that have first-order influence on the overall properties of interest and, at the same time, yields the simplest model. This can only be done through a coordinated sequence of microscopic (small-scale) and macroscopic (continuum-scale) observation, experimentation, and analysis", [119].
- The RVE size can be defined as the "minimum size of a microstructural cell that fulfills the requirement of statistical homogeneity. As such, it is a lower bound: larger microstructural cells behave similarly while smaller microstructural cells do not", [120].

From these definitions appears that the RVE can be defined in two significantly different ways. The first one sees the RVE described as a statically representative sample of the macro homogeneity; the second one, instead, sees the RVE identified as the smallest microstructural material volume element that represents the overall macroscopic properties in an accurate manner. The latter definition leads to RVE sizes smaller than the statistical definition described above, and the minimum RVE size is strictly influenced by the macroscopic loading path, type of material behavior and difference in the properties of heterogeneities. These definitions involve the concepts of periodicity and statistical homogeneity based on the concepts of RVE and RUC.

1.1.2 Remarks on RVE and RUC

As discussed in [121] and illustrated in Fig. 1.1, homogenization analyses are typically performed employing the concept of RVE, characterizing heterogeneous materials with statistically or macroscopically homogeneous microstructures at an opportune scale, or employing the concept of RUC, characterizing periodic heterogeneous materials which are composed by repeating unit cells assembled together into an infinite array. Specifically, the RVE-based homogenization analyses are developed on the coincidence of the homogenized response obtained by imposing homogeneous traction boundary conditions and linear displacement boundary conditions; while the RUC-based homogenization analyses are developed on the combination of periodic displacement boundary conditions and antiperiodic traction boundary conditions. In the literature [122–129], the concepts of RVE and RUC are often confused and used with the same meaning, but several works were published on the comparison of the complete set of homogenized elastic moduli extracted by means of RVE-based and RUC-based homogenization procedure highlighting that, in general, homogenized elastic moduli of an heterogeneous RVE under homogeneous displacement and traction boundary conditions approach to the homogenized elastic moduli of the same RVE under

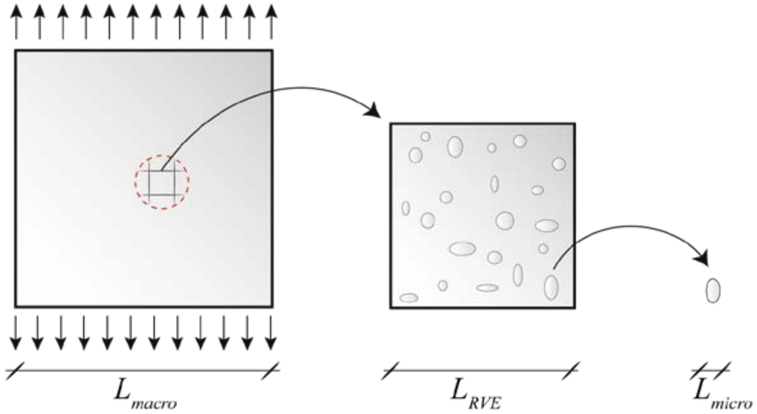

Fig. 1.2 Schematic representation of the scale separation concept

periodic boundary conditions from above and below, respectively, with increasing number of heterogeneities (inclusions or porosities) with a convergence depending on the heterogeneities moduli contrast and the employed approach. This concept will be further investigated in section 1.3 analyzing the most common admissible kinematical boundary conditions employed to perform classical homogenization analyses.

1.1.3 Principle of scale separation

The statement for which the homogenization methods involve the search for a homogenized macroscopic description of any phenomenon incorporates the concept of scale separation, since a macroscopic description has significance if the phenomenon of interest varies only at the microscale. This concept that is crucial, and that it makes possible to look into homogenized descriptions of heterogeneous materials, can be summarized in two requirements:

I. The first, involving the medium, is based on the definition of a characteristic length L_{micro}, which is only permitted if the material has a representative volume element L_{RVE}.

II. The second, involving the phenomenon, is based on the concept that a quantity associated with the phenomenon must exhibit a characteristic length L_{macro} larger than L_{RVE}.

Specifically, with reference to Fig. 1.2 to identify the concept of RVE, three length scales are necessary: one is the macroscopic scale (or macroscale), denoted by L_{macro}, which corresponds to the characteristic size of the considered solid, described as a continuum; the second is the microscopic scale (or microscale), denoted by L_{micro}, which corresponds to the smallest microconstituent (microelement) whose properties and shape are supposed to have a direct influence on the overall response of the continuum infinitesimal material neighborhood; the third scale, denoted by L_{RVE}, is an intermediate scale (also referred to as mesoscopic scale or mesoscale), which corresponds to the size of the RVE. These three scales are related to each other thought the following inequalities:

$$L_{micro} \ll L_{RVE} \ll L_{macro} \tag{1.1}$$

Definitively, it worth to highlight that the concept of scale separation is the sine qua non condition for a global description and that the property of homogenizability only has a meaning for the combination of the material and the phenomenon together.

1.2 Problem setting at finite strain

In the classical continuum mechanics theory, the stress at a material point is dependent by the history of the deformation gradient tensor at

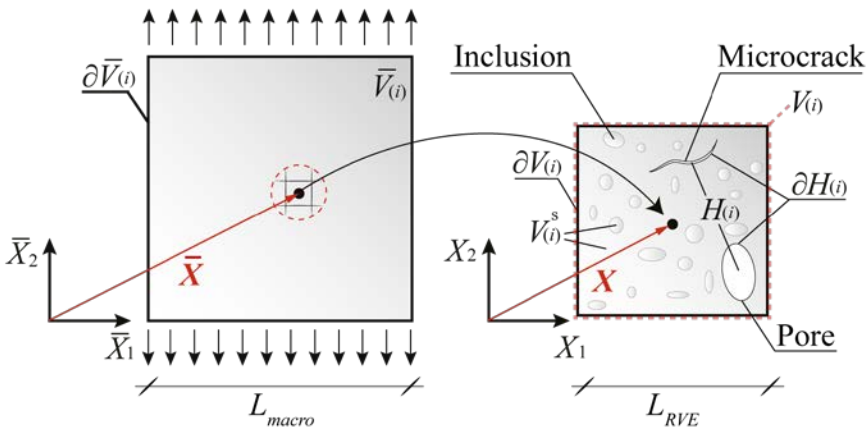

Fig. 1.3 Schematic representation of a random heterogeneous material.

that point, thus exist a tensor-valued functional ζ such that the first Piola-Kirchhoff stress tensor, at any instant *t*, is given by:

$$\boldsymbol{T}_R(\boldsymbol{X},t) = \xi(\boldsymbol{F}(\boldsymbol{X},t)) \tag{1.2}$$

where $\boldsymbol{F}(\boldsymbol{X},t)$ defines the history of the deformation gradient tensor:

$$\boldsymbol{F}(\boldsymbol{X},t) \equiv \boldsymbol{I} + \nabla \boldsymbol{u}(\boldsymbol{X},t) \tag{1.3}$$

with ∇ the reference (or material) gradient operator, $\boldsymbol{u}$ the displacement field, and $\boldsymbol{I}$ the second-order identity tensor.

Phenomenological theories are particularly effective because they often offer a simple mathematical form defined through ordinary differential equations to characterize the mechanical behavior of materials, while for the so-called multiscale constitutive models such theories are replaced by the assumption that $\bar{\boldsymbol{F}}$ and $\bar{\boldsymbol{T}}_R$, at an arbitrary material point $\bar{\boldsymbol{X}}$, are the volume average of the deformation gradient and first Piola-Kirchhoff stress fields over a microscopic cell (RVE), respectively. As shown in Fig. 1.3, a macroscopic material continuum occupying the volume $\overline{V}_{(i)} \subset \Re^3$ with boundary $\partial\overline{V}_{(i)}$ (the overbar refers to the macroscopic scale) can be considered in the undeformed configuration (indicated with subscript (i)) in the Cartesian coordinate system $\overline{X}_1$-$\overline{X}_2$. According to the principle of scale separation, this material continuum, which is generally regarded as a manifold of material points with position vectors $\overline{\boldsymbol{X}}$, is now supposed to consist of a manifold of RVEs centered at $\overline{\boldsymbol{X}}$; the domain of any representative volume element, in the undeformed (or reference) configuration is denoted by $V_{(i)}$, and a local reference Cartesian coordinate system X_1-X_2 is introduced to locate the material points inside the RVE at the microscopic level. The domain of each RVE associated with the infinitesimal neighborhood of $\overline{\boldsymbol{X}}$ is assumed to consist of a solid part $V_{(i)}^s$ and a void part $H_{(i)}$:

$$V_{(i)} = V_{(i)}^s \cup H_{(i)} . \tag{1.4}$$

The void part may consist of pores and cracks, which could be subjected to self-contact phenomena with or without friction. However, for sake of simplicity, RVEs with void parts not intersecting the external boundary $\partial V_{(i)}$ were considered. Homogenized constitutive models at finite strains have been adopted by several authors (for instance [130–132]) developing a geometrically nonlinear extension of the infinitesimal strain theory in the analysis of heterogeneous solids at fine strains. The aim of this paragraph is to establish a variational framework of large- (or finite-) strain multiscale solid constitutive models by means of a kinematical formulation. The essential framework follows the below essentials:

i) the volume averaging relation linking the macro and the micro deformation gradients;

ii) a set of admissible displacements belonging to a subspace of the minimally constrained space of fluctuations compatible with the strain averaging relations;
iii) the RVE equilibrium problem (written in strong form or by means of the principle of virtual work);
iv) the volume averaging relation linking the macro and the micro stresses;
v) the Hill-Mandel principle of Macro-Homogeneity establishing the energy consistency between the different scales.

In the following the main consequences of the above essentials are discussed in detail.

1.2.1 Volume averaging on the deformation gradient and RVE kinematics

The starting point of the classical micromechanical theory of heterogeneous materials at finite strain is the deformation gradient tensor $\overline{\boldsymbol{F}}$ at a point $\overline{\boldsymbol{X}}$ of the macroscopic continuum is the unweighted volume average of the microscopic deformation gradient $\boldsymbol{F}$ over the RVE associated with $\overline{\boldsymbol{X}}$:

$$\overline{\boldsymbol{F}}(\overline{\boldsymbol{X}},t)=\frac{1}{|V_{(i)}|}\int_{V_{(i)}}\boldsymbol{F}(\boldsymbol{X},t)dV_{(i)} \tag{1.5}$$

where $|V_{(i)}|$ is the volume of the RVE in the undeformed configuration and, as shown in Fig. 1.3, $\boldsymbol{X}$ denotes the position of a material point inside the RVE with respect to the local frame X_1-X_2. The microscopic deformation gradient tensor must fulfill the following compatibility equation:

$$\boldsymbol{F}(\boldsymbol{X},t)\equiv\boldsymbol{I}+\nabla_X\boldsymbol{u}(\boldsymbol{X},t) \tag{1.6}$$

where $\boldsymbol{u}(\boldsymbol{X},t)$ denotes the microscopic displacement field of the RVE and ∇_X represents the gradient operator in the material description which in the following text is expressed as ∇ for sake of notation simplicity. It should be noted that Eq. (1.5) is not valid in presence of voids because the microscopic displacement and strain fields are not defined over the void subdomain $H_{(i)}$; a rigorous general definition of the macroscopic strain is:

$$\overline{\boldsymbol{F}}(\overline{\boldsymbol{X}},t)=\frac{1}{|V_{(i)}|}\int_{V_{(i)}^{s}}\boldsymbol{F}(\boldsymbol{X},t)dV_{(i)}-\frac{1}{|V_{(i)}|}\int_{\partial H_{(i)}}\boldsymbol{x}(\boldsymbol{X},t)\otimes\boldsymbol{n}_{(i)}\,dS_{(i)} \tag{1.7}$$

where $\boldsymbol{n}_{(i)}$ denotes the outer unit normal vector at $\boldsymbol{X}\in\partial H_{(i)}$. By applying the divergence theorem to Eq. (1.5), the macroscopic gradient deformation field can be expressed in terms of the boundary displacement:

$$
\begin{aligned}
\overline{\boldsymbol{F}}(\overline{\boldsymbol{X}},t) &= \frac{1}{|V_{(i)}|}\int_{V_{(i)}} \boldsymbol{F}(\boldsymbol{X},t)dV_{(i)} \\
&= \frac{1}{|V_{(i)}|}\Big(\int_{V_{(i)}} \boldsymbol{I}dV_{(i)} + \int_{V_{(i)}} \nabla\boldsymbol{u}(\boldsymbol{X},t)dV_{(i)}\Big) \\
&= \frac{1}{|V_{(i)}|}\Big(V_{(i)} + \int_{\partial V_{(i)}} \boldsymbol{u}(\boldsymbol{X},t)\otimes\boldsymbol{n}_{(i)}\, dS_{(i)}\Big) \\
&= \frac{1}{|V_{(i)}|}\Big(V_{(i)} + \int_{\partial V_{(i)}} (\boldsymbol{x}(\boldsymbol{X},t)-\boldsymbol{X})\otimes\boldsymbol{n}_{(i)}\, dS_{(i)}\Big) \\
&= \frac{1}{|V_{(i)}|}\Big(V_{(i)} + \int_{\partial V_{(i)}} \boldsymbol{x}(\boldsymbol{X},t)\otimes\boldsymbol{n}_{(i)}\, dS_{(i)} - \int_{\partial V_{(i)}} \boldsymbol{X}\otimes\boldsymbol{n}_{(i)}\, dS_{(i)}\Big) \\
&= \frac{1}{|V_{(i)}|}\Big(V_{(i)} + \int_{\partial V_{(i)}} \boldsymbol{x}(\boldsymbol{X},t)\otimes\boldsymbol{n}_{(i)}\, dS_{(i)} - \int_{V_{(i)}} \overbrace{\nabla\boldsymbol{X}}^{\boldsymbol{I}}\, dV_{(i)}\Big) \\
&= \frac{1}{|V_{(i)}|}\Big(V_{(i)} + \int_{\partial V_{(i)}} \boldsymbol{x}(\boldsymbol{X},t)\otimes\boldsymbol{n}_{(i)}\, dS_{(i)} - V_{(i)}\Big) \\
&= \frac{1}{|V_{(i)}|}\int_{\partial V_{(i)}} \boldsymbol{x}(\boldsymbol{X},t)\otimes\boldsymbol{n}_{(i)}\, dS_{(i)}
\end{aligned} \tag{1.8}
$$

where $\boldsymbol{n}_{(i)}$ denotes the outer unit normal vector at $\boldsymbol{X}\in\partial V_{(i)}$. The relation (1.8) naturally defines a constraint on the possible displacement fields of the RVE, i.e. only fields that satisfy Eqs. (1.5) and (1.6) can be admissible. Formally, a microscopic displacement field $\boldsymbol{u}(\boldsymbol{X},t)$ is kinematically admissible if:

$$\boldsymbol{u}(\boldsymbol{X},t)\in\xi, \tag{1.9}$$

where, taking into account Eq. (1.8), the set of kinematically admissible microscopic displacements ξ can be defined exclusively in terms of the RVE boundary displacements:

$$\xi \equiv \left\{ \boldsymbol{v} \in H^1(V_{(i)}) \int_{\partial V_{(i)}} \boldsymbol{v} \otimes \boldsymbol{n}_{(i)} \; dS_{(i)} = V_{(i)} (\overline{\boldsymbol{F}}(\overline{\boldsymbol{X}},t) - \boldsymbol{I}) \right\}. \tag{1.10}$$

where $H^1(V_{(i)})$ denotes the usual Sobolev space of vector valued functions. Definition (1.10) does not change in presence of voids. Without loss of generality, the microscopic displacement field $\boldsymbol{u}(\boldsymbol{X},t)$ can be expressed as a sum of:

I. a displacement $(\boldsymbol{F}(\overline{\boldsymbol{X}},t) - \boldsymbol{I})\boldsymbol{X}$ that varies linearly with $\boldsymbol{X}$ (i.e. linear displacement representing a homogeneous deformation);
II. a nonhomogeneous deformation $\boldsymbol{w}(\boldsymbol{X},t)$ also referred to as fluctuation field;

$$\boldsymbol{u}(\boldsymbol{X},t) = \underbrace{(\overline{\boldsymbol{F}}(\overline{\boldsymbol{X}},t) - \boldsymbol{I})\boldsymbol{X}}_{\text{I}} + \underbrace{\boldsymbol{w}(\boldsymbol{X},t)}_{\text{II}}. \tag{1.11}$$

Note that in stating Eq. (1.11) the fluctuation field can be defined as:

$$\boldsymbol{w}(\boldsymbol{X},t) = \boldsymbol{u}(\boldsymbol{X},t) - (\overline{\boldsymbol{F}}(\overline{\boldsymbol{X}},t) - \boldsymbol{I})\boldsymbol{X} \; . \tag{1.12}$$

Evaluating the divergence of the fluctuation field the following expression is obtained:

$$\begin{aligned}
\nabla \boldsymbol{w}(\boldsymbol{X},t) &= \nabla \boldsymbol{u}(\boldsymbol{X},t) - \nabla[\underbrace{(\overline{\boldsymbol{F}}(\overline{\boldsymbol{X}},t) - \boldsymbol{I})}_{\text{constant respect to } \boldsymbol{X}}]\boldsymbol{X} \\
&= \nabla \boldsymbol{u}(\boldsymbol{X},t) - (\overline{\boldsymbol{F}}(\overline{\boldsymbol{X}},t) - \boldsymbol{I})\underbrace{\nabla \boldsymbol{X}}_{\boldsymbol{I}} \qquad . \\
&= \nabla \boldsymbol{u}(\boldsymbol{X},t) - (\overline{\boldsymbol{F}}(\overline{\boldsymbol{X}},t) - \boldsymbol{I})
\end{aligned} \tag{1.13}$$

Substitution of expression (1.3) into (1.13) gives:

$$\nabla \boldsymbol{w}(\boldsymbol{X},t) = \boldsymbol{F}(\boldsymbol{X},t) - \boldsymbol{I} - \overline{\boldsymbol{F}}(\overline{\boldsymbol{X}},t) + \boldsymbol{I} \tag{1.14}$$

Accordingly, the macroscopic strain field can be expressed as the sum of a homogeneous deformation gradient and a displacement gradient fluctuation field $\nabla \boldsymbol{w}(\boldsymbol{X},t)$:

$$\boldsymbol{F}(\boldsymbol{X},t)=\overline{\boldsymbol{F}}(\overline{\boldsymbol{X}},t)+\nabla\boldsymbol{w}(\boldsymbol{X},t) \quad . \tag{1.15}$$

where the homogeneous contribution coincides with the macroscopic deformation gradient.
From Eq. (1.13) the gradient of the microscopic displacement field can be written as:

$$\nabla\boldsymbol{u}(\boldsymbol{X},t)=\nabla\boldsymbol{w}(\boldsymbol{X},t)+(\overline{\boldsymbol{F}}(\overline{\boldsymbol{X}},t)-\boldsymbol{I}) \tag{1.16}$$

and substituting Eq. (1.16) in (1.8) is obtained that:

$$\begin{aligned}
\overline{\boldsymbol{F}}(\overline{\boldsymbol{X}},t) &= \boldsymbol{I}+\frac{1}{|V_{(i)}|}\int_{V_{(i)}}[\nabla\boldsymbol{w}(\boldsymbol{X},t)+(\underbrace{\overline{\boldsymbol{F}}(\overline{\boldsymbol{X}},t)}_{\text{not dependent of } \boldsymbol{X}}-\boldsymbol{I})]dV_{(i)} \\
&= \boldsymbol{I}+\frac{1}{|V_{(i)}|}\int_{V_{(i)}}\nabla\boldsymbol{w}(\boldsymbol{X},t)dV_{(i)}+\frac{\overline{\boldsymbol{F}}(\overline{\boldsymbol{X}},t)}{|V_{(i)}|}\int_{V_{(i)}}\boldsymbol{I}dV_{(i)}-\frac{1}{|V_{(i)}|}\int_{V_{(i)}}\boldsymbol{I}dV_{(i)} \\
&= \boldsymbol{I}+\frac{1}{|V_{(i)}|}\int_{V_{(i)}}\nabla\boldsymbol{w}(\boldsymbol{X},t)dV_{(i)}+\frac{\overline{\boldsymbol{F}}(\overline{\boldsymbol{X}},t)}{|V_{(i)}|}V_{(i)}-\frac{\boldsymbol{I}}{|V_{(i)}|}V_{(i)} \\
&= \overline{\boldsymbol{F}}(\overline{\boldsymbol{X}},t)+\frac{1}{|V_{(i)}|}\int_{V_{(i)}}\nabla\boldsymbol{w}(\boldsymbol{X},t)dV_{(i)}
\end{aligned} \tag{1.17}$$

and this equality is satisfied when the second term of Eq. (1.18) results equal to 0:

$$\overline{\boldsymbol{F}}(\overline{\boldsymbol{X}},t)=\overline{\boldsymbol{F}}(\overline{\boldsymbol{X}},t)+\underbrace{\frac{1}{|V_{(i)}|}\int_{V_{(i)}}\nabla\boldsymbol{w}(\boldsymbol{X},t)dV_{(i)}}_{=\boldsymbol{0}} \tag{1.18}$$

leading to the following constraint written in terms of RVE boundary displacement:

$$\int_{\partial V_{(i)}}\boldsymbol{w}(\boldsymbol{X},t)\otimes\boldsymbol{n}_{(i)}dS_{(i)}=\boldsymbol{0} \tag{1.19}$$

Formally, a microscopic fluctuation field $\boldsymbol{w}(\boldsymbol{X},t)$ is kinematically admissible if:

$$\boldsymbol{w}(\boldsymbol{X},t) \in \zeta, \tag{1.20}$$

where:

$$\zeta \equiv \left\{ \boldsymbol{v} \in H^1(V_{(i)}) \,|\, \frac{1}{|V_{(i)}|} \int_{\partial V_{(i)}} \boldsymbol{v} \otimes \boldsymbol{n}_{(i)} \; dS_{(i)} = \boldsymbol{0} \right\} \tag{1.21}$$

is the vector space of kinematically admissible displacement fluctuations of the RVE. From the above definition, it follows that, alternatively to Eq. (1.10), the set of kinematically admissible microscopic displacements ξ can be defined as:

$$\xi \equiv \left\{ \boldsymbol{u}(\boldsymbol{X},t) = \overline{\boldsymbol{u}}(\overline{\boldsymbol{X}},t) + (\overline{\boldsymbol{F}}(\overline{\boldsymbol{X}},t) - \boldsymbol{I})\boldsymbol{X} + \boldsymbol{w}(\boldsymbol{X},t) \,|\, \boldsymbol{w}(\boldsymbol{X},t) \in \zeta \right\} \tag{1.22}$$

Then for a given macroscopic displacement $\overline{\boldsymbol{u}}(\overline{\boldsymbol{X}},t)$, and a given macroscopic deformation gradient $\overline{\boldsymbol{F}}(\overline{\boldsymbol{X}},t)$, the set ξ represents a translation of the space ζ .

1.2.1.1 Spaces of displacement rates

In general, is allowed impose further constraints upon the RVE kinematics, and such constraints leads to different classes of macroscopic constitutive models and will define the actual set ξ^* of kinematically admissible displacement of the RVE, which according to Eq. (1.9), must satisfy:

$$\xi^* \subset \xi \tag{1.23}$$

Now another basic assumption of the theory is introduced, requiring that any further constraints imposed on the RVE kinematics be such that the set of kinematically admissible displacement fluctuations ζ^* is a subspace of ζ :

$$\zeta^* \subset \zeta \tag{1.24}$$

Consequently, the actual set of kinematically admissible microscopic displacement is given by:

$$\xi^* \equiv \left\{ \boldsymbol{u} = \bar{\boldsymbol{u}} + (\bar{\boldsymbol{F}} - \boldsymbol{I})\boldsymbol{X} + \boldsymbol{w} \,|\, \boldsymbol{w} \in \zeta^* \right\} \subset \xi \,. \tag{1.25}$$

Thus, the set ξ^* and the associated space of virtual kinematically admissible displacements of the RVE ϖ play together a fundamental role in the variational characterization of the RVE equilibrium problem. The space ϖ can be defined as:

$$\varpi \equiv \left\{ \boldsymbol{\eta} = \boldsymbol{v}_1 - \boldsymbol{v}_2 \,|\, \boldsymbol{v}_1, \boldsymbol{v}_2 \in \xi^* \right\} . \tag{1.26}$$

In view of Eq. (1.25) and the fact that ζ^* is a vector space, it follows from Eq. (1.26) that:

$$\varpi = \zeta^* . \tag{1.27}$$

Further, the same consideration can be applied to the rate form of the microscopic displacement field:

$$\dot{\boldsymbol{u}} = \dot{\bar{\boldsymbol{u}}} + \dot{\bar{\boldsymbol{F}}}\boldsymbol{X} + \dot{\boldsymbol{w}} \tag{1.28}$$

establishing that any set of kinematically admissible fluctuation rate satisfies:

$$\dot{\boldsymbol{w}} \in \varpi \tag{1.29}$$

In brief, as a consequence of the assumption that ζ^* is a subspace of ζ, the functional spaces of kinematically admissible displacement fluctuations together with the fluctuations rate and the functional space of virtual displacements coincide.

1.2.2 RVE equilibrium problem

In order to derive the equilibrium equations of the RVE and to impose the equilibrium condition at each instant *t* of the deformation history, the stress field is identified with the first Piola-Kirchhoff stress tensor:

$$\boldsymbol{T}_R = \boldsymbol{T}_R(\boldsymbol{X},t)\,. \tag{1.30}$$

Since the surface forces are usually much greater than the body forces, due to large surface to volume ratio in micromechanics (according to the principle of scale separation), the assumption of zero body forces appears to be realistic in most practical cases. Thus, assuming that body forces are negligible and that the RVE is subjected to an external traction field $\boldsymbol{t}_R = \boldsymbol{t}_R(\boldsymbol{X},t)$ on its external boundary $\partial V_{(i)}$, the principle of virtual work establishes that the RVE is in equilibrium if and only if the following variational equation holds at each t:

$$\int_{V_{(i)}} \boldsymbol{T}_R(\boldsymbol{X},t):\nabla\boldsymbol{\eta}\; dV_{(i)} = \int_{\partial V_{(i)}} \boldsymbol{t}_R(\boldsymbol{X},t)\cdot\boldsymbol{\eta}\; dS_{(i)} \quad \forall\boldsymbol{\eta}\in\varpi, \tag{1.31}$$

where $\boldsymbol{\eta}$ is the set of virtual displacements, acting as test function in a variational setting, and ϖ is an appropriate space of virtual displacement of the RVE, coinciding with ζ^*. To take into account the contribution from the voids parts of the RVE it is convenient to rewrite Eq. (1.31) in the following form:

$$\begin{aligned}\int_{V^s_{(i)}} \boldsymbol{T}_R(\boldsymbol{X},t):\nabla\boldsymbol{\eta}\; dV_{(i)} &= \int_{\partial V^s_{(i)}} \boldsymbol{t}_R(\boldsymbol{X},t)\cdot\boldsymbol{\eta}\; dS_{(i)}\\ &+ \int_{\partial H^v_{(i)}} \boldsymbol{r}_R(\boldsymbol{X},t)\cdot\boldsymbol{\eta}\; dS_{(i)} \quad \forall\boldsymbol{\eta}\in\varpi,\end{aligned} \tag{1.32}$$

where the internal traction field $\boldsymbol{r}_R(\boldsymbol{X},t)$ is defined as the reference traction exerted upon the solid part of $V_{(i)}$ across the solid–void interface $\partial V_{(i)}$ and $\boldsymbol{t}_R(\boldsymbol{X},t)$ is the first Piola-Kirchhoff traction vector on the external boundary of the RVE.

For sufficiently regular field $\boldsymbol{T}_R(\boldsymbol{X},t)$, the variational formulation reported in Eq. (1.32) can written in the following equivalent strong formulation:

$$\begin{cases} Div\boldsymbol{T}_R(\boldsymbol{X},t)=\boldsymbol{0} & \forall\boldsymbol{X}\in V_{(i)} \\ \boldsymbol{T}_R(\boldsymbol{X},t)\cdot\boldsymbol{n}_{(i)}=\boldsymbol{t}_R(\boldsymbol{X},t) & \forall\boldsymbol{X}\in\partial V_{(i)} \\ [\![\boldsymbol{T}_R(\boldsymbol{X},t)\cdot\boldsymbol{n}_{(i)}]\!]=\boldsymbol{0} & \forall\boldsymbol{X}\in\partial H_{(i)} \end{cases} \tag{1.33}$$

where $\boldsymbol{n}_{(i)}$ is the outer unit normal vector to the relative RVE boundary (external or internal) and $[\![\boldsymbol{T}_R(\boldsymbol{X},t)\cdot\boldsymbol{n}_{(i)}]\!]$ represents the jump of the traction vector across the internal solid-void interface $\partial H_{(i)}$ or across the crack interfaces.

1.2.3 Stress averaging relations

Analogously to Eq. (1.5), it follows that the macroscopic first Piola-Kirchhoff stress tensor $\overline{\boldsymbol{T}}_R(\overline{\boldsymbol{X}},t)$ associated with $\overline{\boldsymbol{X}}$ is the unweighted volume average of the microscopic first Piola-Kirchhoff stress tensor $\boldsymbol{T}_R(\boldsymbol{X},t)$:

$$\overline{\boldsymbol{T}}_R(\overline{\boldsymbol{X}},t)=\frac{1}{|V_{(i)}|}\int_{V_{(i)}}\boldsymbol{T}_R(\boldsymbol{X},t)dV_{(i)} \tag{1.34}$$

Eq. (1.34) is valid strictly in a generalized sense because the microscopic stress field cannot be defined over the void subdomain $H_{(i)}$; thus it can be replaced with:

$$\overline{\boldsymbol{T}}_R(\overline{\boldsymbol{X}},t)=\frac{1}{|V_{(i)}|}\int_{V^s_{(i)}}\boldsymbol{T}_R(\boldsymbol{X},t)dV^s_{(i)}\,. \tag{1.35}$$

Considering the following general relation [133], in which $\boldsymbol{S}$ represents a sufficiently regular tensor fields, $\boldsymbol{v}$ is a vector field and $\boldsymbol{n}$ is the outward unit normal to the boundary $\partial\Omega$ of Ω:

$$\int_{\Omega}\boldsymbol{S}(\nabla\boldsymbol{v})^T\,dV=\int_{\partial\Omega}(\boldsymbol{S}\cdot\boldsymbol{n})\otimes\boldsymbol{v}\,dA-\int_{\Omega}(div\boldsymbol{S})\otimes\boldsymbol{v}\,dV\,, \tag{1.36}$$

and considering also that $\nabla \boldsymbol{X} = \boldsymbol{I}$, the macroscopic stress can be alternatively expressed in terms of RVE boundary tractions as follow:

$$\begin{aligned}
\overline{\boldsymbol{T}}_R(\overline{\boldsymbol{X}},t) &= \frac{1}{|V_{(i)}|}\int_{V_{(i)}} \boldsymbol{T}_R(\boldsymbol{X},t)(\nabla\boldsymbol{X})^T\, dV_{(i)} \\
&= \frac{1}{|V_{(i)}|}\int_{\partial V_{(i)}} (\boldsymbol{T}_R(\boldsymbol{X},t)\cdot\boldsymbol{n})\otimes\boldsymbol{X}\; dS_{(i)} \\
&- \frac{1}{|V_{(i)}|}\int_{V_{(i)}} Div\boldsymbol{T}_R(\boldsymbol{X},t)\otimes\boldsymbol{X}\; dV_{(i)}
\end{aligned} \tag{1.37}$$

Then, introducing the strong form of the equilibrium problem (1.33), the following expression for the homogenized first Piola-Kirchhoff stress tensor in term of RVE boundary tractions is obtained:

$$\begin{aligned}
\overline{\boldsymbol{T}}_R(\overline{\boldsymbol{X}},t) &= \frac{1}{|V_{(i)}|}\int_{V_{(i)}} \boldsymbol{T}_R(\boldsymbol{X},t)(\nabla\boldsymbol{X})^T\, dV_{(i)} \\
&= \frac{1}{|V_{(i)}|}\int_{\partial V_{(i)}} \underbrace{(\boldsymbol{T}_R(\boldsymbol{X},t)\cdot\boldsymbol{n})}_{\boldsymbol{t}_R(\boldsymbol{X},t)}\otimes\boldsymbol{X}\; dS_{(i)} \\
&- \frac{1}{|V_{(i)}|}\int_{V_{(i)}} \underbrace{Div\boldsymbol{T}_R(\boldsymbol{X},t)}_{\boldsymbol{0}}\otimes\boldsymbol{X}\; dV_{(i)} \\
&= \frac{1}{|V_{(i)}|}\int_{\partial V_{(i)}} \boldsymbol{t}_R(\boldsymbol{X},t)\otimes\boldsymbol{X}\; dS_{(i)}
\end{aligned} \tag{1.38}$$

It is worth noting that the average stress must be independent of the origin of the local coordinate system, therefore Eq. (1.38) it is meaningful only if the prescribed surface tractions are self-equilibrated.

1.2.4 Energy averaging relations (Hill-Mandel principle)

In the homogenized constitutive theories a fundamental concept is depicted by the Hill-Mendel principle of Macro-Homogeneity [134] which, based on physical arguments, it establishes that the power of the macroscopic stress must be equal to the volume average of the power of the microscopic stress over the RVE. Thus, in a large strain setting, it requires that the following identity is satisfies at any state of the RVE and for any kinematically admissible microscopic deformation gradient rate field $\dot{\boldsymbol{F}}(\boldsymbol{X},t)$:

$$\overline{\boldsymbol{T}}_R(\overline{\boldsymbol{X}},t):\dot{\overline{\boldsymbol{F}}}(\overline{\boldsymbol{X}},t)=\frac{1}{|V_{(i)}|}\int_{V_{(i)}}\boldsymbol{T}_R(\boldsymbol{X},t):\dot{\boldsymbol{F}}(\boldsymbol{X},t)dV_{(i)} \quad . \tag{1.39}$$

It worth noting that $\dot{\boldsymbol{F}}(\boldsymbol{X},t)$ is said to be kinematically admissible only if:

$$\dot{\boldsymbol{F}}(\boldsymbol{X},t)=\nabla\dot{\boldsymbol{u}}(\boldsymbol{X},t)=\dot{\overline{\boldsymbol{F}}}(\overline{\boldsymbol{X}},t)+\nabla\dot{\boldsymbol{w}}(\boldsymbol{X},t);\ \dot{\boldsymbol{w}}(\boldsymbol{X},t)\in\varpi \tag{1.40}$$

where ϖ is the space of kinematically admissible RVE displacement rates reported in Eq.(1.26) coinciding with the space of kinematically admissible displacement fluctuation and virtual displacements of the RVE.

1.2.4.1 Variational statement of the Hill-Mandel principle

By introduction the definition of the microscopic deformation gradient rate reported in Eq. (1.40) in the right-hand side of the Hill-Mandel principle reported in Eq. (1.39), the variational statement of the principle of macro-homogeneity can be extrapolated:

$$\begin{aligned}
\bar{\boldsymbol{T}}_R : \dot{\bar{\boldsymbol{F}}} &= \frac{1}{|V_{(i)}|} \int_{V_{(i)}} \boldsymbol{T}_R : [\dot{\bar{\boldsymbol{F}}} + \nabla \dot{\boldsymbol{w}}\,] dV_{(i)} \\
&= \frac{1}{|V_{(i)}|} \int_{V_{(i)}} \boldsymbol{T}_R : \dot{\bar{\boldsymbol{F}}} dV_{(i)} + \frac{1}{|V_{(i)}|} \int_{V_{(i)}} \boldsymbol{T}_R : \nabla \dot{\boldsymbol{w}} dV_{(i)} \\
&= \underbrace{\frac{1}{|V_{(i)}|} \int_{V_{(i)}} \boldsymbol{T}_R dV_{(i)}}_{\bar{\boldsymbol{T}}_R} : \dot{\bar{\boldsymbol{F}}} + \frac{1}{|V_{(i)}|} \int_{V_{(i)}} \boldsymbol{T}_R : \nabla \dot{\boldsymbol{w}} dV_{(i)} \\
&= \bar{\boldsymbol{T}}_R : \dot{\bar{\boldsymbol{F}}} + \frac{1}{|V_{(i)}|} \int_{V_{(i)}} \boldsymbol{T}_R : \nabla \dot{\boldsymbol{w}} dV_{(i)}
\end{aligned} \tag{1.41}$$

Hence, the principle is satisfied if and only if:

$$\int_{V_{(i)}} \boldsymbol{T}_R : \nabla \dot{\boldsymbol{w}}\; dV_{(i)} = 0 \quad \forall \dot{\boldsymbol{w}} \in \varpi \tag{1.42}$$

In view of the variational form of the equilibrium problem (1.31) follows that:

$$\int_{V_{(i)}} \boldsymbol{T}_R : \nabla \dot{\boldsymbol{w}} dV_{(i)} = \int_{\partial V_{(i)}} \boldsymbol{t}_R(\boldsymbol{X},t) \cdot \dot{\boldsymbol{w}}\; dS_{(i)} \;\; \forall \dot{\boldsymbol{w}} \in \varpi \tag{1.43}$$

Thus, the above variational equation holds if and only if:

$$\int_{\partial V_{(i)}} \boldsymbol{t}_R(\boldsymbol{X},t) \cdot \dot{\boldsymbol{w}}\; dS_{(i)} = 0 \tag{1.44}$$

In brief, it means that the Hill-Mandel principle of macrohomogeneity holds if and only if the virtual work of the external surface traction of the RVE vanish. The Eq. (1.44) indicates that the principle of Hill – Mandel is analogous to the assumption that the external surface traction of the RVE vanish is purely reactive, as a response to the kinematical constraints imposed on the RVE and cannot be enforced separately.

1.3 Admissible kinematical boundary conditions

The unknown dependent variable of the microscopic equilibrium problem was stated in Section 1.2.1 as the displacement fluctuation field $\boldsymbol{w}(\boldsymbol{X},t)$. The admissible kinematical boundary conditions must be formulated in order to solve the equilibrium problem and thus to evaluate the displacement fluctuation field. Such kinematical boundary conditions must satisfy the kinematical restraints, reported in Eq. (1.19), and the restraint given by the Hill-Mandel principle, reported in Eq. (1.42). In the literature there are three different sets of boundary conditions satisfying the previous reported restraints:

I. Linear displacement boundary conditions;
II. Periodic fluctuation boundary conditions;
III. Uniform traction boundary conditions.

1.3.1 Linear displacement boundary conditions

This set of kinematical boundary conditions is derived by assuming that the RVE boundary displacements are linear in $\boldsymbol{X}$, as follow:

$$\boldsymbol{u}(\boldsymbol{X},t)=(\overline{\boldsymbol{F}}(\overline{\boldsymbol{X}},t)-\boldsymbol{I})\boldsymbol{X} \ . \tag{1.45}$$

Substituting the Eq. (1.45) in Eq. (1.12), this restraint makes the displacements fluctuations field null at the boundary of the RVE:

$$\boldsymbol{w}(\boldsymbol{X},t)=\boldsymbol{0} \quad \forall\boldsymbol{X}\in\partial V_{(i)} \tag{1.46}$$

This boundary condition implies zero body forces and it fully prescribes the displacement of the boundary of the RVE leaving yet undetermined the microstructural fluctuations inside the volume.

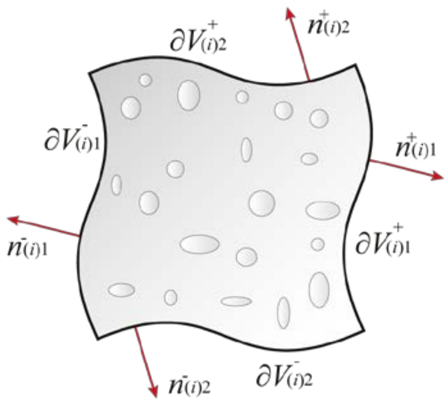

Fig. 1.4 Boundaries of the RVE in the Periodic fluctuation boundary condition

1.3.2 Periodic fluctuation boundary conditions

This set of kinematical boundary conditions is one of the most used in the field of the homogenization theories thanks to its exceptional ability to reproduce the behavior in materials characterized by microstructures with periodic pattern due to the fact that the resulting homogenized properties converge faster to their real values as the RVE size increases. It worth noting that the periodic fluctuation boundary conditions can be applied even if the microstructure is not perfectly periodic.

As for the linear displacement boundary condition, the periodic boundary condition implies zero body forces**.** Assuming that the microstructure is periodic, it leads to consistent displacements of opposing boundary; in particular, as can be seen in Fig. 1.4 this condition establishes a split of the boundary limits in a positive part $\partial V^{+}_{(i)}$ and in a negative part $\partial V^{-}_{(i)}$:

$$\partial V_{(i)} = \partial V^{+}_{(i)1} \cup \partial V^{+}_{(i)2} \cup \partial V^{-}_{(i)1} \cup \partial V^{-}_{(i)2}\,; \tag{1.47}$$

The corresponding outward unit vectors $\boldsymbol{n}^{+}$ and $\boldsymbol{n}^{-}$, respectively normal to $\partial V_{(i)}^{+}$ and $\partial V_{(i)}^{-}$, present the following relation:

$$\boldsymbol{n}^{-}=-\boldsymbol{n}^{+} \tag{1.48}$$

Definitively, the periodic boundary condition on $\partial V_{(i)}$ is given as follow:

$$\boldsymbol{u}(\boldsymbol{X}^{+},t)-\boldsymbol{u}(\boldsymbol{X}^{-},t)=(\overline{\boldsymbol{F}}(\overline{\boldsymbol{X}},t)-\boldsymbol{I})(\boldsymbol{X}^{+}-\boldsymbol{X}^{-}) \tag{1.49}$$

Imposing the Eq. (1.49) at the boundary of the RVE, this condition leads to an anti-periodic traction field and to a periodic fluctuation field as expressed in the following:

$$\boldsymbol{t}_{R}^{+}(\boldsymbol{X},t)=-\boldsymbol{t}_{R}^{-}(\boldsymbol{X},t)\ , \tag{1.50}$$

$$\boldsymbol{w}_{R}^{+}(\boldsymbol{X},t)=\boldsymbol{w}_{R}^{-}(\boldsymbol{X},t)\ . \tag{1.51}$$

In the same way that the Linear boundary condition, this condition satisfies both Equations (1.19) and (1.44).

1.3.3 Uniform traction boundary conditions

This set of kinematical boundary conditions is based on the so-called minimal kinematical admissible constraint that satisfies the compatibility between the macroscopic deformation gradient and the microscale displacement:

$$\int_{\partial V_{(i)}} \boldsymbol{w}(\boldsymbol{X},t)\otimes\boldsymbol{n}_{(i)}\,dS_{(i)}=\boldsymbol{0} \tag{1.52}$$

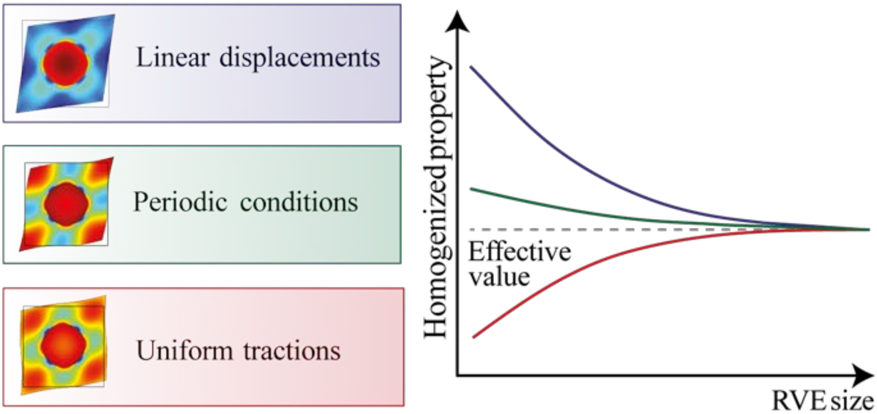

Fig. 1.5 Convergence of the homogenized properties to the effective values with increasing RVE size for different types of BCs.

In brief, it leads to impose a uniform traction field on the RVE boundaries, and it also possible to demonstrate that this constraint leads to uniform traction on the RVE coinciding with the traction of the average stress, as follow:

$$\boldsymbol{t}_R(\boldsymbol{X},t)=\overline{\boldsymbol{T}}_R(\overline{\boldsymbol{X}},t)\cdot\boldsymbol{n}_{(i)}=\boldsymbol{T}_R(\boldsymbol{X},t)\cdot\boldsymbol{n}_{(i)} \tag{1.53}$$

It worth noting that, the traction boundary condition (1.53) is not imposed a priori, thus the uniform traction condition is a consequence of the choice of kinematically admissible fluctuations space. As for the linear and periodic boundary condition models, the uniform traction boundary condition implies zero body force.

1.3.4 Remarks on the boundary conditions

The boundary conditions previously reported can be sorted starting by the less restrictive that is the uniform traction boundary condition, followed by the periodic boundary condition and ended with the linear boundary displacement conditions. It is also worth noting that some authors have been demonstrated that, imposing periodic boundary condition the results converge faster to the theoretical or effective solution [135]. In brief, as is generically sketched in Fig. 1.5, it means that using the same RVE size, periodic boundary condition leads to the closest result to the effective value.

.

2

Finite-strain Multiscale Methods

In the last century, between 1950 and 1990, micromechanics models began to emerge in engineering and science because of the advent of new composite materials technology and nanotechnology. Specifically, the increasing use of these new technologies in the form of microfibers and nanotubes has made necessary to deepen the studies in micromechanics field focusing the attention on the understanding of the relations between microscopic and macroscopic scales. Expanding the classical micromechanical concept with the micro–macro bridging concept it possible to define a new methodology called multiscale modeling. This modeling strategy of materials, that can be treated as an extension of classical micro-macro modeling, has introduced new tools to overcome the difficulties observed dealing with phenomena not well understood and newly observed in new heterogeneous materials and nanomaterials.

2.1 Overview of multiscale methods

The overall structural behavior of composite materials is strongly influenced by several nonlinear phenomena, which take place at the microscopic scale: for instance, microscopic instabilities and contact interaction between crack faces, leading to a highly macroscopic nonlinear response. As a consequence, a rigorous investigation of the mechanical behavior in composite materials subjected to such microstructural nonlinearities, in terms of microcracks and microinstabilities, should require a numerical model able to completely describe all its microscopic details. On the other hand, a fully microscopic model is not appropriate in practice due to the high computational effort, and thus advanced models, such as multiscale methods, are needed to predict failure in composite materials subjected to nonlinear phenomena with a good accuracy and with contained computational effort. Generally speaking, two main subcategories of multiscale approaches can be recognized to study the mechanical behavior of heterogeneous materials [136].

The first class contains problems involving local defects or singularities, such as dislocations, cracks, shocks, and boundary layers, for which a macroscopic model is sufficient for most of the physical domain, and a fine-scale model is only needed in the neighborhood of the singularities or heterogeneities. The second class of problems is that for which a microscopic model is needed everywhere either as a complement to or as a replacement of the macroscopic model, for example a mechanical system for which a macroscopic constitutive phenomenological law is missing. Thus, multiscale methods are usually classified as hierarchical, concurrent or semi-concurrent.

Hierarchical methods are most widely used and computationally the most efficient. In these methods, the different scales are linked together in a hierarchical manner (using, for instance, volume averaging of field variables) implying that distinct scales are coupled and considered in the same domain. For linear responses, this class of methods is extremely effective since homogenized quantities can be easily computed by virtue of the robust theory of linear homogenization, sometimes without requiring numerical microscopic models. On the other hand, for strongly nonlinear problems, hierarchical models become less effective, especially if the fine-scale response is path-dependent. It is worth noting that in the case of failure events, standard hierarchical models are no longer valid.

Concurrent methods are characterized by the presence of a fine-scale model embedded into the coarse-scale model, which is directly and strongly coupled to it, such that the microscale scale model communicates directly with the macro scale model though some coupling procedure. In order to restore the continuity conditions between the two submodels, both compatibility and momentum balance are enforced across the interface. Such models are effective when the subdomain where a higher-order description is required, is small compared to the whole domain.

Semiconcurrent methods are considered as a variation of concurrent coupling methods, in which the micro and macro models run together and communicate with each other simultaneously but a real linking between the micromodels does not exist.

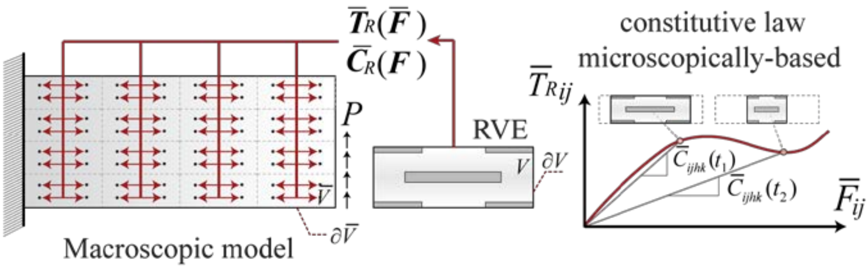

Fig. 2.1 Schematic representation of the hierarchical multiscale approach.

From the coupling point of view, it worth noting that in hierarchical methods the information is passed from the microscale to the macroscale and not vice versa; whereas passage of information in a double-way is permitted in the case of semiconcurrent methods. Concurrent methods are instead classified as interface coupling methods because the coupling happens along an interface shared between the region with distinct length scales.

In the following more detail on the main multiscale strategies is given.

2.1.1 Hierarchical methods

In hierarchical multiscale methods, a macroscopic constitutive model is assumed with parameters determined by fitting the data obtained as the result of the boundary value problem of a microscopic sample whose microstructure is explicitly modeled, as illustrated in Fig. 2.1. In the literature, these numerical homogenization techniques are particularly useful for modeling composite materials since they enable the development of the so-called micromechanically informed constitutive models that can be used in structural computations. Due to the assumption on the type of macroscopic constitutive law, these methods are not suitable for handling nonlinear problems with evolving microstructures; on the other hand, these methods are attractive for large-scale computations, since finite element computations at the microscale are performed a priori.

In hierarchical models (also referred to as sequential models), the following steps have to be performed:

i. identification of a representative volume element (RVE) or a repeating unit cell (RUC), for random or periodic structures, respectively, whose individual constituents are assumed to be completely known, with their constitutive properties;
ii. formulation of the microscopic boundary conditions to be applied to the RVE;
iii. computation of the output macroscopic variables from the results of the microscopic boundary value problem associated with the RVE (micro-to-macro transition or homogenization);
iv. determination of the numerical constitutive law, relating each other the input and output macroscopic variables.

Since during the micro-to-macro transition step the information is passed from lower to higher scales, a “one-way” bottom-up coupling is established between the microscopic and macroscopic scales. As a consequence, such methods are efficient in determining the macroscopic behavior of composites in terms of stiffness and strength, but have a limited predictive capability for problems involving damage phenomena.

Many studies have been addressed to the macroscopic constitutive behavior of composite materials with microscopic defects (see, for instance, [137–140]). In many works, the damage configuration is fixed, since for a pure micromechanical model, the evolution of damage configuration cannot be predicted

More recently, a nonlinear micromechanical model incorporating contact effects and based on homogenization techniques, interface models and fracture mechanics concepts has been proposed in [141,142], where the damage configuration is not assumed a priori, but driven by a fracture criterion. By using this hierarchical model, accurate nonlinear macroscopic constitutive laws are obtained, taking into account the evolution of the microstructural configuration associated with crack growth and contact phenomena at the microscale.

2.1.2 Semiconcurrent methods

When dealing with microscopic nonlinear phenomena a “two-way” coupling between micro- and macrovariables is required, i.e. the homogenized properties have to be updated during the microstructural evolution. In semiconcurrent multiscale methods, also referred to as computational homogenization methods, the macroscopic constitutive response of a heterogeneous material is determined “on the fly” during simulation; these methods have been widely used to predict the mechanical behavior of microstructured materials, due to their flexibility. The most important approaches are those proposed by Guedes and Kikuchi [143], Miehe et al. [144], Feyel and Chaboche [145], Kouznetsova et al. [146].
In section 2.1.2.1 a special attention is devoted to the large class of approaches inspired by the multilevel finite element (FE^2) method introduced by Feyel and Chaboche [29]. This method has been proved to be very efficient in such cases, also for only locally periodic composites. The key idea of such approaches is to associate a microscopic boundary value problem to each integration point of the macroscopic boundary value problem, after discretizing the underlying microstructure. The macroscopic strain provides the boundary data for each microscopic

problem (macro-to-micro transition or localization step). The set of all microscale problems is then solved and the results are passed back to the macroscopic problem in terms of overall stress field and tangent operator (micro-to-macro transition or homogenization step). Localization and homogenization steps are carried out within an incremental-iterative nested solution scheme; thus, the two-scale coupling remains of a weak type. An advantage of semiconcurrent methods over hierarchical methods is that a framework for storing the macroscopic constitutive response is not needed.

In the original formulation of the method, based on a classical first-order homogenization, the large spatial gradients in macroscopic fields cannot be resolved due to supposed validity of the principle of scale separation, therefore they are not suited for studying strain localization phenomena which commonly affect the macroscopic behavior of composites; moreover, softening behaviors cannot be properly analyzed because of the mesh dependence at the macroscopic scale due to the ill-posedness of the macroscopic boundary value problem, as shown in [120].

In order to overcome such limitations, other homogenization paradigms have been proposed in the literature, such as the higher-order computational homogenization schemes and the coupled volume multiscale method in sections 2.1.2.2 and 2.1.2.3, respectively.

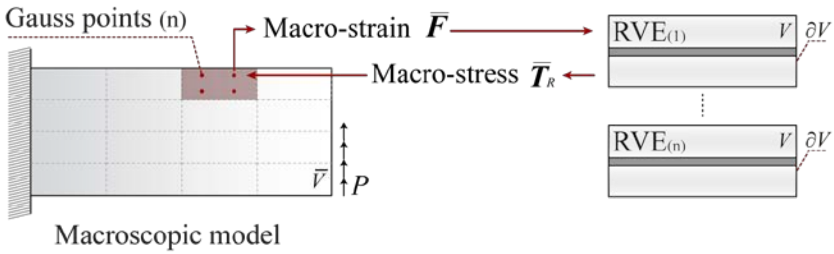

Fig. 2.2 Schematic representation of the (FE^2) semiconcurrent multiscale approach.

2.1.2.1 Multilevel finite element method (FE^2)

The FE^2 method has been introduced by Feyel in [145] and consists in describing the mechanical behavior of heterogeneous structures. After choosing two relevant mechanical scales (referred to as microscale and macroscale), the FE^2 method can be adopted, based on three main ingredients:

i. The identification of a representative volume element (RVE);
ii. A localization rule able to obtain the local solution inside the RVE, for any given macroscopic strain;
iii. A homogenization rule giving the macroscopic stress tensor, starting from the micromechanical stress state.

In this setting, macroscopic phenomenological relationships are not required, even in the case of nonlinear behaviors; indeed, the macroscopic response arises directly from the calculation at the microscopic level.

The FE^2 method is applied by means of a nested solution scheme sketched in Fig. 2.2; for each step of the macroscopic incremental iterative procedure, and for each macroscopic integration point, the macroscopic strain $\overline{\boldsymbol{F}}$ (gradient deformation tensor) is computed based on the current (iterative) macroscopic displacement field. Then, $\overline{\boldsymbol{F}}$ is passed

to the microscopic level, and used to define the boundary conditions to be applied to the RVE attached to the respective macroscopic integration point. After solving every RVE problem, the macroscopic stress tensor $\overline{\boldsymbol{T}}_R$ (first Piola-Kirchhoff stress tensor) is obtained in a post-processing step. Thus, the macroscopic equilibrium can be evaluated, and the next iterations are performed until equilibrium is achieved; after this, the calculations can be continued for the next load increment.
The multilevel finite element method is intrinsically parallel; indeed, all RVE calculations for one macroscopic iteration can be performed simultaneously without any exchange of information between them. Thus, even if this method is computationally costly, the use of parallel processors for the RVE analyses would significantly reduce the total calculation time.

2.1.2.2 High-order computational homogenization

In this section the second-order computational scheme, proposed by Kouznetsova et al. [146] to extend the classical computational techniques, is illustrated. This technique adopts not only the macrostrain tensor (as in first-order schemes) but also its gradient to prescribe the essential boundary conditions on the representative volume element of the given microstructure, leading to a second-order continuum macroscopic model.
For each step of the macroscopic incremental-iterative procedure, and for each macroscopic integration point, the macroscopic deformation gradient tensor and its gradient are computed based on the current (iterative) macroscopic displacement field. Then, these macroscopic quantities are passed to the microscopic level, and used to define the boundary conditions to be applied to the RVE attached to the respective macroscopic integration point. After solving every RVE problem, the

macroscopic stress tensor and the higher-order stress tensor are obtained. Thus, the macroscopic internal nodal forces can be computed, the higher-order equilibrium can be evaluated, and the next iterations are performed until equilibrium is achieved; after this, the calculations can be continued for the next load increment.
The inclusion of strain gradients and higher-order stresses automatically results in the introduction of a length scale parameter in the macroscopic response; this allows to overcome the dependence on the macroscopic discretization, but does not solve the RVE size dependence in the case of softening behaviors, as shown in [147].

2.1.2.3 Coupled-volume multiscale method

A different approach has been proposed by Gitman et al. [147], referred to as coupled volume multiscale method, able to resolve simultaneously the macroscale discretization sensitivity and the RVE size dependence. The main feature of this method is that an RVE is not linked to an infinitely small macroscopic material point, but associated with a macro-element whose size is equals the RVE size.
The coupled volume approach abandons the principle of scale separation and a model parameter (the RVE size) is linked to a numerical parameter (the mesh size); since this approach does not rely upon the existence of an RVE, it can also be used in the presence of softening behaviors. By linking the mesh size to the RVE size, the macroscopic mesh dependence is balanced by different constitutive behaviors arising from different RVE sizes; as a consequence, the macroscopic response shows neither macroscopic mesh dependency nor RVE size dependency. An implementation example of such method is reported in Section 4.3.1.

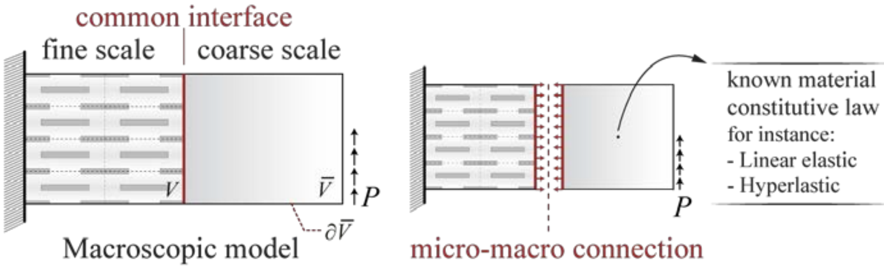

Fig. 2.3 Schematic representation of the concurrent multiscale approach.

2.1.3 Concurrent methods

The main feature of concurrent multiscale methods consists in embedding a microscopic model into the macroscopic one, leading to a strong coupling between different length scales, as sketched in Fig. 2.3; thus two main issues must be addressed in practical application of these methods, i.e. (i) suitable handling the coupling be-tween the fine-scale and the coarse-scale models, and (ii) finding efficient strategies for adding adaptivity during the fine-scale additions to the principal model, in order to reduce the computational costs.

Several concurrent methods have been proposed, based on different theoretical approaches and numerical strategies. According to the length scales involved in the considered physical problem, different choices can be made about the nature of the fine-scale models: on one hand, the microscopic model can be a discrete (molecular or atomistic) model, as in the macroscopic-atomistic-ab initio dynamics (MAAD) approach [148], the quasi-continuum (QC) method [149], the atomistic-to-continuum (AtC) coupling technique [150], and the bridging domain method [151]; on the other hand, the fine-scale model can be described as a continuum [152–154].

Concurrent multiscale methods can be regarded as falling within the class of domain decomposition methods (DDMs), since the numerical model describing the composite structure is decomposed into a fine- and coarse-scale sub-models, which are simultaneously solved, thus establishing a strong "two-way" coupling between different resolutions. In classical domain decomposition methods, the computational domain is divided into smaller subdomains to be simultaneously solved, and a computational strategy is required to make sure that the solutions on different subdomains match each other. Most of concurrent multiscale methods can be classified in overlapping and non-overlapping methods. In most multiscale models, two or more continuum models are strongly coupled to each other, allowing to perform accurate simulations at the microscopic scale within the so-called zone of interest, which is usually adaptively updated during calculations. A heterogeneous multiscale model consisting of several subdomains describing the material at different length scales is considered. Mesoscale models, characterized by a nonlinear material behavior, are only used in those zones of the structure in which damage or instabilities takes place; on the contrary, undamaged regions of the structure are simulated at the macroscale assuming a linear elastic material behavior characterized by effective material parameters. Such an approach combines the advantages of both scales, i.e. the numerical efficiency of macroscale models and the accuracy of microscale models. Moreover, concurrent multiscale methods are able to deal with boundary layer effects in a natural way, by replacing the coarse-scale model with a fine-scale one where periodicity conditions are no longer valid, as in the vicinity of free edges or applied loads or constraints.

The critical aspect of the concurrent multiscale methods is denoted by the connection between critical and the noncritical domains. Hence, to connect subdomains with nonmatching finite element discretization, two alternative methods are commonly adopted.

The first one is based on the enforcing the displacement compatibility in a strong sense, i.e.

$$\bar{\boldsymbol{u}}(\boldsymbol{X}) - \boldsymbol{u}(\boldsymbol{X}) = \boldsymbol{0} \quad \forall \boldsymbol{X} \in \Gamma_c = \bar{V} \cap V \tag{2.1}$$

where $\bar{\boldsymbol{u}}(\boldsymbol{X})$ and $\boldsymbol{u}(\boldsymbol{X})$ are the displacements of the subdomains $\bar{V}$ and V, respectively, and Γ_c represents the common interfaces (boundary in 2D cases) between the noncritical and critical subdomains in the undeformed configuration.

The second one is based on the enforcing the coupling condition (2.1) in an average sense; this strategy represents a weak coupling approach, realized by the mortar method [155]. The compatibility equation is imposed by means of an integral constraint on the common interfaces:

$$\int_{\Gamma_c} (\bar{\boldsymbol{u}}(\boldsymbol{X}) - \boldsymbol{u}(\boldsymbol{X}))dS = 0 \quad with \quad \Gamma_c = \bar{V} \cap V \tag{2.2}$$

allowing pointwise interpenetration or separation between the constrained interfaces.

3

Theoretical and numerical microscopic stability analyses in damaged fiber reinforced composite by using homogenization techniques

The present chapter deals with the macroscopic compressive failure of periodic elastic fiber reinforced composites related to local buckling instabilities promoted by matrix or fiber/matrix micro-cracks under unilateral self-contact. The theoretical modeling of instability and bifurcation phenomena for a microcracked composite material is firstly examined by considering a continuum homogenization approach and a rate formulation. The effects of non-standard rate contributions owing to the full finite deformation formulation adopted to model crack self-contact and depending on both the contact pressure and the deformation gradient rate are highlighted, by determining their influence on macroscopic critical loads at the onset of instability and bifurcation and on corresponding deformation modes. Numerical applications carried out by means of a coupled FE approach are reported in Section 3.4.2 with reference to macroscopic uniaxial loading paths and in Section 3.4.3 with reference to macroscopic biaxial loading paths. In detail, comprehensive parametric analysis with respect to the main microstructural geometrical parameters governing the failure behavior of the composite solid is carried out. Generally speaking, the numerical applications reported in Section 3.4 shown the notable influence of the above non-standard contributions on both critical loads and deformation modes: if they are not included in the analysis as in simplified crack contact interface formulations, a large underestimation of the real failure load of the microcracked composite is obtained.

3.1 Theoretical formulation of the nonlinear homogenization problem

The equilibrium problem of the microstructure, consisting of periodic fiber reinforcements embedded in a microcracked matrix, is formulated with reference to the representative volume element (RVE) shown in Fig. 3.1. The homogenized composite solid occupies the volume $\bar{V}_{(i)}$ and the initial position vector of a generic macroscopic point is referred to as $\bar{\boldsymbol{X}}$. The RVE associated with the generic macroscopic point is

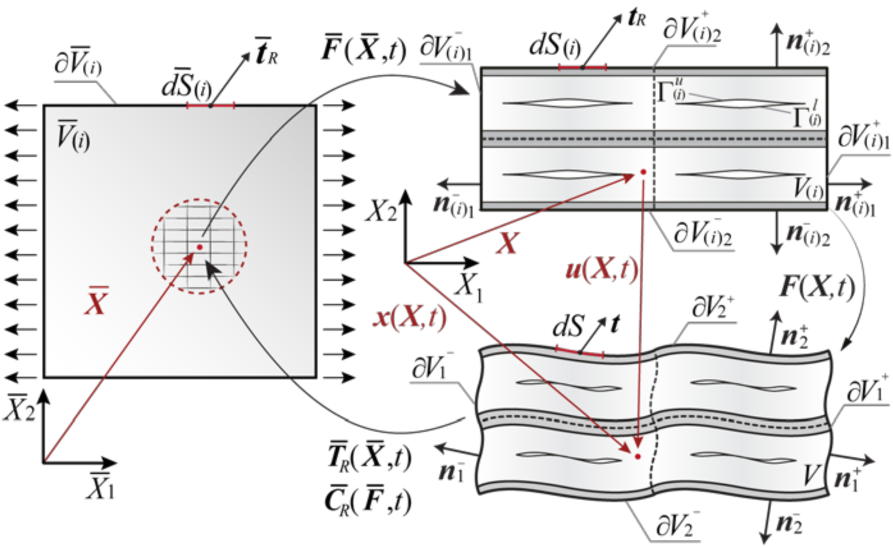

Fig. 3.1 Homogenized solid of a microcracked fiber-reinforced composite material (to the left) and corresponding undeformed and deformed RVE configurations (to the right) attached to a generic material point.

assumed to occupy a volume $V_{(i)}$ in the initial configuration and to contain preexisting cracks whose upper and lower surface are denoted as $\Gamma^u_{(i)}$ and $\Gamma^l_{(i)}$ (the superscript *u* and *l* are respectively referred to upper and lower surface, while the subscript (*i*) is referred to initial configuration). To account for bifurcation and instability phenomena (see, for instance, [21]), the RVE may be composed by an a-priori unknown assembly of unit cells or by a single unit cell of the periodic material. Each point in the undeformed RVE configuration is identified with its position vector $\boldsymbol{X}$ and the nonlinear deformation of the microstructure is denoted by $\boldsymbol{x}(\boldsymbol{X})$, mapping points $\boldsymbol{X}$ of the initial configuration $V_{(i)}$ onto points $\boldsymbol{x}$ of the actual configuration *V*. The displacement field and the deformation gradient at $\boldsymbol{X}$ are respectively defined as $\boldsymbol{u}(\boldsymbol{X}) = \boldsymbol{x}(\boldsymbol{X}) - \boldsymbol{X}$ and $\boldsymbol{F}(\boldsymbol{X}) = \partial \boldsymbol{x}(\boldsymbol{X}) / \partial \boldsymbol{X}$; the solid phases of the

RVE follow a rate independent, incrementally linear constitutive law that can be written in following form:

$$\dot{\boldsymbol{T}}_R = \boldsymbol{C}^R\left(\boldsymbol{X},\boldsymbol{F}\right)\left[\dot{\boldsymbol{F}}\right] \tag{3.1}$$

in which $\dot{\boldsymbol{T}}_R$ is the rate of the first Piola-Kirchhoff stress tensor, $\dot{\boldsymbol{F}}$ is the rate of the deformation gradient and $\boldsymbol{C}^R$ is the corresponding fourth-order tensor of nominal moduli satisfying the major symmetry condition (i.e. $C^R_{ijkl} = C^R_{klij}$). Every loading process, assuming that it produces a unique response called principal equilibrium path, can be parametrized in terms of a time-like parameter $t \geq 0$ monotonically increasing with the evolution of the loading process starting from $t = 0$ in the undeformed configuration. Since t describes the quasi-static deformation path of the composite solid, the rates of field quantities are considered to be the derivative with respect it.

For a hyperelastic material, whose constitutive behavior can be described in terms of strain energy-density function $W\left(\boldsymbol{X},\boldsymbol{F}\right)$, the nominal stress tensor (second-order tensor) and the nominal moduli tensor (fourth-order tensor) can be defined as:

$$\boldsymbol{T}_R = \frac{\partial W\left(\boldsymbol{X},\boldsymbol{F}\right)}{\partial \boldsymbol{F}},\ \boldsymbol{C}^R\left(\boldsymbol{X},\boldsymbol{F}\right) = \frac{\partial^2 W\left(\boldsymbol{X},\boldsymbol{F}\right)}{\partial \boldsymbol{F}\,\partial \boldsymbol{F}} \tag{3.2}$$

whose components are respectively $T_{R\,ij} = \partial W\left(\boldsymbol{X},\boldsymbol{F}\right)/\partial F_{ij}$ and $C^R_{ijkl} = \partial^2 W\left(\boldsymbol{X},\boldsymbol{F}\right)/\partial F_{ij}\partial F_{kl}$. The macroscopic deformation gradient $\bar{\boldsymbol{F}}$ and the first Piola-Kirchhoff stress tensor $\bar{\boldsymbol{T}}_R$, which define the micro-to-macro coupling, can be expressed as:

$$\begin{aligned}\bar{\boldsymbol{F}}(t) &= \frac{1}{\left|V_{(i)}\right|}\int_{\partial V_{(i)}} \boldsymbol{x}\left(\boldsymbol{X},t\right)\otimes \boldsymbol{n}_{(i)}\,dS_{(i)}\\ \bar{\boldsymbol{T}}_R(t) &= \frac{1}{\left|V_{(i)}\right|}\int_{\partial V_{(i)}} \boldsymbol{t}_R\left(\boldsymbol{X},t\right)\otimes \boldsymbol{X}\,dS_{(i)}\end{aligned} \tag{3.3}$$

where $\boldsymbol{t}_R = \boldsymbol{T}_R \boldsymbol{n}_{(i)}$ is the first Piola-Kirchhoff traction vector, $\otimes$ denotes the tensor product and $\boldsymbol{n}_{(i)}$ denotes the outward normal at $\boldsymbol{X} \in \partial V_{(i)}$. In a macrostrain driven loading regime, the microscopic deformation field can be written as a function of the macro-deformation gradient as follow:

$$\boldsymbol{x}(\boldsymbol{X}, t) = \bar{\boldsymbol{F}}(t)\boldsymbol{X} + \boldsymbol{w}(\boldsymbol{X}, t) \tag{3.4}$$

where $\bar{\boldsymbol{F}}(t)\boldsymbol{X}$ is a linear displacement contribution and $\boldsymbol{w}(\boldsymbol{X}, t)$ represents the fluctuation field. The application of (3.3) to the boundary of the RVE leads to the following integral constraint which provides the set of kinematically admissible displacement fluctuations:

$$\int_{\partial V_{(i)}} \boldsymbol{w} \otimes \boldsymbol{n}_{(i)} dS_{(i)} = \boldsymbol{0}, \tag{3.5}$$

which can be satisfied imposing periodic fluctuation field in accordance with the periodic nature of the composite microstructure:

$$\boldsymbol{w}(\boldsymbol{X}^+, t) = \boldsymbol{w}(\boldsymbol{X}^-, t) \text{ on } \partial V_{(i)} . \tag{3.6}$$

Consequently, periodic deformations and antiperiodic tractions are imposed on the boundary of the RVE:

$$\begin{cases} \boldsymbol{x}(\boldsymbol{X}^+, t) - \boldsymbol{x}(\boldsymbol{X}^-, t) = \bar{\boldsymbol{F}}(t)(\boldsymbol{X}^+ - \boldsymbol{X}^-) \\ \boldsymbol{T}_R \boldsymbol{n}_{(i)}(\boldsymbol{X}^+, t) = -\boldsymbol{T}_R \boldsymbol{n}_{(i)}(\boldsymbol{X}^-, t) \end{cases} \text{ on } \partial V_{(i)} \tag{3.7}$$

where the superscripts + and – denote pairs of opposite RVE boundary points.

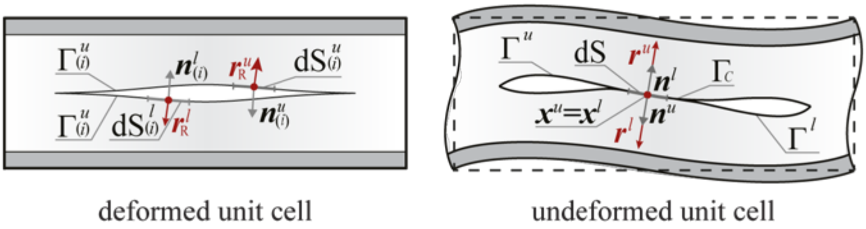

Fig. 3.2 Undeformed and deformed configurations of a unit cell: main parameters characterizing crack surfaces self-contact at a contact point pair $(\boldsymbol{X}^u, \boldsymbol{X}^l)_C$.

The RVE equilibrium boundary value problem at a given macro-deformation gradient is defined by the following equations (see [63,64] for details):

$$\begin{cases} Div\boldsymbol{T}_R\left(\bar{\boldsymbol{F}}(t)+\nabla\boldsymbol{w}(\boldsymbol{X},t)\right)=\boldsymbol{0} & \text{in } B_{(i)} \\ \boldsymbol{T}_R\boldsymbol{n}_{(i)}\left(\boldsymbol{X}^+,t\right)=-\boldsymbol{T}_R\boldsymbol{n}_{(i)}(\boldsymbol{X}^-,t) & \text{on } \partial\mathrm{V}_{(i)} \\ h^l(\boldsymbol{X}^u+\boldsymbol{u}(\boldsymbol{X}^u,t),t)\geq 0 & \\ \sigma_R{}^u(t)\leq 0 & \text{on } \Gamma^u_{(i)} \\ \sigma_R{}^u(t)h^l(\boldsymbol{X}^u+\boldsymbol{u}(\boldsymbol{X}^u,t),t)=0 & \\ \boldsymbol{T}_R\boldsymbol{n}^u_{(i)}dS^u_{(i)}/dS+\boldsymbol{T}_R\boldsymbol{n}^l_{(i)}dS^l_{(i)}/dS=\boldsymbol{0} & \forall\left(\boldsymbol{X}^l,\boldsymbol{X}^u\right)_C \\ \boldsymbol{T}_R\boldsymbol{n}^l_{(i)}=\sigma_R{}^l\boldsymbol{n}^l & \text{on } \Gamma^l_{C(i)} \end{cases} \tag{3.8}$$

where $B_{(i)}$ is the solid part of the RVE reference volume $\mathrm{V}_{(i)}$. Eqs. (3.8) are assumed to be satisfied along a sequence of equilibrium solutions for the RVE generated by macroscopic loading path $\bar{\boldsymbol{F}}(t)$ starting from $\mathrm{V}_{(i)}$ and referred to as the “principal solution path” when a unique solution for each value of the loading parameter t is obtained.

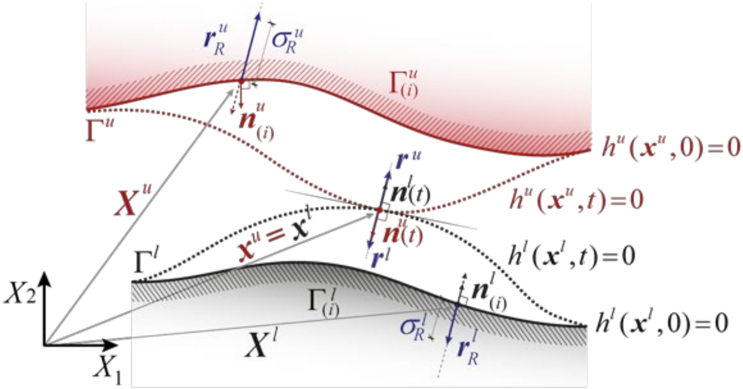

Fig. 3.3 Undeformed and deformed configurations of the crack surfaces, highlighting the pair of crack surface points $(\boldsymbol{X}^l, \boldsymbol{X}^u)_C$ and the main associated parameters.

Specifically, the frictionless unilateral contact conditions:

$$\begin{cases} h^l(\boldsymbol{X}^u + \boldsymbol{u}(\boldsymbol{X}^u,t),t) \geq 0 \\ \sigma_R{}^u(t) \leq 0 \\ \sigma_R{}^u(t) h^l(\boldsymbol{X}^u + \boldsymbol{u}(\boldsymbol{X}^u,t),t) = 0 \end{cases} \quad \text{on } \Gamma_{(i)}^u \tag{3.9}$$

expressed in terms of points $\boldsymbol{X}^u$ of the upper crack surface $\Gamma_{(i)}^u$, consists respectively of the impenetrability and mechanical unilateral conditions. As shown in Fig. 3.2 and in more detail in Fig. 3.3, these conditions $h^u = 0$ and $h^l = 0$ describe the deformed upper and lower crack surfaces, denoted by Γ^u and Γ^l, while $\sigma_R{}^u = \boldsymbol{T}_R \boldsymbol{n}_{(i)}^u \bullet \boldsymbol{n}^u$ is the normal nominal contact reaction on the upper crack surface, with $\boldsymbol{T}_R \boldsymbol{n}_{(i)}^u = \boldsymbol{r}_R^u$ and $\boldsymbol{n}^u$ respectively representing the nominal contact reaction and the deformed outward normal. Within a finite deformation framework, the normal nominal contact reactions on the lower an upper crack contact surfaces are different, i.e. $\sigma_R{}^u \neq \sigma_R{}^l$, whereas the corresponding normal true contact reactions are coincident, i.e. $\sigma^u = \sigma^l = \sigma$.

The following equation, reported in (3.8) :

$$\boldsymbol{T}_R \boldsymbol{n}^u_{(i)} dS^u_{(i)} / dS + \boldsymbol{T}_R \boldsymbol{n}^l_{(i)} dS^l_{(i)} / dS = \boldsymbol{0} \quad \forall \left(\boldsymbol{X}^l, \boldsymbol{X}^u \right)_C \tag{3.10}$$

expresses the balance of linear momentum across the contact interface in the actual deformed configuration Γ_C in terms of nominal contact reactions for each pair of crack surface points $(\boldsymbol{X}^l, \boldsymbol{X}^u)_C$ in contact in the actual deformed configuration defined as follows:

$$\left(\boldsymbol{X}^l, \boldsymbol{X}^u \right)_C = \left\{ \boldsymbol{X}^l \in \Gamma^l_{C(i)}, \boldsymbol{X}^u \in \Gamma^u_{C(i)} \,|\, \boldsymbol{x}(\boldsymbol{X}^l) = \boldsymbol{x}(\boldsymbol{X}^u) \right\}, \tag{3.11}$$

where $\Gamma^l_{C(i)}$ and $\Gamma^u_{C(i)}$ represent portions of the lower and upper crack surfaces in contact in the actual deformed configuration. It imposes that the sum of the true contact reactions $\boldsymbol{r}^u = \boldsymbol{T}^u \boldsymbol{n}^u(t)$ and $\boldsymbol{r}^l = \boldsymbol{T}^l \boldsymbol{n}^l(t)$ acting on the opposite crack surfaces (see Fig. 3.2) vanishes:

$$\boldsymbol{T}^u \boldsymbol{n}^u(t) + \boldsymbol{T}^l \boldsymbol{n}^l(t) = \boldsymbol{0} \text{ on } \Gamma_C , \tag{3.12}$$

where $\boldsymbol{T}$ is the Cauchy stress tensor. In terms of true contact reactions the equation

$$\boldsymbol{T}_R \boldsymbol{n}^l_{(i)} = \sigma_R{}^l \boldsymbol{n}^l \text{ on } \Gamma^l_{C(i)} \tag{3.13}$$

corresponding to the frictionless condition for the lower contact crack surface $\Gamma^l_{C(i)}$, can be equivalently written as $\boldsymbol{r}^l = \sigma^l \boldsymbol{n}^l$. As a consequence, the following relation between the nominal normal contact reaction and the true one acting on the upper and lower crack surfaces can be obtained:

$$\sigma = \sigma_R{}^u dS / dS^l_{(i)} = \sigma_R{}^l dS / dS^u_{(i)}, \quad \forall \left(\boldsymbol{X}^l, \boldsymbol{X}^u \right)_C \tag{3.14}$$

where $dS / dS^l_{(i)}$ can be expressed by using Nanson's formula (similarly for $dS / dS^u_{(i)}$) as $dS / dS^l_{(i)} = J^u \boldsymbol{F}^{u-T} \boldsymbol{n}^u_{(i)} \cdot \boldsymbol{n}^u$ with J denoting the determinant of the deformation gradient.

3.1.1 Rate equilibrium boundary value problem (BVP)

In order to perform the uniqueness and stability analyses along the principal equilibrium path, the RVE quasi-static rate equilibrium solution associated with a superimposed macroscopic deformation gradient rate $\dot{\bar{\boldsymbol{F}}}$, must be determined. The rate equations governing the rate equilibrium solution of the microstructure can be derived from Eqs. (8) by means of asymptotic expansions at a generic time t (see [63] for additional details) and can be defined in terms of the fluctuation rate solution $\dot{\boldsymbol{w}}_{\dot{\bar{\boldsymbol{F}}}}$. In particular, Eqs. (3.8)3 lead to the following rate conditions:

$$\begin{cases} [\![\dot{u}_n(\boldsymbol{X})]\!]_{\Gamma_C} \leq 0 \\ \sigma_R^u [\![\dot{u}_n(\boldsymbol{X})]\!]_{\Gamma_C} = 0 \\ if \;\; \sigma_R^u = 0 \;\; \dot{\sigma}_R^u [\![\dot{u}_n(\boldsymbol{X})]\!]_{\Gamma_C} = 0 \;\; and \;\; \dot{\sigma}_R^u \leq 0, \quad \forall \left(\boldsymbol{X}^l, \boldsymbol{X}^u\right)_C \end{cases} \tag{3.15}$$

where $\dot{u}_n(\boldsymbol{X})$ denotes the projection of the displacement rate along the normal to the deformed lower crack surface $\boldsymbol{n}^l$, $[\![\dot{u}_n(\boldsymbol{X})]\!]_{\Gamma_C} = \dot{u}_n(\boldsymbol{X}^l) - \dot{u}_n(\boldsymbol{X}^u)$ is its jump at a contact point pair $(\boldsymbol{X}^u, \boldsymbol{X}^l)_C$.

By virtue of Eq. (3.4), the normal displacement rate jump can be expressed as a function of the normal fluctuation field rate:

$$[\![\dot{u}_n(\boldsymbol{X})]\!]_{\Gamma_C} = [\![\dot{w}_n(\boldsymbol{X})]\!]_{\Gamma_C} - \boldsymbol{n}^l \bullet \left[\dot{\bar{\boldsymbol{F}}}\left(\boldsymbol{X}^u - \boldsymbol{X}^l\right)\right]. \tag{3.16}$$

The response of the microstructure to the superimposed macroscopic deformation gradient rate can be obtained finding the fluctuation rate solution:

$$\dot{\boldsymbol{w}} \in A^*(\bar{\boldsymbol{F}}, \dot{\bar{\boldsymbol{F}}}) = \left\{ \dot{\boldsymbol{w}} \in H^1\left(V_\#\right) \middle| \begin{matrix} [\![\dot{u}_n]\!]_{\Gamma_C} = 0 \; if \, \sigma_R{}^u < 0 \\ [\![\dot{u}_n]\!]_{\Gamma_C} \leq 0 \; if \, \sigma_R{}^u = 0 \end{matrix} \; \text{on } \Gamma^l_{c(i)} \cup \Gamma^u_{c(i)} \right\} \tag{3.17}$$

such that $\forall \delta\dot{\boldsymbol{w}} \in A^{*}(\bar{\boldsymbol{F}}, \dot{\bar{\boldsymbol{F}}})$ the following inequality is satisfied:

$$\begin{aligned}&\int_{B_{(i)}} \boldsymbol{C}^{R}\left(\boldsymbol{X}, \bar{\boldsymbol{F}}\right)[\dot{\bar{\boldsymbol{F}}} + \nabla \dot{\boldsymbol{w}}_{\dot{\bar{\boldsymbol{F}}}}] \bullet \nabla\left(\delta\dot{\boldsymbol{w}} - \dot{\boldsymbol{w}}\right) dV_{(i)} + \\ &- \int_{\Gamma^{l}_{c(i)} \cup \Gamma^{u}_{c(i)}} \left(-\sigma_{R}\boldsymbol{n}\left(\frac{dS_{(i)}}{dS}\right)^{\bullet} \frac{dS}{dS_{(i)}} + \sigma_{R}\dot{\boldsymbol{n}} \right) \bullet \left(\delta\dot{\boldsymbol{w}} - \dot{\boldsymbol{w}}\right) dS_{(i)} \geq 0\end{aligned} \tag{3.18}$$

where $A^{*}(\bar{\boldsymbol{F}}, \dot{\bar{\boldsymbol{F}}})$ denotes the set of admissible fluctuation rates depending on both the current equilibrium solution associated to $\bar{\boldsymbol{F}}$ and the superimposed macrodeformation gradient rate $\dot{\bar{\boldsymbol{F}}}$, $H^{1}(V_{\#})$ denotes the usual Hilbert space of order one of vector valued functions periodic over *V*, ∇ denotes the gradient operator with respect to $\boldsymbol{X}$, the summation over all the contact crack surface pairs included in the RVE is intended for crack surface integrals involving $\Gamma_{c(i)}{}^{u}$ and $\Gamma_{c(i)}{}^{l}$ and the volume integral is intended to be performed over the solid part $B_{(i)}$ of the RVE reference volume $V_{(i)}$. As a matter of fact extracting the strong form from the above weak inequality, in addition to the rate equilibrium condition of the microstructure and to the rate counterpart of Eq.(3.7)$_2$, it leads to the following crack contact interface rate conditions for every contact point pairs $(\boldsymbol{X}^{l}, \boldsymbol{X}^{u})_{C}$:

$$\begin{cases} \dot{\boldsymbol{r}}_{R}{}^{u}\dfrac{dS^{u}_{(i)}}{dS} + \dot{\boldsymbol{r}}_{R}{}^{l}\dfrac{dS^{l}_{(i)}}{dS} + \ \sigma_{R}{}^{u}\boldsymbol{n}^{u}\left(\dfrac{dS^{u}_{(i)}}{dS}\right)^{\bullet} + \sigma_{R}{}^{l}\boldsymbol{n}^{l}\left(\dfrac{dS^{l}_{(i)}}{dS}\right)^{\bullet} = \boldsymbol{0} \\ \dot{\boldsymbol{r}}^{u/l}_{R} - \left(\dot{\boldsymbol{r}}^{u/l}_{R} \bullet \boldsymbol{n}^{u/l}\right)\boldsymbol{n}^{u/l} = \sigma^{u/l}_{R}\dot{\boldsymbol{n}}^{u/l} \\ \dot{\boldsymbol{r}}^{l}_{R} \bullet \boldsymbol{n}^{l} = \dot{\sigma}_{R}{}^{l} \leq 0 \ \ and \ \ \dot{\sigma}_{R}{}^{l}[\![\dot{u}_{\boldsymbol{n}}]\!]_{\Gamma_{C}} = 0 \ \ \ if \ \ \sigma^{l}_{R} = 0 \end{cases}, \tag{3.19}$$

where $\dot{\boldsymbol{r}}_{R}$ is the nominal contact reaction rate, defined as $\dot{\boldsymbol{r}}_{R} = \dot{\boldsymbol{T}}_{R}\boldsymbol{n}_{(i)}$, the first and second equations represent the rate counterpart of Eqs. (3.8)$_6$

and (3.8)$_7$, whereas the last two are similar to those arising for unilateral contact problems in linear elastostatics.

It is worth noting that when friction phenomena between crack faces must be accounted in the model, additional non-linearities arise in the formulation of the homogenization problem. As a matter of fact, the homogenized rate constitutive law becomes a general nonlinear function instead of a homogeneous of degree one function with respect to the macroscopic deformation gradient rate and additional sources of non-symmetry in the variational inequality characterizing the rate equilibrium problem must be considered.

The above theoretical results can be also used for generic non-periodic RVEs including an arbitrary distribution of heterogeneities and microcracks, for which linear deformations boundary conditions can be applied in place of the periodic ones.

Moreover Eqs. (3.8)$_4$, leads to the rate equilibrium conditions at the crack contact interface Γ_C :

$$\begin{cases} \dot{\boldsymbol{r}}_R{}^u \dfrac{dS^u_{(i)}}{dS} + \dot{\boldsymbol{r}}_R{}^l \dfrac{dS^l_{(i)}}{dS} + & \\ +\sigma_R{}^u \boldsymbol{n}^u \left(\dfrac{dS^u_{(i)}}{dS}\right)^{\bullet} + \sigma_R{}^l \boldsymbol{n}^l \left(\dfrac{dS^l_{(i)}}{dS}\right)^{\bullet} = \boldsymbol{0} & \forall\left(\boldsymbol{X}^l, \boldsymbol{X}^u\right)_C, \\ \dot{\boldsymbol{r}}^l_R - \dot{\sigma}^l_R \boldsymbol{n}^l = \sigma^l_R \dot{\boldsymbol{n}}^l & \text{on} \quad \Gamma^l_{C(i)} \end{cases} \tag{3.20}$$

where $\dot{\boldsymbol{r}}_R = \dot{\boldsymbol{T}}_R \boldsymbol{n}_{(i)}$ is the nominal contact reaction rate and the rates of the referential to actual area element ratio and for the rate of contact surface normal (for both the upper and the lower crack surfaces) can be obtained by using Nanson's formula respectively as:

$$\left(\frac{dS_{(i)}}{dS}\right)^{\bullet} = -\frac{\sigma}{\sigma_R}\frac{dS_{(i)}}{dS}\left(J\boldsymbol{F}^{-T}\boldsymbol{n}_{(i)} \bullet \boldsymbol{n}\right)^{\bullet}, \quad \dot{\boldsymbol{n}} = -\left(\boldsymbol{L}^T - L_n \boldsymbol{1}\right)\boldsymbol{n},, \tag{3.21}$$

where $\boldsymbol{L} = \nabla_x \dot{\boldsymbol{u}}$ is the spatial gradient (namely with respect to $\boldsymbol{x}$) of the displacement rate, also called the velocity gradient, and $L_n = \boldsymbol{Ln} \bullet \boldsymbol{n}$.

3.2 Nonlinear effect arising at the crack contact interface

As a prelude to derive the non-bifurcation condition of the rate response and of the infinitesimal stability condition, the following contact surface integral is examined representing the virtual work of the contact reaction rate acting on the present contact interface in a virtual displacement $\delta\boldsymbol{u} \in A^*(\overline{\boldsymbol{F}}, \dot{\overline{\boldsymbol{F}}})$:

$$\delta L_{rate}\left(\Gamma_c\right) = \int_{\Gamma_{c(i)}{}^l} \left[\dot{\boldsymbol{r}}_R^l \bullet \delta\boldsymbol{u}^l\right] \, dS_{(i)} + \int_{\Gamma_{c(i)}{}^u} \left[\dot{\boldsymbol{r}}_R^u \bullet \delta\boldsymbol{u}^u\right] \, dS_{(i)} \tag{3.22}$$

As it will be shown in the sequel an accurate evaluation of this contact surface integral contribution, including non-standard rate contributions arising from a full finite deformation formulation, is essential to obtain an effective prediction of the critical load levels associated with an angular bifurcation and a primary instability. Using Eq. $(3.20)_1$ the contact surface integral becomes

$$\begin{aligned} \delta L_{rate}\left(\Gamma_c\right) = & \int_{\Gamma_{c(i)}{}^l} \dot{\boldsymbol{r}}_R{}^l \bullet \delta\boldsymbol{u}^l dS^l_{(i)} + \\ & - \int_{\Gamma^u_{c(i)}} \left[\sigma_R{}^l \boldsymbol{n}^l \left(\frac{dS^l_{(i)}}{dS}\right)^{\bullet} + \dot{\boldsymbol{r}}_R{}^l \frac{dS^l_{(i)}}{dS} + \sigma_R{}^u \boldsymbol{n}^u \left(\frac{dS^u_{(i)}}{dS}\right)^{\bullet} \right] \frac{dS}{dS^u_{(i)}} \bullet \delta\boldsymbol{u}^u dS^u_{(i)} \end{aligned} \tag{3.23}$$

In order to substitute $\delta\boldsymbol{u}^u$ with $\delta\boldsymbol{u}^l$ has been made use of Eq. $(3.15)_2$ leading to the following contact surface integral:

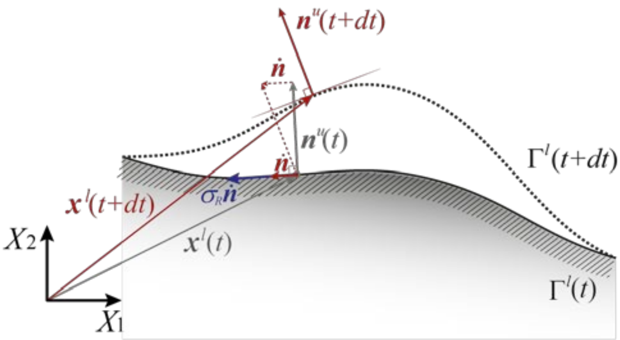

Fig. 3.4 Tangential term related to the rate of the crack surface normal.

$$\begin{aligned} \delta L_{rate}\left(\Gamma_c\right) = & \int_{\Gamma^l_{c(i)}} \dot{\boldsymbol{r}}_R{}^l \bullet [\![\delta \boldsymbol{u}]\!]_{\Gamma_c} \, dS^l_{(i)} + \\ & - \int_{\Gamma^l_{c(i)}} \sigma_R{}^l \left[\left(\frac{dS^l_{(i)}}{dS}\right)^{\bullet} \frac{dS}{dS^l_{(i)}} - \left(\frac{dS^u_{(i)}}{dS}\right)^{\bullet} \frac{dS}{dS^u_{(i)}} \right] \delta u_n{}^l \, dS^l_{(i)} \end{aligned} \quad . \tag{3.24}$$

Moreover taking into account for the frictionless contact model (see Eq. (3.20)$_2$), the contact reaction rate can be written as $\dot{\boldsymbol{r}}_R = \sigma_R \dot{\boldsymbol{n}} + \dot{\sigma}_R \boldsymbol{n}$ and this leads to:

$$\int_{\Gamma^l_{c(i)}} \sigma^l_R \dot{\boldsymbol{n}}^l \bullet [\![\delta \boldsymbol{u}]\!]_{\Gamma_c} \, dS^l_{(i)} - \int_{\Gamma^l_{c(i)}} \sigma_R{}^l \left[\!\!\left[\left(\frac{dS_{(i)}}{dS}\right)^{\bullet} \frac{dS}{dS_{(i)}} \right]\!\!\right]_{\Gamma_c} \delta u_n{}^l \, dS^l_{(i)} \tag{3.25}$$

where it has been considered that:

$$\left(\frac{dS^l_{(i)}}{dS}\right)^{\bullet} \frac{dS}{dS^l_{(i)}} - \left(\frac{dS^u_{(i)}}{dS}\right)^{\bullet} \frac{dS}{dS^u_{(i)}} = \left[\!\!\left[\left(\frac{dS_{(i)}}{dS}\right)^{\bullet} \frac{dS}{dS_{(i)}} \right]\!\!\right]_{\Gamma_c} .$$

Eq. (3.25) shows that the work done by the nominal contact reaction through the virtual displacement consists in both the contribution of the tangential component of the nominal contact reaction rate $\sigma_R \dot{\boldsymbol{n}}$ (since

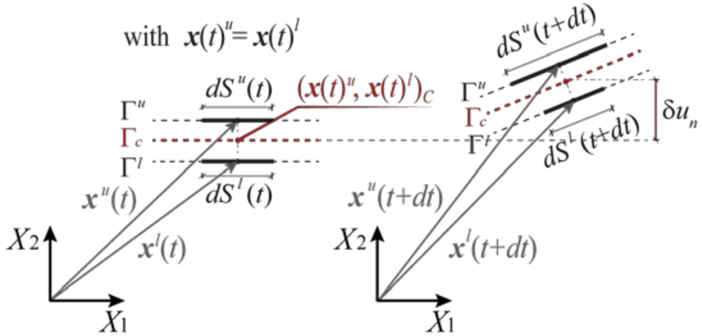

Fig. 3.5 Relative crack surface deformation term.

$\boldsymbol{n}\bullet\dot{\boldsymbol{n}} = 0$), sketched in Fig. 3.4, and of that related to the different variation of the reference to actual surface element ratio $dS^u_{(i)} / dS$ between the lower and upper crack contact surfaces, sketched in Fig. 3.5.

For the sake of brevity in what follows these two contributions will be referred to as tangential contribution and crack surface deformation contribution, respectively. When an interface formulation is adopted to model crack surface self-contact by using a generalized cohesive models with interface traction-separation laws including contact effects arising when normal compression acts on the interface (see [30,156], for instance), the following assumption on crack interface traction continuity for pairs of points coincident in the initial undeformed configuration is usually introduced

$$[\![\boldsymbol{T}_R(\boldsymbol{X})]\!]_{\Gamma_{c(i)}} \boldsymbol{n}^l_{(i)} = \boldsymbol{r}_R{}^l + \boldsymbol{r}_R{}^u = \boldsymbol{0}\,, \tag{3.26}$$

where $[\![\boldsymbol{f}(\boldsymbol{X})]\!]_{\Gamma_{C(i)}} = \boldsymbol{f}(\boldsymbol{X}^l) - \boldsymbol{f}(\boldsymbol{X}^u)$ denotes the jump across the undeformed contact interface in the enclosed field for an initially coincident points pair $(\boldsymbol{X}^l, \boldsymbol{X}^u)_{C(i)}$ defined as:

$$(\boldsymbol{X}^l, \boldsymbol{X}^u)_{C(i)} = \left\{ \boldsymbol{X}^l \in \Gamma^l_{C(i)}, \boldsymbol{X}^u \in \Gamma^u_{C(i)} \,\middle|\, \boldsymbol{X}^l = \boldsymbol{X}^u \right\}. \tag{3.27}$$

Eq. (3.26) allows to formulate an interface constitutive law relating the nominal contact reaction vector $\boldsymbol{r}_R$ to the interface separation $[\![\boldsymbol{u}]\!]_{\Gamma_{C(i)}}$ determined with respect to initially coincident points pair, thus it is uniquely defined and can be referred to both the upper and the lower crack surface (the former being equal in magnitude and opposite in direction to the latter and vice versa). Using the nominal traction continuity condition (3.26) in rate form, the corresponding virtual work of the contact reaction rate acting on the undeformed contact interface $\delta L_{rate}\left(\Gamma_{c(i)}\right)$ can be written as:

$$\delta L_{rate}\left(\Gamma_{c(i)}\right) = \int_{\Gamma^l_{c(i)}} \dot{\boldsymbol{r}}^l_R \bullet [\![\delta \boldsymbol{u}]\!]_{\Gamma_{c(i)}} dS^l_{(i)} = \int_{\Gamma^l_{c(i)}} \sigma^l_R \dot{\boldsymbol{n}}^l \bullet [\![\delta \boldsymbol{u}]\!]_{\Gamma_{c(i)}} dS^l_{(i)} \quad (3.28)$$

It is worth noting that the modified virtual work of the contact reaction rate expressed by (3.28) has a similar structure of those valid for a fixed obstacle problem for which a potential is admitted (see [157]).

Comparison between Eqs. (3.25) and (3.28) points out the presence of non-standard crack contact interface terms coherent with the full finite deformation formulation, which are neglected when an interface constitutive law according to Eq. (3.26) is adopted.

Specifically, the crack surface deformation contribution, i.e. the second surface integral at the right hand side of Eq. (3.25), vanishes owing to the assumed equivalence between the contact reaction pressure on the upper crack surface and that acting on the lower one for initially coincident points pairs $(\boldsymbol{X}^l, \boldsymbol{X}^u)_{C(i)}$, being in turn a direct consequence of the traction continuity condition (3.26). Moreover, the above assumption leads to introduce in the virtual work the displacement jump across the undeformed contact interface in place of that evaluated with reference to the deformed one.

Note that the simplified contact reaction rate virtual work (3.28) becomes equivalent to its full finite deformation version (3.25), when the following equation holds along the deformation process

$$\frac{dS^l_{(i)}}{dS} = \frac{dS^u_{(i)}}{dS} \qquad \forall t \ \ and \ \ \forall(\boldsymbol{X}^u, \boldsymbol{X}^l)_C \tag{3.29}$$

a situation occurring, for instance, when the tangential displacement rate jump at the crack contact interface is always null during the deformation process, implying that every points pair $(\boldsymbol{X}^l, \boldsymbol{X}^u)_C$ in contact in the actual deformed configuration of the crack interface correspond to an initially coincident points pair $(\boldsymbol{X}^l, \boldsymbol{X}^u)_{C(i)}$. However in this case the virtual work of the contact reaction rate becomes globally zero coherently with the contact reaction continuity equation (3.26) which is rigorously valid for a material discontinuity interface without displacement jumps across this discontinuity. As a consequence of (3.29) we have also that $\sigma_R{}^l = \sigma_R{}^u = \sigma\, dS/dS_{(i)}$ where $dS_{(i)}{}^l = dS_{(i)}{}^u = dS_{(i)}$.

3.3 Stability and bifurcation analyses: full finite deformation and interface formulation

As shown in [31,33] the stability criterion of the current equilibrium configuration $V(t)$ can be obtained by considering a small perturbation of the current equilibrium position for a fixed macroscopic deformation gradient ($\dot{\boldsymbol{F}} = \boldsymbol{0}$) due to perturbation forces applied starting from the time t. For small value of the time-like parameter $\tau \geq 0$ describing the evolution of the system (with $\tau = 0$ corresponding to the time t), after the use of the energy balance and consideration of the equilibrium condition in $V(t)$ and of the antiperiodicity condition for the surface tractions, the second order expansion of the work done by the perturbation forces $L_{per}\left(0,\tau\right)$ can be written as:

$$L_{per}\left(0,\tau\right)=\left(\int_{B_{(i)}}\dot{\boldsymbol{T}}_R\bullet\dot{\boldsymbol{F}}dV_{(i)}-\int_{\Gamma^l_{c(i)}\cup\Gamma^u_{c(i)}}\dot{\boldsymbol{r}}_R\bullet\dot{\boldsymbol{u}}\;dS_{(i)}\right)\frac{\tau^2}{2}+\ldots+K\left(\tau\right) \quad (3.30)$$

where $L_{per}\left(0,\tau\right)$ denotes the work done by the perturbation forces, the expression in the round bracket is the second order approximation of the difference between the internal deformation work and the work done by the antiperiodic surface tractions $\boldsymbol{t}_{\mathrm{R}}$ and by the nominal contact reaction $\boldsymbol{r}_{\mathrm{R}}$ during the perturbed motion, $K\left(\tau\right)$ is the kinetic energy of the RVE at time τ and the perturbed motion is defined in terms of the displacement field $\boldsymbol{u}(\boldsymbol{x},\tau)$ compatible with self-contact conditions and with the periodicity boundary conditions for any τ and such that $\boldsymbol{u}(\boldsymbol{x},\tau=0)$ corresponds to the current equilibrium solution. Owing to the assumptions on the perturbed motion, the displacement rate corresponding to the rate of a fluctuation field $\dot{\boldsymbol{u}}(\boldsymbol{x})=\dot{\boldsymbol{w}}(\boldsymbol{x})$ must belong to $A^*(\overline{\boldsymbol{F}},\dot{\overline{\boldsymbol{F}}}=\boldsymbol{0})$.

Using the same arguments that leaded to Eq. (3.25) for the contact surface integral contribution, we obtain the following expression for the functional defined by the round bracket at the left hand side of (3.30) (called the stability functional):

$$\begin{aligned} S\left(\overline{\boldsymbol{F}},\dot{\boldsymbol{w}}\right)=&\int_{B_{(i)}}\boldsymbol{C}^R\left(\boldsymbol{X},\overline{\boldsymbol{F}}\right)[\nabla\dot{\boldsymbol{w}}]\bullet\nabla\dot{\boldsymbol{w}}dV_{(i)}-\int_{\Gamma^l_{c(i)}}\sigma^l_R\dot{\boldsymbol{n}}^l\bullet[\![\dot{\boldsymbol{w}}]\!]_{\Gamma_c}dS^l_{(i)}+\\ &+\int_{\Gamma^l_{c(i)}}\sigma_R{}^l\left[\!\!\left[\left(\frac{dS_{(i)}}{dS}\right)^{\bullet}\frac{dS}{dS_{(i)}}\right]\!\!\right]_{\Gamma_c}\dot{w}_n{}^l dS^l_{(i)} \end{aligned}\quad .\ (3.31)$$

The positivity condition of (3.31) for all $\dot{\boldsymbol{w}}(\boldsymbol{x}) \neq \boldsymbol{0} \in A^*(\bar{\boldsymbol{F}}, \dot{\bar{\boldsymbol{F}}} = \boldsymbol{0})$ ensures the static stability of the considered equilibrium since implies that the external environment must provide additional energy in order to perturb the examined equilibrium configuration. A primary instability is detected at the critical loading parameter t_{cS}, when the minimum eigenvalue associated to the above stability functional first vanishes

$$\Lambda = \min_{\dot{\boldsymbol{w}}(\boldsymbol{x}) \in A^*(\bar{\boldsymbol{F}}, \dot{\bar{\boldsymbol{F}}} = \boldsymbol{0})} \left\{ S\left(\bar{\boldsymbol{F}}, \dot{\boldsymbol{w}}\right) / \int_{B_{(i)}} \nabla \dot{\boldsymbol{w}} \bullet \nabla \dot{\boldsymbol{w}} dV_{(i)} \right\}. \tag{3.32}$$

The corresponding deformation mode for which the stability functional vanishes has been called the instability mode and the associated non-bifurcation criterion of the principal equilibrium path (see [31] for a proof) can be expressed by the following positivity condition for the functional $R\left(\dot{\bar{\boldsymbol{F}}}, \dot{\boldsymbol{w}}_1, \dot{\boldsymbol{w}}_2\right)$ which must be satisfied for every pair of admissible fields $\dot{\boldsymbol{w}}^{(1)} \neq \dot{\boldsymbol{w}}^{(2)} \in A^*(\bar{\boldsymbol{F}}, \dot{\bar{\boldsymbol{F}}})$:

$$\begin{aligned} &\int_{B_{(i)}} \boldsymbol{C}^R\left(\boldsymbol{X}, \bar{\boldsymbol{F}}\right)[\nabla \dot{\boldsymbol{w}}^{(1)} - \nabla \dot{\boldsymbol{w}}^{(2)}] \bullet \left(\nabla \dot{\boldsymbol{w}}^{(1)} - \nabla \dot{\boldsymbol{w}}^{(2)}\right) dV_{(i)} + \\ &- \int_{\Gamma_{c(i)}{}^l} \sigma_R^l \Delta \dot{\boldsymbol{n}}^l \bullet [\![\Delta \dot{\boldsymbol{w}}]\!]_{\Gamma_c} dS_{(i)}^l + \int_{\Gamma_{c(i)}{}^l} \sigma_R{}^l \left[\!\!\left[\Delta \left(\frac{dS_{(i)}}{dS} \right)^{\boldsymbol{\cdot}} \frac{dS}{dS_{(i)}} \right]\!\!\right]_{\Gamma_c} \Delta \dot{w}_n{}^l dS_{(i)}^l > 0 \end{aligned} \tag{3.33}$$

where it has been considered that $\sigma_R^l \boldsymbol{n}^l \bullet \Delta \dot{\boldsymbol{w}}^u = \sigma_R^l \boldsymbol{n}^l \bullet \Delta \dot{\boldsymbol{w}}^l - \sigma_R^l [\![\Delta \dot{w}_n]\!]_{\Gamma_c}$ owing to Eq. $(3.15)_2$, the superscripts (1) and (2) denote two possible solutions $\dot{\boldsymbol{u}}^{(i)} = \dot{\bar{\boldsymbol{F}}} \boldsymbol{X} + \dot{\boldsymbol{w}}_{\dot{\bar{F}}}^{(i)}$ (i=1,2) of the rate problem (3.17) resulting from $\dot{\bar{\boldsymbol{F}}}(t)$, $\Delta \dot{\boldsymbol{w}} = \Delta \dot{\boldsymbol{u}} = \dot{\boldsymbol{u}}^{(1)} - \dot{\boldsymbol{u}}^{(2)}$ denote their difference and similarly for other quantities associated with the two solutions.

Note that the stability condition can be obtained by requiring that the trivial solution $\dot{\boldsymbol{w}} = \boldsymbol{0}$ is unique for homogeneous macroscopic loading

$\dot{\bar{\boldsymbol{F}}}(t)=0$, namely pairing $\dot{\boldsymbol{w}}^{(2)}=\boldsymbol{0}$ supposed as a known solution, with a generic admissible fluctuation field rate $\dot{\boldsymbol{w}}^{(1)}=\dot{\boldsymbol{w}}$. This implies that for homogeneous loading stability implies uniqueness, although the first state for which the stability functional becomes positive-semidefinite on a stable path is ordinarily not a primary bifurcation state ("eigenstate") admitting nontrivial rate solutions ("eigenmodes"), because the deformation sensitive loading mechanism arising due to crack self-contact does not admit a potential.

Accordingly $t_{cE} \geq t_{cS}$ where t_{cE} is the eigenstate loading level, with the equality holding in the case of self-adjoint contact data for which the solution of the variational inequality

$$S_{,\dot{w}}\left(\bar{\boldsymbol{F}},\dot{\boldsymbol{w}}\right)\left[\delta\dot{\boldsymbol{w}}-\dot{\boldsymbol{w}}\right]\geq 0 \quad \forall\,\delta\dot{\boldsymbol{w}}\in A^{*}(\bar{\boldsymbol{F}},\dot{\bar{\boldsymbol{F}}}=\boldsymbol{0}), \tag{3.34}$$

arising when the minimum eigenvalue of the stability functional first vanishes, is at the same time the solution of the variational inequality (3.17) specialized to the case of $\dot{\bar{\boldsymbol{F}}}=\boldsymbol{0}$ (see [31] for additional details).

In the general case of non-homogeneous loading $\dot{\bar{\boldsymbol{F}}}_{(0)}\neq\boldsymbol{0}$, owing to contact nonlinearities, the stability condition excluding possible eigenstate does not ensure uniqueness since an eigenstate does not correspond to a primary bifurcation state; on the other hand as shown in [31] the non-bifurcation condition (3.33) implies stability.

In order to circumvent non-linearities arising from crack self-contact, incrementally linear comparison problems can be adopted as shown in [31], with lower bound predictions for the loading levels at the onset of instability and bifurcation obtained using the incremental comparison problem corresponding to free to penetrate rate conditions on the zone of loose contact or over the whole crack contact interface (namely $[\![\dot{w}_{(0)n}]\!]_{\Gamma_C}$ arbitrary on Γ_c where σ=0 or on the whole Γ_c), whereas upper bound predictions can be obtained with reference to the linear comparison rate problem corresponding to bonding in the normal direction on the zones of loose contact or over the whole crack contact interface (namely $[\![\dot{w}_{(0)n}]\!]_{\Gamma_C}=0$ along Γ_c where $\sigma=0$ or on the whole Γ_c).

The latter kind of comparison solids, referred to as completely free and completely bonded rate problems, can be useful in the case of effective contact, where $\sigma<0\ \forall \boldsymbol{x} \in \Gamma_c$. For instance, for the lower bounds cases we have that $t_{cS}^{F} \le t_{cS}$, $t_{cS}^{F} \le t_c$ or that $t_{cS}^{CF} \le t_{cS} \le t_c$ where t_{cS}^{F} and t_{cS}^{CF} represents the critical load level of the free and completely free rate comparison problems, respectively.

Finally, it is worth noting that the same considerations done in the case of homogeneous loading can be done also for non-homogenous loading conditions $\dot{\bar{\boldsymbol{F}}}(t)\neq\boldsymbol{0}$ in the case of effective contact. As a matter of fact, in this case nonlinearities arising from the unilateral impenetrability rate condition disappear, and the primary eigenstate corresponds to a primary bifurcation, namely $t_{cE}=t_c$ with t_c denoting the primary bifurcation load factor. According to the interface formulation the last crack contact surface integral vanishes and the modified stability functional $S_I\left(\bar{\boldsymbol{F}},\dot{\boldsymbol{w}}\right)$ becomes:

$$S_I\left(\bar{\boldsymbol{F}},\dot{\boldsymbol{w}}\right)=\int_{B_{(i)}}\boldsymbol{C}^R\left(\boldsymbol{X},\bar{\boldsymbol{F}}\right)[\nabla\dot{\boldsymbol{w}}]\bullet\nabla\dot{\boldsymbol{w}}dV_{(i)}-\int_{\Gamma_{c(i)}^{l}}\sigma_R^l\dot{\boldsymbol{n}}^l\bullet[\![\dot{\boldsymbol{w}}]\!]_{\Gamma_{c(i)}}dS_{(i)}^l\ , \tag{3.35}$$

whereas the corresponding functional associated to the non-bifurcation condition assumes the following expression:

$$\begin{aligned}R_I\left(\dot{\bar{\boldsymbol{F}}},\dot{\boldsymbol{w}}_1,\dot{\boldsymbol{w}}_2\right)=&\int_{B_{(i)}}\boldsymbol{C}^R\left(\boldsymbol{X},\bar{\boldsymbol{F}}\right)[\nabla\dot{\boldsymbol{w}}^{(1)}-\nabla\dot{\boldsymbol{w}}^{(2)}]\bullet\left(\nabla\dot{\boldsymbol{w}}^{(1)}-\nabla\dot{\boldsymbol{w}}^{(2)}\right)dV_{(i)}+\\&-\int_{\Gamma_{c(i)}^{l}}\sigma_R^l\Delta\dot{\boldsymbol{n}}^l\bullet[\![\Delta\dot{\boldsymbol{w}}]\!]_{\Gamma_{c(i)}}dS_{(i)}^l\end{aligned}\ . \tag{3.36}$$

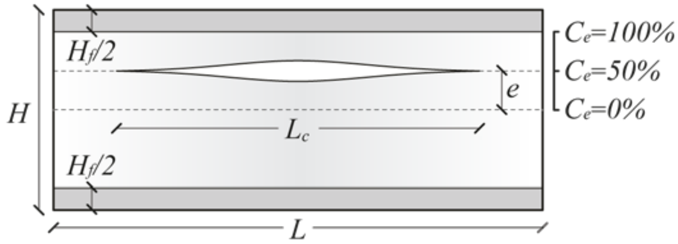

Fig. 3.6 Periodic microgeometrical arrangement of the analyzed unit cell containing a matrix crack ($C_e = 0\%$ and $C_e = 50\%$) or a matrix-fiber interface debonding ($C_e = 100\%$).

Note that when the contact reaction continuity equation (3.26) is assumed rigorously valid, also the crack contact interface integrals in (3.35) and (3.36) vanish. The influence of the above mentioned contact interface integral contributions occurring in the stability and non-bifurcation functionals will be analyzed in Section 3.4.2 and in Section 3.4.3 with reference to practical applications involving fiber-reinforced composite materials.

3.4 Numerical applications on unidirectional fiber reinforced composite materials

The previously developed theory is here applied to analyze the stability and bifurcation behavior of a 2D microcracked layered solid representing the unit cell of a periodic unidirectional fiber-reinforced composite material containing a matrix or fiber/matrix interface crack aligned with the fiber direction, shown in Fig. 3.6. Each microconstituent of the layered solid is assumed to obey the hyperelastic constitutive law. The initial thickness of the fiber layer is denoted with H_f, L denotes the unit cell initial length, L_c the initial crack length, e its eccentricity with respect to the unit cell half height and plane strain conditions are assumed in the X_1-X_2 plane where X_1 is the direction aligned with the fiber direction. The hyperelastic material used to model the microconstituents is the neo-Hookean one and the corresponding strain energy density for plane strain deformations is of the following form:

$$W = \frac{\mu}{2}\left[F_{\alpha\beta}F_{\alpha\beta} - 2 - 2\ln J'\right] + \frac{k-\mu}{2}\left(J'-1\right)^2 \qquad \alpha,\beta = 1,2 \qquad (3.37)$$

where J' is the determinant of the 2D deformation gradient tensor whose components are $F_{\alpha\beta}$, μ is the shear modulus of the solid at zero strain and the parameter k, playing the role of an equivalent 2D bulk modulus, governs its compressibility.

Numerical results devoted to a parametric analysis of the main microstructural geometrical parameters will be carried out with reference to the above described defected fiber-reinforced microstructure. The objective of these results is to analyze the influence of the main microstructural parameters on the uniaxial and biaxial compressive failure behavior of the examined fiber-reinforced composite material, by also pointing out the importance of a full finite deformation formulation of crack self-contact contact nonlinearities in order to obtain an accurate prediction of instability and bifurcation phenomena.

It is worth noting that a composite microgeometry associated to a periodic repetition of matrix microcracks or interface debonding is an ideal model useful from the engineering's point of view to capture the main features of the complex nonlinear behavior of real microstructured defected solids; such microgeometries are frequently used to develop micromechanical models within the homogenization theory, able to explain various failure mechanisms characterizing composite materials (to this end see, for instance, [10, 11, 12, 13, 28, 34, 35, 36]).

3.4.1 Variational problems

In order to obtain the critical load levels and related mode shapes a one-way coupled total Lagrangian finite element (FE) formulation is adopted. Firstly, the RVE principal solution path is computed and then the associated eigenvalue boundary value problems providing the bifurcation and the instability load levels are sequentially solved. Plane strain Lagrange quadratic elements are adopted for all the examined boundary value problems and an augmented Lagrangian method is used to model contact between crack faces. The principal equilibrium solution driven by the macroscopic loading process $\bar{\boldsymbol{F}}(t)$ is determined for discrete values of the loading parameter in the range $0 \le t \le t_{\max}$ by adopting a step size equal to $\Delta \mathrm{t} = 10^{-3}$. A parametric solver with a continuation strategy is adopted and the computations have been carried out by means of the commercial software COMSOL Multiphysics [158]. The contact surface integral contributions arising from crack self-contact studied in section 4, have been accounted in the numerical analysis by introducing additional boundary contributions to the weak formulation of the problem, while the nonlinear contact constraint rate conditions have been accounted in the analysis by means of an extrusion coupling variable approach and using a rate-dependent penalty approach.

In the case of macroscopic loading paths involving effective contact the weak inequalities associated to (3.17) and (3.31) reduces to variational equalities and the impenetrability rate condition becomes an equality constraint with the set of admissible fluctuation rates specializing to

$A_1^*(\bar{\boldsymbol{F}},\dot{\bar{\boldsymbol{F}}}=\boldsymbol{0})=\left\{\dot{\boldsymbol{w}}\in H^1\left(V_{(i)\#}\right)|\left[\!\left[\dot{u}_{\boldsymbol{n}}\right]\!\right]_{\Gamma_c}=0 \text{ on } \Gamma_c\right\}$; in this case a primary eigenstate corresponds to a primary bifurcation, namely t_{cE} = t_c. The critical loads for primary bifurcation and instability $t_c = t_c^S$ are determined as the load parameters for which the lowest eigenvalue Λ of the relevant eigenvalue weak problem first vanishes. In order to evaluate the influence of nonlinear contributions arising from crack self-contact in the examined case of effective contact, the following eigenvalue variational problems associated to both the full finite deformation and simplified approaches have been discretized $\forall\delta\dot{\boldsymbol{w}}\in A_1^*(\bar{\boldsymbol{F}},\dot{\bar{\boldsymbol{F}}}=\boldsymbol{0})$:

$$\int_{B_{(i)}}\boldsymbol{C}^R\left(\boldsymbol{X},\bar{\boldsymbol{F}}\right)[\nabla\dot{\boldsymbol{w}}]\bullet\nabla\delta\dot{\boldsymbol{w}}dV_{(i)}-\Lambda\int_{B_{(i)}}\nabla\dot{\boldsymbol{w}}\bullet\nabla\delta\dot{\boldsymbol{w}}dV_{(i)}$$
$$-\int_{\Gamma^l_{c(i)}}\sigma_R{}^l\left[\!\!\left[\left(\frac{dS_{(i)}}{dS}\right)^{\bullet}\frac{dS}{dS_{(i)}}\right]\!\!\right]_{\Gamma_c}\delta\dot{w}_n{}^l dS^l_{(i)}-\int_{\Gamma^l_{c(i)}}\sigma^l_R\dot{\boldsymbol{n}}^l\bullet\left[\!\left[\delta\dot{\boldsymbol{w}}\right]\!\right]_{\Gamma_c}dS^l_{(i)}=0\quad,\qquad(3.38)$$

giving the primary bifurcation and instability critical load levels for a full finite deformation formulation of crack self-contact (i.e. using functionals (3.31) and (3.33)) which turn out to be coincident since the contact surface terms are self-adjoint for the examined loading path (see [32], for instance);

$$\int_{B_{(i)}}\boldsymbol{C}^R\left(\boldsymbol{X},\bar{\boldsymbol{F}}\right)[\nabla\dot{\boldsymbol{w}}]\bullet\nabla\delta\dot{\boldsymbol{w}}dV_{(i)}-\Lambda\int_{B_{(i)}}\nabla\dot{\boldsymbol{w}}\bullet\nabla\delta\dot{\boldsymbol{w}}dV_{(i)}+$$
$$-\int_{\Gamma_{c(i)}{}^l}\sigma^l_R\dot{\boldsymbol{n}}^l\bullet\left[\!\left[\delta\dot{\boldsymbol{w}}\right]\!\right]_{\Gamma_c}dS^l_{(i)}=0\quad,\qquad(3.39)$$

giving the approximation of Eq. (3.39) in the case of an interface formulation kind (i.e. using functionals (3.35) and (3.36) where only tangential contribution and no crack surface deformation contribution);

$$\int_{B_{(i)}} \boldsymbol{C}^R\left(\boldsymbol{X},\bar{\boldsymbol{F}}\right)[\nabla \dot{\boldsymbol{w}}] \bullet \nabla \delta \dot{\boldsymbol{w}} dV_{(i)} - \Lambda \int_{B_{(i)}} \nabla \dot{\boldsymbol{w}} \bullet \nabla \delta \dot{\boldsymbol{w}} dV_{(i)} = 0 \tag{3.40}$$

giving the additional approximation corresponding to the case in which no crack contact interface contributions are considered according to the contact reaction continuity equation across the undeformed contact interface.

It should be noted that Eq. (3.39) characterizes a primary eigenstate, which in general does not corresponds to a primary instability, since for the interface formulation contact data are not self-adjoint in contrast to the case of the full finite deformation approach. As a matter of fact a primary instability state, preceding a primary bifurcation one, is characterized by the following variational eigenvalue problem arising from (3.35) $\forall \delta \dot{\boldsymbol{w}} \in A_1^*(\bar{\boldsymbol{F}}, \dot{\bar{\boldsymbol{F}}} = \boldsymbol{0})$:

$$\begin{aligned} &\int_{B_{(i)}} \boldsymbol{C}^R\left(\boldsymbol{X},\bar{\boldsymbol{F}}\right)[\nabla \dot{\boldsymbol{w}}] \bullet \nabla \delta \dot{\boldsymbol{w}} dV_{(i)} - \frac{1}{2} \int_{\Gamma^l_{c(i)}} \sigma^l_R \dot{\boldsymbol{n}}^l \bullet [\![\delta \dot{\boldsymbol{w}}]\!]_{\Gamma_c} dS^l_{(i)} + \\ &-\frac{1}{2} \int_{\Gamma^l_{c(i)}} \sigma^l_R \delta \dot{\boldsymbol{n}}^l \bullet [\![\dot{\boldsymbol{w}}]\!]_{\Gamma_c} dS^l_{(i)} - \Lambda \int_{B_{(i)}} \nabla \dot{\boldsymbol{w}} \bullet \nabla \delta \dot{\boldsymbol{w}} dV_{(i)} = 0 \end{aligned} . \tag{3.41}$$

3.4.2 Uniaxial loadings

A parametric analysis has been performed to evaluate the sensitivity of the primary instability and bifurcation critical load factor and of its associated critical modes with respect to the variation of the crack length, fiber thickness and crack eccentricity.

The fiber thicknesses considered in the analysis are $H_f = 0.05H$, $H_f = 0.1H$ and $H_f = 0.2H$; the investigated relative crack length L_C/L ranges from 0 to 0.9 with an increment of 0.1 and the analyzed relative crack

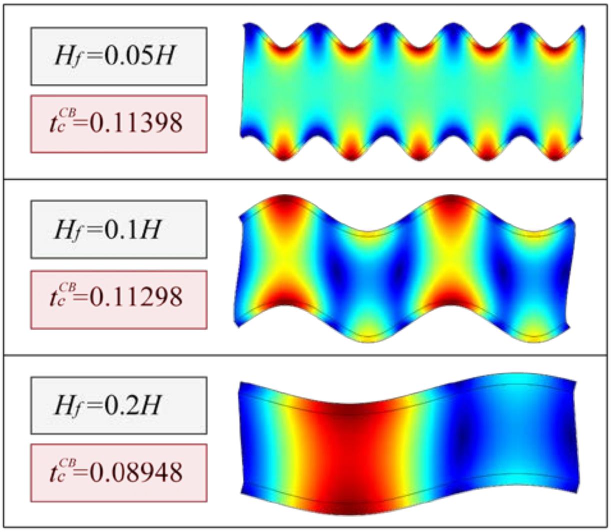

Fig. 3.7 Critical load levels and related mode shapes for the completely bonded comparison rate problem.

eccentricity percentage $C_e = e/(H/2\text{-}H_f/2)\text{x}100$ ranges from 0% to 100% with and increment of 25%. The case where C_e is equal to 100% corresponds to the case of a fiber/matrix interface crack, whereas for the remaining values a matrix crack is obtained. The unit cell L/H ratio is assumed equal to 3.

The typical mesh adopted for the examined unit cell involves 57,084 degrees of freedom and 3400 quadratic Lagrangian quadrilateral elements and is of a structured type. Uniaxial compression test was performed using the following macroscopic loading path along the X_1 direction: $\overline{F}(t) = (1-t)\mathbf{e}_1 \otimes \mathbf{e}_1 + \mathbf{e}_2 \otimes \mathbf{e}_2 + \mathbf{e}_3 \otimes \mathbf{e}_3$.

Note that, since macroscopic rigid body rotations are absent, the scalar parameter t characterizing the macroscopic loading path corresponds to the principal Biot strain in the fiber direction with the minus sign.

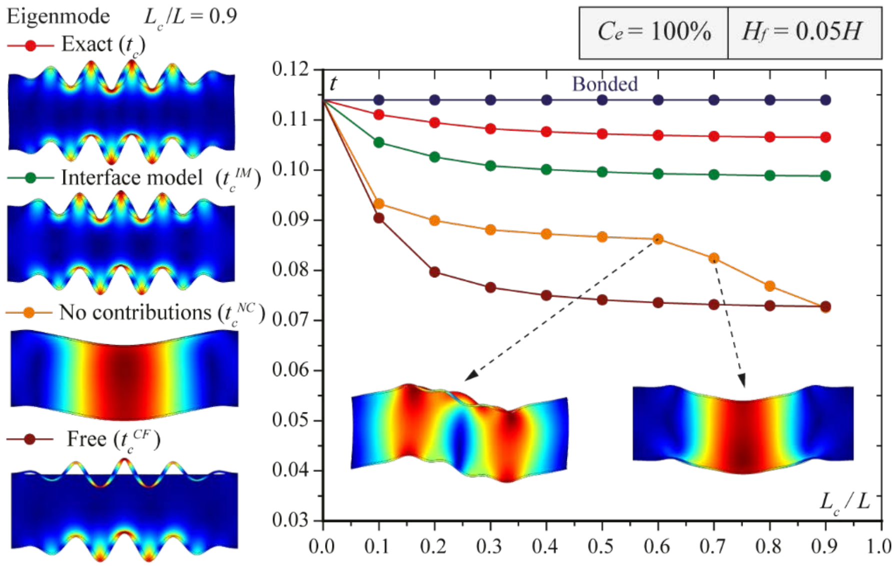

Fig. 3.8 Critical load parameters and mode shape behavior as a function of L_C/L for C_e = 100% and H_f = 0.05H.

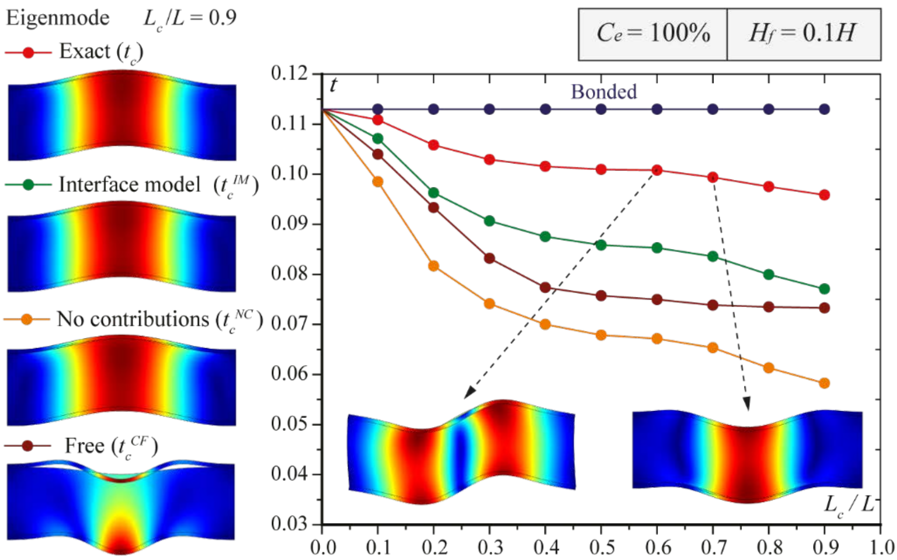

Fig. 3.9 Critical load parameters and mode shape behavior as a function of L_C/L for C_e = 100% and H_f = 0.1H.

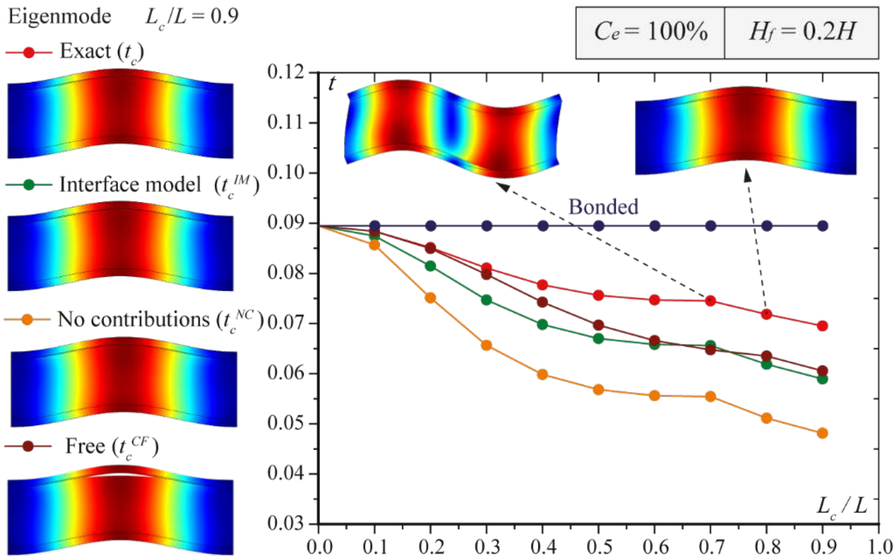

Fig. 3.10 Critical load parameters and mode shape behavior as a function of L_C/L for C_e = 100% and $H_f = 0.2H$.

In the numerical calculations the following hypotheses for the material properties of the microconstituents have been done: κ/μ=10, μ_f/μ_m= 20, μ_m =807 N/mm^2. The behavior of the unit cell along the examined uniaxial macro-deformation path is analyzed in the sequel by determining the critical load levels corresponding to the full finite deformation formulation (referred to as “Exact”), to the interface type of formulation where only tangential contributions are included in the analysis (referred to as “Interface model” with the corresponding critical load levels denoted as t_c^{IM}) and to the case in which no crack contact interface contributions are considered (referred to as “No contributions” with the corresponding critical load levels denoted as t_c^{NC}).

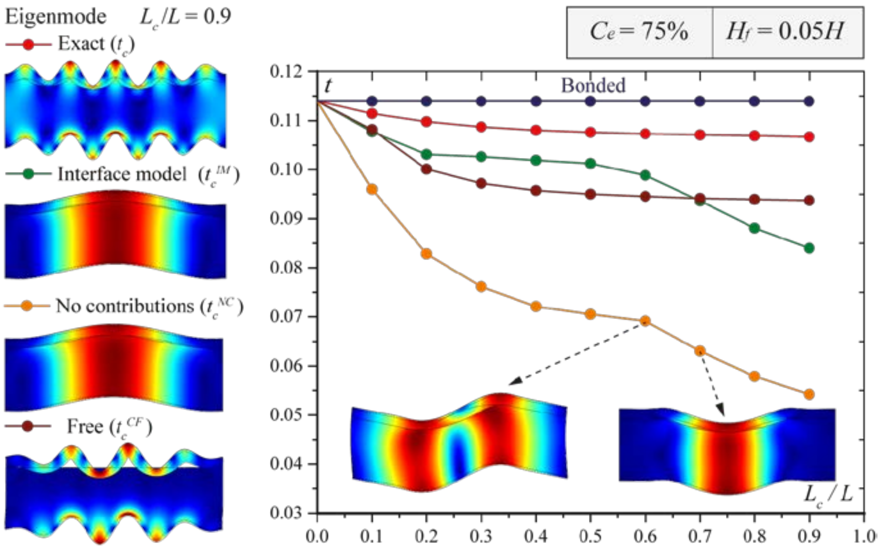

Fig. 3.12 Critical load parameters and mode shape behavior as a function of L_C/L for C_e = 75% and H_f = 0.5H.

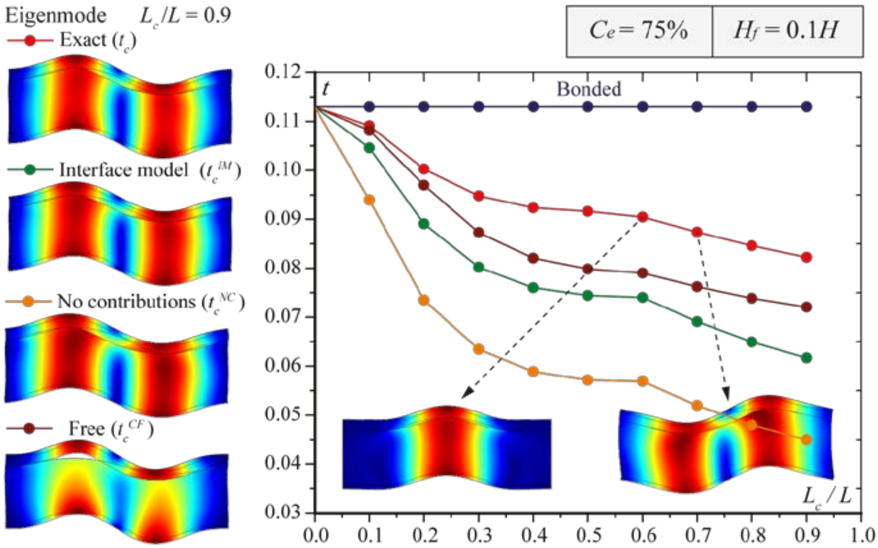

Fig. 3.11 Critical load parameters and mode shape behavior as a function of L_C/L for C_e = 75% and H_f = 0.1H.

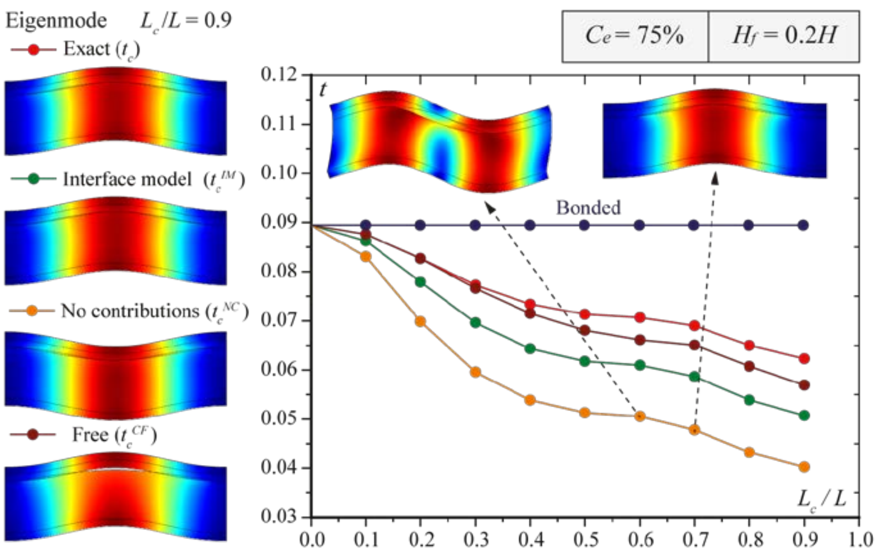

Fig. 3.13 Critical load parameters and mode shape behavior as a function of L_C/L for C_e = 75% and H_f = 0.2H.

Specifically, in the case of the full finite deformation formulation and no crack contact interface contributions the determined critical load levels t_c and t_c^{NC} refer to both primary instability and bifurcation states (which are coincident), while in the case of the interface model the computed critical load levels t_c^{IM} are referred to primary bifurcation states. The equivalence between the primary instability and bifurcation critical load levels, occurring in the former case, have been verified by means of FE calculations, within errors related to the finite element discretization. In the latter case, numerical computations not shown here for the sake of brevity, have pointed out that the largest relative differences

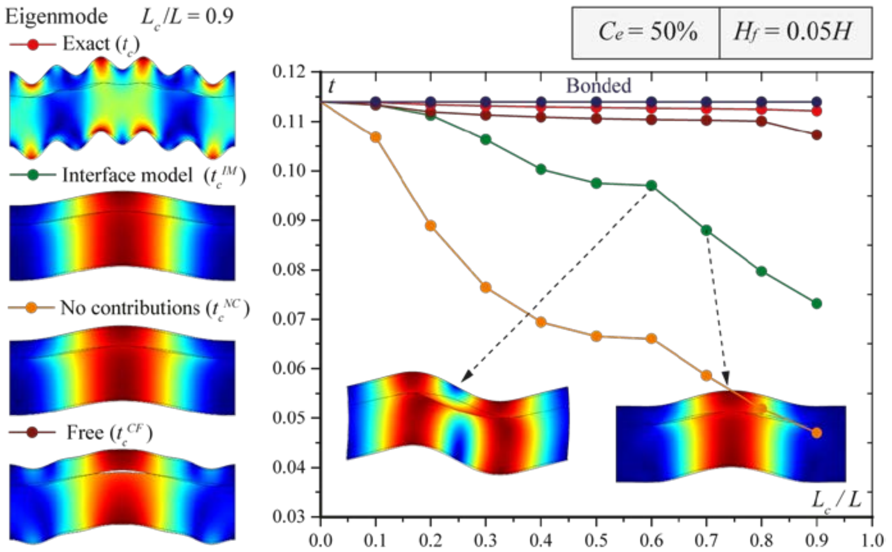

Fig. 3.14 Critical load parameters and mode shape behavior as a function of L_C/L for C_e = 50% and H_f = 0.05H.

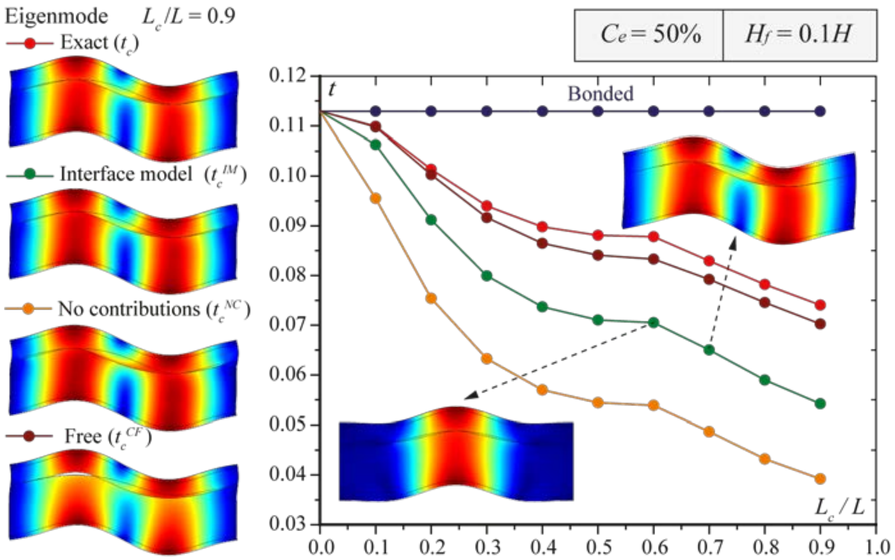

Fig. 3.15 Critical load parameters and mode shape behavior as a function of L_C/L for C_e = 50% and H_f = 0.1H.

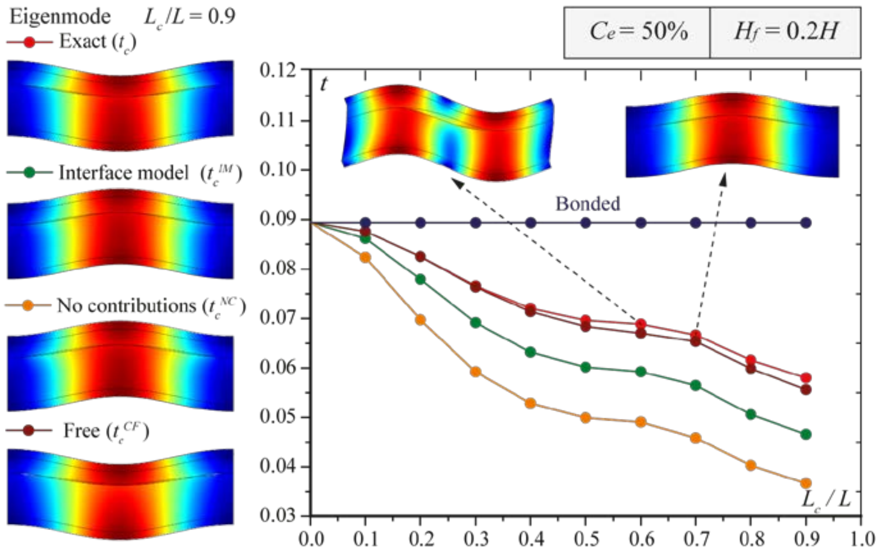

Fig. 3.16 Critical load parameters and mode shape behavior as a function of L_C/L for C_e = 50% and H_f = 0.2*H*.

between primary bifurcation and instability load levels are within 5.96% (occurring for *Lc/L*=0.9, $H_f = 0.05H$ and C_e=0%).

Moreover, in order to obtain upper and lower bounds to the above critical load levels, useful to check the accuracy of the results and to model limit behaviors (i.e. *Lc/L* approaching to zero), the critical load levels of the completely bonded (t_c^{CB}) and free (t_c^{CF}) comparison rate problems have been also computed. The above classes of critical load levels are investigated in order to determine the influence of crack interface self-contact phenomena on the compressive failure of the examined microstructured solid due to instability and bifurcation. The critical values of the load level for the completely bonded rate problem are shown in Fig. 3.7 together with the color surface plots of the critical mode shapes. As the relative fiber thickness ratio increases the critical load level decreases whereas the wavelength of the critical mode shape increases

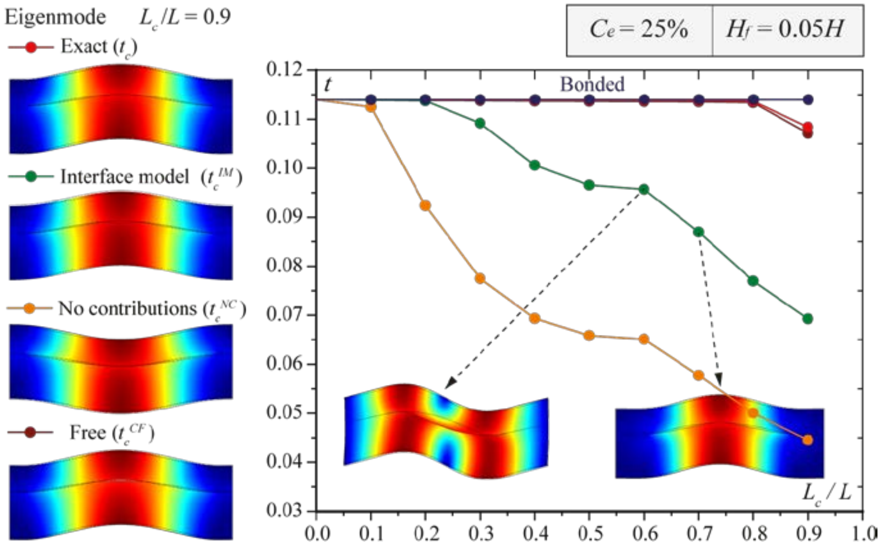

Fig. 3.17 Critical load parameters and mode shape behavior as a function of L_C/L for C_e = 25% and H_f = 0.05H.

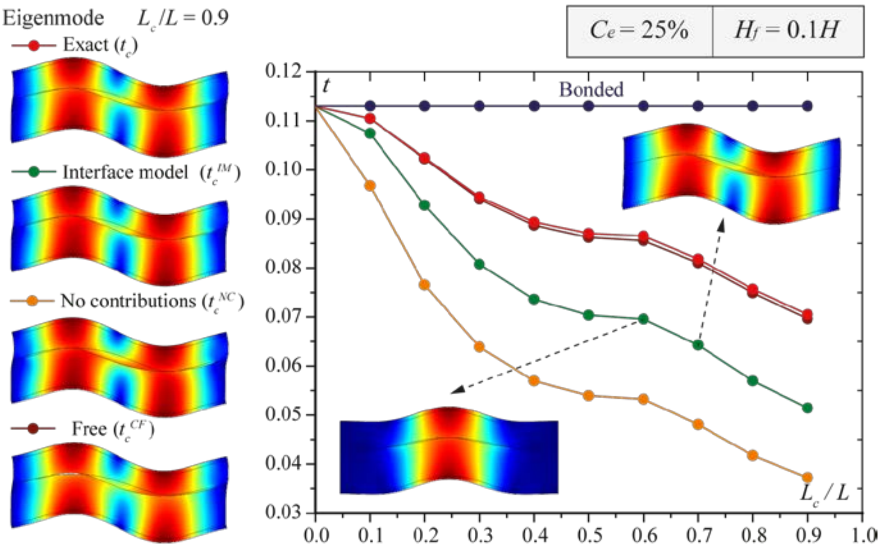

Fig. 3.18 Critical load parameters and mode shape behavior as a function of L_C/L for C_e = 25% and H_f = 0.1H.

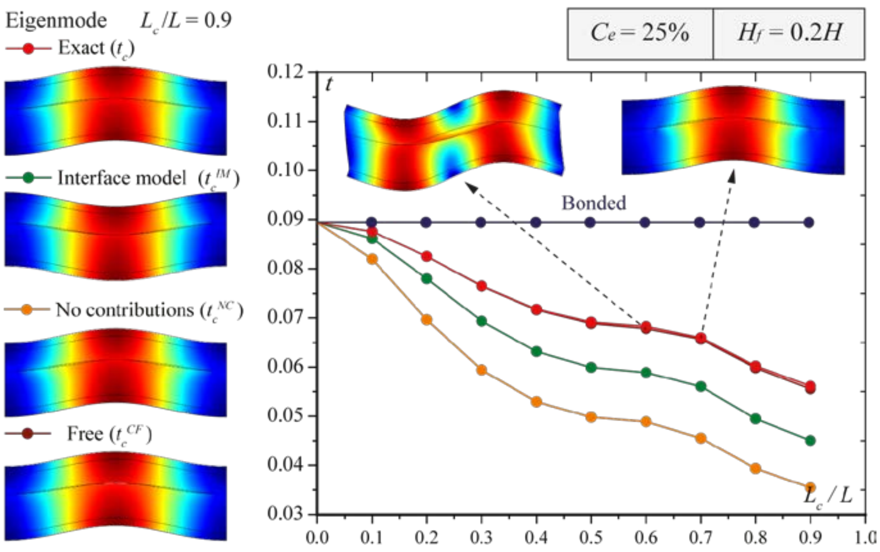

Fig. 3.19 Critical load parameters and mode shape behavior as a function of L_C/L for C_e = 25% and H_f = 0.2H.

with a strong influence on the critical load level magnitude found when H_f/H is greater than *0.1*. In Figs 3.8-3.22, the critical load levels for the different examined crack contact interface formulations have been plotted as a function of the relative crack length L_C/L for the analyzed crack eccentricity and fiber thickness ratios together with the critical mode shapes referred to L_C/L = 0.9.

Generally speaking, it is possible to note that the differences between the critical load levels corresponding to the exact and the simplified formulations (interface model and no crack contributions) increase with the increment of the relative crack length L_C/L: this implies that the role of crack contact interface contributions becomes more important as L_C/L increases. The above differences vanish as L_C/L approaches zero, namely for an undefected composite microstructure for which all the

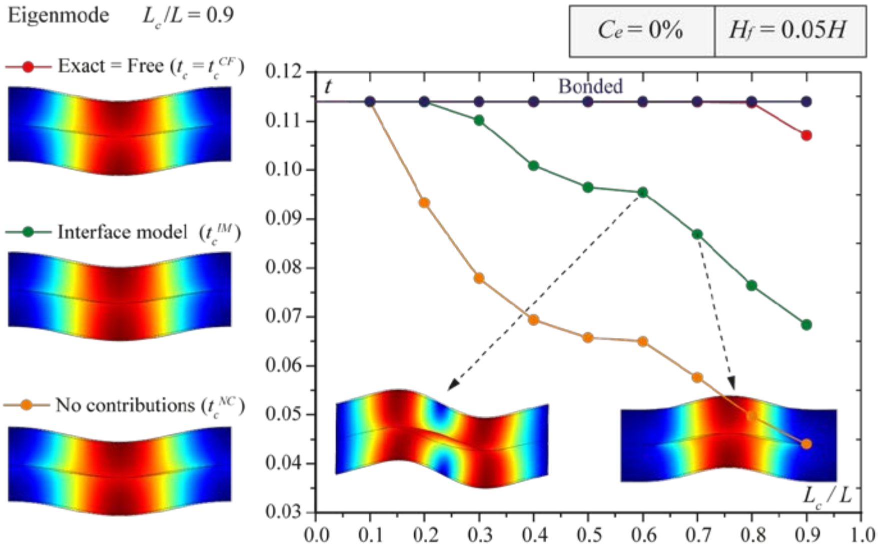

Fig. 3.20 Critical load parameters and mode shape behavior as a function of L_C/L for C_e = 0% and H_f = 0.05H.

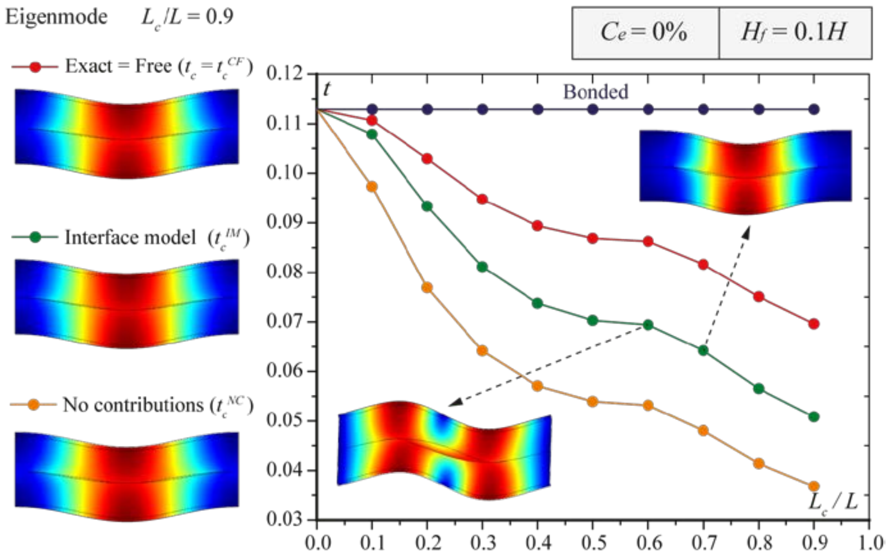

Fig. 3.21 Critical load parameters and mode shape behavior as a function of L_C/L for C_e = 0% and H_f = 0.1H.

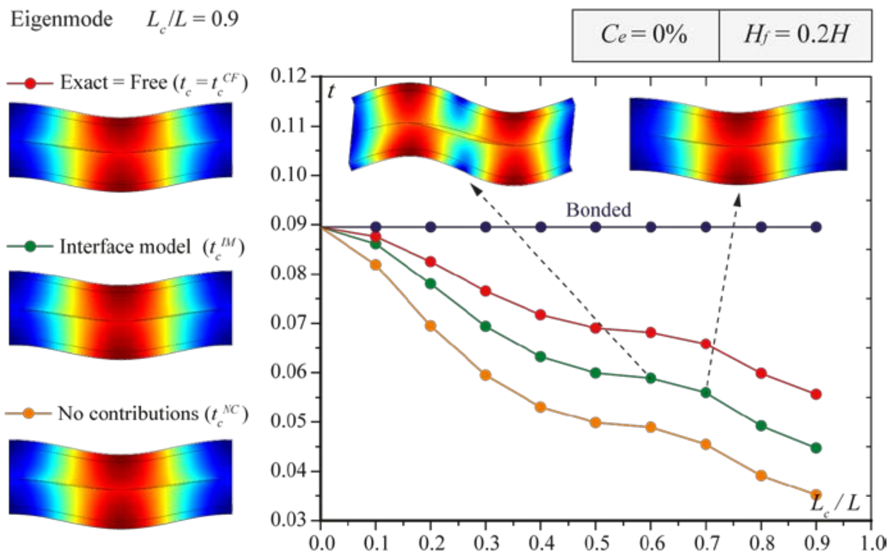

Fig. 3.22 Critical load parameters and mode shape behavior as a function of L_C/L for C_e = 0% and H_f = 0.2H.

critical load levels become coincident with those associated with the completely bonded comparison problem.

The largest percentage relative difference between the exact and simplified formulations $(t_c\text{-}t_c^{NC/IM})/t_c \times 100$ is equal to 35.80% for the interface model (attained when L_c/L=0.9, H_f =0.05H and C_e=50%) and to 58.90% for the formulation without crack contact contributions (attained when L_c/L=0.9, H_f =0.05H and C_e=0%). This highlights the strong role of crack contact interface contributions and the importance of adopting a full finite deformation formulation rather than simplified ones. The results globally evidence that the higher critical load levels are obtained for H_f =0.05H and that both the two simplified formulations give conservative predictions of primary instability and bifurcation load levels (i.e. $t_c^{NC} < t_c^{IM} < t_c$). Furthermore, it should be noted that the model without crack contact interface contributions yields the lowest critical load levels with the exception of the case $H_f = 0.05H$ and C_e=100% (Fig. 3.8), in which the completely free to penetrate estimate becomes the most conservative one. As expected in all the examined cases $t_c^{CF} \leq t_c \leq t_c^{CB}$; moreover except for C_e equal to 100% and 75%, where the critical load factor t_c^{CF} show a more variegated behavior and may be the most conservative one (for C_e=100% and $H_f = 0.05H$), the hierarchy of critical load levels satisfies the following inequalities: $t_c^{NC} < t_c^{IM} < t_c^{CF} \leq t_c \leq t_c^{CB}$. Owing to the symmetry of the loading and of the microstructure, entailing the ineffectiveness of the displacement rate jump contact constraint, for the case with C_e=0% (see Figs.3.20-3.22) the exact and the free-to-penetrate curves are coincident, while, for the cases with C_e=25% and C_e=50% (see Figs.3.14-3.19), are very close. The microstructural arrangement with $H_f = 0.05H$ shows a moderate influence of the critical load level t_c with respect to the relative crack length with less deviation from the bonded case whose critical load levels are independent on the relative crack length. Overall for $C_e \leq 50\%$, the change in crack eccentricity does not result in any important change of the critical load factors, while C_e >50% the results are more influenced by this parameter. In addition, it can be noted for $L_c/L > 0.6$ the critical load factors show a sharp decline. Such behavior, more evident for high values of the relative fiber thickness (H_f =0.1H and H_f =0.2H), is related to the increase of the critical mode shape wavelength which show a trend from local to global.

3.4.3 Biaxial loadings

The theory developed in section 3.3 is here applied to analyze the stability and bifurcation behavior of a 2D microcracked layered solid representing the unit cell of a periodic unidirectional fiber-reinforced composite material containing a matrix or fiber/matrix interface crack aligned with the fiber direction. Firstly, the biaxial path for which the nominal contact pressure vanishes, called decompression limit path, is obtained by means of an analytical solution, then general parametric analyses are carried out by varying fiber thickness and microcrack position with respect to fiber/matrix interface, and different radial macroscopic biaxial loading paths are investigated to identify two-dimensional stability and uniqueness domains in the principal macrostrain space.

3.4.3.1 Analytical results

The previously developed theory is here applied to analyze the stability and bifurcation behavior of a 2D microcracked layered solid representing the unit cell of a periodic unidirectional fiber-reinforced composite material containing a matrix or fiber/matrix interface crack aligned with the fiber direction. The layered solids is subjected to a general biaxial macrodeformation loading path along the axes of orthotropy, namely shearing in the direction parallel $\overline{F}_{12}$ or normal $\overline{F}_{21}$ to the lamination direction is zero, and each constituent is assumed to obey the hyperelastic constitutive law (3.37).
For the examined biaxial macroscopic loading paths, the principal solution, due to the homogeneous properties of each layer, is characterized by constant stresses and strains within each layer; moreover, the fiber and matrix layers, together with crack surfaces, remain flat up to the onset of the first instability or bifurcation state. This implies that the

finite elasticity principal path solution is not affected by the presence of the crack. Along the principal path the macroscopic and local deformation gradient tensors can be related by using geometric considerations according to the following expressions:

$$\begin{cases} F_{11}^{f} = F_{11}^{m} = \bar{F}_{11} \\ \xi F_{22}^{f} + \left(1-\xi\right) F_{22}^{m} = \bar{F}_{22} \end{cases}, \tag{3.42}$$

where $\xi = H_f / H$ and the remaining local deformation gradient tensor components are identically zero. Obtaining F_{22}^{m} as a function of F_{22}^{f} through Eq. (3.42)$_2$, the relation between F_{22}^{f} and the nonzero components of $\bar{\boldsymbol{F}}$ can be obtained by using the traction continuity condition across the fiber/matrix interface $[\![T_{R22}]\!]_{\Gamma_{C(i)}} = 0$, which after considering that the first Piola-Kirchhoff stress tensor components can be calculated as $T_{Rij} = \partial W / \partial F_{ij}$, gives:

$$\frac{\partial W^{m}}{\partial F_{22}^{m}} = \frac{\partial W^{f}}{\partial F_{22}^{f}}, \tag{3.43}$$

where

$$\frac{\partial W^{i}}{\partial F_{22}^{i}} = \mu^{i} F_{22}^{i} + \left[\left(\kappa^{i} - \mu^{i}\right)\left(J^{i} - 1\right) J^{i} - \mu^{i}\right] F_{22}^{i\,-1}, \quad \text{i=m,f} \tag{3.44}$$

Assuming that $k / \mu = \alpha$ and that $\mu^{f} = \beta \mu^{m}$, the principal solution path remains completely defined by the following six material and loading data: ξ, μ^{m}, α, β, $\bar{F}_{22}$, $\bar{F}_{11}$. For given values of α and β, $\alpha = 10$ and $\beta = 20$, it is possible to obtain a simple expression for F_{22}^{f} as a function of $\bar{\boldsymbol{F}}$ when $T_{R22}^{f} = T_{R22}^{m} = 0$, namely when the nominal contact pressure vanishes and the condition of effective contact is lost, the corresponding macroscopic deformation path being denoted as decompression path. The above expression is:

$$F_{22}^{f} = F_{22}^{m} = \bar{F}_{22} = \frac{9\bar{F}_{11} + \sqrt{4 + 117\bar{F}_{11}^{2}}}{2\left(1 + 9\bar{F}_{11}^{2}\right)}, \tag{3.45}$$

implying that when the macroscopic deformation is compressive along the lamination direction ($\bar{F}_{11} < 1$) the corresponding macroscopic deformation in the normal direction must be tensile ($\bar{F}_{22} > 1$). Eqs. (3.44) and (3.45) gives analytical expressions for the contact pressure and for the decompression limit path, respectively, as a function of the underlying principal path solution.

It is worth noting that for the examined biaxial macrodeformation loading path, the stability and bifurcation analyses can be carried out by computing the jump across the crack contact interface with reference to either the undeformed or the deformed interface configurations, since initially coincident points pair coincide to actual contact point pairs, i.e. $[\![f(\boldsymbol{X})]\!]_{\Gamma_C} = [\![f(\boldsymbol{X})]\!]_{\Gamma_{C(i)}}$. Moreover it is possible to prove that due to homogeneity of the deformation within each micro-constituents, the tangential and the crack surface deformation contributions of Eq. (3.25) leading to the contact surface integral contributions of the stability and non-bifurcation functionals, are the same. Adopting an updated Lagrangian formulation with the current configuration taken as a reference (see [159] or additional details), the contact surface integral contributions introduced in Eq. (3.25) can be written as:

$$\int_{\Gamma_C} \sigma \dot{\boldsymbol{n}}^{l} \bullet [\![\delta \boldsymbol{u}]\!]_{\Gamma_C} \, dS - \int_{\Gamma_C} \sigma \left[\!\!\left[\left(\frac{dS_{(i)}}{dS} \right)^{\bullet}_{\boldsymbol{F}=\boldsymbol{I}} \right]\!\!\right]_{\Gamma_C} \delta u_n{}^{l} dS \,, \tag{3.46}$$

where the subscript $\boldsymbol{F}=\boldsymbol{I}$ denotes evaluation in the current configuration. Using Eqs. $(3.21)_1$ in an updated Lagrangian version and $(3.21)_2$ we have that

$$\begin{aligned}
&\dot{\boldsymbol{n}} = -\dot{u}_{2,1}\boldsymbol{e}_1 \\
&\left(\frac{dS_{(i)}^{l/u}}{dS}\right)^{\bullet}_{\boldsymbol{F}=\boldsymbol{I}} = \boldsymbol{L}^{l/u\,\mathrm{T}}\boldsymbol{n}^{l/u}\bullet\boldsymbol{n}^{l/u} - tr\boldsymbol{L}^{l/u} = -\dot{u}_{1,1}
\end{aligned} \tag{3.47}$$

where $\boldsymbol{e}_i$ is the base vector pointing in the direction of the i-th coordinate system axis. Therefore, the tangential and the crack surface deformation contributions can be rewritten as:

$$\begin{aligned}
&\int_{\Gamma_C} \sigma\dot{\boldsymbol{n}}^l \bullet [\![\delta\boldsymbol{u}]\!]_{\Gamma_C}\, dS = -\int_{\Gamma_C} \sigma\dot{u}_{2,1}[\![\delta u_1]\!]_{\Gamma_C}\, dS \\
&-\int_{\Gamma_C} \sigma \left[\!\!\left[\left(\frac{dS_{(i)}}{dS}\right)^{\bullet}_{\boldsymbol{F}=\boldsymbol{I}}\right]\!\!\right]_{\Gamma_C} \delta u_n{}^l dS = \int_{\Gamma_C} \sigma[\![\dot{u}_{1,1}]\!]_{\Gamma_C}\,\delta u_2 dS
\end{aligned} \tag{3.48}$$

Integration by parts of $(3.48)_1$ and taking into account that $\dot{u}_2[\![\delta u_1]\!]$ vanish at both ends of Γ_C and that σ is constant, show that

$$-\int_{\Gamma_C} \sigma\dot{u}_{2,1}[\![\delta u_1]\!]_{\Gamma_C}\, dS = \int_{\Gamma_C} \sigma\dot{u}_2[\![\delta u_{1,1}]\!]_{\Gamma_C}\, dS \tag{3.49}$$

consequently when $\delta\boldsymbol{u} = \dot{\boldsymbol{u}}$ we obtain that in Eq. (3.31) the tangential contribution becomes equal to the crack surface deformation one. Analogously Eq. (3.49) and integration by parts of $(3.48)_2$ when $\delta\boldsymbol{u} = \delta\dot{\boldsymbol{u}}$ show that the contact data become self-adjoint, namely the following expression holds:

$$\begin{aligned}
&\int_{\Gamma_C} \sigma\dot{\boldsymbol{n}}^l \bullet [\![\delta\dot{\boldsymbol{u}}]\!]_{\Gamma_C}\, dS - \int_{\Gamma_C} \sigma \left[\!\!\left[\left(\frac{dS_{(i)}}{dS}\right)^{\bullet}_{\boldsymbol{F}=\boldsymbol{I}}\right]\!\!\right]_{\Gamma_C} \delta\dot{u}_n{}^l dS = \\
&\int_{\Gamma_C} \sigma\delta\dot{\boldsymbol{n}}^l \bullet [\![\dot{\boldsymbol{u}}]\!]_{\Gamma_C}\, dS - \int_{\Gamma_C} \sigma \left[\!\!\left[\delta\left(\frac{dS_{(i)}}{dS}\right)^{\bullet}_{\boldsymbol{F}=\boldsymbol{I}}\right]\!\!\right]_{\Gamma_C} \dot{u}_n{}^l dS
\end{aligned} \tag{3.50}$$

Consequently, as pointed out in section 3, for the examined composite microstructure and macroscopic loading path, a primary instability state coincides with a primary eigenstate. On the other hand, in the case of the interface formulation in which only the first term of Eq. (3.46) is included in the analysis, contact data are not self-adjoint and loss of stability does not leads to a primary eigenstate. Note that along the decompression limit principal path both the nominal contact pressure rate and the interface displacement rate jump are identically zero and bifurcation occurs at a primary eigenstate also in presence of a nonhomogeneous loading path.

3.4.3.2 Numerical results

The purpose of these results is to obtain an accurate prediction of instability and bifurcation phenomena investigating the effects of the abovementioned self-contact nonlinearities in the specific case of biaxial loading regime and for different microstructural arrangements. A total Lagrangian finite element formulation is adopted to obtain the principal solution path of the analyzed unit cell in coupling with the accompanying nonlinear eigenmode boundary value problems giving the bifurcation and the instability critical load factors. The commercial software [158] has been used to obtain the sequence of quasi-static equilibrium solutions in terms of discrete values of the loading parameter t and by adopting a step size equal to $\Delta t = 10^{-3}$.

The boundary value and eigenvalue problems are discretized by means of a displacement-type finite element (FE) approximation using plane strain Lagrange quadratic elements and an augmented Lagrangian method is adopted to model contact between crack surfaces along the principal solution path. Boundary weak contributions has been introduced in the FE model to account for the contact surface integral contributions discussed in Section 3.2, whereas a rate-dependent penalty

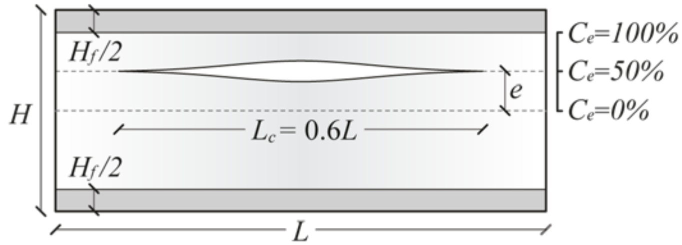

Fig. 3.23 Periodic microgeometrical arrangement of the analyzed unit cell containing a matrix crack ($C_e = 0\%$ and $C_e = 50\%$) or a matrix-fiber interface debonding ($C_e = 100\%$) with a length equal to 0.6*L*.

technique in conjunction with an extrusion coupling variable map has been adopted to impose unilateral contact constraint rate conditions.

The critical loads for bifurcation and instability have been determined as the parameters associated with the lowest zero eigenvalue of the corresponding eigenvalue weak problems (see [160] and the references cited therein, for additional details about the formulation of these eigenvalue problems). Since the examined biaxial loading paths are compressive along the fiber direction and involve effective contact, the nonlinear eigenvalue weak problems have been solved only for the decompression limit path for which the contact pressure vanishes and the impenetrability rate condition must be imposed as an inequality constraint. In this case, the nonlinear eigenvalue problem is solved by adopting an iterative solution strategy consisting in the repeated running of the linear eigenvalue solver by updating the eigenvalue linearization point to the last eigenvalue found. The iteration cycle is stopped when the pointwise estimated error on the normal displacement rate jump is less than a fixed relative tolerance ($\left| \llbracket \dot{w}_n \rrbracket \right| \leq 10^{-3} L_C$). On the other hand, for effective contact, for which the impenetrability rate condition becomes an equality constraint, linear eigenvalue weak problems have been solved. The results of the numerical applications are presented in Figs. 3.24-3.31 and Tabs. 3.1-3.6 depicting the onset-of-failure surfaces of defected periodic fiber-reinforced composites subjected to macroscopic biaxial loadings together with the associated critical load parameters and modes. The sensitivity with respect to the adopted formulation (full finite approach versus simplified ones), of the primary instability and bifurcation critical load factors and of its associated critical modes, is analyzed for different microgeometrical arrangements obtained by varying crack length, fiber thickness and crack eccentricity. The microconstituents are assumed to be characterized by the following material parameters: $k/\mu = 10$, $\mu_f / \mu_m = 20$, $\mu_m = 807 N/mm^2$. With reference to Fig. 3.23 the fiber thicknesses considered in the analysis are $H_f = 0.05H$ and $H_f = 0.1H$; the investigated relative crack length L_C / L is equal to 0.6 in the analyses shown in Figs. 3.24-3.31, whereas it ranges from 0 to 0.9 with an increment of 0.3 in Tabs. 3.1-3.6; the following values for the relative crack eccentricity percentage, defined as $C_e = e/\left(H/2 - H_f/2\right) \times 100$, have been considered: 0%, 50% and 100%.

The adopted unit cell ratio L/H is equal to 3 and the used mesh is of a structured type and involves 3630 quadratic Lagrangian quadrilateral elements. The critical curves identifying the limit of the two-dimensional stability and uniqueness domains are obtained by determining the critical load levels t_c, t_c^{IM} and t_c^{NC} respectively corresponding to: (i) full finite deformation formulation (referred to as “Exact” in the following and associated with conditions (19) and (21)), (ii) interface model formulation with no tangential contribution (“Interface model”, associated with conditions (23) and (24)), (iii) formulation with no crack contact interface contributions (“No contributions”, associated to conditions (25) and (26)). Note that for the interface model formulation, contrarily to the other ones, primary instability does not coincide with primary bifurcation; therefore the associated critical load level t_c^{IM} refers uniquely to primary bifurcation, although FE calculations have pointed out that the relative differences between the corresponding critical load levels are generally low. In addition, in order to model the limit behavior of the solid, upper and lower bounds to the above critical load levels, denoted as t_c^{CB} and t_c^{CF} have been also computed by means of completely bonded (“Bonded”) and completely free (“Free”) comparison rate problems. The composite microstructure has been subjected to radial macroscopic biaxial loading paths in the principal macrostrain space with a macrodeformation gradient tensor expressed as:

$$\overline{F}(t) = (1 - t \cdot \cos\varphi)\mathbf{e}_1 \otimes \mathbf{e}_1 + (1 - t \cdot \mathrm{sen}\varphi)\mathbf{e}_2 \otimes \mathbf{e}_2 + \mathbf{e}_3 \otimes \mathbf{e}_3 . \qquad (3.51)$$

where φ defines the ratio between the principal values $\overline{\lambda}_i$ -1 of the macroscopic Biot strain tensor, $\overline{\lambda}_i$ being the macroscopic principal stretch ratio in the X_i direction. Negative angles correspond to a biaxial regime with compression in X_1 direction and traction in X_2 one, whereas positive angles correspond to a biaxial compression regime in both directions ($\varphi = 0$ corresponding to a uniaxial compression along the fiber direction). The macroscopic onset-of-failure curves calculated here are found for radial paths characterized by $-40° \le \varphi \le +70°$; as a matter of fact for $\varphi > +70°$ very high values of critical load levels (more than 0.35) are obtained associated with large compression levels in the X_2 direction ($\overline{\lambda}_2 - 1 < -0.33$) for which different sources of failure would have already occurred (damage and/or crushing in the matrix, for instance). Moreover for $\varphi < -40°$ radial paths intersect the decompression curve and both the exact and simplified crack contact interface formulations become equivalent since the contributions arising from contact vanish. The decompression limit curve, which does not correspond to a radial path, has been analytically obtained by substituting the components of the macroscopic deformation gradient (3.51) into Eq. (3.45) . The microstructural stability and uniqueness domains for the examined biaxial loading conditions has been presented by using a polar type representation together with the color surface plots of the critical mode shapes. In the plots, the radius corresponds to the opposite of the principal value of the macroscopic Biot strain tensor along X_1 (i.e. $t \cos\varphi$), the angle φ is expressed in degrees and the decompression limit curve is displayed by using a thick dashed line. It is worth noting that, as expected, when the radial paths approaches to the decompression limit curve, the critical load levels of the simplified contact formulations converge to the exact one (i.e. $t_c^{IM} = t_c^{NC} = t_c$).

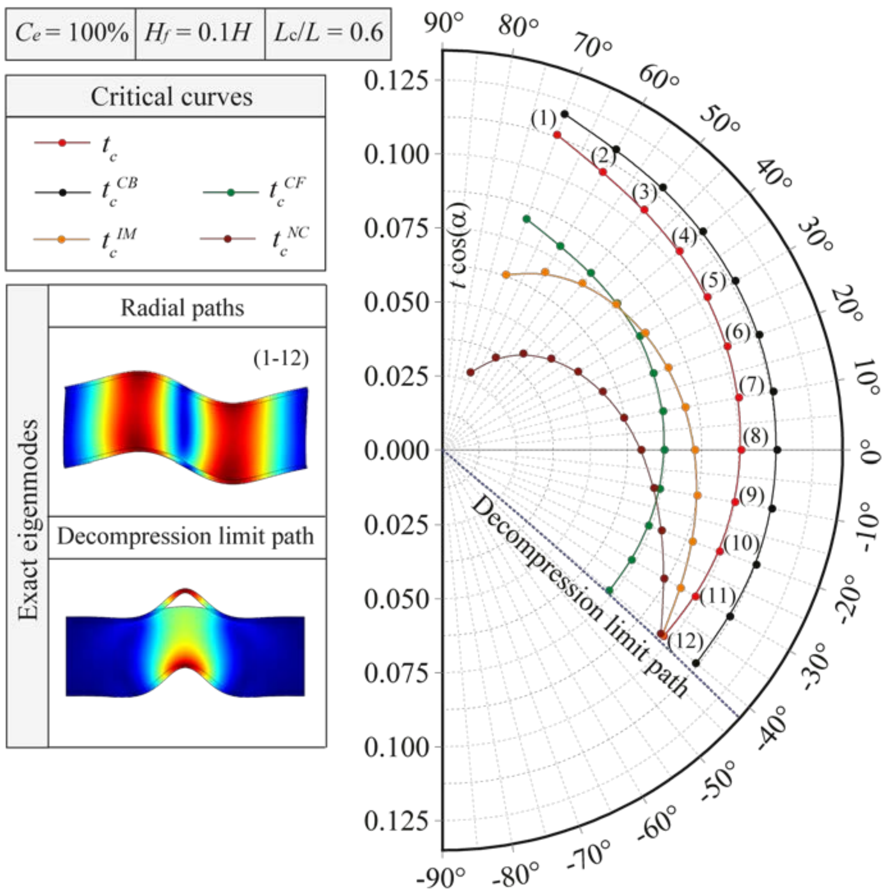

Fig. 3.24 Polar plot of the critical macroscopic strain along the X_1 direction $t\ cos\varphi$ versus the load path angle φ and mode shape behavior for $L_C / L = 0.6$, $H_f = 0.1H$ and $C_e = 100\%$.

Due to the absence of the contact constraint conditions, the completely free comparison problem does not show the same behavior. Note that the curves of the critical values associated with the completely free problem and the exact formulation coincide for $C_e = 0\%$ while the

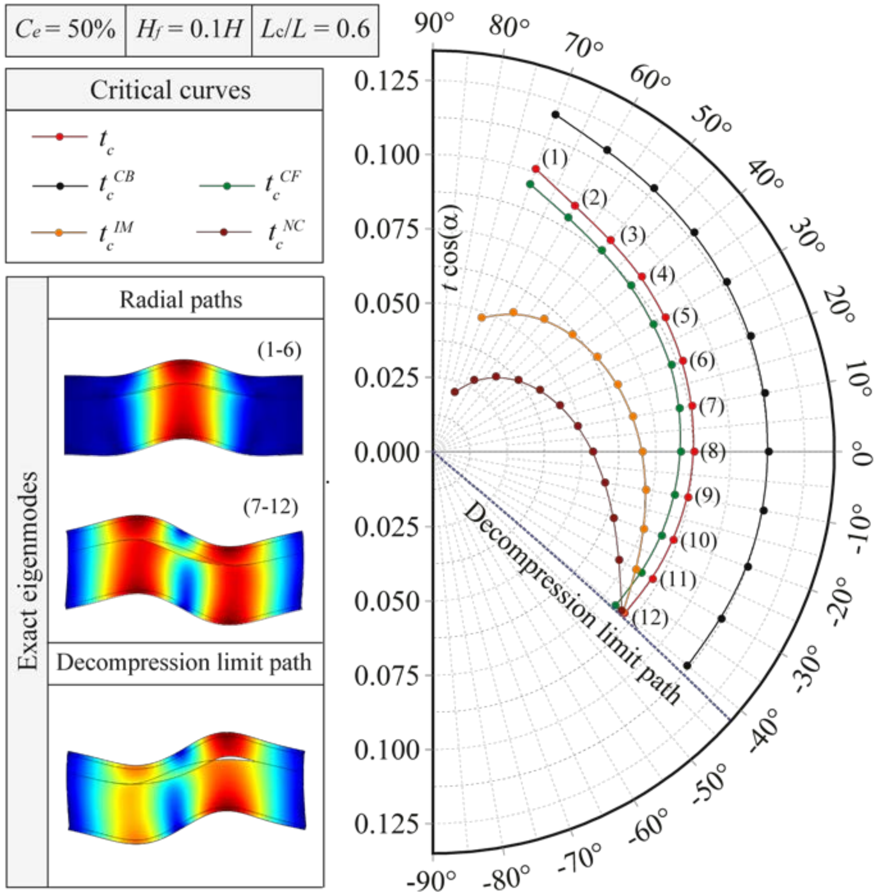

Fig. 3.25 Polar plot of the critical macroscopic strain along the X_1 direction $t \cos\varphi$ versus the load path angle φ and mode shape behavior for $L_C / L = 0.6$, $H_f = 0.1H$ and $C_e = 50\%$.

curves move away as the crack eccentricity increases. Generally speaking the critical curves related to the exact, completely free and bonded formulations are scarcely influenced by the macroscopic loading in the X_2 direction, especially for radial paths with tensile transverse strain ($\varphi < 0°$), with the values of the critical loading level increasing as φ

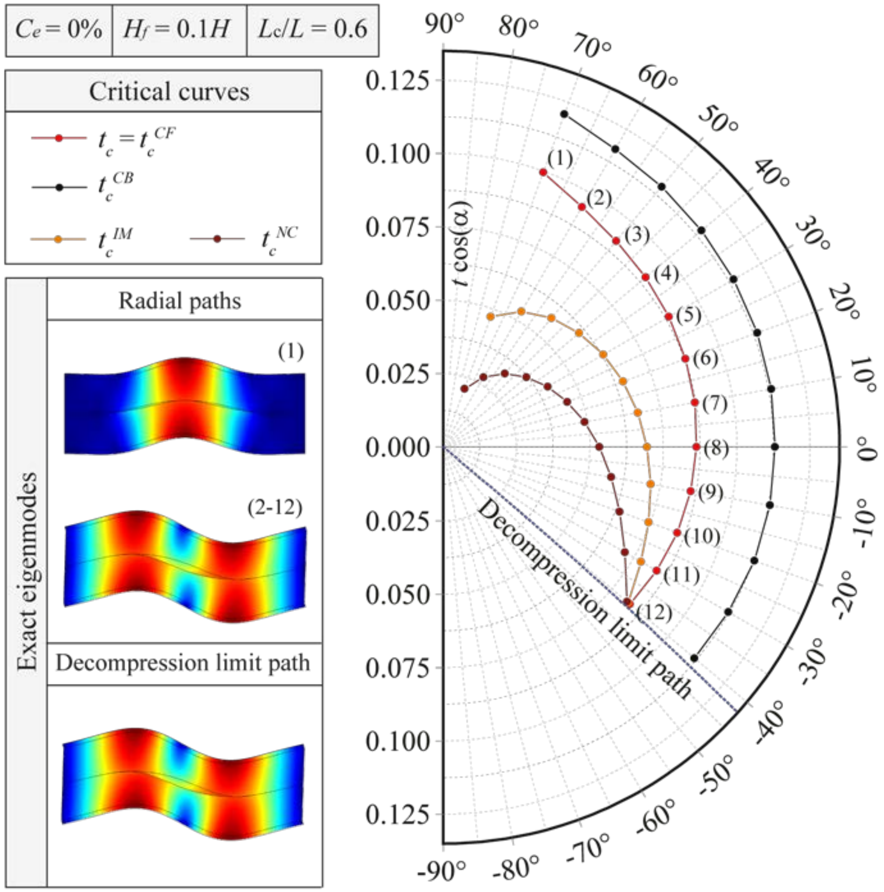

Fig. 3.26 Polar plot of the critical macroscopic strain along the X_1 direction $t \cos\varphi$ versus the load path angle φ and mode shape behavior for $L_C / L = 0.6$, $H_f = 0.1H$ and $C_e = 0\%$.

increases. On the contrary the macroscopic load component in the X_2 direction shows a remarkable influence on the critical load levels of the simplified formulations, with a stabilizing effect for $\varphi < 0°$ (transverse tensile regime), and an instabilizing one for $\varphi > 0°$ (transverse compression regime). Both the examined simplified crack contact interface

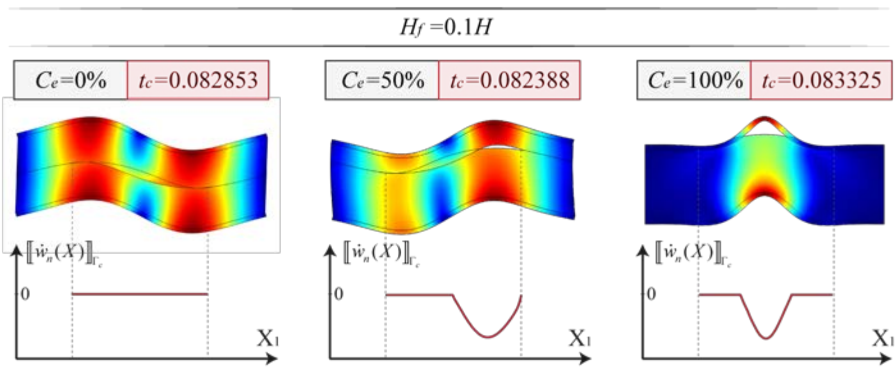

Fig. 3.27 Critical load levels, critical mode shapes and normal displacement rate jump at the crack contact interface for $L_C / L = 0.6$, $H_f = 0.1H$ and C_e equal to 0%, 50% and 100%.

formulations give conservative estimates for the critical load levels with an increasing underestimation as crack eccentricity decreases. The largest underestimation, measured as $(t_c - t_c^{NC}) / t_c \times 100$, is equal to 83% and occurs for the simplified formulation with neglected crack contact contributions at $\varphi = 70°$ with $H_f = 0.1H$ or $H_f = 0.05H$ and $C_e = 0\%$ .The typical critical mode shapes for the exact formulation are shown in Figs. 3.24-3.26 and Figs. 3.28-3.30 and, for the decompression limit path, the behavior of the normal displacement rate jump satisfying the unilateral rate contact constraint is represented in Fig. 3.27 and Fig. 3.31 for all the examined crack eccentricities. For $H_f = 0.1H$ a change in critical mode shape from antisymmetrical to symmetrical as φ increases for C_e equal to 0% and 50% (the change occurring for $\varphi = 70°$ and $\varphi = 20°$, respectively) is shown, whereas it remains always antisymmetrical for C_e equal to 100%. On the other hand, for $H_f = 0.05H$ critical mode shapes remain always symmetrical. As can be seen from Fig. 3.28 for the case with $L_C / L = 0.6$, $H_f = 0.05H$ and $C_e = 100\%$

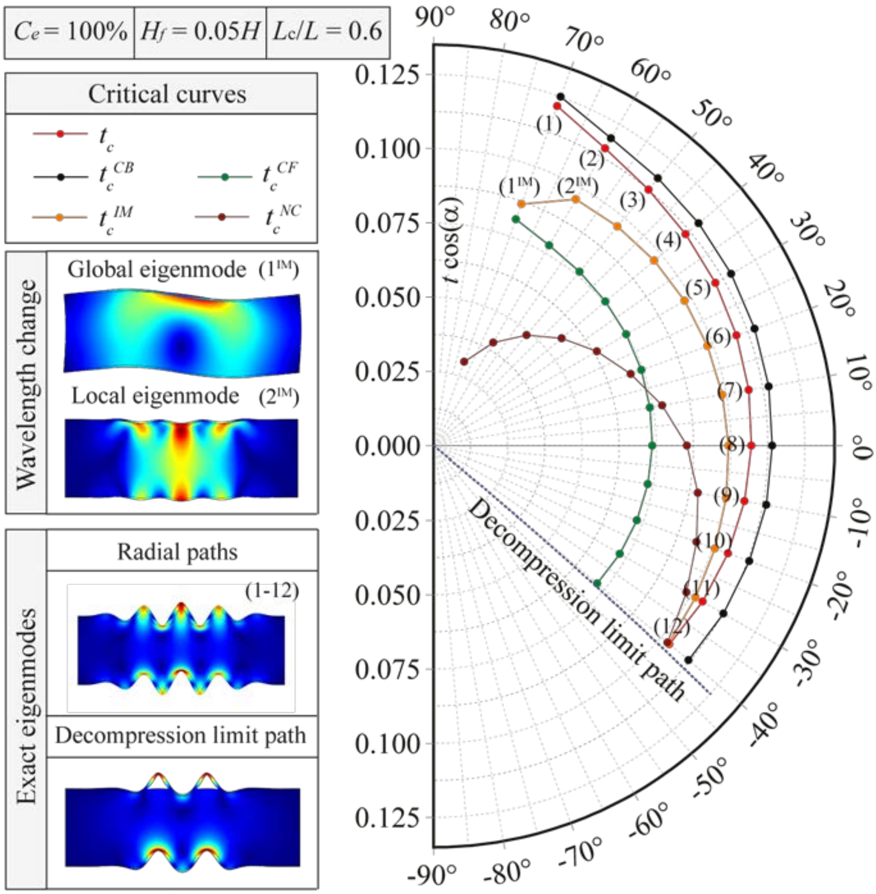

Fig. 3.28 Polar plot of the critical macroscopic strain along the X_1 direction $t\cos\varphi$ versus the load path angle φ and mode shape behavior for $L_C / L = 0.6$, $H_f = 0.05H$ and $C_e = 100\%$.

the Interface Model curve shows a sharp decline for $\varphi = 70°$ owing to a change in the critical mode shape wavelength from local to global. It is worth noting that, when $C_e = 0\%$ (see Fig. 3.26 and Fig. 3.30), the symmetry of the loading and of the microstructure implies a zero displacement rate jump and, as a consequence, the curves corresponding

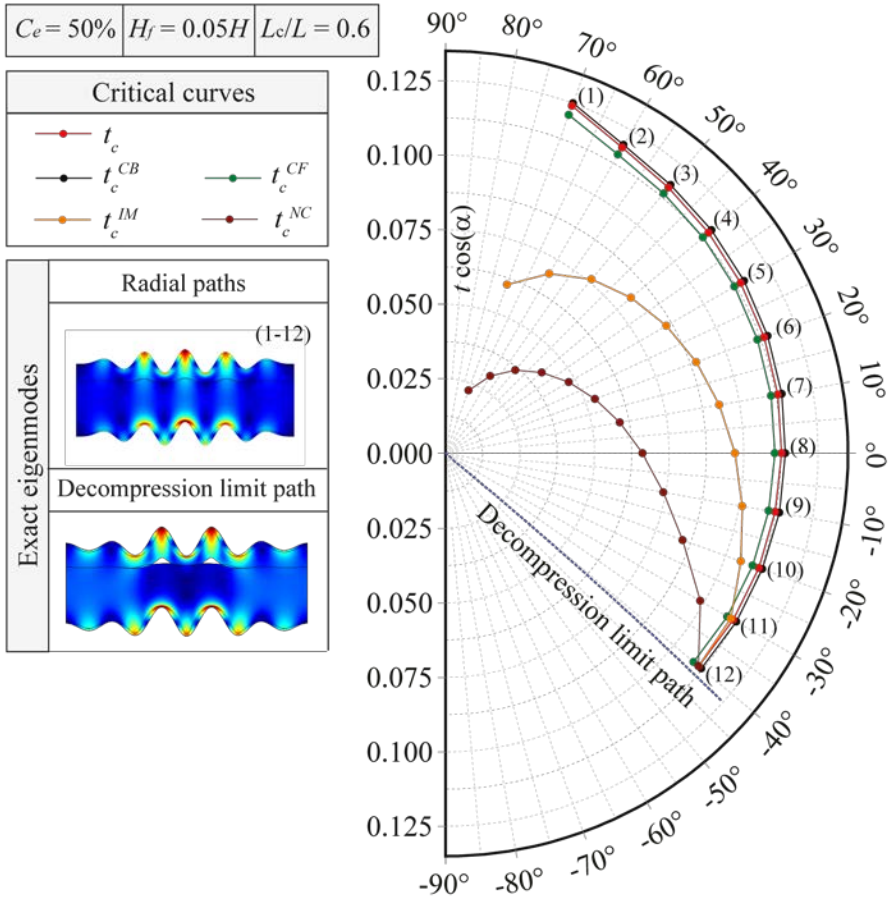

Fig. 3.29 Polar plot of the critical macroscopic strain along the X_1 direction $t\cos\varphi$ versus the load path angle φ and mode shape behavior for $L_C / L = 0.6$, $H_f = 0.05H$ and $C_e = 50\%$.

to the Exact and the Free formulations are coincident. The obtained stability and uniqueness domains show that, as expected, in all the examined cases the following inequalities are fulfilled $t_c^{CF} \leq t_c \leq t_c^{CB}$, that the highest critical load levels occur for $H_f = 0.05H$ and that both the two simplified formulations give conservative predictions of primary instability and bifurcation load levels (i.e. $t_c^{NC} < t_c^{IM} < t_c$).

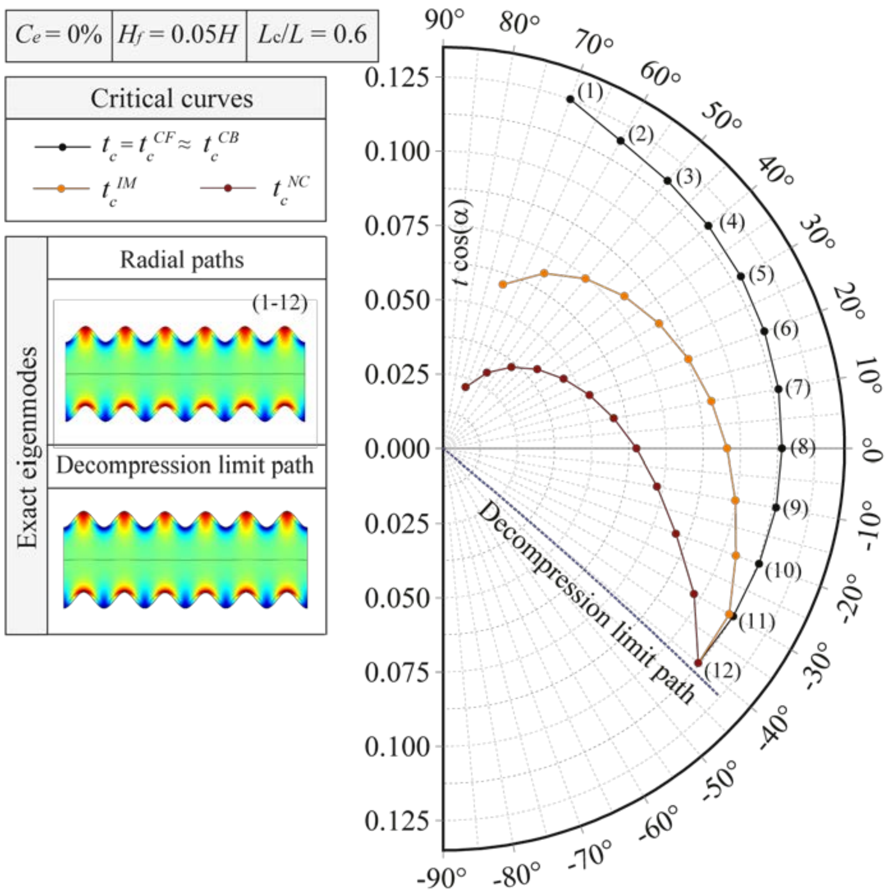

Fig. 3.30 Polar plot of the critical macroscopic strain along the X_1 direction $t\ cos\varphi$ versus the load path angle φ and mode shape behavior for $L_C / L = 0.6$, $H_f = 0.05H$ and $C_e = 0\%$.

As proved in section 4, additional calculations have confirmed that the critical load levels obtained by using only the tangential terms are the same of those obtained by using only the crack surface deformation terms. Moreover, the results also show that for $C_e \leq 50\%$ the change in crack eccentricity does not result in any important change of the critical

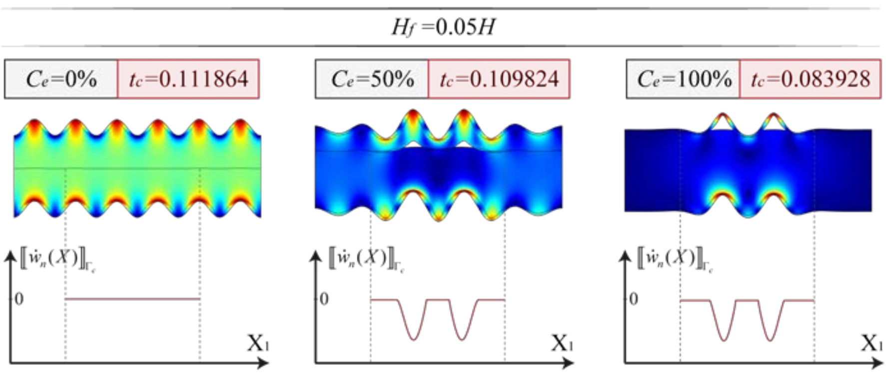

Fig. 3.31 Critical load levels, critical mode shapes and normal displacement rate jump at the crack contact interface for $L_C / L = 0.6$, $H_f = 0.05H$ and C_e equal to 0%, 50% and 100%.

curves, while for $C_e > 50\%$ the obtained critical load factors are stronger influenced by this parameter. Along the decompression limit loading path, owing to the absence of contact pressure, both the simplified and the exact formulations provide the same critical load levels and mode shapes as shown in Figs. 3.24-3.26 and Figs. 3.28-3.30. Comparisons between different critical curves clearly show that as the relative fiber thickness ratio decreases the critical load level increases leading to a decrease of the wavelength of the critical mode shape that strongly influences the critical load level magnitude. In addition to the results shown in the polar plots, in order to better evaluate the crack length influence on the critical load factors, further parametric analyses are carried out for $\varphi = \pm 20°$, varying L_C / L from 0 to 0.9 with an increment of 0.3 and the obtained critical load factors (presented in Tabs. 1-3) have been divided by the critical load factors corresponding to the upper bound t_c^{CB}.

Tab. 3.1 Critical load parameters normalized with respect to t_c^{CB} for different L_C / L values (C_e = 0%, $\varphi = +20°$).

	Dimensionless critical load factors					
	H_f	L_c/L	t_c	t_c^{IM}	t_c^{NC}	t_c^{CF}
C_e = 0%	0.05H	t_c^{CB}	0.12237	0.12237	0.12237	0.12237
		0.3	0.99959	0.90184	0.54983	0.99959
		0.6	0.99925	0.76345	0.45543	0.99925
		0.9	0.96556	0.52686	0.31601	0.96556
	0.1H	t_c^{CB}	0.12103	0.12103	0.12103	0.12103
		0.3	0.84308	0.68017	0.48133	0.84308
		0.6	0.77207	0.57266	0.39512	0.77207
		0.9	0.62653	0.40713	0.26609	0.62653

Tab. 3.2 Critical load parameters normalized with respect to t_c^{CB} for different L_C / L values (C_e = 0%, $\varphi = -20°$).

	Dimensionless critical load factors					
	H_f	L_c/L	t_c	t_c^{IM}	t_c^{NC}	t_c^{CF}
C_e = 0%	0.05H	t_c^{CB}	0.12033	0.12033	0.12033	0.12033
		0.3	0.99968	0.99948	0.86349	0.99968
		0.6	0.99941	0.92652	0.73691	0.99941
		0.9	0.99911	0.69410	0.52302	0.99911
	0.1H	t_c^{CB}	0.11949	0.11949	0.11949	0.11949
		0.3	0.83451	0.76070	0.67148	0.83451
		0.6	0.75513	0.66277	0.56899	0.75513
		0.9	0.60635	0.50176	0.41203	0.60635

Tab. 3.3 Critical load parameters normalized with respect to t_c^{CB} for different L_C / L values (C_e = 50%, $\varphi = +20°$).

	Dimensionless critical load factors					
	H_f	L_c/L	t_c	t_c^{IM}	t_c^{NC}	t_c^{CF}
C_e = 50%	0.05H	t_c^{CB}	0.12237	0.12237	0.12237	0.12237
		0.3	0.99245	0.87356	0.54356	0.97632
		0.6	0.98851	0.77781	0.46379	0.96817
		0.9	0.98561	0.56570	0.32194	0.96088
	0.1H	t_c^{CB}	0.12103	0.12103	0.12103	0.12103
		0.3	0.83791	0.66984	0.47617	0.81619
		0.6	0.78656	0.58184	0.40039	0.74536
		0.9	0.66785	0.43546	0.28373	0.63273

Tab. 3.4 Critical load parameters normalized with respect to t_c^{CB} for different L_C / L values (C_e = 50%, $\varphi = -20°$).

	Dimensionless critical load factors					
	H_f	L_c/L	t_c	t_c^{IM}	t_c^{NC}	t_c^{CF}
C_e = 50%	0.05H	t_c^{CB}	0.12033	0.12033	0.12033	0.12033
		0.3	0.99308	0.98868	0.83842	0.97738
		0.6	0.98911	0.93233	0.74804	0.96916
		0.9	0.96570	0.73849	0.55664	0.91878
	0.1H	t_c^{CB}	0.11949	0.11949	0.11949	0.11949
		0.3	0.82602	0.74993	0.66102	0.80626
		0.6	0.76751	0.67282	0.57672	0.72927
		0.9	0.64355	0.53347	0.43805	0.61159

Tab. 3.5 Critical load parameters normalized with respect to t_c^{CB} for different L_C / L values (C_e = 100%, $\varphi = +20°$).

	Dimensionless critical load factors					
	H_f	L_c/L	t_c	t_c^{IM}	t_c^{NC}	t_c^{CF}
C_e = 100%	0.05H	t_c^{CB}	0.12237	0.12237	0.12237	0.12237
		0.3	0.95471	0.86669	0.67902	0.67307
		0.6	0.94360	0.85279	0.61415	0.64681
		0.9	0.94051	0.84908	0.50496	0.63995
	0.1H	t_c^{CB}	0.12103	0.12103	0.12103	0.12103
		0.3	0.91774	0.76969	0.57069	0.73949
		0.6	0.89978	0.71415	0.50652	0.66676
		0.9	0.85744	0.63536	0.43045	0.65198

Tab. 3.6 Critical load parameters normalized with respect to t_c^{CB} for different L_C / L values (C_e = 100%, $\varphi = -20°$).

	Dimensionless critical load factors					
	H_f	L_c/L	t_c	t_c^{IM}	t_c^{NC}	t_c^{CF}
C_e = 100%	0.05H	t_c^{CB}	0.12033	0.12033	0.12033	0.12033
		0.3	0.94422	0.90460	0.84646	0.67044
		0.6	0.93246	0.89119	0.83269	0.64366
		0.9	0.92900	0.88736	0.82213	0.63696
	0.1H	t_c^{CB}	0.11949	0.11949	0.11949	0.11949
		0.3	0.90385	0.83795	0.75375	0.73326
		0.6	0.88441	0.80003	0.70166	0.66050
		0.9	0.83898	0.73609	0.62760	0.64538

From the results in tables, it is possible to note that the critical load levels obtained by means of simplified formulations in which a biaxial compression regime in both directions is considered ($\varphi = +20°$), give the largest underestimation of exact critical load factors (equal to 73% and attained when $\varphi = +20°$, $H_f = 0.1H$, $L_C / L = 0.9$ and $C_e = 0\%$). The microstructural arrangement with $H_f = 0.05H$ shows that the exact critical load level t_c is scarcely influenced by the relative crack length, as a matter of fact a less deviation from the bonded case, whose critical load levels are independent of the relative crack length, is shown especially in the case of $C_e = 0\%$ where t_c turns out to be coincident with t_c^{CB}. Finally the above results show that the influence of crack contact interface contributions becomes more significant as L_C / L increases and C_e decreases, thus highlighting the strong role of crack contact interface contributions and the importance of adopting a full finite deformation formulation rather than simplified ones for an actual prediction of the failure behavior of a defected composite solid.

4

Multiscale analysis of composite materials at finite deformations

In this chapter two different multiscale modeling approaches are presented for the analysis of the macroscopic behavior of composite materials subjected to general loading conditions involving large deformations. Both multiscale approaches have been suitably validated through comparisons with reference direct numerical simulations, by which the ability of the proposed multiscale approaches to determine the macroscopic behavior in complex microstructured composite materials has been demonstrated.

Section 4.1 deals with the theoretical background of the nonlinear homogenization problem in periodic composite materials subjected to large deformation, focusing in Section 4.1.2 on the theoretical formulation of the microscopic stability condition. In Section 4.2 a description of the modeling techniques employed is given focusing the attention on the couple-volume element methods in Section 4.2.1 and on the novel hybrid proposed multiscale approach in Section 4.2.2. Then from the numerical results point of view, Section 4.3 is devoted to the numerical applications for the microscopic stability analysis in continuously and discontinuously reinforced composite materials, whereas Section 4.4 is devoted to the investigation of the mechanical behavior of bioinspired composite materials in terms of flexibility and penetration resistance.

4.1 Theoretical formulation of microscopic stability for periodic composite solids

The theoretical formulation of the nonlinear homogenization problem reported in Section Fig. 4.1 is here applied in absence of pre-existing crack with reference to the perfectly periodic heterogeneous solids subjected to general loading conditions involving large deformations in the context of the multiscale problems.

A perfectly periodic microstructured solid described by a unit cell attached to a generic material point $\bar{\boldsymbol{X}}$ of the corresponding homogenized solid, as depicted in Fig. 4.1. The deformation of the considered microstructure is defined by the nonlinear mapping $\boldsymbol{x}(\boldsymbol{X}): V_{(i)} \rightarrow V$, relating points $\boldsymbol{X}$ of the initial microstructural configuration $V_{(i)}$ to points $\boldsymbol{x}$ of the current one, V. The deformation gradient at the material point $\boldsymbol{X}$ is $\boldsymbol{F}(\boldsymbol{X}) = \partial \boldsymbol{x}(\boldsymbol{X}) / \partial \boldsymbol{X}$, whereas the corresponding displacement field is $\boldsymbol{u}(\boldsymbol{X}) = \boldsymbol{x}(\boldsymbol{X}) - \boldsymbol{X}$.

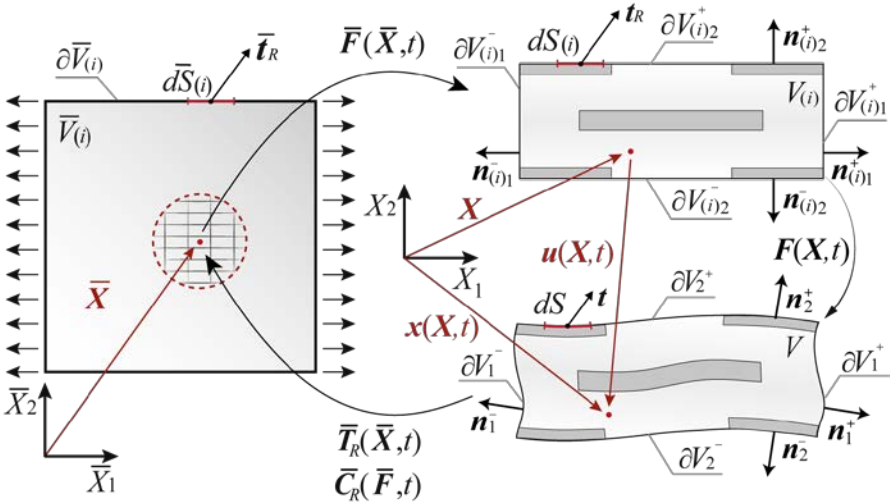

Fig. 4.1 Homogenized solid and the corresponding unit cell in undeformed and deformed configurations attached to a generic material point $\bar{\boldsymbol{X}}$.

4.1.1 Nonlinear homogenization problem: micro-macro coupling and macroscopic response

Each microstructural constituent is characterized by a rate independent material model, whose constitutive response at a microscopic point $\boldsymbol{X}$ is described by an incrementally linear constitutive law:

$$\dot{\boldsymbol{T}}_R = \boldsymbol{C}^R(\boldsymbol{X}, \boldsymbol{F})[\dot{\boldsymbol{F}}], \tag{4.1}$$

relating the rate of deformation gradient tensor, $\dot{\boldsymbol{F}}$, to the rate of the first Piola-Kirchhoff stress tensor, $\dot{\boldsymbol{T}}_R$, via the nominal tangent moduli tensor $\boldsymbol{C}^R$. Moreover, in the case of hyperelastic micro-constituents, the nominal stress tensor and the corresponding moduli tensor can be defined, respectively, as the first and second derivatives of the strain en-

ergy density function $W(\boldsymbol{X},\boldsymbol{F})$ with respect to $\boldsymbol{F}$. As commonly assumed in the context of first-order homogenization schemes, the homogenized constitutive response of the considered microstructure relies on an equilibrium state which neglects body forces, resulting in a divergence-free local stress field $\boldsymbol{T}_R$ in $V_{(i)}$.
In agreement with what reported in Section 3, the following expressions for the macroscopic nominal stress tensor $\bar{\boldsymbol{T}}_R$ and the macroscopic deformation gradient tensor $\bar{\boldsymbol{F}}$ are introduced:

$$\bar{\boldsymbol{T}}_R = \frac{1}{\left|V_{(i)}\right|}\int_{\partial V_{(i)}} \boldsymbol{t}_R(\boldsymbol{X}) \otimes \boldsymbol{X} \; dS_{(i)}, \quad \bar{\boldsymbol{F}} = \frac{1}{\left|V_{(i)}\right|}\int_{\partial V_{(i)}} \boldsymbol{x}(\boldsymbol{X}) \otimes \boldsymbol{n}_{(i)} \; dS_{(i)}, \quad (4.2)$$

with $\otimes$ denoting the tensor product, whereas $\boldsymbol{t}_R$ and $\boldsymbol{n}_{(i)}$ are the traction field and the outward normal, respectively, both evaluated at points $\boldsymbol{X}$ belonging to the external boundary $\partial V_{(i)}$ of the unit cell. The microscopic deformation $\boldsymbol{x}(\boldsymbol{X})$ can be additively split into a linear part, $\bar{\boldsymbol{F}}\boldsymbol{X}$, corresponding to a homogeneous deformation, and a correction part, $\boldsymbol{w}(\boldsymbol{X})$, usually named as fluctuation field, being associated with non-homogeneous deformations as follow:

$$\boldsymbol{x}(\boldsymbol{X}) = \bar{\boldsymbol{F}}\boldsymbol{X} + \boldsymbol{w}(\boldsymbol{X}) \; . \quad (4.3)$$

By applying Eq. $(4.2)_2$, the following integral constraint turns to be required for the fluctuation field:

$$\int_{\partial V_{(i)}} \boldsymbol{w}(\boldsymbol{X}) \otimes \boldsymbol{n}_{(i)} \; dS_{(i)} = \boldsymbol{0} \, . \quad (4.4)$$

According to the periodic nature of the composite microstructure, the constraint (4.4) can be satisfied by enforcing periodic fluctuations:

$$\boldsymbol{w}(\boldsymbol{X}^{+}) = \boldsymbol{w}(\boldsymbol{X}^{-}) \quad (4.5)$$

leading to periodic deformation and antiperiodic tractions on the unit cell boundary, i.e.

$$\begin{cases} \boldsymbol{u}(\boldsymbol{X}^+) - \boldsymbol{u}(\boldsymbol{X}^-) = (\overline{\boldsymbol{F}}(\overline{\boldsymbol{X}}) - \boldsymbol{I})(\boldsymbol{X}^+ - \boldsymbol{X}^-), \\ \boldsymbol{t}_R(\boldsymbol{X}^+) = -\boldsymbol{t}_R(\boldsymbol{X}^-), \end{cases} \quad \text{on } \partial V_{(i)}, \tag{4.6}$$

where $\left(\boldsymbol{X}^+, \boldsymbol{X}^-\right)$ is the couple of points belonging to the opposite sides of the unit cell boundary, denoted as $\partial V_{(i)}^+$ and $\partial V_{(i)}^-$ with outwards normal unit vectors $\boldsymbol{n}^+ = -\boldsymbol{n}^-$ at two associated points $\boldsymbol{X}^+ \in \partial V_{(i)}^+$ and $\boldsymbol{X}^- \in \partial V_{(i)}^-$, respectively, obtained by two translations parallel to the directions of the periodicity vectors spanning the undeformed unit cell $V_{(i)}$. The incremental homogenized response of the given microstructure is determined considering a quasi-static loading path $\overline{\boldsymbol{F}}(t)$ starting from its undeformed configuration $V_{(i)}$, where $t \geq 0$ represents a load parameter increasing monotonically with increasing prescribed macroscopic load and the given microstructure in the current configuration occupies the region V. The associated equilibrium solution at the given macro-deformation gradient can be obtained by solving the following variational problem defined over the unit cell:

$$\int_{V_{(i)}} \boldsymbol{T}_R(\boldsymbol{X}, \overline{\boldsymbol{F}} + \nabla \boldsymbol{w}) \cdot \nabla \delta \boldsymbol{w} \; dV_{(i)} = 0, \quad \forall \delta \boldsymbol{w} \in H^1(V_{(i)\#}), \tag{4.7}$$

where $H^1(V_{(i)\#})$ is the Sobolev space of vector valued functions which are periodic over the unit cell $V_{(i)}$, the subscript $\#$ appended to a region denoting the assumed periodicity properties on its boundary. It is worth noting that arbitrary rigid body motions can be prevented by introducing additional constraints on the unknown fluctuation field. The equilibrium state obtained via the Euler-Lagrange equations associated with the variational formulation (4.7) is characterized by anti-periodic tractions on the external boundary $\partial V_{(i)}$. Moreover, if uniqueness of the equilibrium solution is assumed for each value of the loading parameter, the macroscopic loading path $\bar{\boldsymbol{F}}(t)$ is named as principal solution path.

The incremental homogenized response of the microstructure can be derived after solving the following incremental equilibrium problem defined over the same unit cell subjected to an incremental change in the macroscopic deformation gradient, denoted as $\dot{\bar{\boldsymbol{F}}}(t)$:

$$\int_{V_{(i)}} \boldsymbol{C}^R(\boldsymbol{X},\bar{\boldsymbol{F}})[\dot{\bar{\boldsymbol{F}}}+\nabla\dot{\boldsymbol{w}}]\cdot\nabla\delta\dot{\boldsymbol{w}}\ dV_{(i)}=0, \quad \forall\,\delta\dot{\boldsymbol{w}}\in H^1(V_{(i)\#}), \qquad (4.8)$$

where $\dot{\boldsymbol{w}}$ is the unknown incremental fluctuation field induced by $\dot{\bar{\boldsymbol{F}}}(t)$, and $\boldsymbol{C}^R$ denotes the nominal moduli tensor, whose spatial distribution inside the unit cell is obtained after solving the microscopic problem (4.7). Additional displacement constraints are introduced into the variational problem (4.8) in order to exclude arbitrary incremental rigid body motions. The incremental equilibrium state obtained via the Euler-Lagrange equations associated with Eq. (4.8) is characterized by anti-periodic incremental tractions on $\partial V_{(i)}$ and vanishing incremental tractions on $\partial H_{(i)}$. After solving the incremental problem (4.8) for the microstructure, its homogenized constitutive response is writable as $\dot{\bar{\boldsymbol{T}}}_R=\bar{\boldsymbol{C}}^R(\bar{\boldsymbol{F}})[\dot{\bar{\boldsymbol{F}}}]$, where the homogenized tangent moduli tensor $\bar{\boldsymbol{C}}^R(\bar{\boldsymbol{F}})$ can be expressed by the following relation, obtained by exploiting the fundamental identity $\dot{\bar{\boldsymbol{T}}}_R=\bar{\dot{\boldsymbol{T}}}_R$ (see [161] for details about its derivation):

$$\bar{C}^R_{ijkl}(\bar{\boldsymbol{F}})=\frac{1}{|V_{(i)}|}\int_{V_{(i)}} C^R_{ijmn}(\boldsymbol{X},\bar{\boldsymbol{F}})[I^{kl}_{mn}+\nabla\dot{w}^{kl}_{mn}]\ dV_{(i)}\,, \qquad (4.9)$$

where $\dot{\boldsymbol{w}}^{kl}$ is the incremental fluctuation field induced by unit components of the incremental macroscopic deformation gradient $\dot{\bar{\boldsymbol{F}}}=\boldsymbol{I}^{kl}$ (with $I^{kl}_{mn}=\delta_{mn}\delta_{kl}$).

It is important to recall here that Eq. (4.9), obtained via the unit cell-based homogenization, is strictly valid only if the microstructural equilibrium configuration is incrementally stable, otherwise the homogenized constitutive response must be computed considering a larger representative volume element (RVE), made of a possibly infinite number of unit cells, in order to capture all possible unstable deformation patterns.

4.1.2 Microscopic stability conditions

In the case of hyperelastic micro-constituents with nonconvex strain energy function $W(\boldsymbol{F})$, the homogenized strain energy function $\bar{W}(\bar{\boldsymbol{F}})$ can be obtain by solving the following minimization problem:

$$\bar{W}(\bar{\boldsymbol{F}}) = \inf_{k \in N} \left\{ \min_{\boldsymbol{w} \in H^1(k^N \mathrm{V}_{(i)\#})} \left\{ \frac{1}{k^N \left| \mathrm{V}_{(i)} \right|} \int_{k^N \mathrm{V}_{(i)}} W\left(\boldsymbol{X}, \bar{\boldsymbol{F}} + \nabla \boldsymbol{w}\right) dV_{(i)} \right\} \right\}, \quad (4.10)$$

defined over all possible ensembles of $k^N = [0,k]^N$ unit cells, with $N = \{2,3\}$ and k an arbitrary integer.

In the presence of eventual micro-buckling mechanisms, the solution of the minimization problem (4.10) allows to determine the size of the representative volume element associated with the fluctuation field capturing the minimizing buckling mode. However, the direct application of Eq. (4.10) may require a huge computational effort, connected to the need of investigating a full space at the microscopic scale. Therefore, a one-cell homogenization is preferable for numerical applications, obtained by taking $k = 1$ in Eq. (4.10). In general, such a homogenization problem provides only an upper bound for the macroscopic strain energy, denoted as $\bar{W}^1\left(\bar{\boldsymbol{F}}\right)$, which becomes coinciding with the actual value $\bar{W}(\bar{\boldsymbol{F}})$ only in the absence of micro-instabilities.

It can be shown that the region of validity for one-cell homogenization, i.e. the region of the macro-strain space for which $\overline{W}^1(\overline{\boldsymbol{F}}) = \overline{W}(\overline{\boldsymbol{F}})$, can be found in a rigorous manner by means of a microstructural stability analysis. For a given RVE subjected to a prescribed macro-deformation $\overline{\boldsymbol{F}}$, such a microstructural stability condition relies on the positive definiteness of the following stability functional, written in a full Lagrangian setting:

$$S(\overline{\boldsymbol{F}}, \dot{\boldsymbol{w}}) = \int_{k^N V_{(i)}} \boldsymbol{C}^R(\boldsymbol{X}, \overline{\boldsymbol{F}} + \nabla \boldsymbol{w})[\nabla \dot{\boldsymbol{w}}(\boldsymbol{X})] \cdot \nabla \dot{\boldsymbol{w}}(\boldsymbol{X}) \, dV_{(i)} \,, \qquad (4.11)$$

for all incremental fluctuations $\dot{\boldsymbol{w}}$ satisfying the periodicity conditions on the RVE boundaries, with the additional constraint $\nabla \dot{\boldsymbol{w}}(\boldsymbol{X}) \neq \boldsymbol{0}$. It follows that the critical load parameter t_c associated with the primary instability is detected when the minimum eigenvalue of $S(\overline{\boldsymbol{F}}, \dot{\boldsymbol{w}})$, taken over all admissible incremental fluctuations periodic on the ensemble of k^N unit cells, first vanishes, namely:

$$\Lambda(t_c) = \inf_{k \in N} \left\{ \min_{\dot{\boldsymbol{w}} \in H^1(k^N V_{(i)\#})} \left\{ \frac{S(\overline{\boldsymbol{F}}(t_c), \dot{\boldsymbol{w}})}{\int_{k^N V_{(i)}} \nabla \dot{\boldsymbol{w}} \cdot \nabla \dot{\boldsymbol{w}} \, dV_{(i)}} \right\} \right\} = 0 \,. \qquad (4.12)$$

At this load, the initially stable and unique principal solution loses its uniqueness due to the existence of eigenmodes (i.e. non-trivial incremental periodic solutions to the homogeneous incremental equilibrium problem). Therefore, the microscopic stability region, defined as $t \,|\, \Lambda(\overline{\boldsymbol{F}}(t)) > 0$ and characterized by an identical deformation for all the unit cells inside the considered RVE, necessarily coincides with the region of validity for one-cell homogenization.

Finally, it is worth recalling that a classical macroscopic stability analysis, based on the strong ellipticity condition for the homogenized moduli tensor, although being less computationally expensive in practical numerical applications, is not accurate in general, providing a non-conservative estimation of the primary microscopic instability load in the occurrence of instability modes of local kind (see [162–169] for additional details).

4.2 Description of the proposed multiscale approaches

In this section, in order to delineate which class of multiscale approach is more effective in the determination of the macroscopic behavior of advanced composite materials (fiber reinforced and nacre-like composites) in a large deformation context, more information about the computational implementation of the proposed multiscale approaches are given. Specifically, a semiconcurrent model called coupled-volume approach has been adopted to evaluate the microscopic instability critical load factor in composite materials reinforced with long fibers; later, a novel hybrid multiscale model has been proposed, firstly, to evaluate the microscopic instability in composite materials with staggered microstructure, secondly, to investigate the mechanical behavior of bio-inspired nacre-like composite materials in terms of flexibility and penetration resistance.

4.2.1 Coupled-volume multiscale approach (semiconcurrent)

Generally speaking, the concept behind the semiconcurrent models can be summarized in 4 steps:

(i) *macrodomain computation*: the heterogeneous material is described as homogeneous with effective properties without the necessity to assume constitutive assumptions:

(ii) *downscaling:* once the macroscopic domain is discretized, at every Gauss point (integration or quadrature point) is linked a microscopic boundary value problem and the information about the macroscopic gradient deformation field (input) is transferred into the microscopic domain in terms of displacement boundary conditions;

(iii) *microdomain computation:* at the microscopic level, each microconstituent of the heterogeneous material is described by a constitutive assumption allowing to solve the n boundary value problems linked to the n Gauss points in different manners (FEM, Voronoi cell FEM, Fast Fourier Transforms etc.)

(iv) *upscaling:* the homogenization procedure is performed on the microscopic level for each iteration needed to the solver to achieve the macroscopic convergence in terms of macroscopic stress tensor and macroscopic tangent moduli tensor, which results in the homogenized relations that has to transferred to the macroscopic level.

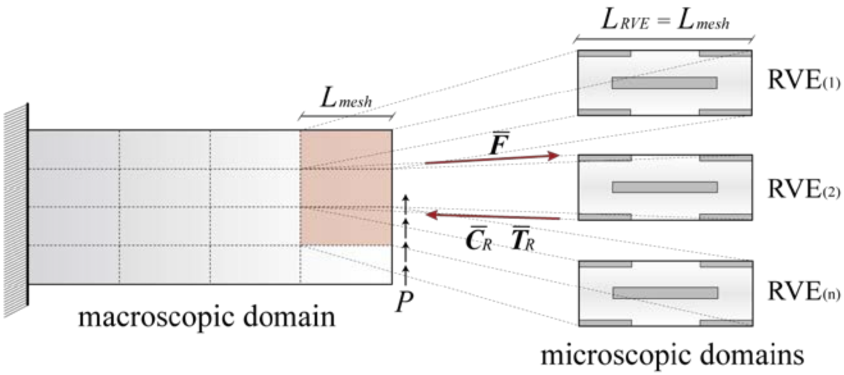

Fig. 4.2 Schematic of a coupled-volume multiscale approach belonging to the class of semiconcurrent models.

The proposed semiconcurrent multiscale approach for the microstructural stability analysis of locally periodic composite materials relies on a coupled-volume multiscale model [170] according to which two nested equilibrium problems are solved at the same time (as sketched in Fig. 4.2). The approach leaves the concept that a finite microscopic cell size should be linked to an infinitely small macroscopic material point and adopting the concept that the macroscopic and the microscopic mesh sizes are uniquely linked following the rule that the macroscopic element size is equal to the microscopic cell size. This semiconcurrent approach is able to solve the mechanical problem associated to the macroscopic model in absence of an explicitly defined macroscopic constitutive law, and it is also effective to investigate the behavior of materials subjected to strong nonlinearities for which the RVE cannot be found. Based on the information given above, about the semiconcurrent multiscale modeling strategy, the implementation of the coupled-volume multiscale approach may be described by the steps which has been graphically summarized in Fig. 4.3.The resulting two-scale equilibrium problem, written in an incremental form, reads as follows:

find $\dot{\bar{\boldsymbol{u}}} \in H^1(\overline{V}_{(i)}), \dot{\boldsymbol{w}} \in H^1(\overline{V}_{(i)} \times V_{(i)\#})$ such that:

$$\left.\begin{array}{ll}
\overbrace{\int_{\overline{V}_{(i)}} \dot{\bar{\boldsymbol{T}}}_R \cdot \nabla \delta \dot{\bar{\boldsymbol{u}}} \; d\overline{V}_{(i)} = \int_{\overline{V}_{(i)}} \dot{\bar{\boldsymbol{f}}} \cdot \delta \dot{\bar{\boldsymbol{u}}} \; d\overline{V}_{(i)} + \int_{\partial \overline{V}_{(i)}} \dot{\bar{\boldsymbol{t}}}_R \cdot \delta \dot{\bar{\boldsymbol{u}}} \; d\overline{S}_{(i)}}^{\text{Coarse-scale problem}} & \forall \delta \dot{\bar{\boldsymbol{u}}} \in H^1(\overline{V}_{(i)}) \\
\underbrace{\int_{V_{(i)}} \boldsymbol{C}^R [\dot{\bar{\boldsymbol{F}}} + \nabla \dot{\boldsymbol{w}}] \cdot \nabla \delta \dot{\boldsymbol{w}} \; dV_{(i)} = 0}_{\text{Fine-scale problem}} & \forall \delta \dot{\boldsymbol{w}} \in H^1(V_{(i)\#})
\end{array}\right\} , \quad (4.13)$$

where $H^1(\overline{V}_{(i)})$ is the Sobolev space of vector valued functions defined on $\overline{V}_{(i)}$ and satisfying the homogeneous displacement-type conditions on its boundary, whereas $H^1(\overline{V}_{(i)} \times V_{(i)\#})$ is the Sobolev space of vector valued functions defined over the Cartesian product $\overline{V}_{(i)} \times V_{(i)\#}$ and satisfying the periodic fluctuation conditions over the unit cell boundaries.

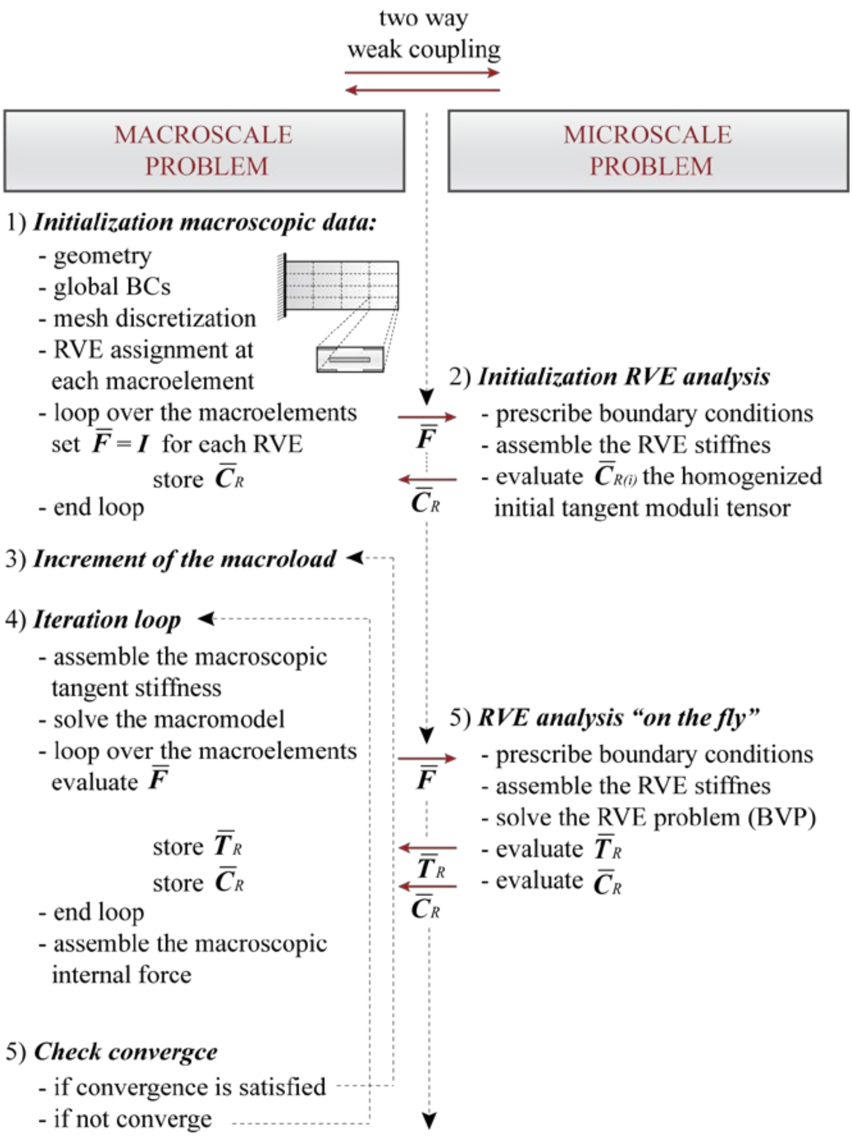

Fig. 4.3 Multiscale scheme implementation for the coupled volume multiscale method.

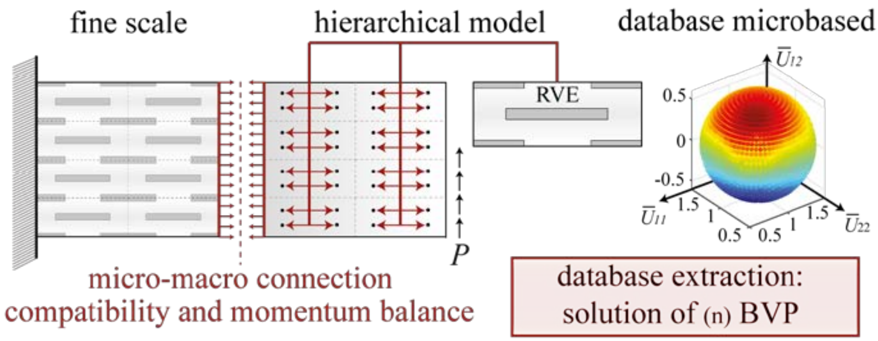

Fig. 4.4 Schematic of the hybrid hierarchical/concurrent multiscale approach.

Moreover, $\dot{\bar{\boldsymbol{f}}}$ and $\dot{\bar{\boldsymbol{t}}}_R$ denotes respectively the body and surface incremental forces externally applied on the macroscopic body.
The two-scale incremental equilibrium problem (4.13) turns to be two-way coupled. Indeed, the unit cell problem is driven by the incremental macroscopic deformation gradient $\dot{\bar{\boldsymbol{F}}}$. Once the boundary value problem is solved for the unit cell, the rate of the macroscopic first Piola-Kirchhoff stress $\dot{\bar{\boldsymbol{T}}}_R$ is computed via the first of Eqs.(3.3) The information transfer between the two scales is sketched in Fig. 4.3. It is worth noting that the choice of using the deformation gradient $\boldsymbol{F}$ (together with its work-conjugate stress measure $\boldsymbol{T}_R$) rather than the Green-Lagrange strain $\boldsymbol{E}^{(2)}$ (and its work-conjugate stress measure $\boldsymbol{T}^{(2)}$) to drive the homogenization process is convenient for prescribing the periodic boundary conditions (BCs) on the RVE.

4.2.2 Hybrid hierarchical/concurrent multiscale approach

The key idea of the proposed hybrid hierarchical/concurrent multiscale approach is to combine a hierarchical and a concurrent approach overcoming the limitation given by semiconcurrent approaches in the capturing of boundary layer effects, localization of deformation, coalescence of microcracks and other kind of nonlinearities. As shown in Fig. 4.4, the hybrid multiscale method can be implemented taking advantage from a concurrent approach identifying the so-called critical domains in which is employed an explicit modeling of the microstructure (fine scale domain) and the associated nonlinear phenomena (material, geometrical, damage, friction, etc.), and taking advantage from a hierarchical approach implementing, in the remaining domain, an homogenized constitutive law in the form of nonlinear microscopically-based database. Usually, the critical domains are characterized by a microstructural evolution or some other notable geometrical or material nonlinearities which requires a numerical model able to describe all its microscopic phenomena leading to a more considerable computational effort; as a matter of fact, the identification of the regions where the fine scale is required and regions where it is not is the most important step. Contrary to the coupled-volume multiscale approach in which each RVE linked at the macroelement is solved (as boundary value problem BVP) for each time step of the macroscale problem, in the hybrid multiscale approach this step has been now replaced with the application of a microscopically-based nonlinear database extracted in a preprocessing step. Thus, as explained in Section 4.2.2.1 the macroscopic stress and the macroscopic tangent moduli tensor are stored in a nonlinear database in the form of unstructured point cloud and they are transferred in the macroscopic model by using an interpolation method.

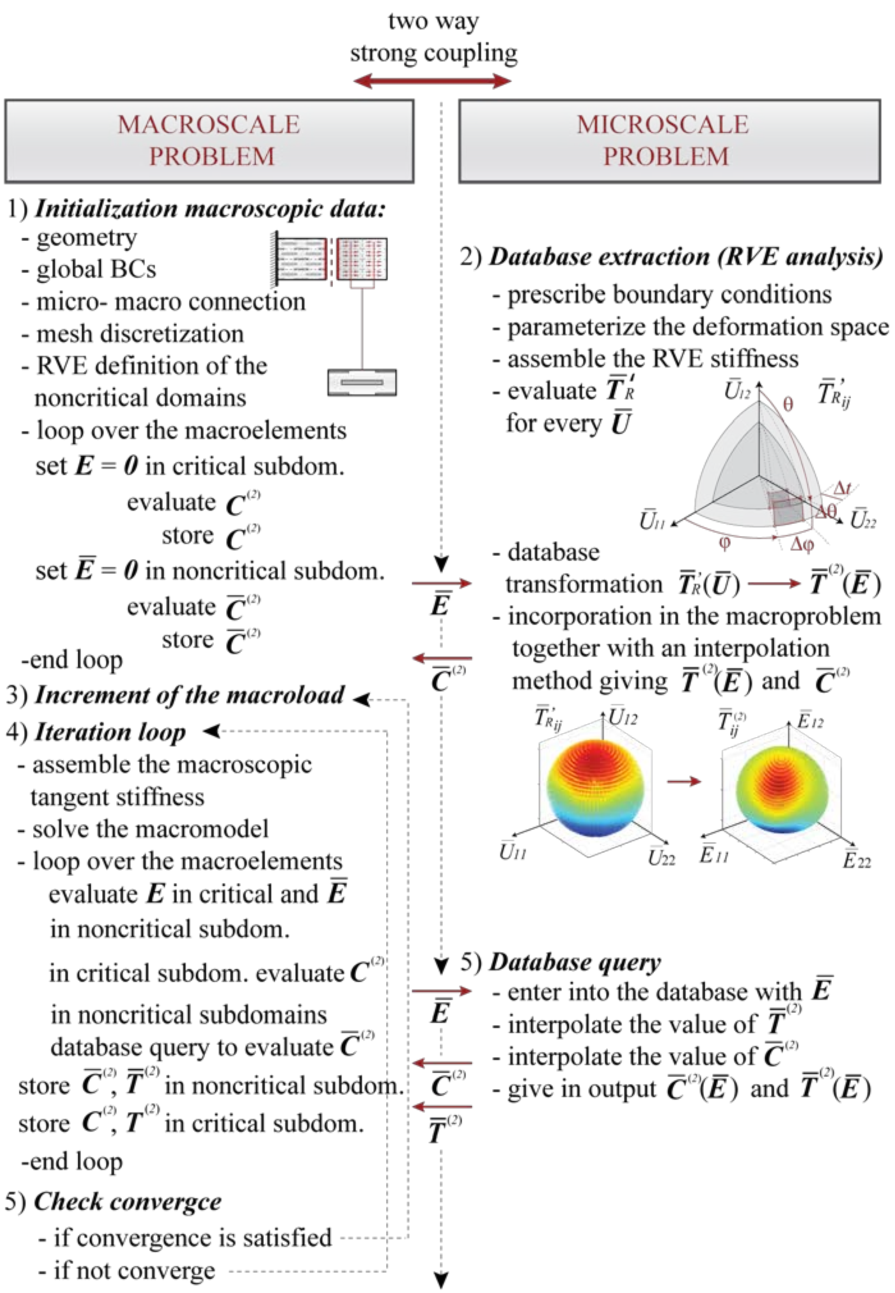

Fig. 4.5 Multiscale scheme implementation for the hybrid hierarchical/concurrent multiscale method.

The procedure adopted to implement the hybrid multiscale approach can be summarized in the following steps and has been graphically summarized in Fig. 4.5:

(i) *macrodomain computation*: the heterogeneous material is split in two subdomains: critical and noncritical. In the critical subdomains every heterogeneity is modeled explicitly together with the nonlinear phenomena acting at the microscopic scale and assuming as known their constitutive properties. In the noncritical subdomains there is not the necessity to assume constitutive assumptions because this information will be extracted from a nonlinear microscopically-based database.

(ii) *Downscaling:* once the macroscopic subdomains are discretized, compatibility and momentum balance are imposed on the common interface between critical and noncritical subdomains and then, a representative volume element is identified to evaluate the homogenized behavior of the noncritical subdomains.

(iii) *microdomain computation and database extraction:* at the microscopic level, each microconstituent of the representative volume element is described by a constitutive law. The RVE is analyzed to create a numerical data point in the macroscopic deformation space parametrized by using spherical coordinates and spaced by radial strain paths; the macroscopic stresses are evaluated for every time step and stored in a database matching the information on strains with information on stresses and tangent moduli.

(iv) *upscaling:* the extracted database is then incorporated in noncritical subdomains of the macroscopic model. During the procedure of solving the macroscopic problem, the microscopically-based database is interrogated to extract the information in terms of macroscopic stress tensor and macroscopic tangent moduli tensor until the macroscopic convergence is reached.

More information about the step (iii) are given in the following section.

4.2.2.1 Microscopically-based database extraction

The microscopically-based database represents a constitutive equation that receives in input a macroscopic strain tensor and gives in output a macroscopic stress tensor. Three alternative strategies can be adopted to extract the database:

i) the first one is based on the macroscopic First-Piola Kirchhoff tensor $\bar{\boldsymbol{T}}_R$ defined as a function of the macroscopic gradient deformation tensor $\bar{\boldsymbol{F}}$:

$$\bar{\boldsymbol{T}}_R = \bar{\boldsymbol{T}}_R\left(\bar{\boldsymbol{F}}(t)\right). \tag{4.14}$$

This strategy leads to a simple definition of the RVE boundary conditions (as reported in Section 1.3), but in a planar setting, $\bar{\boldsymbol{F}}$ is a tensor whose components are: $\bar{F}_{11}$, $\bar{F}_{12}$, $\bar{F}_{21}$ and $\bar{F}_{22}$; for this reason, a numerical data point database, based on the macroscopic gradient tensor, must be parametrized on a four-dimensional space leading to an high computationally effort and leading also to the adoption of complex interpolation methods;

ii) the second one is based on the macroscopic Second-Piola Kirchhoff tensor $\bar{\boldsymbol{T}}^{(2)}$ defined as a function of its conjugate strain so-called Green-Lagrange strain tensor $\bar{\boldsymbol{E}}^{(2)}$:

$$\bar{\boldsymbol{T}}^{(2)} = \bar{\boldsymbol{T}}^{(2)}\left(\bar{\boldsymbol{E}}^{(2)}(t)\right). \tag{4.15}$$

This strategy leads to a complex definition of the RVE boundary conditions which are classically written in terms of the macroscopic gradient deformation tensor. In a planar setting, $\overline{\boldsymbol{E}}^{(2)}$ is a symmetric tensor whose component are: $\overline{E}_{11}$, $\overline{E}_{12}=\overline{E}_{21}$, $\overline{E}_{22}$ and, as a consequence, a numerical data point based on the macroscopic Green-Lagrange strain tensor can be parametrized on a three-dimensional space leading to a lower computational effort compared to the first strategy. However, the complexity involved in the imposition of boundary conditions makes this strategy unsuitable.

iii) the third strategy is based on the space of the macroscopic right stretch tensor $\overline{\boldsymbol{U}}$ defined as a function of a restricted First-Piola Kirchhoff stress tensor $\overline{\boldsymbol{T}}_R^{'}$ leading to the extraction of the so-called reduced database:

$$\overline{\boldsymbol{T}}_R^{'}=\overline{\boldsymbol{T}}_R^{'}\left(\overline{\boldsymbol{U}}(t)\right). \tag{4.16}$$

This strategy is able to take the advantages of the first two proposed strategies, overcoming their complexities, by exploiting the objectivity property of the macroscopic strain energy function $\overline{W}$ and stating that the constitutive properties of the homogenized material are not influenced by the rotational part of the macroscopic deformation. This statement is based on the following relation [98]:

$$\overline{W}(\overline{\boldsymbol{Q}}\overline{\boldsymbol{F}})=\overline{W}(\overline{\boldsymbol{F}}) \quad \forall\overline{\boldsymbol{Q}}\in Orth^{+}\ , \tag{4.17}$$

where $\overline{W}$ is defined as:

$$\overline{W}=\frac{1}{\left|V_{(i)}\right|}\int_{V_{(i)}}W\left(\boldsymbol{X},\boldsymbol{F}\right)dV \tag{4.18}$$

and $\bar{\boldsymbol{Q}}$ is an arbitrary proper orthogonal tensor. Eq. (4.17) is a direct consequence of the assumed objectivity of W and leads to the following form of the constitutive law:

$$\bar{\boldsymbol{T}}_{\boldsymbol{R}}(\bar{\boldsymbol{F}}) = \bar{\boldsymbol{R}}\bar{\boldsymbol{T}}'_R(\bar{\boldsymbol{U}}) \ , \tag{4.19}$$

where $\bar{\boldsymbol{T}}_R'$ is the restriction of $\bar{\boldsymbol{T}}_{\boldsymbol{R}}(\bar{\boldsymbol{F}})$ to positive-definite symmetric tensors (Psym), $\bar{\boldsymbol{U}}$ is the macroscopic right stretch tensor involved with the polar decomposition $\bar{\boldsymbol{F}} = \bar{\boldsymbol{R}}\bar{\boldsymbol{U}}$ and $\bar{\boldsymbol{R}}$ is the macroscopic rotation tensor. Since the response function $\bar{\boldsymbol{T}}_{\boldsymbol{R}}(\bar{\boldsymbol{F}})$ is completely determined by its restriction to positive-definite symmetric tensors, during the database creation phase we can assume that $\bar{\boldsymbol{R}} = \boldsymbol{I}$ and $\bar{\boldsymbol{F}} = \bar{\boldsymbol{U}}$ in order to determine the restricted response function $\bar{\boldsymbol{T}}'_R(\bar{\boldsymbol{U}})$. Definitely, in a planar setting, $\bar{\boldsymbol{U}}$ is a symmetric tensor whose component are: $\bar{U}_{11}$, $\bar{U}_{12} = \bar{U}_{21}$, $\bar{U}_{22}$ and, as a consequence, the reduced database can be parametrized on a three-dimensional space by using spherical coordinates .

The third strategy represents the most suitable for a greater computational savings. As shown in Fig. 4.6, the three-dimensional strain space,

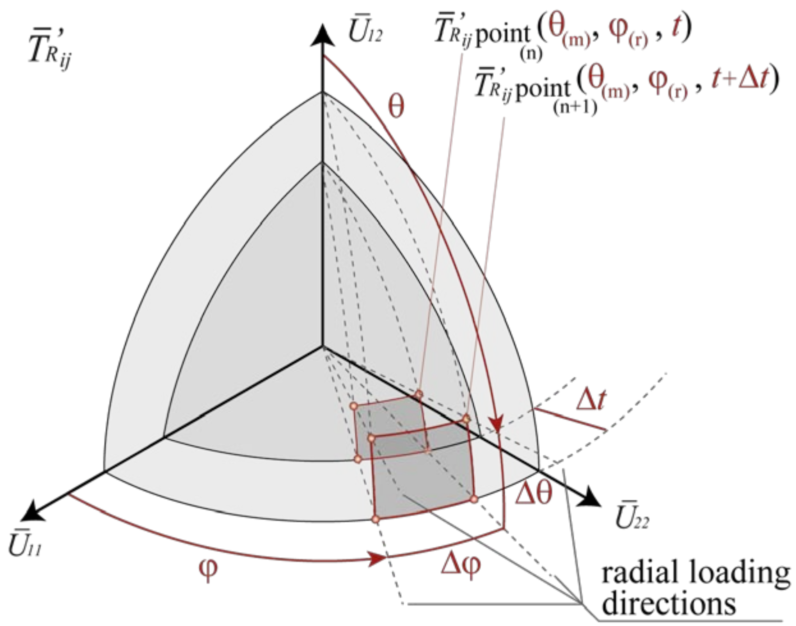

Fig. 4.6 A $\overline{U}_{11}$-$\overline{U}_{12}$-$\overline{U}_{22}$ strain space parametrized by spherical coordinates and leading to radial loading paths.

defined by the axis $\overline{U}_{11}$, $\overline{U}_{12}$ and $\overline{U}_{22}$, is scanned fixing the radial direction (by varying θ from 0° to 180° and φ from 0° to 360°) and incrementing the time-like parameter t. The macroscopic right stretch tensor given as input at the RVE boundary value problem is defined by the following matrix:

$$\overline{\boldsymbol{U}}(t)=\begin{bmatrix} 1+t\cos\varphi\sin\theta & t\cos\theta & 0 \\ t\cos\theta & 1+t\sin\varphi\sin\theta & 0 \\ 0 & 0 & 1 \end{bmatrix}. \tag{4.20}$$

Each point corresponding to the restricted macroscopic first Piola-Kirchhoff stress is evaluated in a time step t of the imposed radial loading path. The reduced database representing the nonlinear homogenized

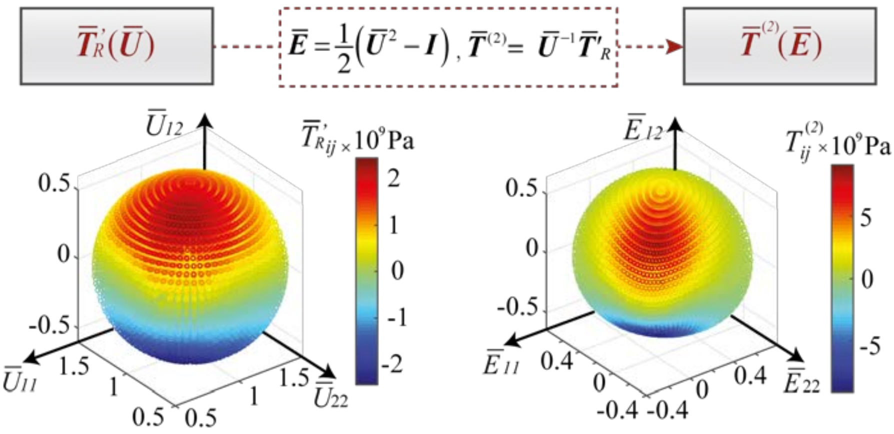

Fig. 4.7 Example of reduced database transformation.

constitutive law can be hence extracted by imposing an appropriate number of radial loading paths and time step (Δt). The database extraction procedure was implemented via a MATLAB script integrated with the finite element code COMSOL Multiphysics 5.4 by means of a parametric sweep able to swept θ and φ through a prefixed range of values. Since the variational formulation of the adopted numerical environment is written in terms of the second Piola-Kirchhoff stress, $\bar{\boldsymbol{T}}^{(2)}=\bar{\boldsymbol{F}}^{-1}\bar{\boldsymbol{T}}_R$. and the Green-Lagrange strain, $\bar{\boldsymbol{E}}=(\bar{\boldsymbol{F}}^T\bar{\boldsymbol{F}}-\boldsymbol{I})/2$, before linking the reduced database to the noncritical subdomains, a database transformation step is needed. For this reason, the previously discussed reduced database must be transformed using the following relations:

$$\bar{\boldsymbol{E}}=\frac{1}{2}\left(\bar{\boldsymbol{U}}^2-\boldsymbol{I}\right), \tag{4.21}$$

$$\bar{\boldsymbol{T}}^{(2)}=\bar{\boldsymbol{U}}^{-1}\bar{\boldsymbol{T}}'_R, \tag{4.22}$$

leading to a work-conjugated stress/strain database function of $\bar{\boldsymbol{E}}$ and $\bar{\boldsymbol{T}}^{(2)}$, as shown in Fig. 4.7. It worth noting that the obtained macroscopic stress will be also used to compute the tangent constitutive matrix by using the following relation:

$$\overline{\boldsymbol{C}}^{(2)} = \frac{\partial \overline{\boldsymbol{T}}^{(2)}}{\partial \overline{\boldsymbol{E}}}, \tag{4.23}$$

where $\partial \overline{\boldsymbol{T}}^{(2)} / \partial \overline{\boldsymbol{E}}$ is a fourth-order tensor whose component are $\overline{C}^{(2)}_{ijhk} = \partial \overline{T}^{(2)}_{ij} / \partial \overline{E}_{hk}$. The transformed database is implemented by means of an external material routine and a linear interpolation function is adopted to interpolate the macro-stress/macro-strain database that is loaded in the model as unstructured file data in which the values of the function are matched in a discrete generic point cloud.

4.3 Numerical microscopic stability analysis

The above described multiscale approaches are here adopted in order to compute sequentially the principal solution path for the macroscopic models and the minimum eigenvalue of the microscopic structural stability functional, respectively, with the aim to perform the microscopic stability analysis of microstructured solids as described in Section 4.2. The multiscale strategies have been applied to differently arranged fiber-reinforced composite materials subjected to quasi-static and monotonically increasing macroscopic loads, in order to investigate their effectiveness in terms of both numerical accuracy and computational efficiency. Three numerical examples have been considered, the first one , reported in Section 4.3.1, being solved by means of the semi-concurrent multiscale approach described in Section 4.2.1 and the latter two, in Section 4.3.2, being analyzed via the novel hybrid hierarchical/concurrent multiscale strategy described in Section 4.2.2.

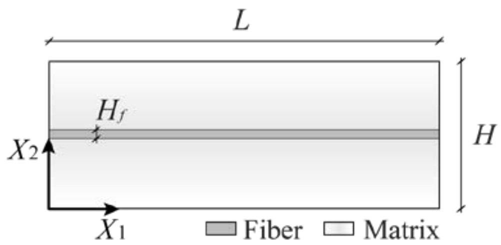

Fig. 4.8 Microgeometrical arrangement of periodic RVE corresponding to a unidirectional fiber reinforced composite material. The gray area represents the soft material (matrix) and the gray area represent the stiff material (fiber).

4.3.1 Application of the semi-concurrent multiscale approach

The first multiscale application considers a composite material reinforced with continuous fibers arranged according to a unidirectional pattern. The associated layered microstructure is made of two sequentially repeated homogeneous layers, the thinner one representing the reinforcement and the other standing for the matrix, and it is characterized by the periodic unit cell sketched in Fig. 4.8. Moreover, the material interface between the two bulk phases is assumed to be perfect, meaning that no displacement discontinuity is allowed to occur. The constitutive law associated to the microscopic constituents is the neo-Hookean one and the corresponding strain energy density for plane strain deformations is of the following form:

$$W = \frac{\mu}{2}\left[F_{\alpha\beta}F_{\alpha\beta} - 2 - 2\ln J'\right] + \frac{k-\mu}{2}\left(J'-1\right)^2 \quad \alpha,\beta = 1,2 \tag{4.24}$$

where J' is the determinant of the 2D deformation gradient tensor whose components are $F_{\alpha\beta}$, μ is the shear modulus of the solid at zero strain and the parameter k plays the role of an equivalent 2D bulk mod-

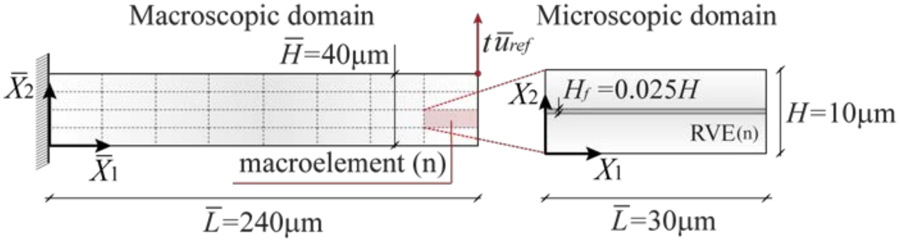

Fig. 4.9 A cantilever composite beam reinforced with continuous fibers and subjected to concentrated vertical force at the free end of the beam leading to a macroscopic displacement $t\bar{u}_{ref}$.

ulus governing the material compressibility. The dimensions of the considered unit cell in the X_1 and X_2 directions (in the reference configuration), denoted as L and H, are chosen such that their ratio L/H is equal to 3 and L is equal to 30 μm, whereas the thickness of the fiber (i.e. the reinforcement layer), indicated with H_f, is set as $0.025H$, associated with a fiber volume fraction of 2.5%. The dimension of the macroscopic model in the $\bar{X}_1$ and $\bar{X}_2$ directions are $\bar{L} = 240$ μm and $\bar{H} = 40$ μm, respectively. The relative stiffness ratio μ_f / μ_m between fiber and matrix is assumed to be equal to 200, with $\mu_m = 807$ MPa, being the shear modulus at zero strain of the matrix material. The bulk modulus is defined by k and is assumed to be equal to 10 μ for both materials.

As shown in Fig. 4.9, the coupled-volume multiscale approach has been implemented to model a cantilever composite beam reinforced with continuous fibers and subjected to concentrated vertical force at the free end of the beam leading to a macroscopic displacement $t\bar{u}_{ref}$ with $\bar{u}_{ref} = 1$ μm. A convergence analysis, reported in Fig. 4.10, to the RVE size has been incorporated in the numerical procedure to assess the local

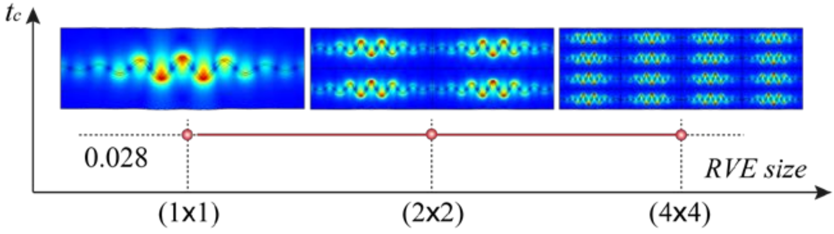

Fig. 4.10 Convergence analysis to the RVE size incorporated in the numerical procedure.

nature of the instability mode and, as a consequence, to verify the correspondence between the repeated unit cell (RUC) and the representative volume element (RVE).

The microscopic instability critical load factor has been firstly evaluated by means of a graphical extrapolation on a force-displacement curve and, successively, by means of a rigorous microscopic stability analysis following the theoretical development reported in Section 4.1. To evaluate the accuracy and the effectiveness of the adopted multiscale model, the obtained results have been compared with the stability analysis performed on a direct numerical model based on the explicit discretization of the heterogeneities of the composite microstructure. In Fig. 4.11 the macroscopic multiscale model (MNS) is reported together with their linked microscopic representative volume elements (32 RVEs) giving also more information about the mesh discretization and number of degrees of freedom involved (DOFs). Specifically, the adopted mesh of the macroscopic model involves 32 bilinear rectangular macroelements and 90 degrees of freedom, while the microscopic RVEs involves 2,160 bilinear rectangular elements and 4,592 degrees of freedom. In the figure is shown also the deformed configuration at the onset of microscopic instability induced by critical load factor t_c^{MNS}

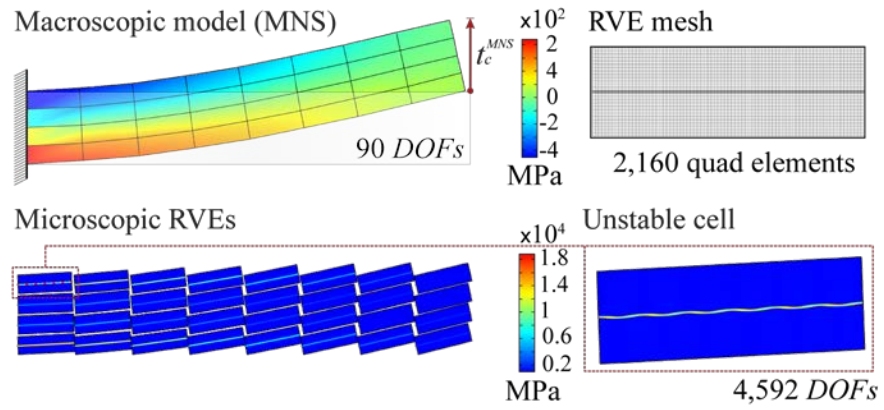

Fig. 4.11 Multiscale numerical simulations (MNS) on a cantilever beam at the onset of microscopic instability corresponding to the critical load factor t_c^{MNS}

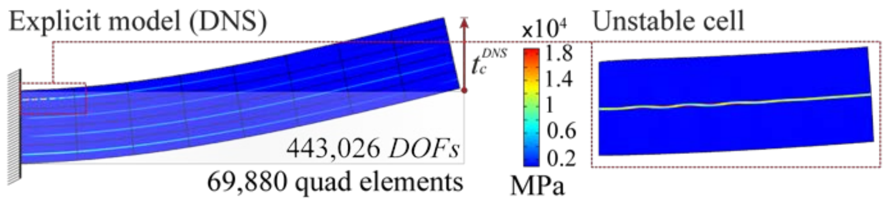

Fig. 4.12 Direct numerical simulations (DNS) on a cantilever beam at the onset of microscopic instability corresponding to the critical load factor t_c^{DNS} .

and leading to a macroscopic vertical displacement $\bar{u}(t_c^{MNS}) = t_c^{MNS}\bar{u}_{ref}$. In Fig. 4.12 the explicit model of the direct numerical simulation (DNS) is reported giving information about the number of degrees of freedom and showing the deformed configuration at the onset of the microscopic instability induced by critical load factor t_c^{DNS} and leading to a macroscopic vertical displacement $\bar{u}(t_c^{DNS}) = t_c^{DNS}\bar{u}_{ref}$. Specifically, the adopted mesh involves 69,880 bilinear rectangular elements and 443,026 degrees of freedom.

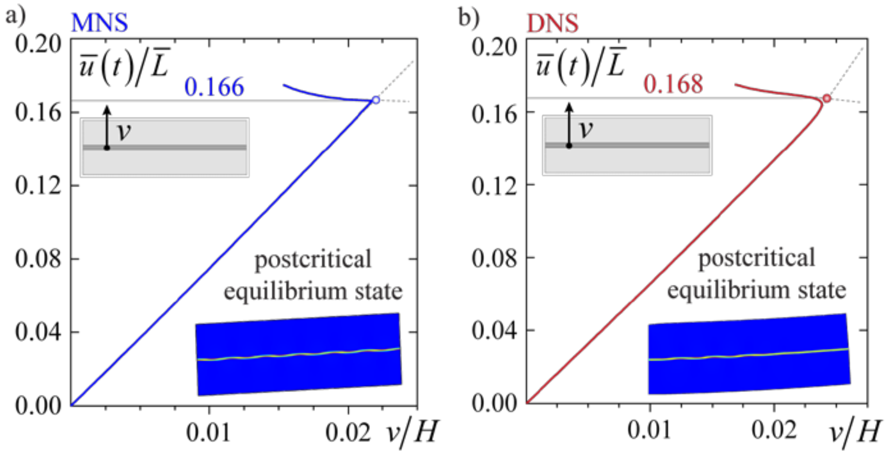

Fig. 4.13 Comparison between the graphical extrapolation of the instability critical load factor of a cantilever beam obtained by using a multiscale numerical simulation a) and a direct numerical simulation b).

It is worth noting that both analyses predict the same cell (i.e. the upper left one) as the critical cell undergoing local instability.

The graphic extrapolation of the critical load factors based on both the numerical models are reported in Fig. 4.13, in which on the left side (Fig. 4.13a) the results of a multiscale numerical simulation (MNS) are shown, while on the right side (Fig. 4.13b) the results of a direct numerical simulation (DNS) are shown. The force-displacement curve was obtained by plotting on the x-axis the local vertical displacement v at the fiber-matrix interface of the most compressed unit cell involved by local instability, normalized with respect to the height of the unit cell H (v / H) and by plotting on the y-axis the macroscopic vertical displacement $\bar{u}(t)$ normalized with respect to the macroscopic model length $\bar{L}$ ($\bar{u}(t) / \bar{L}$). With reference to Fig. 4.13a, the normalized critical load factor obtained by using the semiconcurrent multiscale method is equal to $\bar{u}(t_c^{MNS}) / \bar{L} = 0.164$ leading to a critical load factor $t_c^{MNS} = 39.8$; while

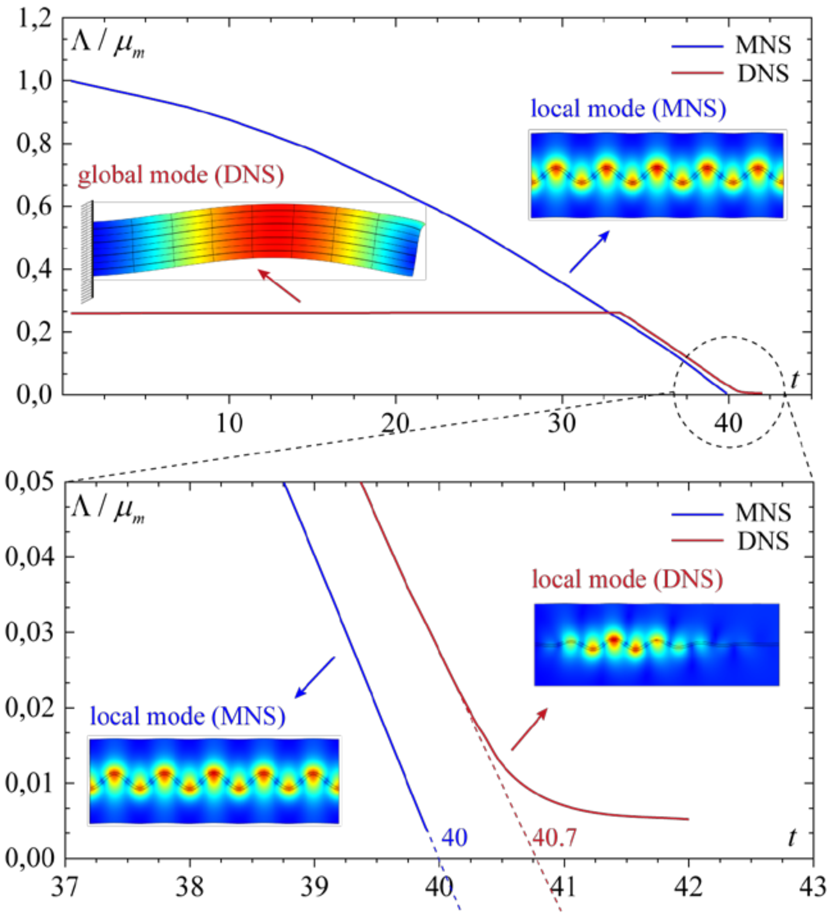

Fig. 4.14 Normalized minimum eigenvalue plotted as a function of the time-like parameter t giving the critical load factor extracted by means of a rigorous microscopic instability analysis on a cantilever beam.

with reference to Fig. 4.13b, the normalized critical load factor obtained by using an explicit discretization of the heterogeneous microstructure is equal to $\overline{u}(t_c^{DNS})/\overline{L} = 0.168$ leading to an instability critical load factor $t_c^{MNS} = 40.3$. Comparing the results in terms of percent variance that is defined by the following relation:

$$e\% = \frac{t_c^{\mathrm{MNS}} - t_c^{\mathrm{DNS}}}{t_c^{\mathrm{DNS}}}\%, \tag{4.25}$$

a relative percentage error equal to -1.24% is obtained. It confirms a good numerical accuracy of the adopted multiscale approach. Subsequently, as shown in Fig. 4.14, the critical load factors have been evaluated also by performing a microscopic stability analysis, comparing also the related mode shapes. The figure clearly shows that, with reference to the direct numerical analysis (blue line), a global instability mode is related to low value of the load, highlighting the competition between global and local instability modes at increasing load factor. On the contrary, with reference to a multiscale numerical simulation based on the semiconcurrent multiscale approach (red line), the same behavior is not captured since this set of semiconcurrent approaches is not able to evaluate boundary layer effect given by external constraints. In addition, as can see in the zoom of the below side of the figure, it worth noting that the minimum eigenvalue tends to zero without attaining this value, due to the presence of imperfections, and a linear extrapolation technique has been adopted to obtain this estimation. Specifically, respectively for the semiconcurrent multiscale numerical simulation and the direct numerical simulation, the following critical load factors have been estimated $t_c^{\mathrm{MNS}} = 40$ and $t_c^{\mathrm{DNS}} = 40.7$. To summarize, resulting a relative percentage error less than 2% ($e\% = -1.72\%$), both the methods highlight a good prediction of the critical load factor in the case of microscopic instability, but the same accuracy is not exhibited in the prediction of the instability mode shapes because of the difficulty of the semiconcurrent multiscale approaches to account for boundary layer effects.

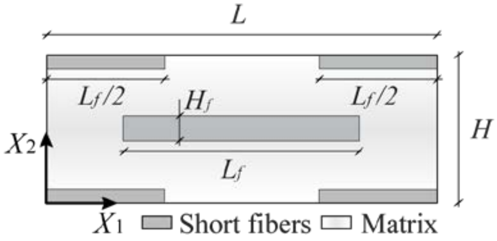

Fig. 4.15 Microgeometrical arrangement of periodic RVE corresponding to a discontinuously fiber reinforced composite material with a staggered pattern. The gray area represents the soft material (matrix) and the gray area represent the stiff material (short fibers).

4.3.2 Application of the hybrid multiscale approach

The two following multiscale applications considers a composite material reinforced with discontinuous fibers arranged according to a staggered pattern. The associated microstructure, characterized by the periodic unit cell sketched in Fig. 4.15, is made of two materials, the stiffer one representing the reinforcements in the form of elongated particles or short fibers and the softer one standing for the matrix. The constitutive law characterizing the mechanical behavior of the microconstituent is the same of the first application reported in Section 4.3.1, see Eq.(4.24), together with the associated material parameters. The dimensions of the considered unit cell in the X_1 and X_2 directions are denoted respectively by $H = 100 \cdot \left(2 \cdot L_f \cdot H_f\right) / \left(L \cdot V_f\right)$ and $L = 400\ \mu\text{m}$, whereas the length of the short fibers is indicated with $L_f = 0.7L$ and the thickness is denoted by $H_f = L_f / 50$, associated with a fiber volume fraction of 12%. The dimensions of the macroscopic model in the $\overline{X}_1$ and $\overline{X}_2$ directions are $\overline{L} = 6400\ \mu\text{m}$ and $\overline{H} = 915\ \mu\text{m}$, respectively. The relative stiffness ratio μ_f / μ_m between fiber and matrix is assumed to

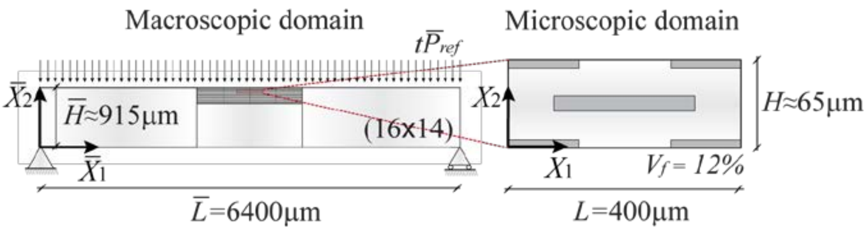

Fig. 4.16 A simply support composite beam reinforced with staggered discontinuous fibers and subjected to a distributed load $t\overline{P}_{ref}$.

be equal to 20, with $\mu_m = 807$ MPa, being the shear modulus at zero strain of the matrix material. The matrix bulk modulus is defined by $k_m = 2\mu_m$ and the fiber bulk modulus is defined by $k_f = 10\mu_f$.
In the first application, reported in Fig. 4.16, the novel hybrid multiscale approach has been implemented to model a simply supported beam reinforced with staggered discontinuous fibers and subjected to a distributed load on the whole elongation of the beam equal to $t\,\overline{P}_{\mathrm{ref}}$ with $P_{\mathrm{ref}} = 1\,e^7$ N/m .
As in the previous application of Section 4.3.1, the microscopic instability critical load factor has been firstly evaluated by means of a graphical extrapolation on a force-displacement curve and, successively, by means of a rigorous microscopic stability analysis comparing then both the results with a direct numerical simulation.
The macroscopic multiscale model (MNS) is reported in Fig. 4.25 together with the number of degrees of freedom contained in the model: 80,564. In the figure is shown also the deformed configuration at the onset of microscopic instability induced by a macroscopic distributed load $t_c^{MNS}\overline{P}_{ref}$. In Fig. 4.26 the explicit model (DNS) is reported in the deformed configuration at the onset of the microscopic instability that is induced by a macroscopic distributed load $t_c^{DNS}\overline{P}_{ref}$. As expected, by

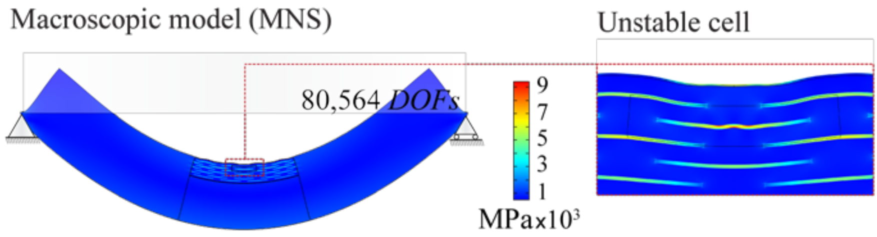

Fig. 4.17 Multiscale numerical simulations (MNS) on a simply supported beam at the onset of microscopic instability corresponding to the critical load factor t_c^{MNS}.

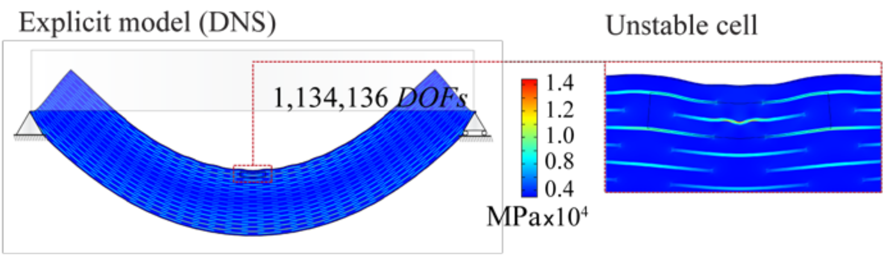

Fig. 4.18 Direct numerical simulations (DNS) on a simply supported beam at the onset of microscopic instability corresponding to the critical load factor t_c^{DNS}.

using an explicit discretization of the microstructure a considerably high number of degrees of freedom is involved: 1,134,136 leading to unpracticable computational cost.

The critical load factors are firstly determined by means a graphic extrapolation performed on the force-displacement curves. Fig. 4.19 illustrates the graphic extrapolations performed respectively on the multiscale model, Fig. 4.19a, and on the direct model, Fig. 4.19b. On the x-axis is plotted the displacement $v^* = v - v_{mean}$ normalized with respect to the height of the unit cell H (v^*/H), whereas on the y-axis is plotted

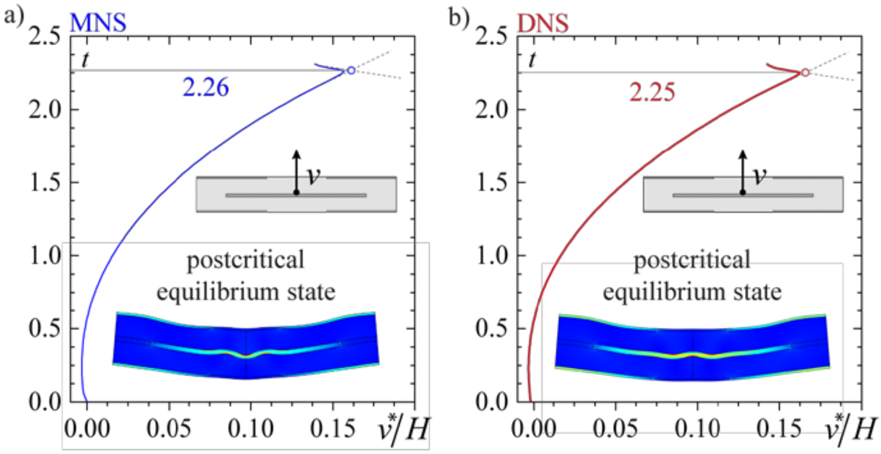

Fig. 4.19 Comparison between the graphical extrapolation of the instability critical load factor of a simply supported beam obtained by using a multiscale numerical simulation a) and a direct numerical simulation b).

the load factor t; where v represents the vertical displacement the fiber-matrix interface of the most compressed unit cell involved by local instability and v_{mean} represents the mean of the vertical displacement in the midsection of the beam.

With reference to Fig. 4.19a, the critical load factor obtained by using the hybrid multiscale method is equal to $t_c^{\mathrm{MNS}} = 2.26$; while with reference to Fig. 4.19b, the critical load factor obtained by using an explicit discretization of the heterogeneous microstructure is equal to $t_c^{\mathrm{DNS}} = 2.25$, leading to a relative percentage error equal to $e\% = 0.44\%$. The good agreement between MNS and DNS results confirms the good accuracy of the hybrid multiscale method proposed in the determination of the local instability critical load factor in discontinuously reinforced composite materials subjected to large deformations. To investigate deeply the accuracy of the proposed multiscale method the critical load factors have been evaluated also by performing a rigorous microscopic

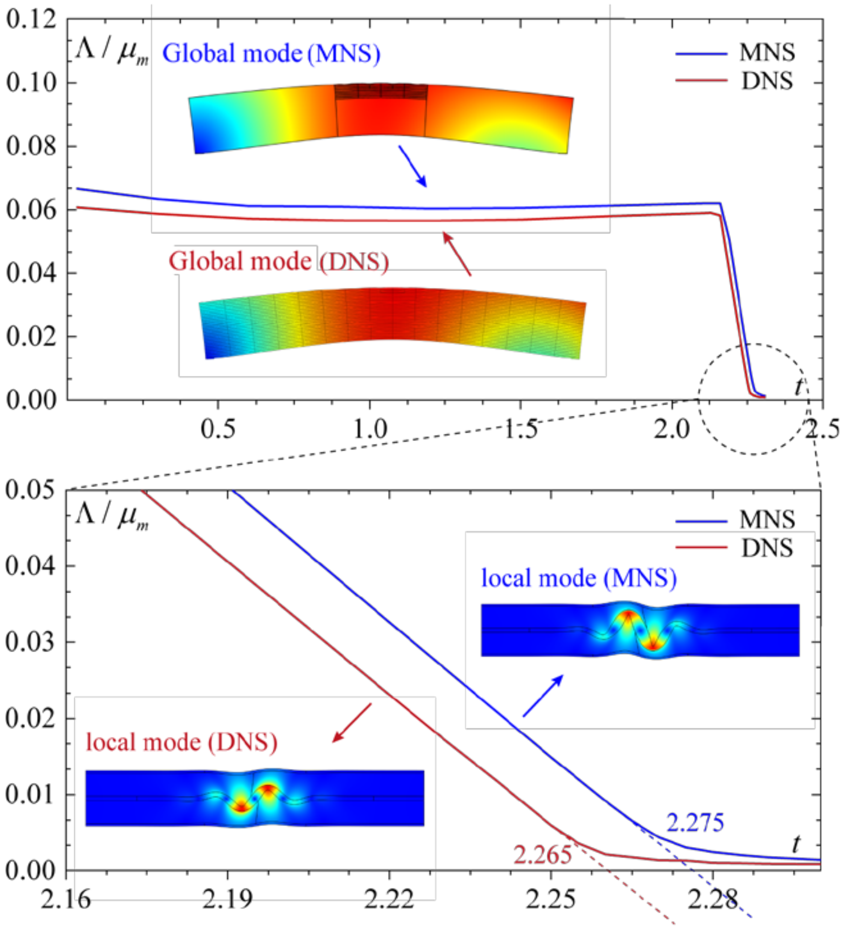

Fig. 4.20 Normalized minimum eigenvalue plotted as a function of the time-like parameter t giving the critical load factor extracted by means of a rigorous microscopic instability analysis on a simply supported beam.

stability analysis, reported in Fig. 4.20, comparing also the related critical mode shapes.

From this figure it can be seen that, contrarily to the first application, with reference to both the direct numerical analysis (blue line) and the multiscale numerical analysis (red line) a global instability mode is obtained at low value of the load, highlighting in the both cases the competition between global and local instability modes at increasing load factor and the good agreement between the shape of the global critical modes.

In this application, also, it worth noting that the obtained local mode shapes are perfectly coincident and that the minimum eigenvalues tend to zero without attaining this value, due to the presence of imperfections. Thus, a linear extrapolation technique has been adopted obtaining the following critical load factor estimations: $t_c^{\mathrm{MNS}} = 2.275$ and $t_c^{\mathrm{DNS}} = 2.265$. With a relative percentage error equal to $e\% = 0.44\%$, both the investigated methods highlight a very good prediction of the critical load factor in the case of microscopic instability and a very good prediction of the critical instability mode shape, showing a more pronounced accuracy in the capturing of the local instability mode than the global ones. These results demonstrate that the proposed hybrid multiscale method, contrarily to the semiconcurrent method, is able to account for boundary layer effects leading to more accurate results.

In the second application, reported in Fig. 4.21, to further investigate the accuracy of the proposed multiscale approach under different loading conditions, the hybrid strategy has been implemented to model a clamped plate reinforced with staggered discontinuous fibers and subjected to a concentrated load acting on the top boundary in correspondence of the midsection of the plate. The dimension of the considered unit cell in X_1 and X_2 directions are denoted as $L = 100 \cdot \left(2 \cdot L_f \cdot H_f\right) / \left(L \cdot V_f\right)$ and $H = 400\mu\mathrm{m}$, where $L_f = 0.7L$ represents the length of the short fibers, $H_f = L_f / 50$ represent the thickness of the fibers, whereas $V_f = 7\%$ represents the volume fraction of the

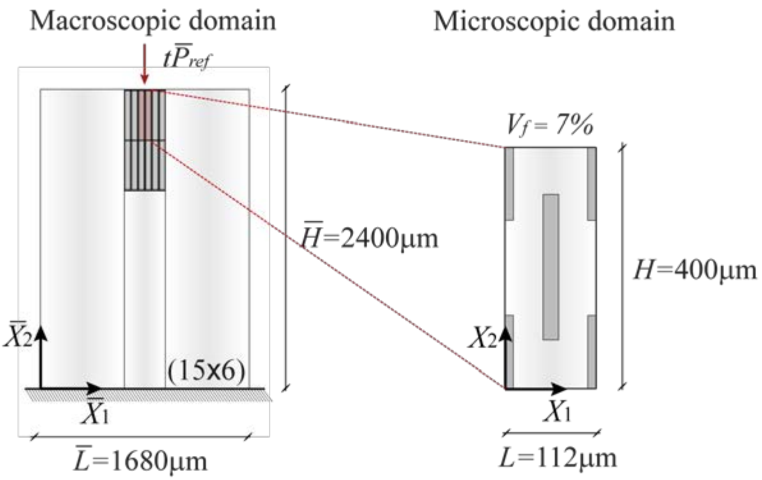

Fig. 4.21 A clamped plate composite beam reinforced with staggered discontinuous fibers and subjected to a concentrated load $t\overline{P}_{ref}$ acting in the middle of the plate.

stiffer phase. The dimensions of the macroscopic model in the $\overline{X}_1$ and $\overline{X}_2$ directions are $\overline{L} = 1680$ μm and $\overline{H} = 2400$ μm, respectively
The relative stiffness ratio μ_f / μ_m between fiber and matrix is assumed to be equal to 10, with $\mu_m = 807$ MPa, being the shear modulus at zero strain of the matrix material. The bulk modulus is defined by k and is assumed to be equal to 10 μ for both materials.
It worth noting that, if a material consisting of a thin stiff layer and a softer substrate is subjected to a sufficiently large compressive load, a buckling or wrinkling surface instability can occur, as shown in [172]. Because of the interest in the microscopic instability of the short fibers embedded in a soft matrix, to avoid this type of instability, a thin stiffer layer has been inserted on the top of the plate. The thickness of the layer is equal to $H_f / 2$ and the material is characterized by linear elastic constitutive response with elastic modulus equal to 200GPa and $\upsilon = 0$.

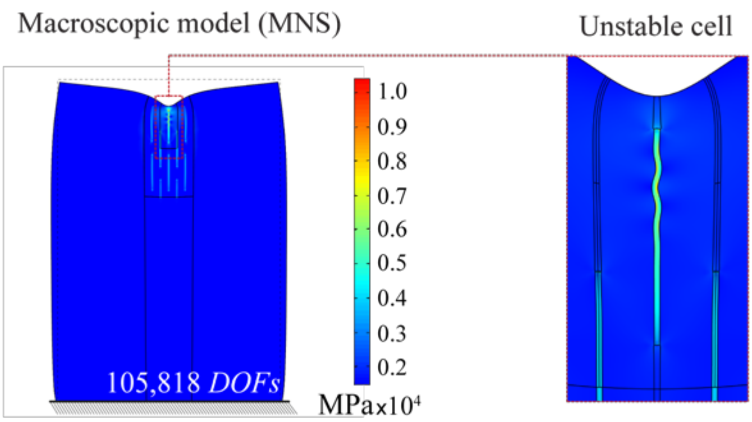

Fig. 4.22 Multiscale numerical simulation (MNS) on a clamped plate at the onset of microscopic instability corresponding to the critical load factor t_c^{MNS}.

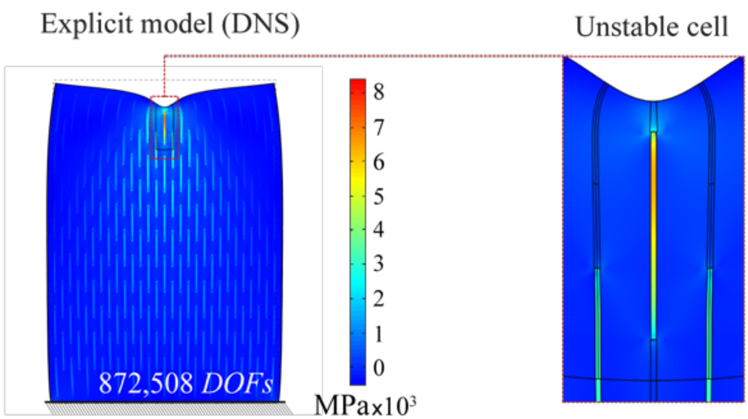

Fig. 4.23 Direct numerical simulation (DNS) on a clamped plate at the onset of microscopic instability corresponding to the critical load factor t_c^{DNS}.

The deformed configurations corresponding to the onset of microscopic instability obtained by means of a multiscale numerical simulation (MNS) and by means of a direct numerical simulation (DNS) are respectively reported in Fig. 4.22 and Fig. 4.23. Also in this application,

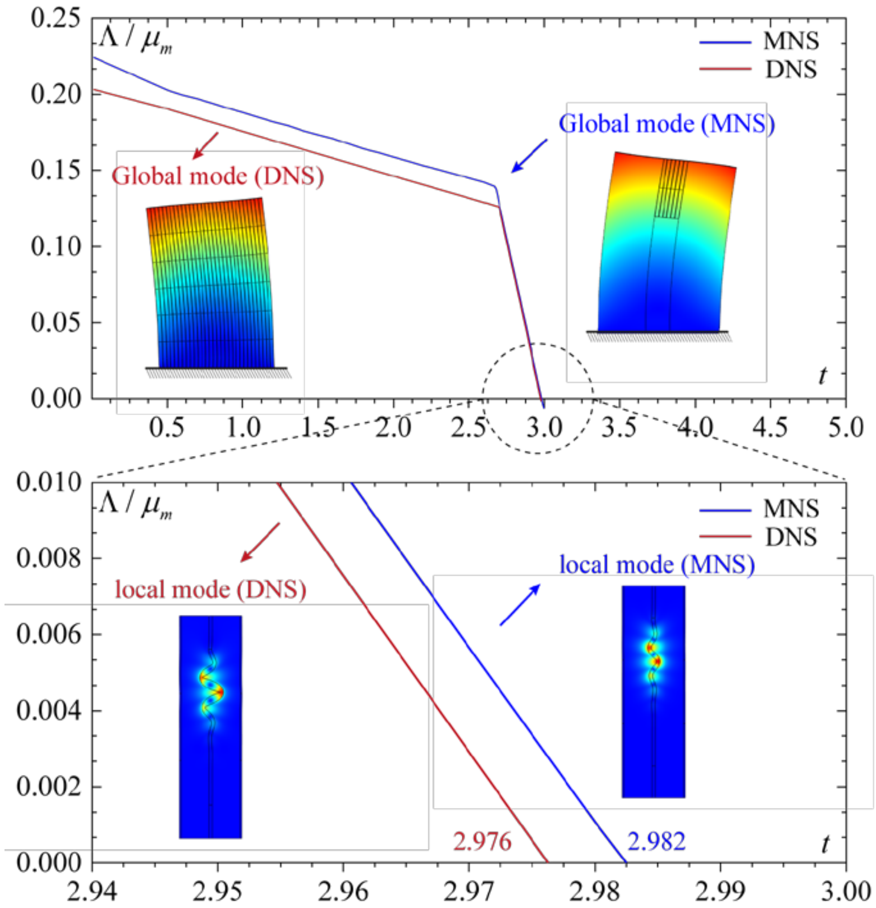

Fig. 4.24 Normalized minimum eigenvalue plotted as a function of the time-like parameter *t* giving the critical load factors extracted by means of a rigorous microscopic instability analysis on a clamped plate.

it is clearly highlighted that the adopted hybrid multiscale approach leads to a model with a lower number of DOFs and, as a consequence, it leads to a lower computational effort. Specifically, the multiscale

model is characterized by 105,818 DOFs, whereas the explicit model is characterized by more than 8 times the number of multiscale DOFs.
The microscopic instability critical load factors, reported in Fig. 4.24, have been evaluated by means a microscopic stability analysis comparing also the related critical mode shapes for low and high values of the load. The following results are obtained respectively by using a multiscale numerical simulation (MSN), $t_c^{\mathrm{MNS}} = 2.976$, and a direct numerical simulation (DNS), $t_c^{\mathrm{DNS}} = 2.982$, leading to a relative percentage error equal to $e\% = 0.2\%$. Also in this application, the critical mode shapes, obtained by means of a MSN and a DNS, are perfectly coincident, thus, it demonstrates again the good accuracy of the proposed hybrid multiscale method in the prediction of the local and global mode shapes.
Definitely, the obtained results are in good agreement with that obtained above in the first hybrid multiscale application, leading to the consideration that the proposed hybrid multiscale approach has been shown more effective than the semiconcurrent approach for obtaining accurate prediction of the critical load levels associated to microscopic instabilities and the related critical mode shapes, being able to account for effectively the boundary layer effect and, as a consequence, the competition between global and local critical mode shapes during the loading phase.

4.4 Investigation of the mechanical behavior of bio-inspired nacre-like composite materials

A numerical investigation of the mechanical behavior of staggered composites characterized by a bio-inspired nacre-like microstructure in a large deformation context is here performed. The bio-inspired materials, combining stiff and soft constituents at different length scales, exhibit superior mechanical properties in comparison with conventional materials, for instance, the capacity to withstand significant stress and deformation providing high load-carrying capacity and stiffness. These results are focused on the prediction of both penetration resistance and flexibility of the composite material. To this end, the previously developed hybrid hierarchical/concurrent multiscale method has been here employed, being able to perform several parametric nonlinear analyses with very high numerical accuracy and low computational cost. In detail, several results, giving more information about the influence of the main microstructural parameters on the macroscopic mechanical behavior, were obtained deducing how the main geometrical parameters (i.e. platelets aspect ratio and volume fraction) of inclusions can be manipulated to enhance the overall protecto-flexibility of bio-inspired nacre-like composites.

4.4.1 Theoretical background of the RVE problem

To describe the finite deformation of a continuous body, we introduce the position vectors $\boldsymbol{X}$ and $\boldsymbol{x}$, corresponding to the reference (undeformed) and deformed configuration, respectively. Each point of the undeformed configuration at the time t, has position $\boldsymbol{x}$ given by $\boldsymbol{x}=\boldsymbol{x}(\boldsymbol{X},t)$. The relation between $\boldsymbol{X}$ and $\boldsymbol{x}$ is defined by $\boldsymbol{x}(\boldsymbol{X},t)=\boldsymbol{u}(\boldsymbol{X},t)+\boldsymbol{X}$ in which $\boldsymbol{u}(\boldsymbol{X},t)$ is the displacement vector field and the deformation gradient tensor is defined as $\boldsymbol{F}\left(\boldsymbol{X},t\right)=\partial\boldsymbol{x}\left(\boldsymbol{X}\right)/\partial\boldsymbol{X}$. Then, the Jacobian $J\equiv\det\mathbf{F}$ defines the volume change of the body with respect the reference configuration. The constitutive behavior of a hyperelastic material can be described in terms of an objective strain energy-density function $W\left(\boldsymbol{X},\boldsymbol{F}\right)$ and hence, the first Piola-Kirchhoff stress tensor can be defined as

$$\boldsymbol{T}_R=\frac{\partial W\left(\boldsymbol{X},\boldsymbol{F}\right)}{\partial\mathbf{F}} \tag{4.26}$$

The corresponding Cauchy stress tensor and second Piola-Kirchhoff stress tensor are related to the first Piola-Kirchhoff stress tensor via $\boldsymbol{\sigma}=J^{-1}\mathbf{P}\mathbf{F}^T$ and $\boldsymbol{T}^{(2)}=\mathbf{F}^{-1}\boldsymbol{T}_R$, respectively. For a neo-Hookean material, the strain energy function is given as

$$W(\boldsymbol{F})=\frac{1}{2}\mu\left(I_1-3\right)-\mu\ln\left(J\right)+\frac{1}{2}\lambda\left[\ln(J)\right]^2 \tag{4.27}$$

where μ is the shear modulus of the material, $I_1=tr(\boldsymbol{C})$ is the first invariant of the right Cauchy-Green deformation tensor $\boldsymbol{C}=\boldsymbol{F}^T\boldsymbol{F}$, λ is the first Lamé parameter that is related to the bulk modulus k (modulus of compressibility) and to the shear modulus**.** Considering deformation applied quasi-statically and the absence of body forces, the equation of motion can be written in the undeformed configuration as

$$Div\boldsymbol{T}_R=\mathbf{0}\,. \tag{4.28}$$

Then, the homogenization problem for a heterogeneous solid, whose periodic microstructure consists of stiff rectangular platelets separated by thin layers of soft material (bio-inspired nacre-like composite material) is formulated in the following. The microstructural equilibrium problem is here formulated in terms of the deformation gradient ***F*** and of its conjugate stress measure $\boldsymbol{T_R}$ because is convenient in defining the

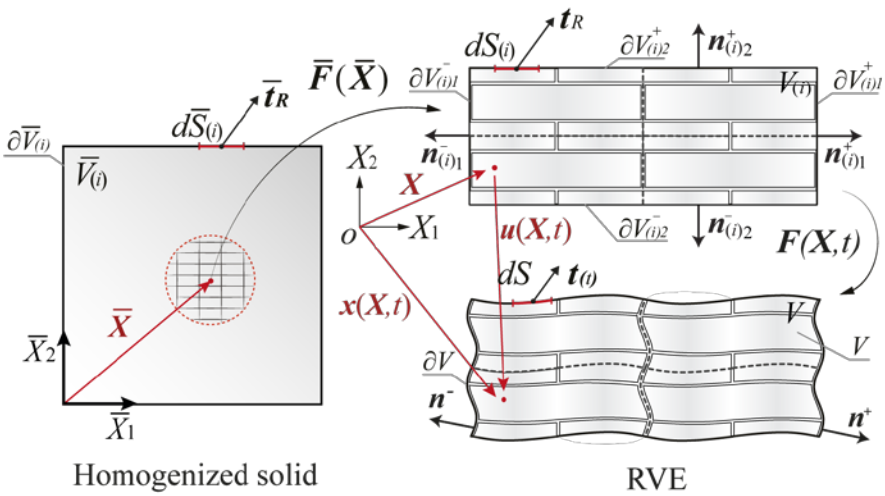

Fig. 4.25 2D Representation of the homogenized solid of a staggered composite material (on the left) and of its corresponding undeformed and deformed RVE configurations (on the right) attached to a generic macroscopic material point in the X_1-X_2 plane

essential boundary conditions (BCs) on the unit cell. With reference to Fig. 4.25 the volume of the homogenized solid denoted by $\bar{V}_{(i)}$ in the undeformed reference configuration is enclosed by the surface $\partial\bar{V}_{(i)}$, on which the first Piola–Kirchhoff traction vector $\bar{\boldsymbol{t}}_R$ acts (note that the subscript (i) is referred to variables in the initial configuration). The RVE is assumed to be associated with an infinitesimal neighborhood of a generic macroscopic material point $\bar{\boldsymbol{X}}$. Each microstructural constituent is characterized by an incrementally linear relationship between the first Piola-Kirchhoff stress rate tensor $\dot{\boldsymbol{T}}_{\boldsymbol{R}}$ and the deformation gradient rate tensor $\dot{\boldsymbol{F}}$ as follow: $\dot{\boldsymbol{T}}_{\boldsymbol{R}} = \boldsymbol{C}^{\boldsymbol{R}}(\boldsymbol{X},\boldsymbol{F})[\dot{\boldsymbol{F}}]$ in which $\boldsymbol{C}^{\boldsymbol{R}}(\boldsymbol{X},\boldsymbol{F})$ is the fourth-order tensor of nominal moduli satisfying the major symmetry condition ($C^R{}_{ijhk} = C^R{}_{hkij}$). This constitutive law is representative of a large class of rate-independent materials (including hyperelastic ones), and every loading process can be parametrized in terms of a time-like parameter t ≥ 0 monotonically increasing (t = 0 in the undeformed configuration).The rates of field quantities are evaluated as the derivatives with respect the parameter t that describes the quasi-static deformation path of the composite solid. The micro- and macro-scales can be coupled by the common relations that define the macroscopic first Piola-Kirchhoff stress tensor $\bar{\boldsymbol{T}}_R$ and the macroscopic deformation gradient $\bar{\boldsymbol{F}}$ as a function of boundary data of the traction field $\boldsymbol{t}_R$ and of the deformation field $\boldsymbol{x}(\boldsymbol{X},t)$, respectively:

$$\begin{aligned}\bar{\boldsymbol{T}}_R(t) &= \frac{1}{|V_{(i)}|}\int_{\partial V_{(i)}} \boldsymbol{t}_R(\boldsymbol{X},t)\otimes \boldsymbol{X}\,dS_{(i)}\\ \bar{\boldsymbol{F}}(t) &= \frac{1}{|V_{(i)}|}\int_{\partial V_{(i)}} \boldsymbol{x}(\boldsymbol{X},t)\otimes \boldsymbol{n}_{(i)}\,dS_{(i)}\end{aligned}, \tag{4.29}$$

in which $\otimes$ denotes the tensor product, $\boldsymbol{n}_{(i)}$ the outward normal at $\boldsymbol{X}\in\partial V_{(i)}$ and $\boldsymbol{t}_R=\boldsymbol{T}_R\boldsymbol{n}_{(i)}$ the nominal traction vector. In a macrostrain-driven loading regime it is assumed that the microscopic deformation field can be additively split into a linear part and a fluctuating part:

$$\boldsymbol{x}(\boldsymbol{X},t)=\bar{\boldsymbol{F}}(t)\boldsymbol{X}+\boldsymbol{w}(\boldsymbol{X},t) \tag{4.30}$$

where $\bar{\boldsymbol{F}}(t)\boldsymbol{X}$ is a linear displacement contribution and $\boldsymbol{w}(\boldsymbol{X},t)$ is the fluctuation field. Inserting the definition of the microscopic deformation field into the definition of the macroscopic deformation field, it provides an integral constraint that a microscopic displacement fluctuation field should satisfy to be kinematically admissible:

$$\int_{\partial V_{(i)}} \boldsymbol{w}\otimes\boldsymbol{n}_{(i)}\,dS_{(i)}=\boldsymbol{0}\,. \tag{4.31}$$

Then the macro-micro transition is achieved by imposing the appropriate boundary condition on the RVE displacement fluctuation field.

Hence, in accordance with the periodic nature of the staggered composite microstructure, periodic boundary displacement fluctuations can be imposed on the boundaries $\partial V_{(i)}$ of the RVE satisfying the previously mentioned integral constraint:

$$\boldsymbol{w}\left(\boldsymbol{X}^{+},t\right)=\boldsymbol{w}\left(\boldsymbol{X}^{-},t\right) \text{ on } \partial V_{(i)} \tag{4.32}$$

where the superscripts + and – denote pairs of opposite RVE boundary points. The imposed periodicity conditions are written as

$$\boldsymbol{T}_R\boldsymbol{n}_{(i)}\left(\boldsymbol{X}^{+},t\right)=-\boldsymbol{T}_R\boldsymbol{n}_{(i)}(\boldsymbol{X}^{-},t) \text{ on } \partial V_{(i)} \tag{4.33}$$

$$\boldsymbol{w}\left(\boldsymbol{X}^{+},t\right)=\boldsymbol{w}\left(\boldsymbol{X}^{-},t\right) \text{ on } \partial V_{(i)} \tag{4.34}$$

representing antiperiodic traction (4.33) and periodic deformation (4.34) imposed on the boundary of the RVE. Finally, the equilibrium boundary value problem at given macrodeformation gradient is governed by the following equations:

$$\begin{cases} Div\boldsymbol{T}_R=\boldsymbol{0} \text{ in } V_{(i)} \\ \boldsymbol{T}_R\boldsymbol{n}_{(i)}\left(\boldsymbol{X}^{+},t\right)=-\boldsymbol{T}_R\boldsymbol{n}_{(i)}(\boldsymbol{X}^{-},t) \text{ on } \partial \mathrm{V}_{(i)} \end{cases} . \tag{4.35}$$

Solving this boundary value problem, the macroscopic constitutive quantities that are essential to proceed with the stress-strain database determination can then be extracted by applying appropriate volume averages (4.29).

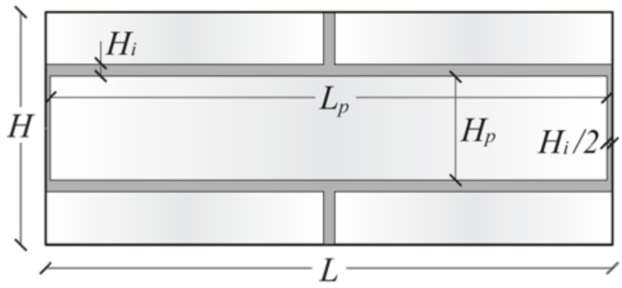

Fig. 4.26 2D Periodic microgeometrical arrangement of bio-inspired nacre-like composite. The white and gray areas represent the hard inclusions (platelets) and the soft interphase (matrix) respectively.

4.4.2 Numerical applications

The multiscale analysis technique described in Section 4.2.2 is here applied to analyze the penetration resistance and the flexibility of bio-inspired composites with nacre-like microstructure. The periodic unit cell shown in Fig. 4.26 describes the investigated representative volume element, containing hard platelets connected by soft matrix materials and arranged in an overlapping brick-and-mortar pattern.

The thickness of the matrix interphase is denoted with H_i, H and L denote the height and the length of the unit cell respectively, H_p and L_p denote the height and the length of platelets. With reference to [48], since linear elastic model can provide adequate approximation for material behavior for small strains (typically not exceeding 5%), the stiff platelets are modeled as linear elastic material with elastic modulus E_p = 1.8 GPa and Poisson's ratio υ = 0.42, while the soft interphase is modeled as nearly incompressible neo-Hookean material with initial shear modulus μ_i = 0.21 MPa (a bulk modulus equal to $1000\mu_i$ is adopted to simulate the incompressibility condition). The length of the platelets is L_p = 20 mm, the amount of hard inclusions in a unit cell is defined by:

$$v_f = \frac{\left(L_p H_p\right)}{\left(L_p + H_i\right)\left(H_p + H_i\right)} \tag{4.36}$$

and the platelets aspect ratio is defined by:

$$w = \frac{L_p}{H_p}. \tag{4.37}$$

Multiscale parametric analyses were performed to analyze the influence of the platelets volume fraction and the platelets aspect ratio on the flexibility and on the penetration resistance by varying the main microstructural geometrical parameters (v_f and w) with reference to the above described microstructure. The flexibility was investigated employing a three-point bending test on beams composed by a 14x4 unit cell assembly (column × row), as shown in Fig. 4.27a in which the real microstructure is introduced only in correspondence of the vertical concentrated load where the local effects are more intense. The penetration resistance was investigated employing an indentation test on a rectangular sample composed by a 6×4 unit cell assembly using a spherical indenter with radius equal to $L/4$, as shown in Fig. 4.27b.
Numerical simulations were performed using the finite element code COMSOL Multiphysics 5.4 considering a 2D system in plane-strain conditions applying displacement-controlled loadings in a quasi-static regime. The typical mesh adopted for the examined unit cell is of a structured type and involves quadratic Lagrangian quadrilateral elements. The contact condition between the indenter and the sample was modeled by a penalty method which is rather simple and robust, based on inserting a stiff spring bed, active only in compression, between the

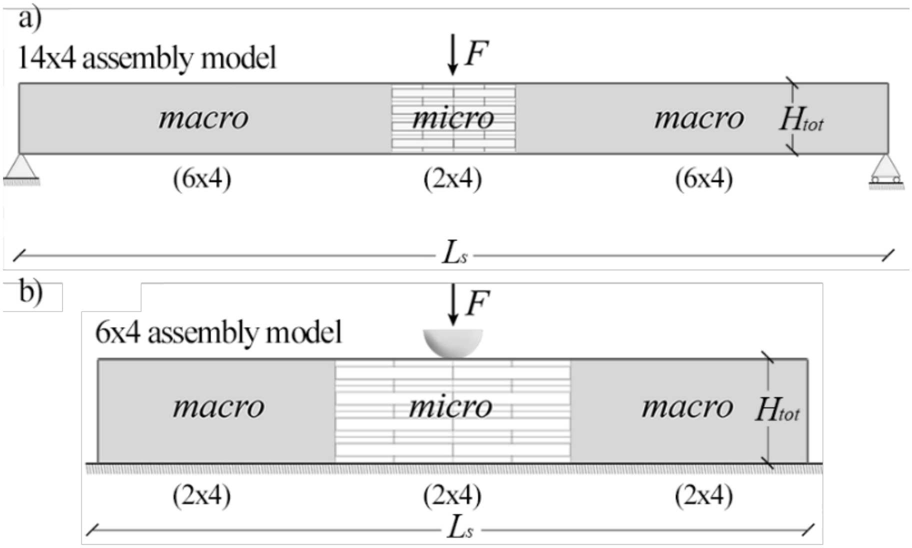

Fig. 4.27 Schematic of the geometric multiscale models adopted to simulate numerically the three-point bending test (a) and the indentation test (b).

contacting boundaries. First of all, validation and mesh convergence tests of the multiscale model were reported comparing numerical results obtained by means of a multiscale numerical simulation (MNS) with numerical results obtained by means of a direct numerical simulation (DNS) in which the composite microstructure is explicitly modeled. As shown in Fig. 4.28a and Fig. 4.28b both the multiscale models give a slightly stiffer response (with respect to the DNS simulations) and a higher influence of the degrees of freedom on the response is observed for the indentation test simulations. Anyway, for both the examined tests, no more than 20,000 degrees of freedom are needed for the multiscale approach to obtain a response in good agreement with the direct model results, thus saving between 50 and 60% of computational effort required for a full-scale direct numerical analysis.

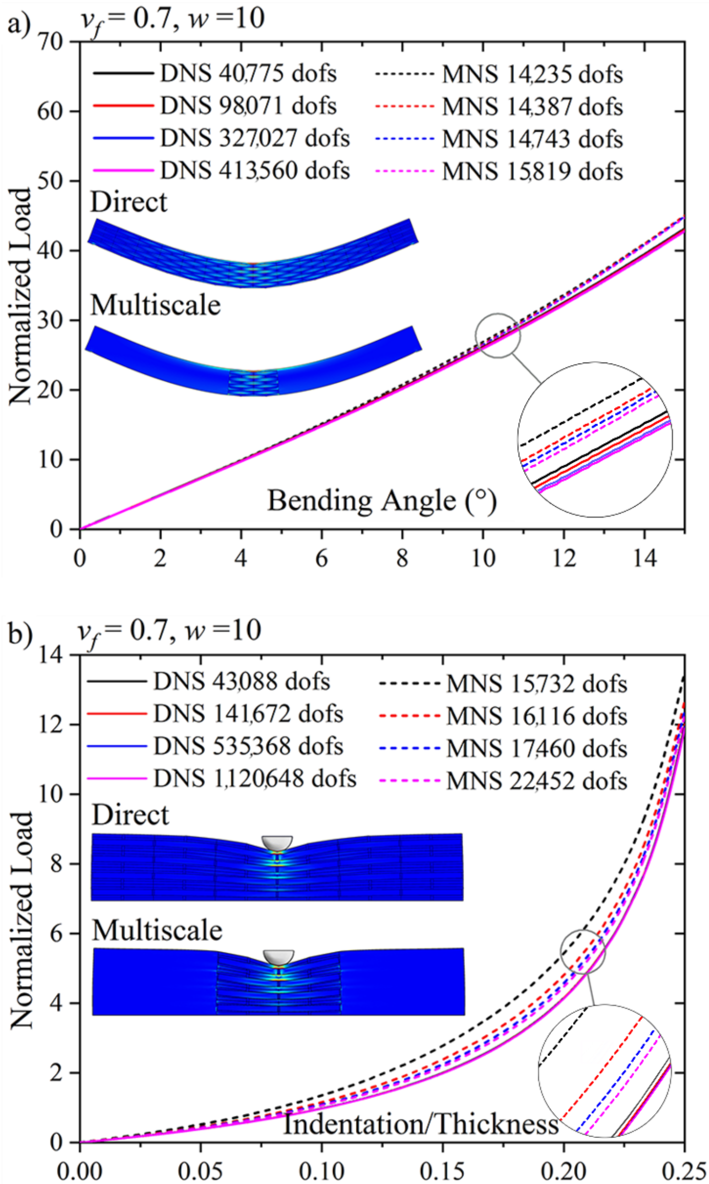

Fig. 4.28 Normalized bending load vs. bending angle (a) and normalized indentation load vs. normalized indentation depth (b) with different mesh size using direct (DNS) and multiscale (MNS) numerical simulations.

4.4.2.1 Numerical investigation of the flexibility property

With reference to the three-point bending test, the dependence of the normalized bending load on the bending angle for nacre-like composite structures with inclusions volume fraction ranging from 0.5 to 0.9 with increments of 0.1, and platelets aspect ratio ranging from 6 to 10 with increments of 2, is shown in Fig. 4.29. The normalized bending load is defined as

$$\mathrm{M} = \frac{FL_s}{\mu_i H_{tot} H_p z} \tag{4.38}$$

where L_s is the distance between the supports, H_{tot} is the total height of the beam and z is the out-of-plane depth, while the bending angle is defined as:

$$\alpha = atan\left(\frac{2\delta}{L_{tot}}\right) \tag{4.39}$$

where δ is the vertical displacement in the middle of the beam and L_{tot} is the total length of the beam. The flexibility decreases with an increase in volume fraction, as well as with an increase in aspect ratio. Nacre-like microstructures with volume fraction equal to 0.9 (green lines) results in a more pronounced decrease of flexibility leading, for instance, to values of the normalized load approximately doubled with respect to arrangements with volume fraction equal to 0.8 (fuchsia lines), at fixed inclusions aspect ratio.

The composite flexibility is further investigated by plotting the relative bending stiffness as function of aspect ratio in Fig. 4.30a and volume fraction in Fig. 4.30b. The relative bending stiffness represents a non-dimensional bending stiffness taken as the tangent bending stiffness of the composite beam divided by the tangent bending stiffness of the

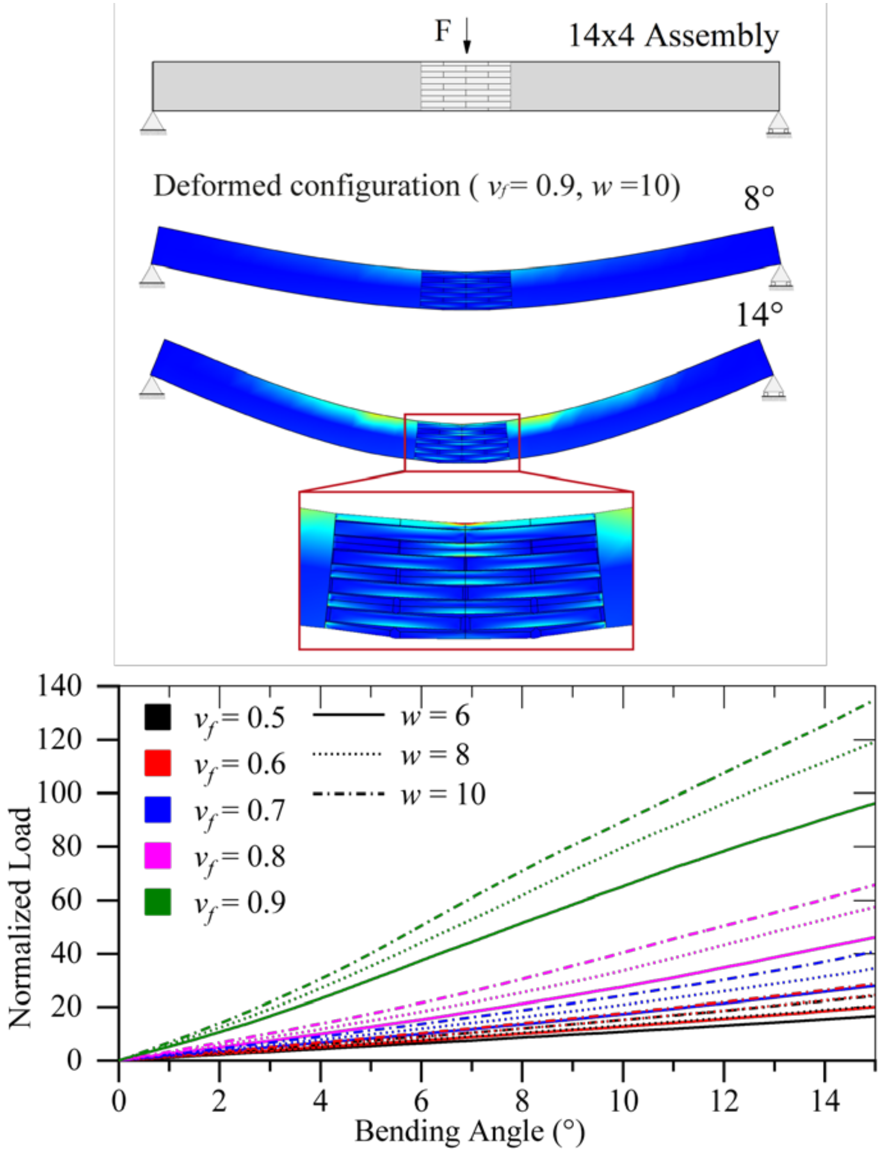

Fig. 4.29 Normalized bending load vs. bending angle (a) and normalized indentation load vs. normalized indentation depth (b) with different mesh size using direct (DNS) and multiscale (MNS) numerical simulations.

homogeneous beam ($v_f = 0$). Since the relative bending stiffness changes with bending angle, the initial tangent stiffness (measured at $\alpha = 1°$) and the finite tangent stiffness ($\alpha = 15°$) were plotted. The initial stiffness is presented by filled symbols, while the finite stiffness is denoted by hollow symbols. The results show that both initial and finite stiffness increase with an increase in both aspect ratio and volume fraction. In particular, an almost linear dependence on the aspect ratio at fixed volume fraction (Fig. 4.30a), and a superlinear dependence on the volume fraction at fixed aspect ratio (Fig. 4.30b) are reported. In other words, the investigated microstructure shows a more pronounced stiffening effect with increasing volume fraction, especially for the finite stiffness values. On the contrary, as shown in Fig. 4.30a, the aspect ratio has a small effect on the bending stiffness (especially for the initial values), which becomes negligible for low volume fractions (v_f ranging between 0.5 and 0.6). Furthermore, the difference between the finite and initial bending stiffness increases for increasing values of both volume fraction and aspect ratio, and becomes negligible for low volume fractions regardless the considered aspect ratio, meaning that the bending behavior of the given microstructure is nearly linear in these cases (see Fig. 4.30b).

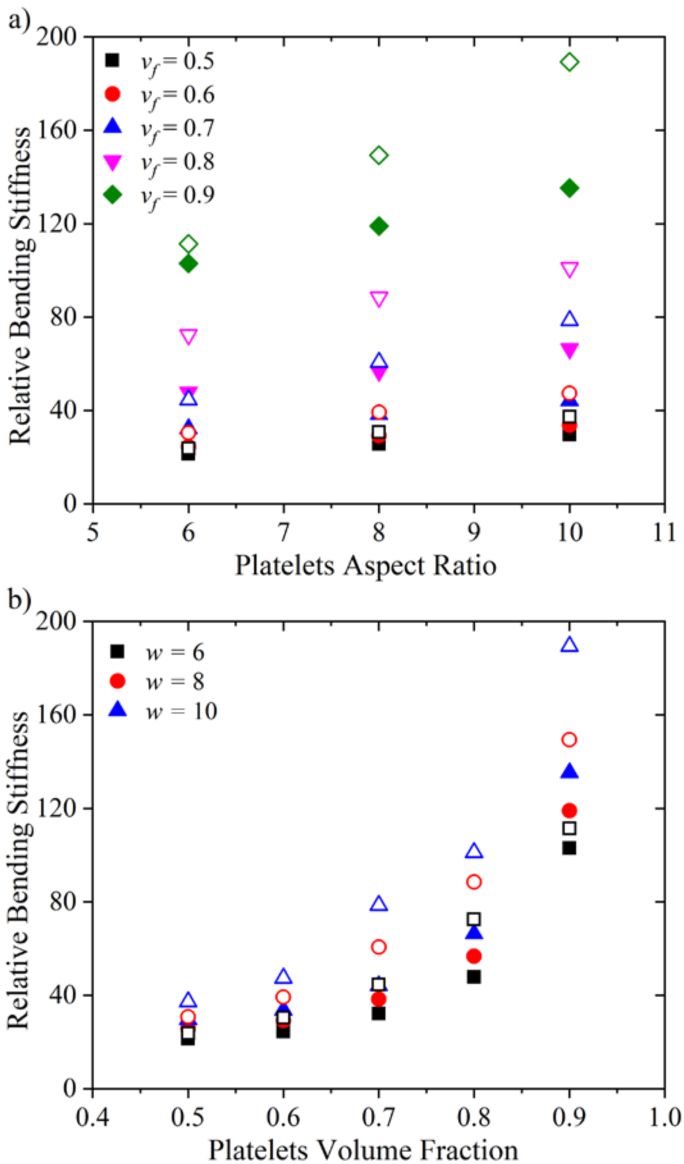

Fig. 4.30 Relative bending stiffness vs. platelets aspect ratio a) and platelets volume fraction b). The solid and hollow symbols are for initial and finite relative bending stiffness, respectively.

4.4.2.2 Numerical investigation of the penetration resistance property

The dependence of the normalized indentation load on the normalized indentation depth with an inclusions volume fraction ranging from 0.5 to 0.9 with increments of 0.1, and a platelets aspect ratio ranging from 6 to 10 with increments of 2 is shown in Fig. 4.31. The normalized indentation load is defined as

$$P = \frac{F}{\mu_i H_{tot} z} \tag{4.40}$$

which is plotted as function of the normalized indentation depth:

$$\Delta = \frac{\delta}{H_{tot}} \tag{4.41}$$

where δ is the vertical displacement at the top of the midsection, coinciding with the central point of the contact area with the indenter. The indentation load levels increase with an increase in inclusions volume fraction, while the aspect ratio provides a slight influence on the indentation load levels. The penetration stiffness increases with increasing indentation depth, as will be shown in more detail next. High volume fractions and low aspect ratios offer the greatest penetration resistance, with the exception of the case with $v_f = 0.9$ (green line), which shows the highest penetration resistance offered with $w = 10$ for levels of the normalized indentation depth greater than 0.12. The influence of the inclusions volume fraction and aspect ratio on the material resistance against indentation is further analyzed by plotting the relative penetration stiffness as function of these parameters in Fig. 4.32. The relative penetration stiffness is defined here as the tangent penetration stiffness of the composite sample normalized to the tangent penetration stiffness of the homogeneous sample ($v_f = 0$).

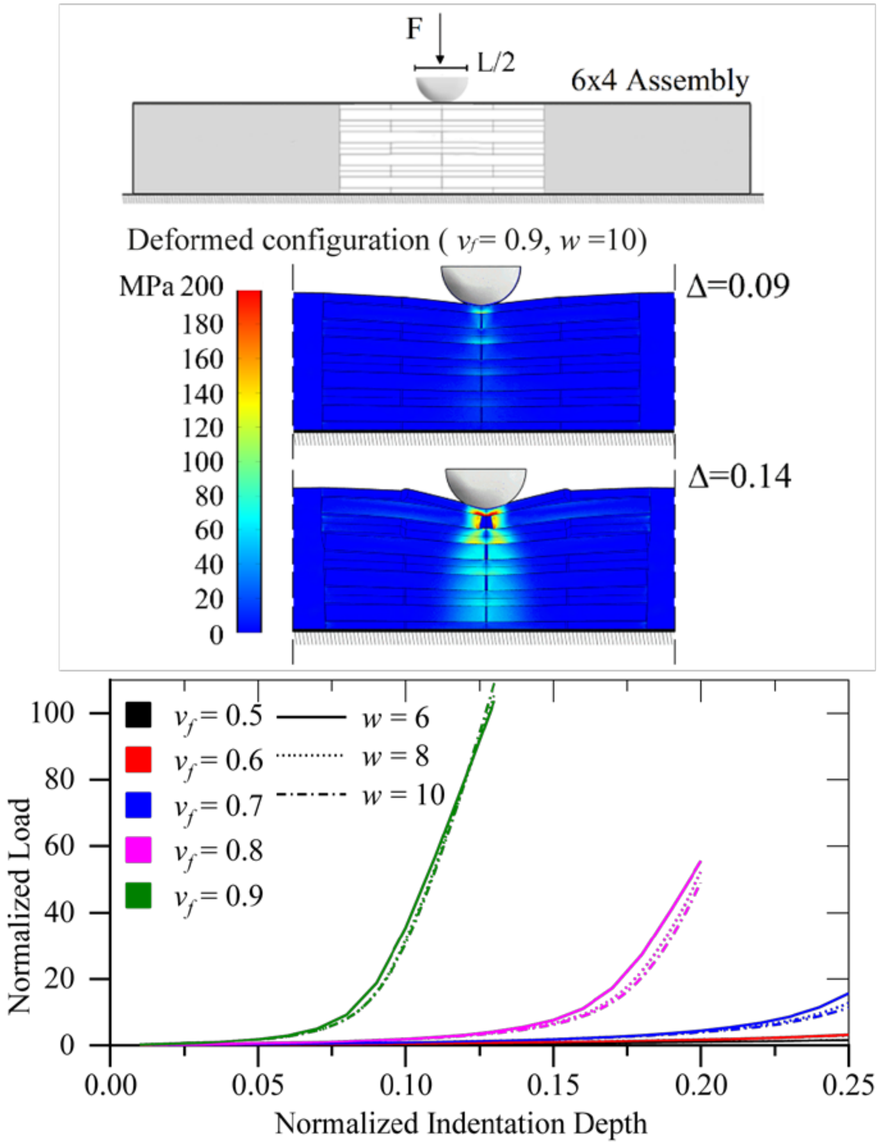

Fig. 4.31 Normalized indentation load vs. normalized indentation depth considering an v_f ranging from 0.5 to 0.9 with increments of 0.1, and w ranging from 6 to 10 with increments of 2.

Since the relative penetration stiffness changes with depth indentation, the initial tangent stiffness is measured at $\Delta = 0.01$ and the finite tangent stiffness is measured at when the tangent stiffness approaches a limit constant value (this occurs generally for the last value of Δ before convergence problems appear).

As in the previous analyzed case, both initial and finite penetration stiffness increase with increasing volume fraction. Moreover, the finite penetration stiffness is much higher than the initial value reflecting the highly nonlinear behavior due to a combination of geometrical and material nonlinearity, mostly for high values of volume fraction (see Fig. 4.32c and Fig. 4.32d). The aspect ratio provides a relatively small influence on both the initial and the final penetration stiffness. In detail, the finite penetration stiffness increases with increasing aspect ratio for volume fraction values ranging from 0.5 to 0.7, while decreases for volume fraction equal to 0.8 and 0.9. Consistent with the previous observation, Fig. 4.32d shows that merely for the cases with $v_f = 0.8$ and 0.9 the maximum value of finite relative penetration stiffness is given by the highest value of aspect ratio ($w = 10$).

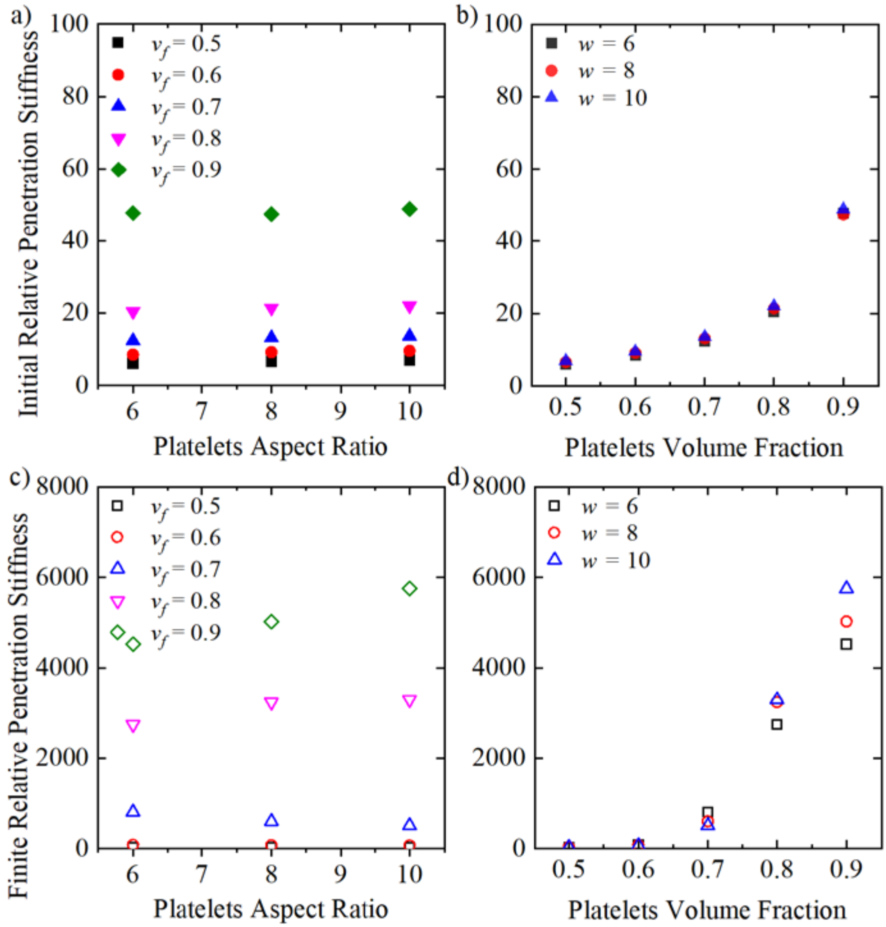

Fig. 4.32 Relative penetration stiffness vs. platelets aspect ratio: a) initial and c) finite values. Relative penetration stiffness vs. platelets volume fraction: b) initial and d) finite values.

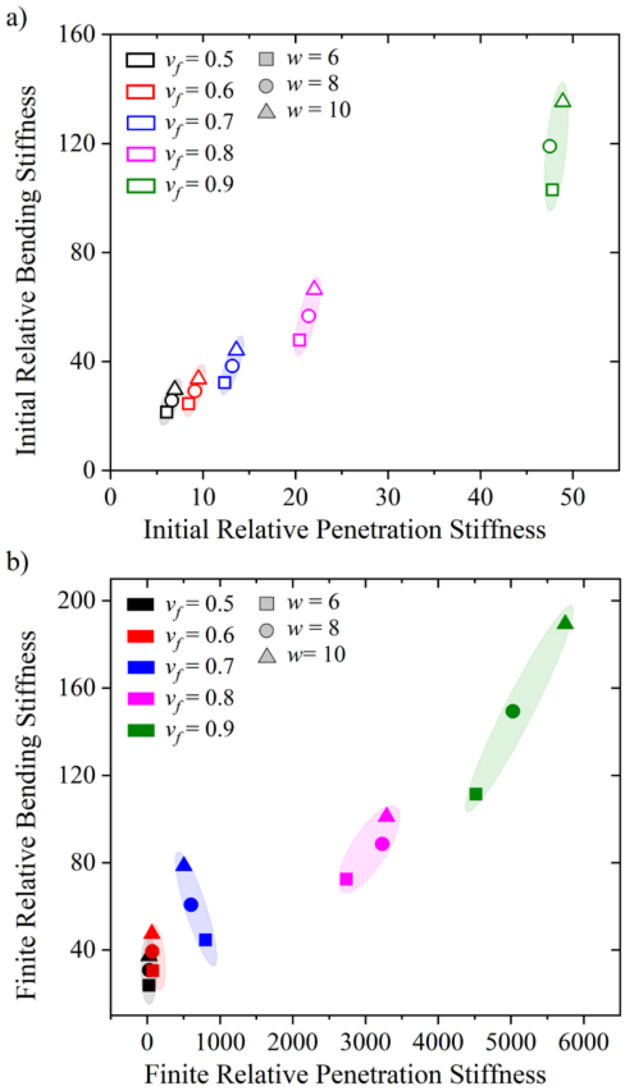

Fig. 4.33 Relative bending stiffness vs. relative penetration stiffness: a) initial and b) finite values.

4.4.2.3 Numerical investigation of the combined protecto-flexibility property

To better investigate the flexibility and the penetration stiffness in a coupled manner, the relative bending stiffness was plotted as function of the relative penetration stiffness in Fig. 4.33a and Fig. 4.33b, showing that an increase in penetration protection is accompanied by an increase in bending stiffness (decrease in flexibility) except for the finite relative bending stiffness with $v_f < 0.8$.

In particular, with $v_f = 0.5$ and 0.6, the finite relative bending stiffness can be varied without affecting the finite relative penetration stiffness, which is however negligible with respect to higher volume fractions (see black and red points of Fig.13b). Fig. 4.33 clearly shows that the volume fraction strongly influences the penetration stiffness (both initial and finite values) while slightly affecting the bending stiffness, especially for higher values of v_f. Moreover, it can be seen that the aspect ratio influences scarcely the initial penetration stiffness (see Fig.13a) while influencing moderately both the finite penetration and bending stiffness, except with $v_f < 0.7$, for which no significant influence is reported (see Fig. 4.33b). These figures also show that the penetration resistance can be tailored as a function of the flexibility properties by opportunely varying the examined microstructural geometrical parameters. In particular, Fig. 4.33b shows that different combinations of v_f and w may lead to the similar values of the desired finite flexibility and penetration resistance. In particular, once the desired finite relative bending stiffness is assigned to the nacre-like material, the volume fraction and the platelets aspect ratio can be optimized such that the desired relative penetration stiffness is reached. For instance, after choosing a finite relative bending stiffness of about 100, a finite relative penetration stiffness ranging between 3,500 and 4,500 can be achieved either for v_f = 0.8 and w > 10 or for v_f = 0.9 and w < 6. Then, the contrasting combination of penetration protection and flexibility, called protecto-flexibility, was taken as the ratio $\Omega = C_P / C_B$ between the normalized indentation stiffness C_P and the normalized bending stiffness C_B. The influence of the microstructural geometry of the composite on Ω is shown in Fig. 4.34, in which Ω is plotted as function of aspect ratio (a,b) and volume fraction (c,d). This figure clearly shows that the protecto-flexibility increases with increasing volume fraction and decreasing aspect ratio except for the cases with v_f = 0.9 and w = 8, 10, shown in Fig. 4.34d, where Ω is lower compared to the cases with v_f = 0.8 and w = 8, 10. Note that the finite protecto-flexibility is very sensitive to changes in volume fraction and aspect ratio, on the contrary, the initial protecto-flexibility does not change significantly with a change in volume fraction or aspect ratio. We can observe that volume fractions of 0.8 and 0.9 are optimal to achieve the best combinations of flexibility and penetration resistance. Considering the initial protecto-flexibility, we can see that, for each fixed aspect ratio, the highest value is obtained for v_f = 0.9 as shown in Fig. 4.34a; on the other hand, at finite deformations, the highest value, of about 40, is obtained for v_f = 0.9 and w = 6. For this value of aspect ratio, the general trend is that increasing value of the volume fraction are associated with increasing value of the protecto-flexibility. Such a trend is not reported for higher aspect ratios, i.e. w = 8 and 10, where the optimal value of the volume fraction to achieve the highest protecto-flexibility is v_f = 0.8. Finally, it is worth noting that the finite protecto-flexibility is more important, being in general two orders of magnitude greater than the initial one. This means than the protecto-flexibility properties appear in the considered staggered nacre-like material only at large deformation, essentially due to the delayed activation of the penetration stiffness.

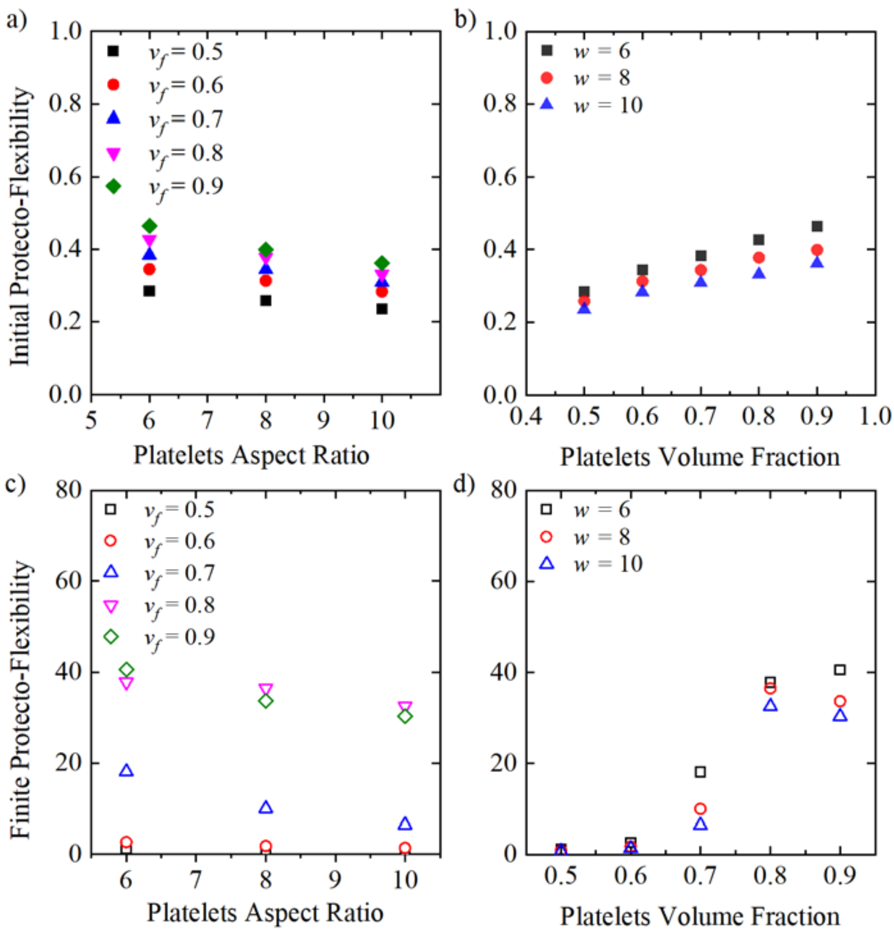

Fig. 4.34 Normalized indentation-to-bending stiffness ratio (protecto-flexibility) vs. platelets aspect ratio: a) initial and c) finite values. Protecto-flexibility vs. platelets volume fraction: b) initial and d) finite values.

Conclusions

In this thesis the nonlinear macroscopic mechanical response of advanced composite materials has been investigated by using nonlinear homogenization techniques and advanced computational multiscale models. Such advanced modelling techniques constitute an effective tool to model materials with complex microstructures, providing a link between the macroscopic behavior and the underlying microstructural phenomena, accounting for different types of nonlinearity, such as large deformation, fracture, contact, instability, etc. The basis of the homogenization techniques at finite strain has been discussed together with a classification (based on the type of coupling between the different scales) of the principal multiscale models proposed in the past literature. The main goal of this thesis is to provide theoretical and numerical methods capable to model the mechanical response of heterogeneous materials (fiber- or particle-reinforced composites) in a large deformation context predicting the failure in terms of loss of stability considering also the interaction between microfractures and contact. A theoretical study has been developed to obtain the nonlinear homogenized response of periodic composite solids, by including also the effects of instabilities occurring at the microscopic level and the interaction between microfractures and buckling instabilities. Subsequently, based on the previous theoretical development, a first numerical study has been performed to investigate the interaction between microfractures and buckling instabilities in unidirectional fiber-reinforced composite materials. A second numerical study, performed by using advanced multiscale computational strategies, has been then conducted to analyze the microstructural instability in locally periodic composite materials reinforced with continuous or discontinuous fibers and subjected to general loading conditions at finite strain. For this purpose, a novel hybrid multiscale approach has been also proposed with the aim to overcome the limitations observed in semiconcurrent approaches. It has been proved that such a method is really effective to evaluate the microscopic instability in composite materials affected by boundary layer effects, and ultimately it could be used in a productive way to the optimal design of complex microstructured composite materials.

In the first part of the thesis, with reference to Section 3, an original investigation of the macroscopic failure behavior of periodic elastic fiber reinforced composites, as a consequence of the interactions between microscopic fiber buckling instabilities and matrix or fiber/matrix interface microcracks, was presented in a compressive large deformation context. The effects of unilateral self-contact at the crack contact interface occurring due to compression, have been also included in the analysis. As reported in Section 3.4, the investigated failure mode is of central importance for an accurate prediction of the load carrying capacity of unidirectional fiber-reinforced or layered composites loaded prevalently in compression along the fiber direction, since the interaction between buckling instabilities and fractures may lead to a strong decrease in the compressive strength of the composite material with a premature failure of the composite solid often associated to crack propagation phenomena.

In order to perform an accurate analysis of the above-mentioned failure behavior, a rigorous full finite deformation continuum formulation of the composite microstructure has been proposed able to account for the interaction between local fiber buckling and matrix or fiber/matrix interface microcracks by modeling unilateral self-contact along crack surfaces. The adopted formulation made it possible to highlight the presence of non-standard rate contributions arising from crack self-contact interface mechanisms that have proved to play a fundamental role in order to obtain a realistic prediction of the macroscopic critical load of the composite solid. To this end, the first part of the thesis is devoted to the theoretical formulation of instability and bifurcation phenomena for microcracked composite materials subjected to a macrostrain driven loading path. The theory adopts a quasistatic finite strain continuum rate approach and a variational setting. In addition, the role of non-standard crack contact interface rate contributions in the framework of the stability and non-bifurcation analysis of the composite material is investigated, by examining the virtual work of the contact reaction rate acting on the contact interface.

Novel analytical developments have shown that the contributions to the virtual work of the contact reaction rate and, consequently, to the stability and non-bifurcation functionals, arising from a full finite deformation formulation of crack self-contact mechanisms consist of two contact surface integral terms: namely a tangential term related to the tangential component of the nominal contact reaction rate and a crack surface deformation term associated with the different variation of the reference to actual surface element ratio between the lower and upper crack contact surfaces.

Original comparisons with simplified formulations which do not adopt a full finite deformation approach to model contact phenomena occurring along crack surfaces and based on a cohesive interface type of approach are given in Section 3.4.2 and Section 3.4.3. Specifically, assuming the nominal traction continuity condition with reference to the undeformed crack contact interface, as usually done in order to formulate a cohesive interface constitutive law relating the nominal contact reaction vector to the interface separation, leads to neglect the surface integral related to the crack surface deformation term in the virtual work of the contact reaction rate and to formulate the tangential one with reference to the jump across the undeformed contact interface of the virtual displacement.

Moreover, it is shown that when nominal contact reaction continuity condition is assumed rigorously valid, as for a material discontinuity interface without displacement jumps, also the tangential term vanishes and the virtual work of the contact reaction rate becomes globally zero. According to the two above mentioned simplified formulations, namely the interface model and the model without crack contact interface contributions, the corresponding modified stability and non-bifurcation conditions have been formulated as a way to determine the related primary instability and bifurcation critical load levels, which can be considered approximations of the exact ones associated to the full finite deformation crack contact model.

First of all, as reported in 3.4.2, the influence of the above mentioned contact interface integral contributions occurring in the stability and non-bifurcation functionals have been analyzed by means of novel numerical results developed with reference to a practical application involving the uniaxial compressive failure of a fiber-reinforced composite material containing a matrix or a fiber/matrix microcrack aligned with the fiber direction. Hyperelastic material models have been adopted to model both the microconstituents and a nonlinear FE model of the composite material has been developed by solving in a coupled way the global and the rate eigenvalue boundary value problems providing the bifurcation and the instability load levels both for the exact and the simplified formulations. An extensive set of numerical results has been obtained with reference to the above application model, including different geometrical configurations for the defected microstructure. To this end the sensitivity of the primary instability and bifurcation critical load factor and of its associated critical modes with respect to the variation of the crack length, fiber thickness and crack eccentricity, has been evaluated. Limit behaviors of the defected microstructures, also useful to check the accuracy of the results, have been examined by calculating the critical load levels of the completely bonded and free comparison rate problems, giving upper and lower bounds to the exact critical load level, respectively. The main conclusion obtained for the uniaxial case is that non-standard contributions arising from a full finite deformation formulation of crack interface contact have a notable influence on critical loads and deformation modes, since, if they are not included in the analysis (as in simplified crack contact interface formulations), a large

underestimation of the real failure load of the microcracked composite was found with an increasing underestimation as crack eccentricity decreases and relative crack length increases; this highlights the importance of adopting a full finite deformation formulation of crack self-contact contact nonlinearities, rather than simplified ones, in order to obtain an accurate prediction of instability and bifurcation phenomena. Subsequently, further analytical development and parametrical analyses have been reported in Section 3.4.3 with reference to a biaxial loading condition. With reference to hyperelastic microconstituents, analytical results for the determination of the so-called decompression limit path (where the nominal contact pressure vanishes) have been reported in Section 3.4.3.1. Then, in Section 3.4.3.2, general parametric analyses have been developed including various load conditions and different microgeometrical arrangements to investigate the influence of the above-mentioned non-standard contributions in a biaxial loading condition. Firstly, with reference to biaxial radial loading paths in the principal macrostrain space, the critical curves identifying the limit of the two-dimensional stability and uniqueness domain for the composite microstructure have been determined for different crack eccentricity ratios. Secondly, in order to better evaluate the crack length influence on the critical load factors, further parametric analyses have been carried out for two different radial paths ($\varphi = \pm 20°$). In addition, the limit behaviors of the composite microstructure have been determined using appropriate comparison rate problems.
The obtained critical curves and deformation modes in biaxial loading regime show that they are strongly influenced by the nonlinear contributions arising from crack interface self-contact mechanisms. As a matter of fact, considering simplified crack contact interface formulations, a large underestimation of the real failure load of the microcracked

composite was found with an increasing underestimation as crack eccentricity decreases and relative crack length increases. Specifically, the largest percentage relative difference between the critical load levels corresponding to the exact and the simplified formulations is equal to 73% obtained for the formulation neglecting all crack self-contact contributions; this highlights that a realistic prediction of the macroscopic critical load of defected composite materials subjected to biaxial loading requires a full finite deformation formulation of crack self-contact nonlinearities**.**

In the second part of the thesis, the failure behavior of periodic elastic fiber reinforced composites has been further investigated by means of different multiscale strategies.

Specifically, with reference to Section 4 two multiscale modeling strategies have been adopted to analyze the microstructural instability in locally periodic fiber-reinforced composite materials subjected to general loading conditions in a large deformation context.

The first adopted strategy is a semi-concurrent multiscale method consisting in the derivation of the macroscopic constitutive response of the composite structure together with a microscopic stability analysis through a two-way computational homogenization scheme.

The second approach is a novel hybrid hierarchical/concurrent multiscale approach able to combine the advantages inherent in the use of hierarchical and concurrent approaches and based on a two-level domain decomposition. The aim of the proposed technique is to adopt a hierarchical multiscale approach in domains in which the assumption of scale separation is satisfied (homogenized domains), combined with a concurrent approach in domains in which, due to strain or stress localization phenomena, this condition is no longer satisfied (fine-scale domains). In detail, fine-scale domains are characterized by a micro-structural description that requires a numerical model able to completely describe all its microscopic details and may contain heterogeneities, singularities or/and defects. Homogenized domains, instead, use information obtained by an RVE at the fine scale to describe the mechanical behavior of the homogenized material characterizing coarse-scale domains; specifically, a microscopically informed macroscopic constitutive relation in the form of macro-stress/macro-strain database previously extracted, in conjunction with an interpolation method, has been implemented in a finite element model. The viability and accuracy of the proposed multiscale approaches in the context of the microscopic stability analysis in defected composite materials have been appropriately evaluated through comparisons with reference direct numerical simulations.

As a first numerical application, the proposed semi-concurrent multiscale approach has been used to predict local instabilities in a cantilever composite beam reinforced with continuous fibers and an estimation of the instability critical load has been initially obtained by using a load-displacement curve. The numerical accuracy of the multiscale approach has been assessed by the comparison with a direct numerical simulation, based on a fully meshed model. The error on the estimated critical load between the two analyses is of about 1%, mainly due to both macroscopic gradients in stresses and strains and boundary layer effects. Then, the critical load factor has been also estimated by rigorous microscopic stability analysis. The good numerical accuracy of the semi-concurrent method is confirmed by a small error on the critical load, less than 2%. Interestingly, with reference to the direct numerical analysis, the competition between global and local modes has been highlighted; on the contrary, with reference to the semiconcurrent multiscale approach, the same behavior is not captured since this category of semiconcurrent approaches is not capable to evaluate boundary layer effect given by external constraints In addition, the predicted local mode is not coincident with the reference one, due to the fact that boundary layer effects are not accounted for.

As second numerical application, the novel hybrid multiscale approach has been applied to composite materials reinforced with staggered discontinuous fibers. The first case concerns the bending problem for a simply supported composite beam and the numerical accuracy of the multiscale approach has been assessed by the comparison with a direct numerical simulation. A very small error on the estimated critical load between the two analyses is found, less than 0.5%. The critical load factor has been also estimated by a rigorous microscopic stability analysis. In this case, the competition between global and local modes is captured by both direct and multiscale analyses and the very good numerical accuracy of the concurrent method is confirmed by the very small error on the extrapolated critical load, of about 0.5%. Moreover, the predicted local mode is perfectly coincident with the reference one, due to the fact that boundary layer effects are accounted for. The last case, concerns a clamped composite plate under a concentrated load and the great numerical accuracy of the hybrid method is confirmed by the very small error on the critical load, of about 0.2%. Moreover, also in this case, the predicted local mode is perfectly coincident with the reference one. In conclusions, suitable comparisons with direct numerical simulations have shown that the hybrid multiscale approach is more accurate in obtaining both critical load levels and related microscopic instability modes, thanks to its capability of capturing both macroscopic gradients in stresses and strains and boundary layer effects.

With reference to Section 4.4, the present thesis ends with an investigation of the mechanical behavior of nacre-like composite materials in a large deformation context by using the previously mentioned hybrid multiscale approach overcoming a computationally expensive full-scale modeling. Motivated by the need to design a body protective bio-inspired material architecture, we examine two competing properties, i.e. penetration resistance and flexibility. Mimicking nacre's hierarchical brick-and-mortar structure in 3D printed microstructured composite materials is an efficient approach to achieve structural materials with high mechanical performances, but the task to determine the macroscopic response of microstructured materials taking into account their microscopic nonlinear mechanical behavior usually requires a rigorous description of all microstructural details leading to impracticable computational efforts. A comprehensive parametric analysis with respect to platelets aspect ratio and volume fraction, representing the main geometrical parameters governing the macroscopic behavior of the bio-inspired nacre-like composite material, is performed analyzing its flexibility and penetration resistance. Initially, validation and mesh convergence tests of the multiscale model were reported comparing the numerical results obtained by using multiscale and direct numerical simulations and it was deduced that using a multiscale model an amount of computational effort between 50 and 60% is saved with respect to a full-scale numerical model. Then, the flexibility is investigated by means of a three-point bending test on beams, in which the real microstructure is introduced in correspondence of the vertical concentrated load. In particular, both the initial and the finite tangent stiffness are computed as functions of aspect ratio and volume fraction. The results show that flexibility decreases with an increase in both volume fraction and aspect ratio. In detail, the investigated microstructure shows a pronounced stiffening effect for larger values of the volume fraction, especially for the finite stiffness. On the contrary, the bending stiffness (especially the initial one) is only slightly influenced by the aspect ratio, especially for lower volume fractions (v_f ranging between 0.5 and 0.6). Moreover, the bending stiffening effect associated with the occurrence of large deformations increases for increasing values of both volume fraction and aspect ratio, and becomes negligible for low volume fractions regardless the considered aspect ratio; in fact, in this case, the bending response of the given microstructure remains almost linear. Next, the penetration resistance was investigated by employing an indentation test on a rectangular sample using a spherical indenter and modeling the contact between the indenter and the sample. The results show that the indentation load levels increase with an increase in the stiff phase volume fraction, while the aspect ratio provides a small influence on the indentation load levels. The penetration stiffness increases with increasing indentation depth, and high volume fractions and low aspect ratio offer the greatest penetration resistance, with the exception of the greatest tested volume fraction ($v_f = 0.9$), for which the highest penetration resistance is reached for the highest tested aspect ratio (w = 10). The influence of the stiff phase volume fraction and the platelets aspect ratio on the material resistance against indentation is further analyzed by plotting the initial and the finite tangent penetration stiffness as functions of these parameters. The finite penetration stiffness is higher than the initial value, reflecting the nonlinear behavior due to a combination of geometrical and material nonlinearity, mostly for high values of volume fraction. Both initial and finite penetration stiffness increases with an increase in volume fraction, with stiffness increase more prominent in the range of high-volume fractions. On the other hand, the aspect ratio provides only a relatively small influence on the penetration stiffness, with a negligible influence on the initial values.

Next, from the comparison between the relative bending stiffness and relative penetration stiffness, it can be observed that the volume fraction strongly influences the penetration stiffness (mainly the finite value), while it slightly influences the bending stiffness. Moreover, generally speaking, an increase in penetration protection is accompanied by an increase in bending stiffness. In particular, with volume fraction values up to 0.6, the finite relative bending stiffness can be varied without affecting the finite relative penetration stiffness, which is however negligible with respect to that achieved with higher volume fractions.

These results demonstrate that the penetration resistance can be tailored as a function of the flexibility by opportunely varying inclusions volume fraction and/or aspect ratio.

Finally, the performance requirements of penetration resistance and flexibility are incorporated in a single parameter, called protecto-flexibility, which was evaluated for different values of aspect ratio and volume fraction, to investigate the role of the main microstructural parameters in this integrated measure. It is worth noting that the protecto-flexibility is very sensitive to changes in volume fraction and aspect ratio, on the contrary, the initial protecto-flexibility does not change significantly with a change in volume fraction or aspect ratio. The numerical results have shown that the finite protecto-flexibility is more important, since, generally speaking, it is two orders of magnitude greater than the initial one. This is essentially due to the delayed activation of the penetration stiffness, associated with the occurrence of large deformations.

Generally speaking, the best combinations of flexibility and penetration resistance are obtained with high volume fractions (equal or greater than 0.8), regardless of the considered aspect ratio. However, for very high aspect ratios (starting from w = 8) and for volume fraction values greater than 0.8, a further increase in the volume fraction inevitably leads to a reduction of the protecto-flexibility. This counter-intuitive result demonstrates that, in the presence of highly elongated platelets, a limited range of variation for the volume fraction (around the value of 0.8 for the specific staggered microstructure) guarantees the optimal coupled protection/flexibility behavior.

The reported findings can provide guidelines to enhance mechanical properties of bio-inspired nacre-like composite materials manipulating the main microstructural geometry parameters. Specifically, a careful selection of volume fraction and aspect ratio can provide optimized designs to grant protection against penetration while preserving flexibility. It is worth also noting that the hybrid multiscale techniques developed in this thesis are reliable and can be effectively used to conduct further research on the optimization of microstructural configurations in advanced composite structures subjected to different form of nonlinearities.

Bibliography

[1] N. Fantuzzi, L. Leonetti, P. Trovalusci, F. Tornabene, Some Novel Numerical Applications of Cosserat Continua, Int. J. Comput. Methods. 15 (2018) 1850054. https://doi.org/10.1142/S0219876218500548.

[2] P.I. Galich, V. Slesarenko, S. Rudykh, Shear wave propagation in finitely deformed 3D fiber-reinforced composites, Int. J. Solids Struct. 110–111 (2017) 294–304. https://doi.org/10.1016/j.ijsolstr.2016.12.007.

[3] W. Xu, Y. Wu, M. Jia, Elastic dependence of particle-reinforced composites on anisotropic particle geometries and reinforced/weak interphase microstructures at nano- and micro-scales, Compos. Struct. 203 (2018) 124–131. https://doi.org/10.1016/j.compstruct.2018.07.009.

[4] S. Ko, J. Yang, M.E. Tuttle, M. Salviato, Effect of the platelet size on the fracturing behavior and size effect of discontinuous fiber composite structures, Compos. Struct. 227 (2019) 111245. https://doi.org/10.1016/j.compstruct.2019.111245.

[5] H. Le Ferrand, Modeling the effect of microstructure on elastic wave propagation in platelet-reinforced composites and ceramics,

Compos. Struct. 224 (2019) 111105. https://doi.org/10.1016/j.compstruct.2019.111105.
[6] Y. Kim, H. Jeong, G.X. Gu, S. Ryu, A three-dimensional fracture pattern diagram of staggered platelet structures, Compos. Struct. 220 (2019) 769–775. https://doi.org/10.1016/j.compstruct.2019.04.017.
[7] A.N. D., B.Z. T., O. Polit, P. B., G. M., Large amplitude free flexural vibrations of functionally graded graphene platelets reinforced porous composite curved beams using finite element based on trigonometric shear deformation theory, Int. J. Non-Linear Mech. 116 (2019) 302–317. https://doi.org/10.1016/j.ijnonlinmec.2019.07.010.
[8] L. Benabou, N. Benseddiq, M. Naït-Abdelaziz, Comparative analysis of damage at interfaces of composites, Compos. Part B Eng. 33 (2002) 215–224. https://doi.org/10.1016/S1359-8368(02)00004-5.
[9] S. Li, G. Wang, E. Morgan, Effective elastic moduli of two dimensional solids with distributed cohesive microcracks, Eur. J. Mech. - ASolids. 23 (2004) 925–933. https://doi.org/10.1016/j.euromechsol.2004.07.002.
[10] D. Bruno, F. Greco, P. Lonetti, P. Nevone Blasi, Influence of micro-cracking and contact on the effective properties of composite materials, Simul. Model. Pract. Theory. 16 (2008) 861–884. https://doi.org/10.1016/j.simpat.2008.05.006.
[11] F. Greco, Homogenized mechanical behavior of composite microstructures including micro-cracking and contact evolution, Eng. Fract. Mech. 76 (2009) 182–208. https://doi.org/10.1016/j.engfracmech.2008.09.006.
[12] M. Brieu, F. Devries, Micro-mechanical approach and algorithm for the study of damage appearance in elastomer composites, Compos. Struct. 46 (1999) 309–319.
[13] D. Wang, M.M. Abdalla, Global and local buckling analysis of grid-stiffened composite panels, Compos. Struct. 119 (2015) 767–776. https://doi.org/10.1016/j.compstruct.2014.09.050.
[14] F. Feyel, J.-L. Chaboche, FE2 multiscale approach for modelling the elastoviscoplastic behaviour of long fibre SiC/Ti composite materials, Comput. Methods Appl. Mech. Eng. 183 (2000) 309–330. https://doi.org/10.1016/S0045-7825(99)00224-8.

[15] F. Greco, L. Leonetti, P. Lonetti, P. Nevone Blasi, Crack propagation analysis in composite materials by using moving mesh and multiscale techniques, Comput. Struct. 153 (2015) 201–216. https://doi.org/10.1016/j.compstruc.2015.03.002.
[16] F. Greco, L. Leonetti, P. Nevone Blasi, Adaptive multiscale modeling of fiber-reinforced composite materials subjected to transverse microcracking, Compos. Struct. 113 (2014) 249–263. https://doi.org/10.1016/j.compstruct.2014.03.025.
[17] L. Feo, F. Greco, L. Leonetti, R. Luciano, Mixed-mode fracture in lightweight aggregate concrete by using a moving mesh approach within a multiscale framework, Compos. Struct. 123 (2015) 88–97. https://doi.org/10.1016/j.compstruct.2014.12.037.
[18] K. Yu, H. Hu, S. Chen, S. Belouettar, M. Potier-Ferry, Multi-scale techniques to analyze instabilities in sandwich structures, Compos. Struct. 96 (2013) 751–762. https://doi.org/10.1016/j.compstruct.2012.10.007.
[19] Q.Z. He, H. Hu, S. Belouettar, G. Guinta, K. Yu, Y. Liu, F. Biscani, E. Carrera, M. Potier-Ferry, Multi-scale modelling of sandwich structures using hierarchical kinematics, Compos. Struct. 93 (2011) 2375–2383. https://doi.org/10.1016/j.compstruct.2011.03.026.
[20] N. Triantafyllidis, B.N. Maker, On the Comparison Between Microscopic and Macroscopic Instability Mechanisms in a Class of Fiber-Reinforced Composites, J. Appl. Mech. 52 (1985) 794. https://doi.org/10.1115/1.3169148.
[21] G. Geymonat, S. Muller, N. Triantafyllidis, Homogenization of nonlinearly elastic materials, microscopic bifurcation and macroscopic loss of rank-one convexity, Arch. Ration. Mech. Anal. 122 (1993) 231–290. https://doi.org/10.1007/BF00380256.
[22] C. Miehe, J. Schröder, M. Becker, Computational homogenization analysis in finite elasticity: material and structural instabilities on the micro- and macro-scales of periodic composites and their interaction, Comput. Methods Appl. Mech. Eng. 191 (2002) 4971–5005. https://doi.org/10.1016/S0045-7825(02)00391-2.
[23] S. Nezamabadi, J. Yvonnet, H. Zahrouni, M. Potier-Ferry, A multilevel computational strategy for handling microscopic and macroscopic instabilities, Comput. Methods Appl. Mech. Eng. 198 (2009) 2099–2110. https://doi.org/10.1016/j.cma.2009.02.026.

[24] J.C. Michel, O. Lopez-Pamies, P. Ponte Castañeda, N. Triantafyllidis, Microscopic and macroscopic instabilities in finitely strained fiber-reinforced elastomers, J. Mech. Phys. Solids. 58 (2010) 1776–1803. https://doi.org/10.1016/j.jmps.2010.08.006.

[25] F. Greco, R. Luciano, A theoretical and numerical stability analysis for composite micro-structures by using homogenization theory, Compos. Part B Eng. 42 (2011) 382–401. https://doi.org/10.1016/j.compositesb.2010.12.006.

[26] V. Slesarenko, S. Rudykh, Microscopic and macroscopic instabilities in hyperelastic fiber composites, J. Mech. Phys. Solids. 99 (2017) 471–482. https://doi.org/10.1016/j.jmps.2016.11.002.

[27] M.D. Nestorović, N. Triantafyllidis, Onset of failure in finitely strained layered composites subjected to combined normal and shear loading, J. Mech. Phys. Solids. 52 (2004) 941–974. https://doi.org/10.1016/j.jmps.2003.06.001.

[28] G. Cricrì, R. Luciano, Homogenised properties of composite materials in large deformations, Compos. Struct. 103 (2013) 9–17. https://doi.org/10.1016/j.compstruct.2013.03.015.

[29] F. Greco, R. Luciano, Analysis of the Influence of Incremental Material Response on the Structural Stability, Mech. Adv. Mater. Struct. 12 (2005) 363–377. https://doi.org/10.1080/15376490500182156.

[30] G. Bilbie, C. Dascalu, R. Chambon, D. Caillerie, Micro-fracture instabilities in granular solids, Acta Geotech. 3 (2008) 25–35. https://doi.org/10.1007/s11440-007-0046-8.

[31] F. Greco, A study of stability and bifurcation in micro-cracked periodic elastic composites including self-contact, Int. J. Solids Struct. 50 (2013) 1646–1663. https://doi.org/10.1016/j.ijsolstr.2013.01.036.

[32] D. Bruno, F. Greco, R. Luciano, P. Nevone Blasi, Nonlinear homogenized properties of defected composite materials, Comput. Struct. 134 (2014) 102–111. https://doi.org/10.1016/j.compstruc.2013.11.018.

[33] F. Greco, L. Leonetti, R. Luciano, P. Nevone Blasi, Effects of microfracture and contact induced instabilities on the macroscopic response of finitely deformed elastic composites, Compos. Part B Eng. 107 (2016) 233–253. https://doi.org/10.1016/j.compositesb.2016.09.042.

[34] S. Nezamabadi, M. Potier-Ferry, H. Zahrouni, J. Yvonnet, Compressive failure of composites: A computational homogenization approach, Compos. Struct. 127 (2015) 60–68. https://doi.org/10.1016/j.compstruct.2015.02.042.
[35] S. Rudykh, G. deBotton, Instabilities of Hyperelastic Fiber Composites: Micromechanical Versus Numerical Analyses, J. Elast. 106 (2012) 123–147. https://doi.org/10.1007/s10659-011-9313-x.
[36] D. Bigoni, M. Ortiz, A. Needleman, Effect of interfacial compliance on bifurcation of a layer bonded to a substrate, Int. J. Solids Struct. 34 (1997) 4305–4326. https://doi.org/10.1016/S0020-7683(97)00025-5.
[37] D. Bruno, F. Greco, An asymptotic analysis of delamination buckling and growth in layered plates, Int. J. Solids Struct. 37 (2000) 6239–6276. https://doi.org/10.1016/S0020-7683(99)00281-4.
[38] O. Rabinovitch, Nonlinear (buckling) effects in RC beams strengthened with composite materials subjected to compression, Int. J. Solids Struct. 41 (2004) 5677–5695. https://doi.org/10.1016/j.ijsolstr.2004.04.031.
[39] H. Zhao, Z. Yang, L. Guo, Nacre-inspired composites with different macroscopic dimensions: strategies for improved mechanical performance and applications, NPG Asia Mater. 10 (2018) 1–22. https://doi.org/10.1038/s41427-018-0009-6.
[40] H. Kakisawa, T. Sumitomo, The toughening mechanism of nacre and structural materials inspired by nacre, Sci. Technol. Adv. Mater. 12 (2011) 064710. https://doi.org/10.1088/1468-6996/12/6/064710.
[41] F. Barthelat, H.D. Espinosa, An Experimental Investigation of Deformation and Fracture of Nacre–Mother of Pearl, Exp. Mech. 47 (2007) 311–324. https://doi.org/10.1007/s11340-007-9040-1.
[42] B. Ji, H. Gao, Mechanical properties of nanostructure of biological materials, J. Mech. Phys. Solids. 52 (2004) 1963–1990. https://doi.org/10.1016/j.jmps.2004.03.006.
[43] K. Ko, S. Jin, S.E. Lee, I. Lee, J.-W. Hong, Bio-inspired bimaterial composites patterned using three-dimensional printing, Compos. Part B Eng. 165 (2019) 594–603. https://doi.org/10.1016/j.composites b.2019.02.008.

[44] L.S. Dimas, M.J. Buehler, Modeling and additive manufacturing of bio-inspired composites with tunable fracture mechanical properties, Soft Matter. 10 (2014) 4436. https://doi.org/10.1039/c3sm52890a.
[45] P. Tran, T.D. Ngo, A. Ghazlan, D. Hui, Bimaterial 3D printing and numerical analysis of bio-inspired composite structures under in-plane and transverse loadings, Compos. Part B Eng. 108 (2017) 210–223. https://doi.org/10.1016/j.compositesb.2016.09.083.
[46] Y. Kim, Y. Kim, F. Libonati, S. Ryu, Designing tough isotropic structural composite using computation, 3D printing and testing, Compos. Part B Eng. 167 (2019) 736–745. https://doi.org/10.1016/j.compositesb.2019.03.039.
[47] S. Rudykh, C. Ortiz, M.C. Boyce, Flexibility and protection by design: imbricated hybrid microstructures of bio-inspired armor, Soft Matter. 11 (2015) 2547–2554. https://doi.org/10.1039/C4SM02907K.
[48] V. Slesarenko, K.Y. Volokh, J. Aboudi, S. Rudykh, Understanding the strength of bioinspired soft composites, Int. J. Mech. Sci. 131–132 (2017) 171–178. https://doi.org/10.1016/j.ijmecsci.2017.06.054.
[49] V. Slesarenko, N. Kazarinov, S. Rudykh, Distinct failure modes in bio-inspired 3D-printed staggered composites under non-aligned loadings, Smart Mater. Struct. 26 (2017) 035053. https://doi.org/10.1088/1361-665X/aa59eb.
[50] M.F. Funari, F. Greco, P. Lonetti, A moving interface finite element formulation for layered structures, Compos. Part B Eng. 96 (2016) 325–337. https://doi.org/10.1016/j.compositesb.2016.04.047.
[51] F. Greco, L. Leonetti, P. Lonetti, A novel approach based on ALE and delamination fracture mechanics for multilayered composite beams, Compos. Part B Eng. 78 (2015) 447–458. https://doi.org/10.1016/j.compositesb.2015.04.004.
[52] N. Triantafyllidis, M.D. Nestorović, M.W. Schraad, Failure Surfaces for Finitely Strained Two-Phase Periodic Solids Under General In-Plane Loading, J. Appl. Mech. 73 (2005) 505–515. https://doi.org/10.1115/1.2126695.
[53] K. Bertoldi, M.C. Boyce, S. Deschanel, S.M. Prange, T. Mullin, Mechanics of deformation-triggered pattern transformations and

superelastic behavior in periodic elastomeric structures, J. Mech. Phys. Solids. 56 (2008) 2642–2668. https://doi.org/10.1016/j.jmps.2008.03.006.

[54] J. Li, V. Slesarenko, S. Rudykh, Auxetic multiphase soft composite material design through instabilities with application for acoustic metamaterials, Soft Matter. 14 (2018) 6171–6180. https://doi.org/10.1039/C8SM00874D.

[55] J. Li, S. Rudykh, Tunable microstructure transformations and auxetic behavior in 3D-printed multiphase composites: The role of inclusion distribution, Compos. Part B Eng. 172 (2019) 352–362. https://doi.org/10.1016/j.compositesb.2019.05.012.

[56] D. Bruno, F. Greco, P. Lonetti, P.N. Blasi, G. Sgambitterra, An investigation on microscopic and macroscopic stability phenomena of composite solids with periodic microstructure, Int. J. Solids Struct. 47 (2010) 2806–2824. https://doi.org/10.1016/j.ijsolstr.2010.06.013.

[57] G. Cricrì, R. Luciano, Homogenised properties of composite materials in large deformations, Compos. Struct. 103 (2013) 9–17. https://doi.org/10.1016/j.compstruct.2013.03.015.

[58] M.D. Nestorović, N. Triantafyllidis, Onset of failure in finitely strained layered composites subjected to combined normal and shear loading, J. Mech. Phys. Solids. 52 (2004) 941–974. https://doi.org/10.1016/j.jmps.2003.06.001.

[59] V. Slesarenko, S. Rudykh, Microscopic and macroscopic instabilities in hyperelastic fiber composites, J. Mech. Phys. Solids. 99 (2017) 471–482. https://doi.org/10.1016/j.jmps.2016.11.002.

[60] S. Rudykh, K. Bertoldi, Stability of anisotropic magnetorheological elastomers in finite deformations: A micromechanical approach, J. Mech. Phys. Solids. 61 (2013) 949–967. https://doi.org/10.1016/j.jmps.2012.12.008.

[61] N. Triantafyllidis, M.D. Nestorović, M.W. Schraad, Failure Surfaces for Finitely Strained Two-Phase Periodic Solids Under General In-Plane Loading, J. Appl. Mech. 73 (2006) 505. https://doi.org/10.1115/1.2126695.

[62] N. Arora, A. Batan, J. Li, V. Slesarenko, S. Rudykh, On the Influence of Inhomogeneous Interphase Layers on Instabilities in Hyperelastic Composites, Materials. 12 (2019) 763. https://doi.org/10.3390/ma12050763.

[63] F. Greco, A study of stability and bifurcation in micro-cracked periodic elastic composites including self-contact, Int. J. Solids Struct. 50 (2013) 1646–1663. https://doi.org/10.1016/j.ijsolstr.2013.01.036.
[64] F. Greco, L. Leonetti, R. Luciano, P. Nevone Blasi, Effects of microfracture and contact induced instabilities on the macroscopic response of finitely deformed elastic composites, Compos. Part B Eng. 107 (2016) 233–253. https://doi.org/10.1016/j.compositesb.2016.09.042.
[65] O. Rabinovitch, Interaction, instability, and simultaneity of debonding processes in flexure of masonry walls strengthened on two sides with FRP, Int. J. Fract. 177 (2012) 1–24. https://doi.org/10.1007/s10704-012-9741-z.
[66] F. Greco, L. Leonetti, C.M. Medaglia, R. Penna, A. Pranno, Nonlinear compressive failure analysis of biaxially loaded fiber reinforced materials, Compos. Part B Eng. 147 (2018) 240–251. https://doi.org/10.1016/j.compositesb.2018.04.006.
[67] F. Greco, P. Lonetti, R. Luciano, P. Nevone Blasi, A. Pranno, Nonlinear effects in fracture induced failure of compressively loaded fiber reinforced composites, Compos. Struct. 189 (2018) 688–699. https://doi.org/10.1016/j.compstruct.2018.01.014.
[68] I. Babuška, Homogenization Approach In Engineering, in: R. Glowinski, J.L. Lions (Eds.), Comput. Methods Appl. Sci. Eng., Springer Berlin Heidelberg, Berlin, Heidelberg, 1976: pp. 137–153. https://doi.org/10.1007/978-3-642-85972-4_8.
[69] W. Voigt, Theoretische Studien über die Elasticitätsverhältnisse der Krystalle, 1887.
[70] G. Sachs, Plasticity problems in metals, Trans. Faraday Soc. 24 (1928) 84. https://doi.org/10.1039/tf9282400084.
[71] A. Reuss, Berechnung der Fließgrenze von Mischkristallen auf Grund der Plastizitätsbedingung für Einkristalle ., ZAMM - Z. Für Angew. Math. Mech. 9 (1929) 49–58. https://doi.org/10.1002/zamm.19290090104.
[72] G.I. Taylor, Plastic strain in metals, J. Inst. Met. 62 (1938) 307–324.
[73] J.D. Eshelby, The determination of the elastic field of an ellipsoidal inclusion, and related problems, Proc. R. Soc. Lond. Ser. Math.

Phys. Sci. 241 (1957) 376–396. https://doi.org/10.1098/rspa.1957.0133.

[74] R. Hill, Continuum micro-mechanics of elastoplastic polycrystals, J. Mech. Phys. Solids. 13 (1965) 89–101. https://doi.org/10.1016/0022-5096(65)90023-2.

[75] E. Kröner, Berechnung der elastischen Konstanten des Vielkristalls aus den Konstanten des Einkristalls, Z. Phys. 151 (1958) 504–518. https://doi.org/10.1007/BF01337948.

[76] Z. Hashin, S. Shtrikman, A variational approach to the theory of the elastic behaviour of multiphase materials, J. Mech. Phys. Solids. 11 (1963) 127–140. https://doi.org/10.1016/0022-5096(63)90060-7.

[77] R. Hill, Elastic properties of reinforced solids: Some theoretical principles, J. Mech. Phys. Solids. 11 (1963) 357–372. https://doi.org/10.1016/0022-5096(63)90036-X.

[78] T. Mori, K. Tanaka, Average stress in matrix and average elastic energy of materials with misfitting inclusions, Acta Metall. 21 (1973) 571–574. https://doi.org/10.1016/0001-6160(73)90064-3.

[79] J.R. Willis, Bounds and self-consistent estimates for the overall properties of anisotropic composites, J. Mech. Phys. Solids. 25 (1977) 185–202. https://doi.org/10.1016/0022-5096(77)90022-9.

[80] I.M. Babuska, Homogenization and its application. Mathematical and computa-tional problems, in: 1976. https://researchers.dellmed.utexas.edu/en/publications/homogenization-and-its-application-mathematical-and-computational (accessed October 25, 2019).

[81] E. Kröner, Zur plastischen verformung des vielkristalls, Acta Metall. 9 (1961) 155–161. https://doi.org/10.1016/0001-6160(61)90060-8.

[82] J.W. Hutchinson, Bounds and Self-Consistent Estimates for Creep of Polycrystalline Materials, Proc. R. Soc. Math. Phys. Eng. Sci. 348 (1976) 101–127. https://doi.org/10.1098/rspa.1976.0027.

[83] S. Nemat-Nasser, M. Obata, Rate-Dependent, Finite Elasto-Plastic Deformation of Polycrystals, Proc. R. Soc. Math. Phys. Eng. Sci. 407 (1986) 343–375. https://doi.org/10.1098/rspa.1986.0101.

[84] P.P. Castañeda, The effective mechanical properties of nonlinear isotropic composites, J. Mech. Phys. Solids. 39 (1991) 45–71. https://doi.org/10.1016/0022-5096(91)90030-R.

[85] P. Suquet, Effective Properties of Nonlinear Composites, in: P. Suquet (Ed.), Contin. Micromechanics, Springer Vienna, Vienna, 1997: pp. 197–264. https://doi.org/10.1007/978-3-7091-2662-2_4.
[86] J.R. Willis, Upper and lower bounds for non-linear composite behaviour, Mater. Sci. Eng. A. 175 (1994) 7–14. https://doi.org/10.1016/0921-5093(94)91038-3.
[87] S. Nemat-Nasser, M. Hori, Micromechanics: Overall Properties of Heterogeneous Materials, North-Holland, Amsterdam ; New York, 1993.
[88] A. Zaoui, R. Masson, Micromechanics-based modeling of plastic polycrystals: an affine formulation, Mater. Sci. Eng. A. 285 (2000) 418–424. https://doi.org/10.1016/S0921-5093(00)00687-0.
[89] E. Sánchez-Palencia, Non-homogeneous media and vibration theory, Springer-Verlag, 1980.
[90] M. Artola, G. Duvaut, Homogenization Results for a Class of Nonlinear Stationary Diffusion Problems, in: Var. Methods Mech. Solids, Elsevier, 1980: pp. 227–231. https://doi.org/10.1016/B978-0-08-024728-1.50039-2.
[91] P. Suquet, ed., Homogenization Techniques for Composite Media, Springer Berlin Heidelberg, Berlin, Heidelberg, 1987. https://doi.org/10.1007/3-540-17616-0.
[92] Winan E., Principles multiscale modeling | Mathematical modelling and methods, Camb. Univ. Press. (n.d.). https://www.cambridge.org/it/academic/subjects/mathematics/mathematical-modelling-and-methods/principles-multiscale-modeling, https://www.cambridge.org/it/academic/subjects/mathematics/mathematical-modelling-and-methods (accessed October 25, 2019).
[93] Winan E., Engquist B., Lao X.T., Ren W.Q., The heterogeneous multiscale method: A review, Commun Comput Phys. 2(3) (2007) 367–450.
[94] J. Fish, Multiscale Methods, Oxford University Press, 2009. https://doi.org/10.1093/acprof:oso/9780199233854.001.0001.
[95] J. Fish, Bridging the scales in nano engineering and science, J. Nanoparticle Res. 8 (2006) 577–594. https://doi.org/10.1007/s11051-006-9090-9.

[96] Y. Sheng, M. Sousani, D. Ingham, M. Pourkashanian, Recent Developments in Multiscale and Multiphase Modelling of the Hydraulic Fracturing Process, Math. Probl. Eng. 2015 (2015) 1–15. https://doi.org/10.1155/2015/729672.

[97] M. Ţene, M.S. Al Kobaisi, H. Hajibeygi, Algebraic multiscale method for flow in heterogeneous porous media with embedded discrete fractures (F-AMS), J. Comput. Phys. 321 (2016) 819–845. https://doi.org/10.1016/j.jcp.2016.06.012.

[98] P.R. Budarapu, S. Kumar, B.G. Prusty, M. Paggi, Stress transfer through the interphase in curved-fiber pullout tests of nanocomposites, Compos. Part B Eng. 165 (2019) 417–434. https://doi.org/10.1016/j.compositesb.2018.12.116.

[99] I. Wudtke, H. Talebi, M. Silani, F. Werner, A hierarchical multiscale approach to mechanical characterization of heat affected zone in welded connections, Comput. Mater. Sci. 96 (2015) 396–402. https://doi.org/10.1016/j.commatsci.2014.08.053.

[100] D. Lyu, H. Fan, S. Li, A hierarchical multiscale cohesive zone model and simulation of dynamic fracture in metals, Eng. Fract. Mech. 163 (2016) 327–347. https://doi.org/10.1016/j.engfracmech.2016.06.005.

[101] F. Feyel, J.-L. Chaboche, FE2 multiscale approach for modelling the elastoviscoplastic behaviour of long fibre SiC/Ti composite materials, Comput. Methods Appl. Mech. Eng. 183 (2000) 309–330. https://doi.org/10.1016/S0045-7825(99)00224-8.

[102] T. Belytschko, S. Loehnert, J.-H. Song, Multiscale aggregating discontinuities: A method for circumventing loss of material stability, Int. J. Numer. Methods Eng. 73 (2008) 869–894. https://doi.org/10.1002/nme.2156.

[103] V. Kouznetsova, M.G.D. Geers, W.A.M. Brekelmans, Multiscale constitutive modelling of heterogeneous materials with a gradient-enhanced computational homogenization scheme, Int. J. Numer. Methods Eng. 54 (2002) 1235–1260. https://doi.org/10.1002/nme.541.

[104] V.P. Nguyen, O. Lloberas-Valls, M. Stroeven, L.J. Sluys, Homogenization-based multiscale crack modelling: From micro-diffusive damage to macro-cracks, Comput. Methods Appl. Mech. Eng. 200 (2011) 1220–1236. https://doi.org/10.1016/j.cma.2010.10.013.

[105] C.V. Verhoosel, J.J.C. Remmers, M.A. Gutiérrez, A partition of unity-based multiscale approach for modelling fracture in piezoelectric ceramics, Int. J. Numer. Methods Eng. 82 (2009) 966–994. https://doi.org/10.1002/nme.2792.
[106] C.V. Verhoosel, J.J.C. Remmers, M.A. Gutiérrez, R. de Borst, Computational homogenization for adhesive and cohesive failure in quasi-brittle solids, Int. J. Numer. Methods Eng. 83 (2010) 1155–1179. https://doi.org/10.1002/nme.2854.
[107] I.M. Gitman, H. Askes, L.J. Sluys, Coupled-volume multiscale modelling of quasi-brittle material, Eur. J. Mech. - ASolids. 27 (2008) 302–327. https://doi.org/10.1016/j.euromechsol.2007.10.004.
[108] F. Greco, G. Sgambitterra, Validation of Homogenization Techniques for Locally Periodic Fiber-Reinforced Composites with Interfacial Debonding, Mech. Adv. Mater. Struct. 20 (2013) 638–651. https://doi.org/10.1080/15376494.2011.643283.
[109] H. Talebi, M. Silani, S.P.A. Bordas, P. Kerfriden, T. Rabczuk, MOLECULAR DYNAMICS/XFEM COUPLING BY A THREE-DIMENSIONAL EXTENDED BRIDGING DOMAIN WITH APPLICATIONS TO DYNAMIC BRITTLE FRACTURE, Int. J. Multiscale Comput. Eng. 11 (2013) 527–541. https://doi.org/10.1615/IntJMultCompEng.2013005838.
[110] P.R. Budarapu, R. Gracie, S.P.A. Bordas, T. Rabczuk, An adaptive multiscale method for quasi-static crack growth, Comput. Mech. 53 (2014) 1129–1148. https://doi.org/10.1007/s00466-013-0952-6.
[111] H. Talebi, M. Silani, T. Rabczuk, Concurrent multiscale modeling of three dimensional crack and dislocation propagation, Adv. Eng. Softw. 80 (2015) 82–92. https://doi.org/10.1016/j.advengsoft.2014.09.016.
[112] P.R. Budarapu, J. Reinoso, M. Paggi, Concurrently coupled solid shell-based adaptive multiscale method for fracture, Comput. Methods Appl. Mech. Eng. 319 (2017) 338–365. https://doi.org/10.1016/j.cma.2017.02.023.
[113] A. Shojaei, G. Li, J. Fish, P.J. Tan, Multi-scale constitutive modeling of Ceramic Matrix Composites by Continuum Damage Mechanics, Int. J. Solids Struct. 51 (2014) 4068–4081. https://doi.org/10.1016/j.ijsolstr.2014.07.026.

[114] F. Greco, L. Leonetti, R. Luciano, P. Nevone Blasi, An adaptive multiscale strategy for the damage analysis of masonry modeled as a composite material, Compos. Struct. 153 (2016) 972–988. https://doi.org/10.1016/j.compstruct.2016.06.066.

[115] W.J. Drugan, J.R. Willis, A micromechanics-based nonlocal constitutive equation and estimates of representative volume element size for elastic composites, J. Mech. Phys. Solids. 44 (1996) 497–524. https://doi.org/10.1016/0022-5096(96)00007-5.

[116] P. Evesque, Fluctuations, Correlation and Representative Elementary Volume (REV) in Granular Materials, ArXivcond-Mat0506385. (2005). http://arxiv.org/abs/cond-mat/0506385.

[117] V. Phu Nguyen, O. Lloberas-Valls, M. Stroeven, L. Johannes Sluys, On the existence of representative volumes for softening quasi-brittle materials – A failure zone averaging scheme, Comput. Methods Appl. Mech. Eng. 199 (2010) 3028–3038. https://doi.org/10.1016/j.cma.2010.06.018.

[118] R. Hill, Elastic properties of reinforced solids: Some theoretical principles, J. Mech. Phys. Solids. 11 (1963) 357–372. https://doi.org/10.1016/0022-5096(63)90036-X.

[119] S. Nemat-Nasser, M. Hori, Micromechanics: overall properties of heterogeneous materials, 2nd rev. ed, Elsevier, Amsterdam ; New York, 1999.

[120] I.M. Gitman, H. Askes, L.J. Sluys, Representative volume: Existence and size determination, Eng. Fract. Mech. 74 (2007) 2518–2534. https://doi.org/10.1016/j.engfracmech.2006.12.021.

[121] A. Drago, M. Pindera, Micro-macromechanical analysis of heterogeneous materials: Macroscopically homogeneous vs periodic microstructures, Compos. Sci. Technol. 67 (2007) 1243–1263. https://doi.org/10.1016/j.compscitech.2006.02.031.

[122] C. Huet, Application of variational concepts to size effects in elastic heterogeneous bodies, J. Mech. Phys. Solids. 38 (1990) 813–841. https://doi.org/10.1016/0022-5096(90)90041-2.

[123] S. Hazanov, C. Huet, Order relationships for boundary conditions effect in heterogeneous bodies smaller than the representative volume, J. Mech. Phys. Solids. 42 (1994) 1995–2011. https://doi.org/10.1016/0022-5096(94)90022-1.

[124] S. Hazanov, M. Amieur, On overall properties of elastic heterogeneous bodies smaller than the representative volume, Int. J.

Eng. Sci. 33 (1995) 1289–1301. https://doi.org/10.1016/0020-7225(94)00129-8.
[125] S. Pecullan, L.V. Gibiansky, S. Torquato, Scale effects on the elastic behavior of periodic andhierarchical two-dimensional composites, J. Mech. Phys. Solids. 47 (1999) 1509–1542. https://doi.org/10.1016/S0022-5096(98)00111-2.
[126] G.L. Povirk, Incorporation of microstructural information into models of two-phase materials, Acta Metall. Mater. 43 (1995) 3199–3206. https://doi.org/10.1016/0956-7151(94)00487-3.
[127] M. Jiang, K. Alzebdeh, I. Jasiuk, M. Ostoja-Starzewski, Scale and boundary conditions effects in elastic properties of random composites, Acta Mech. 148 (2001) 63–78. https://doi.org/10.1007/BF01183669.
[128] W.J. Drugan, J.R. Willis, A micromechanics-based nonlocal constitutive equation and estimates of representative volume element size for elastic composites, J. Mech. Phys. Solids. 44 (1996) 497–524. https://doi.org/10.1016/0022-5096(96)00007-5.
[129] A.A. Gusev, Representative volume element size for elastic composites: A numerical study, J. Mech. Phys. Solids. 45 (1997) 1449–1459. https://doi.org/10.1016/S0022-5096(97)00016-1.
[130] C. Miehe, J. Schotte, J. Schröder, Computational micro–macro transitions and overall moduli in the analysis of polycrystals at large strains, Comput. Mater. Sci. 16 (1999) 372–382. https://doi.org/10.1016/S0927-0256(99)00080-4.
[131] K. Terada, I. Saiki, K. Matsui, Y. Yamakawa, Two-scale kinematics and linearization for simultaneous two-scale analysis of periodic heterogeneous solids at finite strain, Comput. Methods Appl. Mech. Eng. 192 (2003) 3531–3563. https://doi.org/10.1016/S0045-7825(03)00365-7.
[132] K. Matsui, K. Terada, K. Yuge, Two-scale finite element analysis of heterogeneous solids with periodic microstructures, Comput. Struct. 82 (2004) 593–606. https://doi.org/10.1016/j.compstruc.2004.01.004.
[133] M.E. Gurtin, An Introduction to Continuum Mechanics, Academic Press, 1982.
[134] R. Hill, A self-consistent mechanics of composite materials, J. Mech. Phys. Solids. 13 (1965) 213–222. https://doi.org/10.1016/0022-5096(65)90010-4.

[135] K. Terada, M. Hori, T. Kyoya, N. Kikuchi, Simulation of the multi-scale convergence in computational homogenization approaches, Int. J. Solids Struct. 37 (2000) 2285–2311. https://doi.org/10.1016/S0020-7683(98)00341-2.

[136] M.G.D. Geers, V.G. Kouznetsova, K. Matouš, J. Yvonnet, Homogenization Methods and Multiscale Modeling: Nonlinear Problems, in: E. Stein, R. de Borst, T.J.R. Hughes (Eds.), Encycl. Comput. Mech. Second Ed., John Wiley & Sons, Ltd, Chichester, UK, 2017: pp. 1–34. https://doi.org/10.1002/9781119176817.ecm2107.

[137] F.G. Yuan, N.J. Pagano, X. Cai, Elastic moduli of brittle matrix composites with interfacial debonding, Int. J. Solids Struct. 34 (1997) 177–201. https://doi.org/10.1016/S0020-7683(96)00003-0.

[138] P. Bisegna, R. Luciano, Bounds on the overall properties of composites with debonded frictionless interfaces, Mech. Mater. 28 (1998) 23–32. https://doi.org/10.1016/S0167-6636(97)00046-X.

[139] H. Teng, Transverse stiffness properties of unidirectional fiber composites containing debonded fibers, Compos. Part Appl. Sci. Manuf. 38 (2007) 682–690. https://doi.org/10.1016/j.compositesa.2006.10.002.

[140] A. Caporale, R. Luciano, E. Sacco, Micromechanical analysis of interfacial debonding in unidirectional fiber-reinforced composites, Comput. Struct. 84 (2006) 2200–2211. https://doi.org/10.1016/j.compstruc.2006.08.023.

[141] D. Bruno, F. Greco, P. Lonetti, P. Nevone Blasi, Influence of micro-cracking and contact on the effective properties of composite materials, Simul. Model. Pract. Theory. 16 (2008) 861–884. https://doi.org/10.1016/j.simpat.2008.05.006.

[142] F. Greco, Homogenized mechanical behavior of composite micro-structures including micro-cracking and contact evolution, Eng. Fract. Mech. 76 (2009) 182–208. https://doi.org/10.1016/j.engfracmech.2008.09.006.

[143] J. Guedes, N. Kikuchi, Preprocessing and postprocessing for materials based on the homogenization method with adaptive finite element methods, Comput. Methods Appl. Mech. Eng. 83 (1990) 143–198. https://doi.org/10.1016/0045-7825(90)90148-F.

[144] C. Miehe, J. Schröder, J. Schotte, Computational homogenization analysis in finite plasticity Simulation of texture development in polycrystalline materials, Comput. Methods Appl. Mech. Eng. 171 (1999) 387–418. https://doi.org/10.1016/S0045-7825(98)00218-7.

[145] F. Feyel, J.-L. Chaboche, FE2 multiscale approach for modelling the elastoviscoplastic behaviour of long fibre SiC/Ti composite materials, Comput. Methods Appl. Mech. Eng. 183 (2000) 309–330. https://doi.org/10.1016/S0045-7825(99)00224-8.

[146] V. Kouznetsova, M.G.D. Geers, W.A.M. Brekelmans, Multi-scale constitutive modelling of heterogeneous materials with a gradient-enhanced computational homogenization scheme, Int. J. Numer. Methods Eng. 54 (2002) 1235–1260. https://doi.org/10.1002/nme.541.

[147] I.M. Gitman, H. Askes, L.J. Sluys, Coupled-volume multi-scale modelling of quasi-brittle material, Eur. J. Mech. - ASolids. 27 (2008) 302–327. https://doi.org/10.1016/j.euromechsol.2007.10.004.

[148] F.F. Abraham, J.Q. Broughton, N. Bernstein, E. Kaxiras, Spanning the continuum to quantum length scales in a dynamic simulation of brittle fracture, Europhys. Lett. EPL. 44 (1998) 783–787. https://doi.org/10.1209/epl/i1998-00536-9.

[149] E.B. Tadmor, M. Ortiz, R. Phillips, Quasicontinuum analysis of defects in solids, Philos. Mag. A. 73 (1996) 1529–1563. https://doi.org/10.1080/01418619608243000.

[150] G.J. Wagner, W.K. Liu, Coupling of atomistic and continuum simulations using a bridging scale decomposition, J. Comput. Phys. 190 (2003) 249–274. https://doi.org/10.1016/S0021-9991(03)00273-0.

[151] S.P. Xiao, T. Belytschko, A bridging domain method for coupling continua with molecular dynamics, Comput. Methods Appl. Mech. Eng. 193 (2004) 1645–1669. https://doi.org/10.1016/j.cma.2003.12.053.

[152] P. Raghavan, S. Ghosh, Concurrent multi-scale analysis of elastic composites by a multi-level computational model, Comput. Methods Appl. Mech. Eng. 193 (2004) 497–538. https://doi.org/10.1016/j.cma.2003.10.007.

[153] F.J. Vernerey, M. Kabiri, An adaptive concurrent multiscale method for microstructured elastic solids, Comput. Methods Appl. Mech. Eng. 241–244 (2012) 52–64. https://doi.org/10.1016/j.cma.2012.04.021.
[154] S. Ghosh, J. Bai, P. Raghavan, Concurrent multi-level model for damage evolution in microstructurally debonding composites, Mech. Mater. 39 (2007) 241–266. https://doi.org/10.1016/j.mechmat.2006.05.004.
[155] C. Bernardi, Y. Maday, A.T. Patera, Domain Decomposition by the Mortar Element Method, in: H.G. Kaper, M. Garbey, G.W. Pieper (Eds.), Asymptot. Numer. Methods Partial Differ. Equ. Crit. Parameters, Springer Netherlands, Dordrecht, 1993: pp. 269–286. https://doi.org/10.1007/978-94-011-1810-1_17.
[156] V. Tvergaard, Cohesive zone representations of failure between elastic or rigid solids and ductile solids, Eng. Fract. Mech. 70 (2003) 1859–1868. https://doi.org/10.1016/S0013-7944(03)00128-0.
[157] Q. Nguyen, X. Chateau, Buckling of elastic structures in unilateral contact with or without friction, Eur. J. Mech. - ASolids. 10 (1991) 1–17.
[158] COMSOL AB. COMSOL 5.3 Multiphysics user's guide, (2017).
[159] D. Bruno, F. Greco, R. Luciano, P. Nevone Blasi, Nonlinear homogenized properties of defected composite materials, Comput. Struct. 134 (2014) 102–111. https://doi.org/10.1016/j.compstruc.2013.11.018.
[160] F. Greco, P. Lonetti, R. Luciano, P.N. Blasi, A. Pranno, Nonlinear effects in fracture induced failure of compressively loaded fiber reinforced composites, Compos. Struct. (2018). https://doi.org/10.1016/j.compstruct.2018.01.014.
[161] S. Nemat-Nasser, Averaging theorems in finite deformation plasticity, Mech. Mater. 31 (1999) 493–523. https://doi.org/10.1016/S0167-6636(98)00073-8.
[162] F. Greco, P. Lonetti, R. Luciano, P. Nevone Blasi, A. Pranno, Nonlinear effects in fracture induced failure of compressively loaded fiber reinforced composites, Compos. Struct. 189 (2018) 688–699. https://doi.org/10.1016/j.compstruct.2018.01.014.

[163] F. Greco, L. Leonetti, C.M. Medaglia, R. Penna, A. Pranno, Nonlinear compressive failure analysis of biaxially loaded fiber reinforced materials, Compos. Part B Eng. 147 (2018) 240–251. https://doi.org/10.1016/j.compositesb.2018.04.006.

[164] D. Bruno, F. Greco, P. Lonetti, P.N. Blasi, G. Sgambitterra, An investigation on microscopic and macroscopic stability phenomena of composite solids with periodic microstructure, Int. J. Solids Struct. 47 (2010) 2806–2824. https://doi.org/10.1016/j.ijsolstr.2010.06.013.

[165] F. Greco, A study of stability and bifurcation in micro-cracked periodic elastic composites including self-contact, Int. J. Solids Struct. 50 (2013) 1646–1663. https://doi.org/10.1016/j.ijsolstr.2013.01.036.

[166] F. Greco, R. Luciano, A theoretical and numerical stability analysis for composite micro-structures by using homogenization theory, Compos. Part B Eng. 42 (2011) 382–401. https://doi.org/10.1016/j.compositesb.2010.12.006.

[167] F. Greco, L. Leonetti, R. Luciano, P. Nevone Blasi, Effects of microfracture and contact induced instabilities on the macroscopic response of finitely deformed elastic composites, Compos. Part B Eng. 107 (2016) 233–253. https://doi.org/10.1016/j.compositesb.2016.09.042.

[168] D. Bruno, F. Greco, R. Luciano, P. Nevone Blasi, Nonlinear homogenized properties of defected composite materials, Comput. Struct. 134 (2014) 102–111. https://doi.org/10.1016/j.compstruc.2013.11.018.

[169] F. Greco, P. Lonetti, P.N. Blasi, G. Sgambitterra, Macroscopic Stability Analysis in Periodic Composite Solids, in: A. Öchsner, L.F.M. da Silva, H. Altenbach (Eds.), Mater. Complex Behav., Springer Berlin Heidelberg, Berlin, Heidelberg, 2010: pp. 213–242. https://doi.org/10.1007/978-3-642-12667-3_14.

[170] I.M. Gitman, H. Askes, L.J. Sluys, Coupled-volume multi-scale modelling of quasi-brittle material, Eur. J. Mech. - ASolids. 27 (2008) 302–327. https://doi.org/10.1016/j.euromechsol.2007.10.004.

[171] R.W. Ogden, Extremum principles in non-linear elasticity and their application to composites—I, Int. J. Solids Struct. 14 (1978) 265–282. https://doi.org/10.1016/0020-7683(78)90037-9.

[172] D. Lee, N. Triantafyllidis, J.R. Barber, M.D. Thouless, Surface instability of an elastic half space with material properties varying with depth, J. Mech. Phys. Solids. 56 (2008) 858–868. https://doi.org/10.1016/j.jmps.2007.06.010.